MODEL WAVE IMPULSE LOADS ON CAISSON BREAKWATERS: AERATION, SCALE AND STRUCTURAL RESPONSE.

by

MICHAEL JAMES ALEXIS WALKDEN

A thesis submitted to the University of Plymouth
in partial fulfilment for the degree of

DOCTOR OF PHILOSOPHY

School of Civil and Structural Engineering
Faculty of Technology

May 1999

What we observe is not nature itself,
but nature exposed to our method of questioning

Werner Hisenberg

Michael James Alexis Walkden

MODEL WAVE IMPULSE LOADS ON CAISSON BREAKWATERS: AERATION, SCALE AND STRUCTURAL RESPONSE.

Abstract

The prediction of wave impact loads on prototype caisson breakwaters from the results of physical model tests is considered, with particular attention given to the effects of air, breaker shape, structural response and scale. A review of related literature is presented from which it is concluded that the different aspects of the problem may be related through the force impulse. Large scale soliton impacts are used to show the importance of entrapped air in determining the form of the load time history. Small scale waves with artificially high levels of entrained air and highly controlled drop impacts are used to show and quantify an inverse relationship between entrained air and impact load maxima. Specially developed aeration probes and analysis techniques are used to show the influence of entrapped air on pressure maxima and quantify entrained air levels in small scale fresh water breaking waves. A definition of the force impulse is proposed and used to investigate its variation with breaker shape. The impulse magnitude is shown to be relatively invariant for regular wave impacts compared to a large scatter in impulse form. A numerical model of caisson dynamics is used to predict structural motion and to calculate a series of dynamic amplification factors. The prediction of structural response to obtain effective static loads through the use of these factors is investigated and achieved through the adoption of an 'equivalent impulse' concept. The scatter in impulse form is found to cause large variations in effective static loads between nominally identical impact events. The equivalent impulse concept is used to solve this problem. A comparison is made between the form and magnitude of the force impulses of the small and large scale waves. The results indicate that the impulse magnitude may be relatively free of scale effects. An example is given in which the results of a small scale test are interpreted, scaled and processed to account for the effects of entrained air and structural response in order to predict large scale effective static loads. These are shown to compare well with predictions made using measured large scale force time histories and the numerical caisson model.

Contents

List of figures

List of tables

Principal symbols

β	Void fraction
ν	Dynamic amplification factor
ρ	Density
C	Damping coefficient
F	Force
F_0	Impact force at 0 % aeration
F_β	Impact force at β % aeration
F_{max}	Maximum impact force
$F_{max.eq}$	Equivalent maximum impact force
FRF	Force reduction factor
F_{stat}	Effective static force
g	Acceleration due to gravity
H	Wave height
I_{goda}	Impulse magnitude defined by Goda
I_{mp}	Impulse magnitude
$I_{mp.average}$	Average impulse magnitude
IP	Impulse proportion, normalised impulse magnitude
I_{pr}	Pressure rise impulse
K	Stiffness coefficient
M	Mass
N_H	Scale ratio of wave height
N_L	Scale ratio of length
N_T	Scale ratio of time
P	Pressure
P_{max}	Maximum impact pressure
R_{p0}	Electrical resistance of an unvoided medium
R_{pl}	Electrical resistance in a voided medium
t_{end}	Moment at which the force impulse ends
T	Wave period
T_{fr}	Force rise time

T_d	Force impulse duration
$T_{d.eq}$	Equivalent force impulse duration
T_n	Natural period
T_{pmax}	Time of occurrence of maximum impact pressure
T_{pr}	Pressure rise time
T_r	Rise time
x	Displacement
$\dot{x}$	Velocity
$\ddot{x}$	Acceleration

Acknowledgements

The EU marine science and technology program (MAST) and the University of Plymouth provided most of the financial support for this project.

The study was supervised by Peter Hewson and Professor Geoff Bullock. I would like to thank Peter for his continual support, encouragement and sound judgement and Geoff for getting me into research in the first place and his well timed and well considered advice.

The co-operation and collaboration of other institutions has been particularly important to this work. I would therefore like to thank Professor Oumeraci, and the Universities of Hannover and Braunschweig for enabling the large scale experiments in the Grosser Wellen Kanal, and Peter Klammer and Adam Crawford for their help in carrying them out. Other experiments were made possible by the University of Edinburgh's Mechanical Engineering Department and, in particular, the generous help of Tom Bruce. I would also like to acknowledge the education, advice and experience I received from my colleagues during MAST II and MAST PROVERBS.

Thanks to all of those who kept me sane, and some of those who had the opposite effect, during the considerable length of time it took me to prepare this thesis. I am grateful to far too many people to mention here but I would like to thank Alison for being there, Hamish 'Young Dude' with whom I learned something of the poetry of waves, Andy Ratquiff for his perspective in times of emergency and my father who was also my editor.

I would also like to thank those who take the time to read some of this thesis. I hope you quickly see its purpose (Ch's 3, 7, 8 & 9, in particular) and can excuse its faults.

This work is dedicated to my mother, Nina Beaven.

AUTHOR'S DECLARATION

At no time during the registration for the degree of Doctor of Philosophy has the author been registered for any other University award.

This study was financed with the aid of an EU Marine Science and Technology (MAST) contract.

A program of advanced study was undertaken which included a MAST course on the probabilistic design of coastal structures and a postgraduate course in coastal engineering.

Publications

Walkden, M.J. and Bruce T. (1999). "Scatter in wave impact load maxima: a review". *Paper presented at the ASCE Coastal Structures Conference, Santander.*

Walkden, M.J., Wood, D.J., Bruce, T. and Peregrine, D.H. "Seaward loads on Caisson Breakwaters". *Paper presented at MAST PROVERBS workshop in Caen, Submitted to the Journal of Coastal Engineering in Oct. '98.*

Muller, G., and Walkden, M. (1998) "Survivability assessment of shoreline OWC wave power stations". *Proceedings OMAE 1998, requested for review for the OMAE Journal.*

Walkden, M., Muller, G. and Bruce, T. (1998). "Low-cost particle image velocimetry: system and application". *Proceedings of the Offshore and Polar Engineering Conference.*

Walkden, M.J., Hewson, P.J., and Bullock, G.N., 1996, "Wave Impulse Prediction for Caisson Design". *Paper presented at the 25th International Conference on Coastal Engineering, Orlando, USA.*

Walkden, M.J., Crawford, A.R., Bird, P.A.D., Hewson, P.J., and Bullock, G.N. (1995). "Wave Impact Loading on Vertical Structures". *Paper presented at the ICE Coastal Structures and Breakwaters conference, London, April, Thomas Telford, pp 273-286, Ed. Clifford, J.E.*

Crawford, A., Walkden, M., Bullock, G., Bird, P., Hewson, P. and Griffiths, J. (1994). "Wave impacts on sea walls and breakwaters". *Paper presented at the ASCE International Conference on Coastal Dynamics, pp 656 - 670.*

Signed Mike WALKden

Date 10/10/99

Chapter 1

Introduction

Caisson breakwaters are structures built in the near-shore to reflect wave energy in order to create artificial harbours. They are usually made as a vertically sided rectangular caisson mounted on a rubble mound. These structures have many modes of failure including partial or overall collapse of the caisson, as well as erosion and slip failure of the mound or seabed. The principle mode is landward sliding of the caisson due to the forces created during the reflection of impinging waves. It is this mode which is considered in this thesis. For a complete description of the other failure modes the reader is referred to the final report of EU MAST PROVERBS (European Union, Marine Science and Technology project - Probabilistic Design Tools for Vertical Breakwaters) which is currently in print.

It is difficult to predict the impact loads caused by breaking waves largely because of uncertainties associated with the prediction of breaker form. This is one of the reasons why physical model tests are sometimes used. They have the advantage that if the model, foreshore, and incident wave field are correctly modelled, appropriate breaker forms emerge naturally. The interpretation of the results of such tests is not straightforward. It is believed that the forces caused by an impacting wave depend upon the scale of that wave. It is also believed that the importance of scale arises because of differences between the aeration characteristics of model and prototype waves. This thesis investigates the nature of the relationships between aeration, scale, and impact loads in a context which is relevant to the design of caisson breakwaters; its objectives are:

- To obtain measurements of aeration within small scale impacting waves.
- The development of a methodology for the prediction of prototype design loads from model results taking into account scale and dynamic behaviour.
- The investigation of breaking wave force impulses, i.e. how its magnitude and form varies with aeration, scale and breaker shape.

These are met through unique tests: simultaneous measurements of aeration and impact loads, comparative large and small scale flume tests and the use of drop tests to understand the effects of aeration.

A large part of this work was conducted for MCS II (EU MAST project -Monolithic Caisson Structures II) and PROVERBS. Consequently some of its results and conclusions have been accepted and adopted by PROVERBS as part of its final report. This project is also a part of ongoing work into wave impact loading based at the University of Plymouth (UoP). This began in the 1980's with field measurements on seawalls in southern England which highlighted the importance of wave aeration. In the early 1990's more field work and some laboratory work was conducted which included measurements of wave aeration. Although these projects provided some background knowledge for this work the equipment and methodology used to measure aeration was different. Entirely original probes and analysis techniques were developed by the author during this study.

There is one UoP based study of wave loads which is contemporary with this work. This is a comprehensive field study of the wave loads occurring on the breakwater of the UK Channel Island of Alderney. This field data would have benefited this project greatly and allowed a more extensive validation of the ideas and methodology proposed in this thesis. Unfortunately this field data awaits publication and so is unavailable at this time.

This study began with a review of related literature which is described in Chapter two. It revealed three important gaps in knowledge:

- There was no unifying framework of ideas with which aeration, scale, structure response and impact loads could be linked.
- Although the effects of aeration have been a subject of speculation and some theoretical description, these have not been supported by measurements of aeration in small scale impacting waves.
- Laboratory based scale tests of impact loads on vertical walls had not been done, or at least not reported.

Significant progress was made in these three areas during this work. The first is discussed in Chapter three, in which a new framework of ideas based on the force impulse is proposed. The development of new probes and analysis techniques for the measurement of

aeration in model impacting waves is described in Chapter four, whilst Chapter five describes the various experiments conducted. These include small and large scale wave impact tests, a series of aerated drop tests and other ancillary experiments. The new aeration equipment was found to function well and provided original and unique data on air in impacting model waves which is given in Chapter six. This revealed that only a small amount of air was mixed into the waves during impact and also allowed the description of a relationship between impact load and air trapped between the wave and wall. The importance of this air in determining the shape of the load time history is also shown with large scale solitary waves. The results of the drop tests are analysed to show a relationship between the quantities of air mixed into the water and reductions in force maxima.

A definition for the force impulse is proposed in Chapter seven and used to investigate the relationship between impulse magnitude and breaker form. Regular wave impact data is used to show that the impulse form can be highly scattered, even for nominally identical impact events. In Chapter eight the relationship between hydrodynamic loading and structural dynamic behaviour is considered and a mass-spring-dashpot model is used to provide dynamic amplification factors. Both the model and these factors are then used to predict structure response to measured wave impact loads. It is shown that dynamic amplification factors over-predict. A solution is proposed using 'equivalent' impulses which represent the impulse magnitude and form as a simple triangle. A technique for overcoming the natural scatter in impulse form to account for structure response is also proposed.

A comparison between the large and small scale test results is made in Chapter nine. This is done in an unorthodox way due to a lack of geometric similarity in the model boundary conditions. The results suggest that the Froude criterion describes the scaling of the impulse magnitude. An example is given of the prediction of a large scale wave impact load from small scale data which includes a means of accounting for structure response, and the effects of scale/aeration on the impulse form.

The results support the hypothesis proposed in Chapter three that a framework of ideas based on the force impulse can be used to relate aeration, scale, structural dynamics and impact loads. The new approach provides a method with which to predict prototype design loads for the landward sliding failure mode. Given natural limitations in the scope of this study the approach requires more development before being used in practice.

Chapter 2

Literature review

2.0 Introduction

This chapter describes some of the literature which was reviewed during this study. A simple explanation of wave impact phenomena is first presented to establish terminology and provide a foundation for discussion. The section which follows provides background understanding of the need for physical models of wave impacts, the role that they play in research and the difficulties associated with them. Following this is a broad review of studies which have considered and modelled aeration in wave impacts. Reviews of work concerned with scaling, structure response and breaker shape are presented in subsequent sections. Finally, several standard design methods are examined to reveal how they have overcome gaps in knowledge to provide the means of predicting wave impact loads for the purposes of design.

Wave impacts are complex phenomena and our understanding of them is still emerging. Consequently a broad based review of the subject is difficult to divide into discrete classifications and many of the publications mentioned below appear in more than one section.

2.1 Wave impact phenomena

Non-breaking ideal sinusoidal deep water waves appear to progress because of the phased orbital motion of water particles within them, as illustrated in Figure 2.1. No individual particle translates with the wave so there is no mass transport of water.

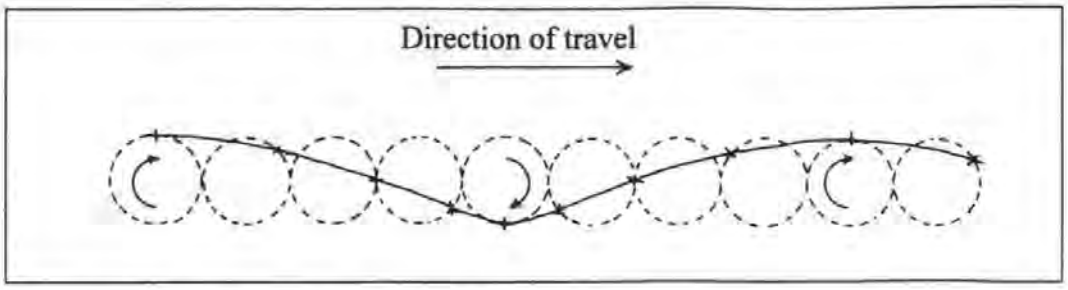

Figure 2.1. Orbital water motion within a wave.

Consequently it is the orbiting particles of water, rather than the waves, which have momentum. In contrast, when a wave has shoaled and steepened the orbital motion is deformed into mainly horizontal translational movement. As a consequence, breaking waves can be understood as having intrinsic momentum. When a wave arrives at a reflecting barrier, such as a vertical wall, and its momentum is affected, it produces a force (F) and experiences an equal and opposite reaction. This force is equal to the rate of momentum change.

$$F = \frac{dMo}{dt}$$

Where Mo is the wave momentum, so that;

$$\int F\,dt = total\ change\ in\ momentum$$

The momentum is the product of the mass (m) and velocity (V) of the wave, therefore;

$$dMo = \frac{\partial Mo}{\partial m}dm + \frac{\partial Mo}{\partial V}dV$$

In order to describe m and V theoretically it is necessary to predict the external form of the wave and its internal kinematic field. At present this can not be achieved except for some special cases. However, wave impact forces can be measured relatively easily in laboratory flumes. A force time history which was recorded during the impact of a two dimensional small scale model wave on a vertical wall is shown in Figure 2.2.

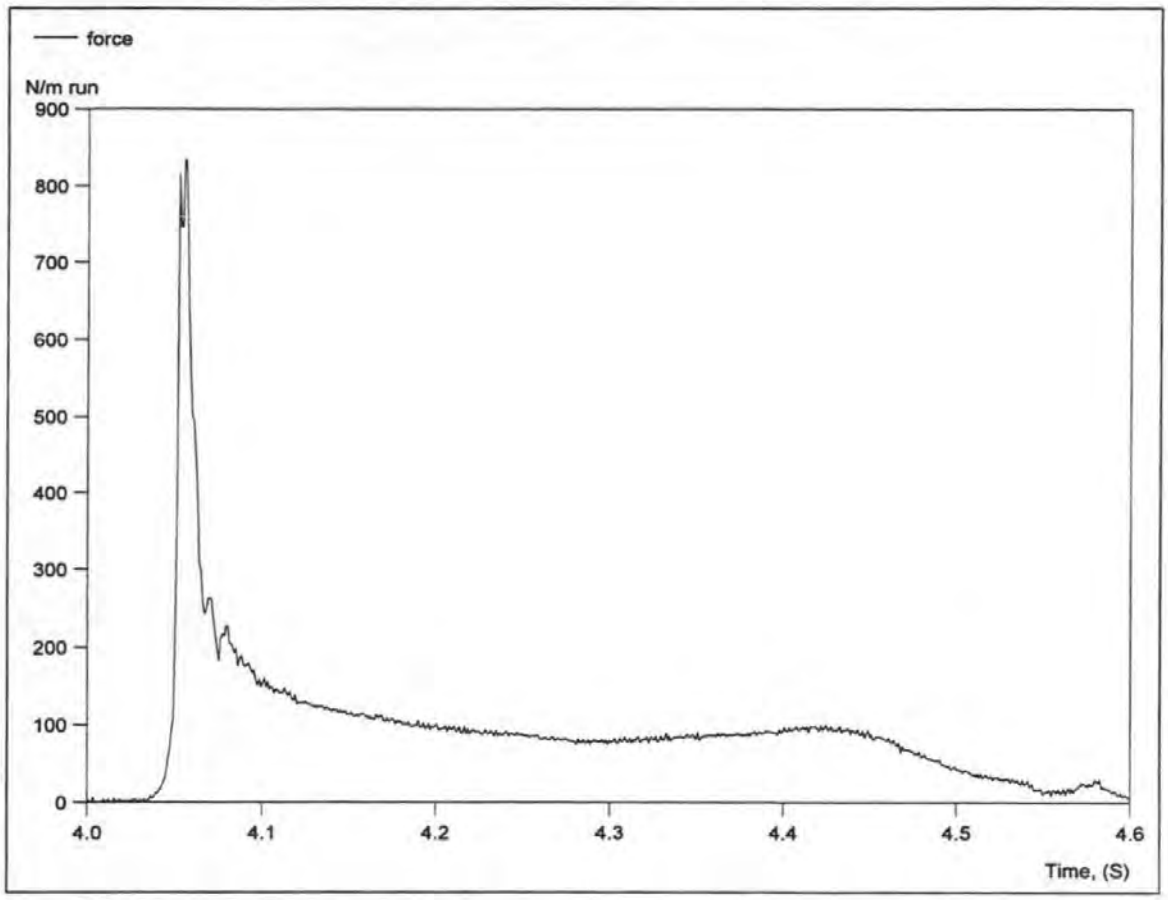

Figure 2.2. Example force time history.

More detail of the early stages of this impact can be seen in Figure 2.3, which also highlights features of the force time history that have received attention during wave impact research.

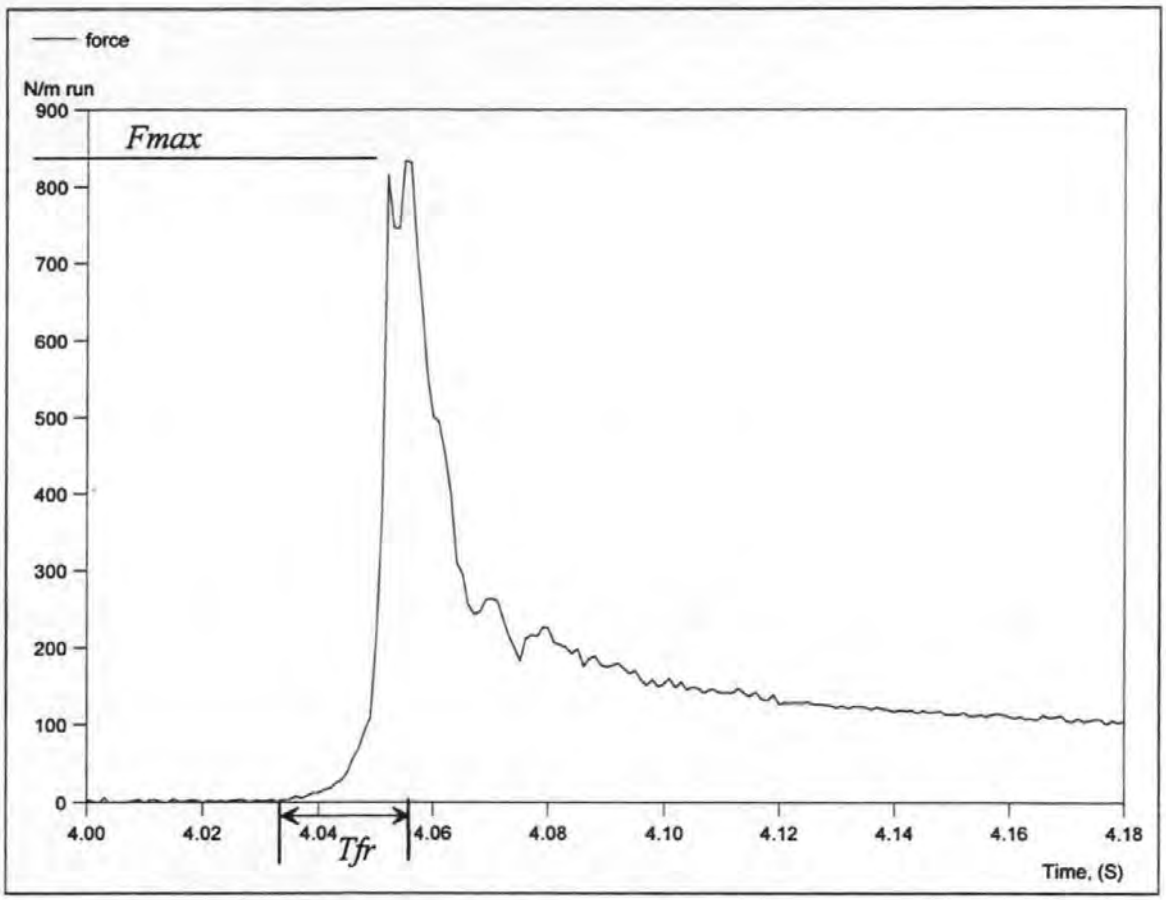

Figure 2.3. Expanded section of Figure 2.2, showing the maximum impact force F_{max} and the rise time T_{fr}.

Force time histories, such as the one shown in Figures 2.2 and 2.3 were obtained through spacewise integration of pressure time histories recorded at a variety of elevations on the wall (see section 7.1 for a description of how this was done). Two of the pressure time histories that contributed to this force time history are shown in Figure 2.4.

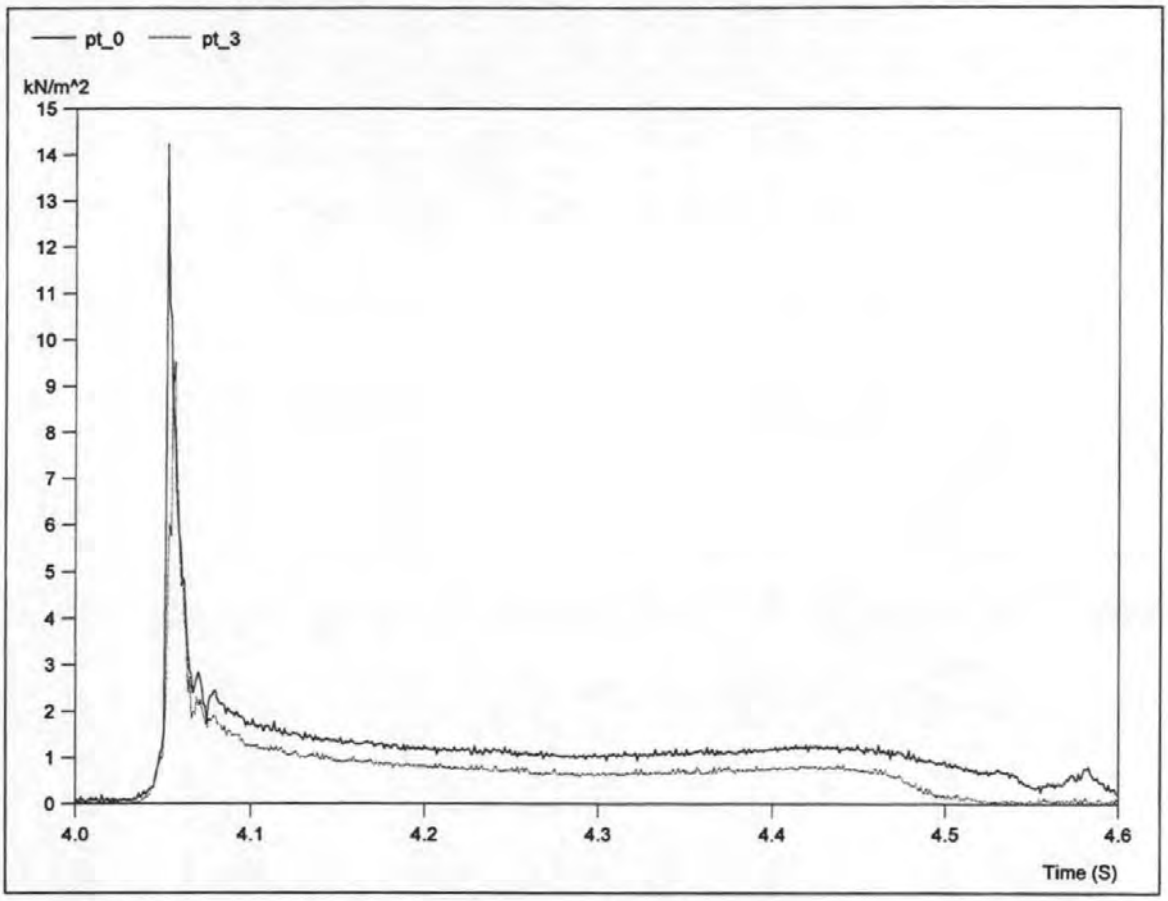

Figure 2.4. Two pressure time histories recorded at different elevations during the same impact.

More detail of one of these pressure time histories is shown in Figure 2.5. This figure also shows the properties of pressure time histories that have been often been measured during wave impact research.

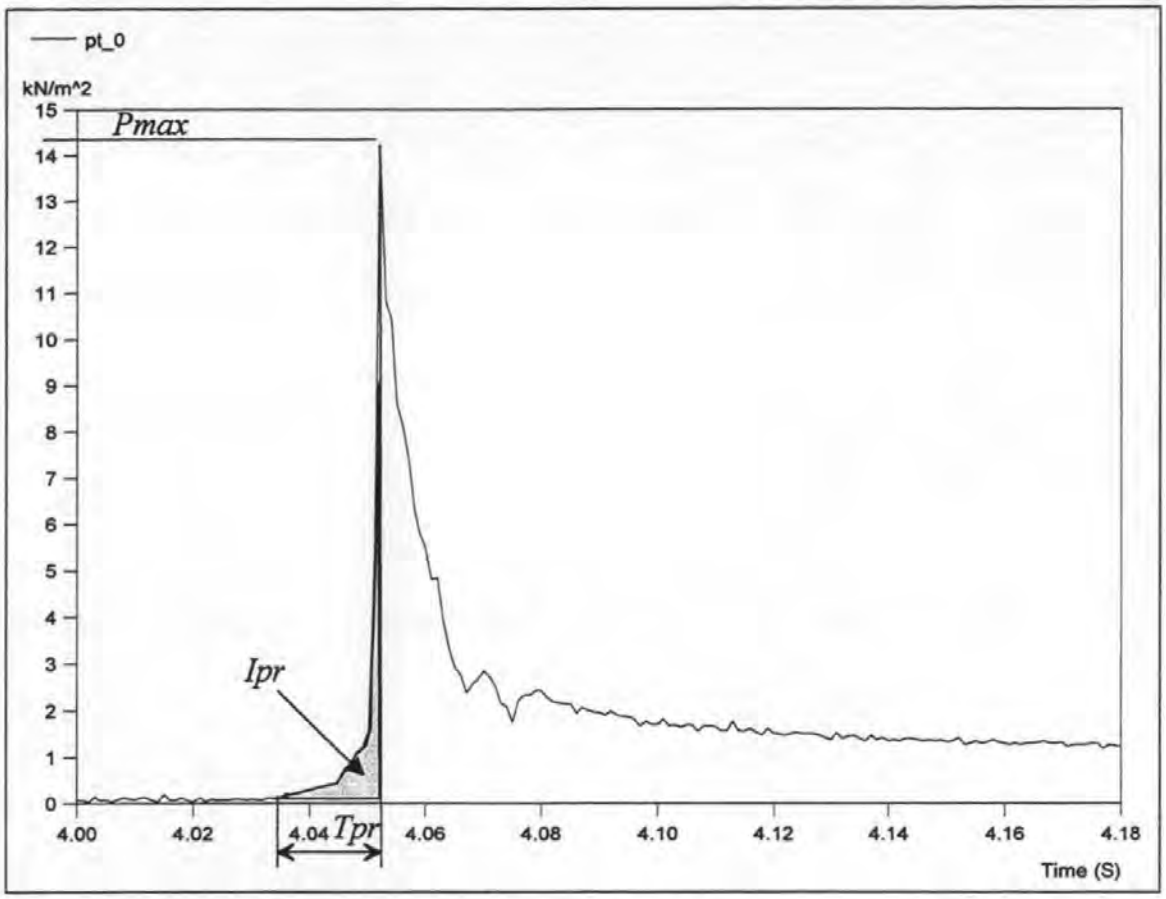

Figure 2.5. Expanded view of a pressure time history showing pressure maxima (P_{max}), rise time (T_{pr}) and pressure rise impulse (I_{pr}).

As was indicated above, the pressure and force time histories depend upon both the external shape and the internal kinematics of the wave. For this reason it is necessary to specify breaker shape when discussing and comparing impact loads. Since there is no universally agreed standard set of breaker shape definitions, the following is proposed and will be used throughout this study;

1 'Steep': the wave is steep but not overhanging.

2 'Flip-through': a direct impact of the wave front on the wall is preceded and prevented by the rapid rise of a tongue of water at the wall.

3 'Small air pocket': the crest of the wave overhangs, trapping a small pocket of air.

4 'Large air pocket': a more developed impact, the overhanging crest traps a larger pocket of air.

5 'Toe breaker': the wave crest plunges to the toe of the caisson.

6 'Beach breaker': the wave crest plunges onto the berm.

These breaker shapes are illustrated in Figure 2.6.

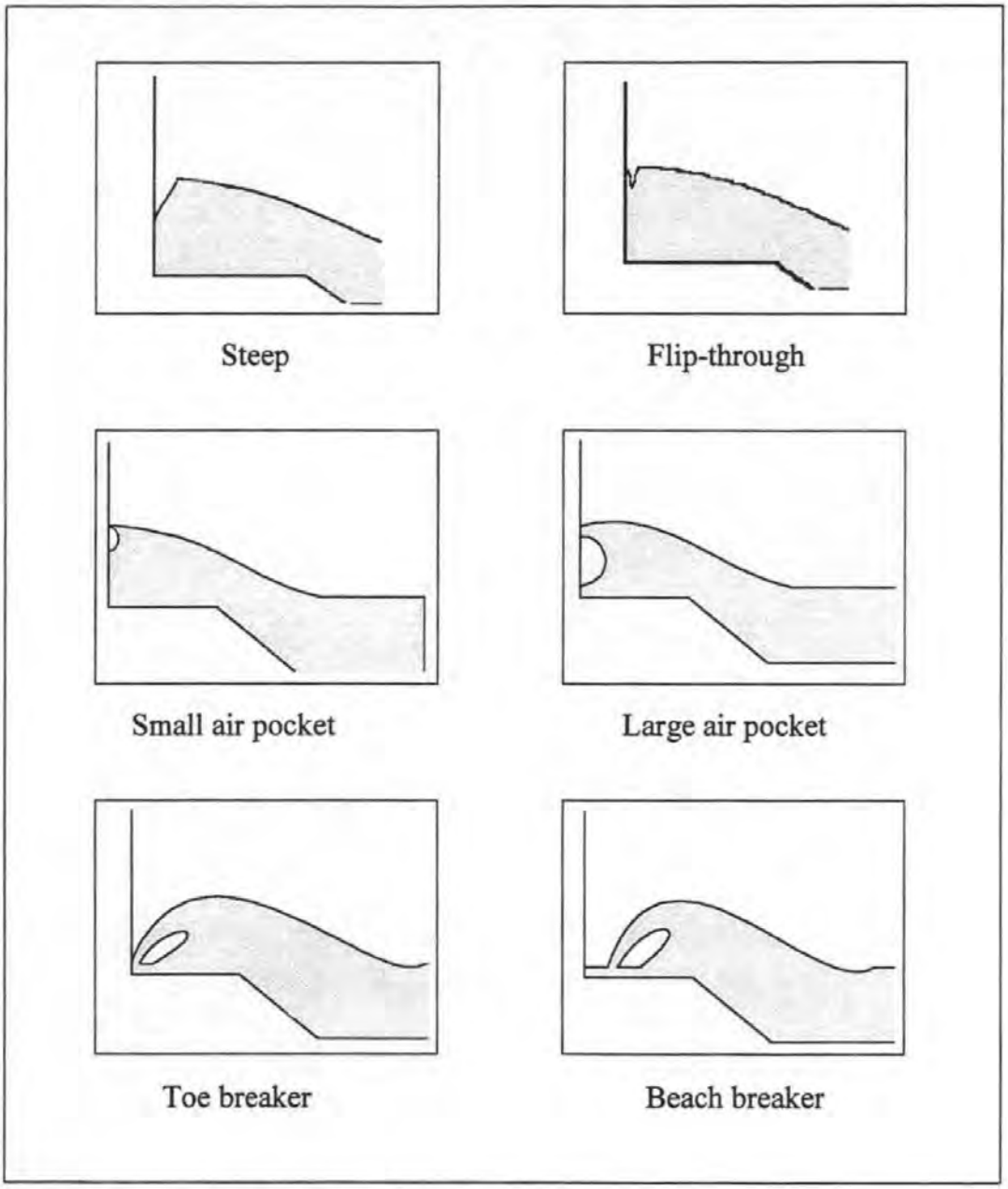

Figure 2.6. A range of impacting wave shapes.

Waves more developed than the beach breaker arrive at the wall as a turbulent jet or bore. These breaker types and the loads associated with them are discussed in greater detail in Chapter 6.

Because the breaker shape is significant in determining impact pressures and forces, any parameter which influences breaker shape must also have an effect. These parameters include water depth, wave height, period and angle of approach, also the foreshore topography and roughness. It is believed that air can also have significant effects on wave impact loads. These effects have been discussed in many publications although there have been relatively few attempts to make experimental observations or obtain measurements. It

can be deduced from the available literature that the role played by aeration depends upon whether or not it exists as a separate phase and, if so, whether it is open to atmosphere. Three forms of aeration will be defined for the purposes of this study; expelled air, entrapped pockets and entrained bubbles (see Figure 2.7).

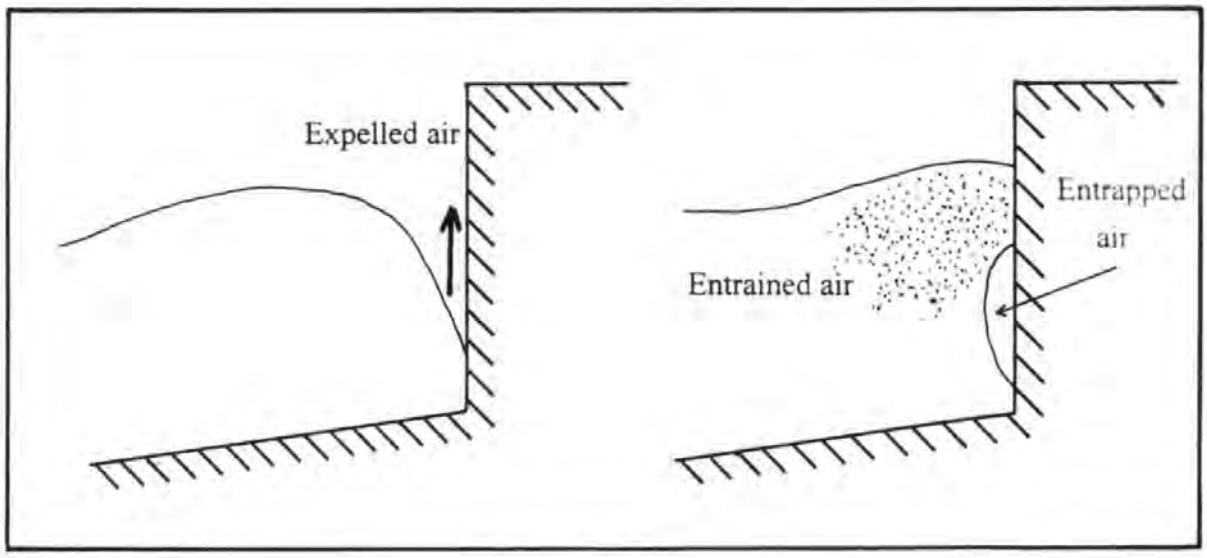

Figure 2.7. Three roles of aeration in wave impacts.

Most of the air located between the wave and the wall must be expelled before the wave can make physical contact. The associated rise in air pressure causes a force to act on the wall and retards the closure of the wave. Air entrapment occurs when air which was not expelled is sealed against the wall as the wave crest impinges. It may exist as a whole or broken pocket and can cause multiple pressure peaks and pressure oscillations. Entrained air exists as part of a two phase mixture with the water and acts to increase compressibility and reduce sound speed and density.

Another phenomenon which is related but which will not be discussed here is wave deformation due to wind force. An offshore wind can smooth the wave front and hold it up so that it remains stable at steepnesses greater than would otherwise occur. Conversely, if a strong wind blows onshore then the wave may be blown over prematurely.

2.2 Background

This first section of reviewed literature establishes the need for physical model wave impact tests and for developments in the way their results are interpreted. The advantages of physical model tests over field work and numerical modelling are considered and then the standard guidance available for the interpretation of their results is reviewed. Finally, the need for a clear and uniform methodology for wave impact testing is established by considering some of the sources of variance between the results of different tests.

2.2.1 Field studies

The most direct way of gaining insight into the impact of marine waves is to conduct field measurements. There have been relatively few studies which have taken such measurements because they tend to be expensive and difficult to conduct. Some of the difficulties have eased with developments in technology, whilst others can only be lessened by the selection of a good location.

Reports of early studies (pre 1938) are very difficult to obtain. Consequently a comprehensive review will not be attempted here. The reader is instead directed to the review provided by Minikin (1950) and to three studies specifically dedicated to field measurements, Blackmore (1982), Muller (1993) and Crawford (1999).

The first modern field measurements were conducted by Rouville *et al,* (1938) using a vertical array of three piezoelectric pressure transducers attached to a harbour wall at Dieppe. The maximum recorded impact pressure of 689 kN/m^2, which was caused by a 2.5 m wave, remains the highest marine wave impact pressure measured to date. Photographs were used to estimate wave characteristics and water velocities during the impact. Statistical analysis showed that only 2 % of wave impacts resulted in impact pressures. The results of this study were later used by Minikin (1950) to develop a method of predicting impact loading.

Miller *et al,* (1974) conducted marine measurements of wave impacts on a vertical cylinder which was fixed in the surf zone. Although loads on cylinders may not be directly comparable to those on a vertical wall the study did demonstrate that these loads vary with

breaker shape. The largest average pressure of 41 kN/m^2 was associated with the impacts of bores.

Blackmore and Hewson (1984) measured impact pressures on sea walls in southern Britain. Most of the measurements were obtained at Ilfracombe which had a rocky and irregular foreshore with an average slope of 1:30. Wave heights, periods and water depths were also recorded. The maximum pressure of 49 kN/m^2 occurred with a 3.6 m 4.3 second wave. This relatively low pressure was attributed to high levels of air entrainment induced by the rocky foreshore; 0.04 % of all impinging waves were found to produce impact pressures. The results were developed into a semi-empirical method for the prediction of impact loading which included an aeration term λ (see Blackmore and Hewson, 1984). This method is described in more detail in section 2.6.5.

Muller (1993) showed impact pressure maxima, pressure time histories and pressure profiles which were recorded on the sloping front face of a wave power station. This was located at the end of a rough and rocky gully on the island of Islay off the west coast of Scotland. Pressures were recorded at 100 Hz during 28 days of storms with five transducers. The maximum recorded impact pressure was 51 kN/m^2 with only 0.011 % of storm waves producing impulsive pressures. The apparently low pressures were attributed to the irregularity of the physical boundary conditions experienced by the approaching waves. The data was statistically analysed to predict a 1/50 year design load which was compared to predictions made using the design methods of Goda (1974), Minikin (1950) and Blackmore and Hewson (1984). The first two were found to be unsuitable whilst the last gave the closest conservative prediction although the range of recommended λ values was not broad enough to include the roughness of the Islay site. The measurements were therefore used in conjunction with the results of model tests to provide broader definitions of λ.

New field measurements have recently been recorded on the near vertical masonry breakwater at the U.K. Channel Island of Alderney (see Crawford, 1999). The location and orientation of the structure mean that the waves arrive with little reduction in height, often with their crests nearly parallel to the breakwater. Significant wave heights exceeding 7 metres are experienced during most winters in this location.

Pressures were measured by means of five pressure transducers. The active surface of each was an 18.5 mm diameter acetyl piston that was coupled to a tension-compression load cell which had a natural frequency of 18 kHz. This arrangement minimised risks of corrosion and thermal shock and enabled the measurement of sub-atmospheric pressures. Quantities of aeration were also recorded by measuring the conductivity of a 20 kHz electrical field which was generated across the face of each pressure transducer using two rectangular stainless steel electrodes placed 100 mm apart. Supporting instrumentation included an array of six pressure transducers on the sea bed, which provided directional spectra, incident and reflected wave heights, as well as the mean direction of wave approach. Measurements of temperature and water conductivity were also taken so that the salinity could be calculated. This was needed for the calibration of the aeration equipment.

Because this field study was completed during the autumn of 1998, only limited data has been published so far. Crawford *et al* (1997) show the largest impact recorded by that time which occurred when the significant wave height was calculated to be 3.1 m and the energy spectrum peaked at 7.4 seconds. The maximum impact pressure (P_{max}), which occurred at the mean water level, was greater than 100 kN/m^2. The aeration levels are reported to have varied during the impact from a maximum of more than 15 % during the impulse to around 5 - 8 % during the quasi-static part of the load. It was concluded that high values of P_{max} and low values of T_{pr} tended to occur when the aeration levels were low. It was also found that both the temporal and spatial extent of the pressure impulses tended to increase with the aeration level. They suggest the possibility that higher aeration could cause the pressure impulse to act simultaneously over a greater area on the wall and so increase the peak impulsive force.

Field measurements are, by their nature, of great value since they provide direct information of real events. However, they have provided only limited insights into the nature of wave impact loading. This is because of the rarity of such studies, the lack of control over field conditions and the difficulty of obtaining comprehensive supporting data. For example, the range of reported impact pressure maxima is extreme, with more than an order of magnitude between the values given by Rouville and those of Miller, Muller and Blackmore & Hewson. New data is emerging and new studies are planned, but at present the database of marine information is very limited.

2.2.2 Numerical models

A general advantage of numerical models is that coastal engineers can use them to rapidly test wave-structure interaction for a variety of conditions, thereby accelerating the identification of optimum design solutions. This is not easy to do for breaking waves because they can not be described with the usual theories. Deep water methods such as first order Stokes (Airy) and shallow water finite amplitude theories such as higher order Stokes, non linear shallow water, Cnoidal wave theory and solitary wave theory can not resolve the steep and overhanging wave fronts which occur during breaking. There are two types of model currently in development which are able to do this, those based on the Laplace equation and others which solve the Navier-Stokes equation.

Laplace models were the first to describe overturning waves (Longuet-Higgins & Cokelet, 1976, Dold and Peregrine, 1984). Pressure impulse models, based on the solution of the Laplace equation were later developed to describe wave impact loads (Cooker and Peregrine, 1990 and Cooker 1990), the motion of a large pocket of entrapped air (Topliss, 1994) and the influence of entrapped air 'bouncing back' into the impacting wave (Wood, 1998, and Wood *et al*, 1999). The solution of the Laplace equation is limited to incompressible, inviscid and irrotational flow within impermeable boundaries, consequently they can not, at present, resolve the wave motion during the whole impact. Nevertheless, predictions made with these models have been compared well to experimental data (Hattori *et al*, 1992, Chan, 1994, Losada *et al*, 1995, Walkden *et al*, 1999).

Wave impact models based on the solution of the Navier-Stokes equation can fully describe the two dimensional velocity field of a wave beyond the point of overturning (van der Meer, 1994). Little published information is currently available on such models but they have been shown to provide descriptions of breakers after the point of plunging. At present they can not deal with entrained air or vertical walls and require considerable computing power. The latter of these problems will be lessened as computers evolve, the former requires further development and validation against measurements of aeration in model and marine tests.

It can be concluded that whilst numerical models of breaking and impacting waves are developing into useful research tools they require further improvement and adaptation. In order to make their predictions of impact loads more realistic the effects of aeration have to be included. This in turn requires the measurement of aeration in impacting waves.

2.1.6 Current guidance for the interpretation of physical model test results

There are two procedures recommended by BS 6349 for the design of caisson breakwaters, the method due to Goda, which is described below, and the prediction of design loads by means of physical model tests. The guidance provided for the interpretation of the results of such tests is limited;

> "When impacts due to breaking waves on vertical face structures are measured, the same scaling laws do not apply to all types of impact mainly because air entrainment cannot be modelled at suitable scales. Generally the Froude relationship is used as there is evidence to suggest that this gives a conservative result."

Hughes (1993) adopted the classification of wave impact types used by Lundgren (1968, see Figure 2.8 and section 2.3.1) and suggested that Froude scaling should only be used for 'ventilated shock' type impacts.

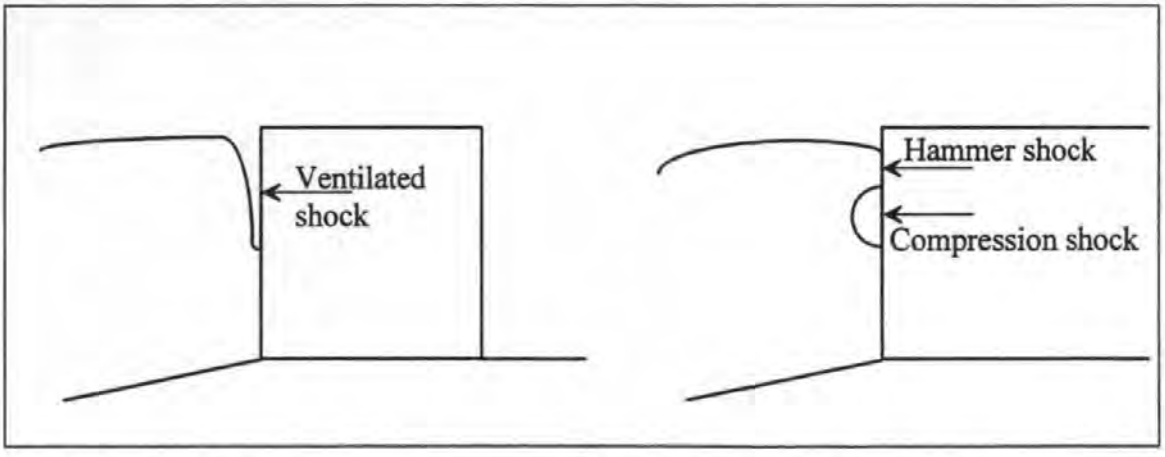

Figure 2.8. Shock classification of Lundgren (1968), see also Hughes (1993).

A scale relationship is provided for the peak pressures of 'compression shocks' which was derived by both Mitsuyasu (1966) and Lundgren (1968) and was originally based on the compression model of Bagnold (1939). It has never been validated.

Lundgren originally proposed that 'hammer shock' impacts would produce water hammer pressures but such high magnitudes have never been observed. Hughes instead suggested the use of a model due to Kamel (1970) which accounts for the compressibility of the wall (see section 2.3.2). Although this is a more complete description of a compression impact it still over-predicts. Hughes states that when compared to experimental data it appears to over-predict by a factor of two. In fact, Kamel states in the original paper that the maximum measured wave impact pressure from approximately 3700 events was eight times smaller than the predicted value. The data set was supplemented with a series of drop test results, the maximum of which was 50 % of the predicted level with an average of only 3 %. Kamel attributed the deviation between measurements and predictions to both entrained aeration and the entrapment of air between the water and wall. Hughes also cites aeration as the cause of scale effects and suggests that until its effects are known, model experiments should be conducted at as large a scale as possible.

2.2.3 Sources of variation in the results of physical model tests

In addition to being used for assessing the suitability of a particular breakwater design, physical model tests have also been a productive means of conducting research into wave impacts. They are cheaper and more controlled than marine measurements and allow investigation of situations for which there are no analytical or numerical solutions. They can, in principle, be used to study each of the important parameters by varying each one in turn and measuring its effect on the impact load. In practice, this is not a simple task because of the large number of important parameters. The problem is compounded when some test parameters are not reported and when test methodology has a significant influence on results. This section describes results which illustrate sources of variance in impact load between nominally identical impact events or between different studies other than the generally acknowledged parameters.

Denny (1951) measured impact forces and pressures with a mobile heavy sprung wave wall and two pressure transducers. One transducer functioned by moving against a spring within an electromagnetic field, the other was an apparatus which included a mobile diamond which recorded peak pressure by indenting a brass plate. Waves of three heights were measured all of which had similar steep and slightly overhanging wave fronts.

A significant finding on the importance of water surface disturbance emerged because of the limited time available for the experiments. Four hundred and thirty two, 294 mm solitary waves were initially tested and fifteen to twenty minutes was allowed for the water to calm between each. This slow test rate was later increased and waves were continuously generated by motivating the paddle with a reverse stroke to absorb the reflected wave before immediately generating the next. Four hundred and forty three 172 mm waves and one thousand and sixty eight 343 mm waves were tested using this method, each in the disturbed water of the previous impact.

As is shown in Figure 2.9, it was found that the normalised distributions of P_{max} were similar for the two wave heights in disturbed water but the values for the waves in clean water were almost twice as high. This leads to the conclusion that there is a relationship between wave height and peak pressure, at least for the same breaker shape, but a comparison of P_{max} between waves is only meaningful if they have similar levels of surface disturbance. This disturbance is essentially the interference pattern of unwanted, stochastic, high frequency and low energy waves so will be referred to as 'Noise'.

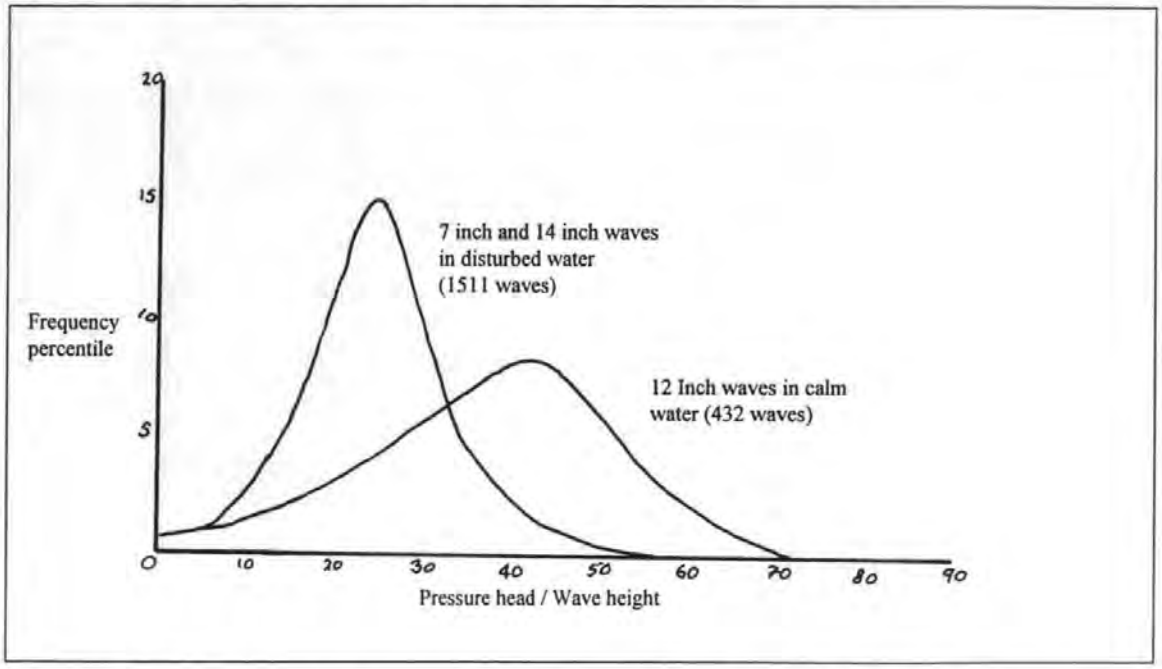

Figure 2.9. Pressure maxima recorded by Denny (1951), showing the effect of wave noise.

It is worth noting that although the clean waves produced a statistically higher distribution of impact pressures, the noisy waves had a tendency to produce a few extreme values so that the highest normalised impact pressure was caused by a noisy wave. For the 343 mm high waves this might be explained by the greater number tested, but there were similar

numbers of 172 mm and 294 mm waves. Denny used a simple breaking soliton, other researchers have used different types of wave. It is known that impact loads are strongly dependent on breaker shape; there is some evidence that the type of wave used to form the breaker is also significant.

Several different wave types have been used, these include solitary waves (Bagnold 1939, Denny 1951, Hayashi and Hattori 1958, Walkden *et al*, 1995), regular waves (Ross 1955, Plakida 1970, Whillock 1987, Kirkgoz 1990, Schmidt *et al*, 1992, Schultz 1992, Graham *et al*, 1993, Hattori and Arami 1992, Hattori *et al,* 1994, Crawford *et al*, 1994, Muller and Whittaker, 1995, Walkden *et al*, 1995, Walkden *et al*, 1996), the first breaking wave of a regular train (Richert 1968, Walkden *et al*, 1998) frequency and amplitude modulated wave packets (Chan and Melville 1988, Rapp and Melville 1990, Oumeraci *et al*, 1995) and random waves (Schmidt *et al*, 1992, Allsop *et al*, 1996, Vicinanza, 1997, McKenna, 1997). Each of these may be used to generate a whole range of breaker shapes, including, for the last two methods, freak waves.

Results from tests which used different wave types should be compared with caution. For example Richert (1968) only recorded loads from the first breaker of a regular train because this produced the highest pressures. Those results might not therefore be considered suitable for comparison with regular wave data. Bagnold's pressure profiles show high loads above the still water level whereas other researchers show peak pressures at the still water level. This is because the relative breaker height is greater for solitary waves than for regular waves (see for example Raichlen and Papanicolaou, 1988). Differences in wave type can provide a wide scope for interpretation between the results of different tests. Weggel and Maxwell (1970), for example, assumed that because the waves tested by Bagnold were solitary, they had a wave steepness of zero.

Clearly the size of the active surface of a pressure transducer, its location and sample rate will all influence the recorded pressures. Fuhrboter (1986) demonstrated problems which can arise when comparing experimental results even with similar measurement systems. Wave impact loads were measured on geometrically similar revetments which were an order of magnitude different in scale. These showed that normalised values of P_{max} were greater in the large scale model than they were at small scale. The discrepancy was caused

by the use of the same transducers in both tests. The large scale pressure measurements had greater spatial resolution and were therefore able to record more localised pressures.

The temporal resolution of a wave pressure record is determined by the transducer sample frequency. Witte (1990) studied the effect of sample frequency on recorded values of peak pressure. A 1 μs sample interval was used to record pressures from the impact of a 250 mm, two second wave and the resulting pressure time history was assumed to have perfect fidelity. This record was then filtered by differing degrees and the resulting pressure attenuation was calculated. A sample frequency of 62.5 kHz reduced peak pressures by approximately 1 %. This result might be criticised because the natural frequency of the pressure transducers was 60 kHz and therefore one would expect any higher sample frequency to give no further improvement in temporal resolution.

Oumeraci *et al*, (1994) calculated the percentage attenuation of values of force, pressure, pressure impulse and force impulse, as functions of sample frequency, their results are reproduced in Figure 2.10.

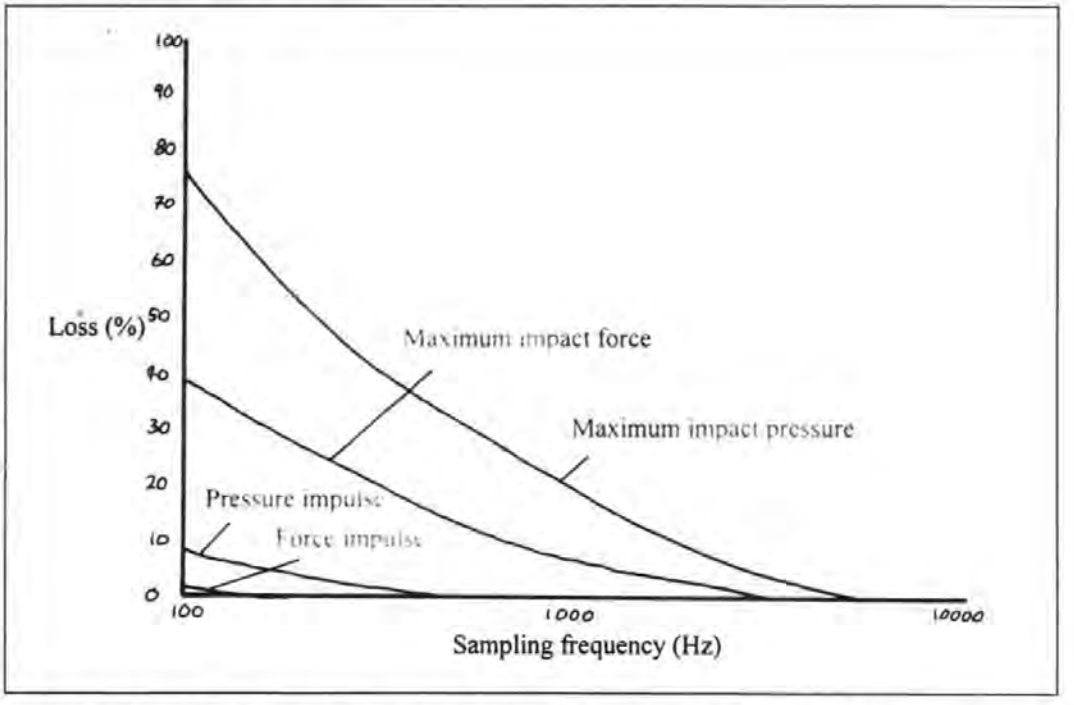

Figure 2.10. The influence of sample rate on measured loads, from Oumeraci, *et al*, (1994).

The maximum impact pressure is the most strongly influenced by sample frequency. Spatial and temporal integration decrease sensitivity so that F_{max} is attenuated to a lesser degree than P_{max}, whilst the impulses (pressures, I_p and force I_f) are influenced least of all. It

can be seen from this graph that if P_{max} is the measured dependent variable of a wave impact test then a high sample rate is required. If the force impulse is of interest then a lower sample rate is sufficient.

2.2.4 Summary

Physically modelling wave impact loads for the purposes of research or design has some natural advantages over other methods. Field work can produce valuable data but it is expensive and very difficult to control. It also requires considerable supporting information to aid interpretation. Under some conditions numerical methods have been successfully applied to model wave loads, but they are still under development. A major drawback at present is that they can not deal with the effects of aeration. Despite the advantages of physical model tests the guidance available for the interpretation of their results is very limited. One of the reasons for this may be the variance in the results produced by different studies. This variance can be attributed to at least three causes:

- The complexity of the physics of wave loading and the large number of influencing parameters.
- Differences in methodology between studies.
- The selection of the maximum impact pressure, which is highly transient and localised, as the measured dependent variable.

2.3 Aeration and wave impact loads

Waves in marine breaker zones always contain air bubbles introduced through a variety of mechanical, chemical and biological processes. In the open sea or at a gently sloping shore the principle means of aeration is spilling of the crest, a process by which the wave dissipates excess energy (Longuet-Higgins and Turner, 1974, Fuhrboter, 1970). When waves break against a boundary such as a vertical wall, air entrapment can also occur, as well as additional entrainment during up-rushing and down-rushing.

Although it is generally agreed that aeration complicates wave impact loads there is no overall consensus of opinion regarding its effects. Ross (1955), Richert (1968) and Lundgren (1968) believed that aeration prevents the occurrence of water hammer pressures. Kirkgoz (1982) believed that the highest impact pressures occur with no air entrapment whilst Bagnold (1939) thought that an air pocket was necessary precondition for impact pressures to occur. Chan and Melville (1988) and Hattori and Arami (1992) showed with laboratory measurements that although impulse pressures could occur without aeration, when air was entrapped the pressures increased. Aeration appears to influence impact loads in three distinct roles, as expelled air, entrapped pockets and entrained bubbles.

2.3.1 Entrapped and expelled air

The first paper to discuss the significance of entrapped and expelled air was authored by Bagnold (1939). He considered the expulsion of air during the arrival of the wave front at the wall and suggested that air entrapment occurred when the angle at the point of contact between structure, water and air is less than $\tan^{-1}(U / C_a)$, where U is the horizontal velocity of the approaching wave front and C_a is the sound speed in air.

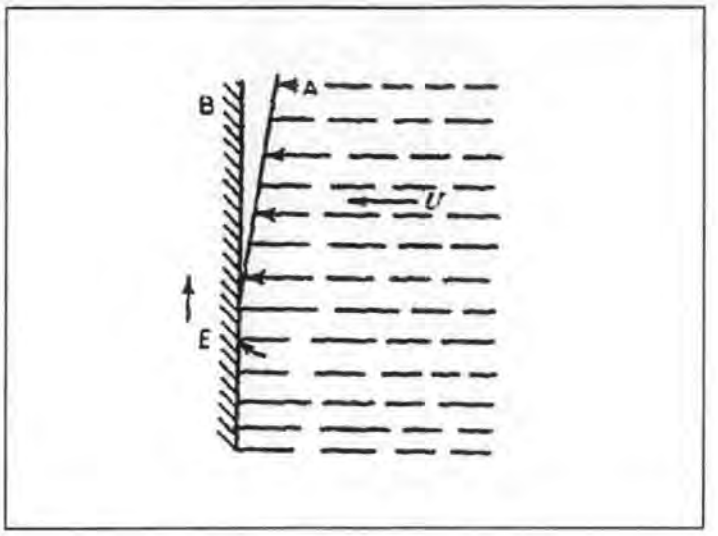

Figure 2.11. Air expelled from the front of an advancing wave, from Bagnold, (1939).

Under this condition, it was argued, the air would not be completely expelled before the upper part of the wave impinged on the wall. Bagnold believed that it was only under these conditions that high impulse pressures could occur, otherwise, it was reasoned, pressures generated at the junction between the wall, water and air would immediately escape to atmosphere. A series of wave impact tests were conducted to investigate air pocket impacts.

Solitary 245 mm high waves were tested in an 11 m long tank with a water depth of 460 mm. The waves shoaled over a 14 / 90 slope to break onto a wall which was instrumented with one high response piezoelectric pressure transducer which had an active surface diameter of 18 mm. This was placed at various elevations in the wall during different tests. After impact the reflected wave travelled back to the stationary paddle which was then motivated to absorb the reflected wave and create another.

The highest recorded pressure was 552 kN/m^2, although typical values ranged from 55 to 124 kN/m^2. This study was the first to demonstrate the existence of double peak impacts and pressure oscillations during the decompression of the impulse. The former phenomena was attributed to the impact of minor jets during the collapse of the air pocket, whilst the second is shown in results but not commented upon. Bagnold concluded that impulse pressures only occurred at the air pocket and did not vary within it. The pressure distribution was therefore rectangular at the air pocket and hydrostatic below. It is not clear

how Bagnold decided upon this distribution since only one transducer was used and P_{max} was highly variable between tests.

By describing the compression of a pocket of air a model for impact pressures was proposed based on an 'effective length' concept. It was observed that the pressure rise impulse (I_{pr}) was more consistent than P_{max}. The motive water contributing to the generation of the pressure rise impulse was likened to a piston behind the air pocket, as illustrated in Figure 2.12.

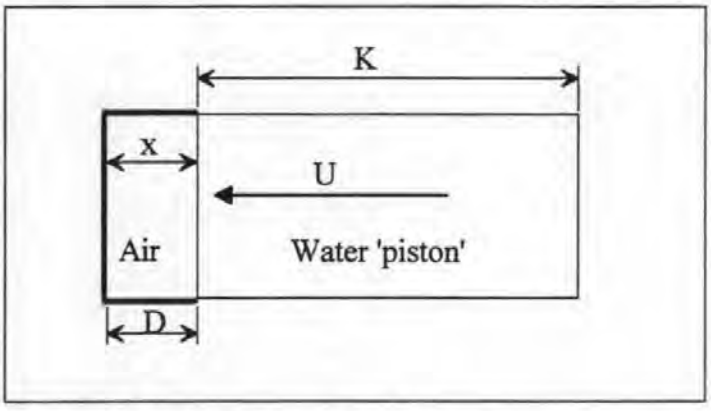

Figure 2.12. Piston concept of Bagnold.

With this assumption the momentum of the piston becomes equal to the impulse experienced on the wall in front of the pocket;

$$K\rho U = \int_{t(p=0)}^{t(p=p\max)} p dt$$

K was called the 'effective length' of the piston and was found by assuming that U was the incident wave celerity, and by measuring I_{pr} through experimentation. Bagnold then linked K to the wave height via the air pocket, postulating that K is a constant proportion (0.2) of the wave height. A comparison was then made with field results recorded by Rouville *et al,* (1938) in which a reasonable prediction was made of the upper limit of the prototype pressure rise impulse.

The form of the pressure rise impulse was provided by modelling the compression of the air using;

$$p = Ax^{-\gamma}$$

$$\gamma = c_p/c_v$$

Where c_p and c_v are the specific heat capacities at constant pressure and volume respectively, and;

$$A = p_0 D^{\gamma}$$

where p_0 is atmospheric pressure. The relationship between pressure and plunger motion was given by;

$$p = \rho K (d^2x/dt^2) + p_0$$

Therefore;

$$\rho K (d^2x/dt^2) + Ax^{-\gamma} + p_0 = 0$$

Integration and the initial condition that $u = U$ when $x = D$ provides;

$$u^2 = (dx/dt)^2 = U^2 - (2A/((\gamma - 1)\rho K))[(1/x)^{(\gamma-1)} - (1/D)^{(\gamma-1)}] + (2p_0/\rho K)(D - x) \quad (2.1)$$

An exact solution for the integration of this expression was not found, so adiabatic compression was assumed and a graphical integration was carried out to find a number of pressure time curves. An approximation of the peak pressure was given by;

$$(p_{max} - p_0) = 2.7 (((\rho U^2 K)/D)$$

to within +/-10 % between 2 and 10 atmospheres.

For a given wave the magnitude of P_{max} is therefore determined by the initial air pocket thickness. Variations in the form of measured pressure time history were attributed to deformations in the wave shape, whilst the stochastic variation in pressure maxima was attributed to the sensitivity of the pocket thickness to minor shape changes.

Although the experimental results apparently show good agreement with predictions using the air pocket theory, Bagnold was never able to measure the thickness of the air pocket, it was only estimated from the pressure rise time, and so was not able to prove his model.

It has since been shown that many of Bagnold's assumptions were incorrect. Impact pressures can occur without the entrapment of air (Kirkgoz, 1983, Cooker and Peregrine, 1990, Walkden *et al*, 1995), when air is entrapped the high pressures can originate in the wave crest rather than the pocket (Walkden *et al*, 1995), impulse pressures occur below the pocket, (Chan and Melville, 1988) and the air pocket height is clearly not directly proportional to the wave height. Despite these incorrect assumptions the effective length concept has been used by several researchers since, and has been incorporated in both the design methods of Minikin (1950) and Blackmore and Hewson (1984).

Mitsuyasu (1966) provided an approximate solution to Bagnold's pocket compression formula (equation 2.1) by rearranging the right hand side, to obtain;

$$u^2 = U^2 - (2\,p_0)/(\rho\,K)\{D/(\gamma - 1)[(x/D)^{(1-\gamma)} - 1] - (D - x)\}$$

introducing $X = D - x$ and expanding $(1 - X/D)^{1-\gamma}$ to the second order provided,

$$dX/dt = +/- U[1 - (p_0\gamma X^2)/(\rho K U_0^2 D)]^{1/2}$$

From this a more exact solution for peak pressure is obtained from D, K and U. An approximate solution for the variation in air pressure through time is given as;

$$p_{max}/p_0 = 1 +/- 1.18(\rho K U^2)/(p_0 D)^{1/2} + 1.2(\rho K U^2/p_0 D)$$

Lundgren (1968) provided an energy based version of this model for certain types of impact. He first classified impacts according to three generation mechanisms termed ventilation shocks, hammer shocks and compression shocks, as described above in section 2.1.6. The proposed upper limit provided for the hammer shock is the water hammer pressure provided by von Karman (1928). The model proposed for the ventilated shock impact assumed that the time necessary for the pressure to rise (T_{pr}) was equal to the duration of the expulsion of air, this was approximated by;

$$T_{pr} = A/(H_b\, C)$$

Where A is the air volume, H_b is the breaker height, and C is the wave celerity.

It was assumed that the pressure rise could be represented with a simple cosine function;

$$p = 0.5\, P_{max}\, (1 - \cos \pi\, t/T_{pr})$$

In which P_{max} is the average pressure over the height of the breaking wave. The mass of water contributing to the impulse was assumed to be;

$$M_{hy} = 0.5\, \rho\, H_b^2$$

So that;

$$P_{max} = 0.5\, r\, c^2/A\, H_b^2$$

A is assumed to be $0.2\, H_b^2$

No predictive formula was provided for the compression shock, instead the balance of energy was considered based on Bagnold's piston concept. The kinetic energy of the incoming piston at the moment of closure was equated to the pneumatic energy in the air pocket at maximum pressure. This was considered at model and prototype scale to provide the graph shown in Figure 2.13. This was intended for use in the prediction of full scale pressures from model scale measurements.

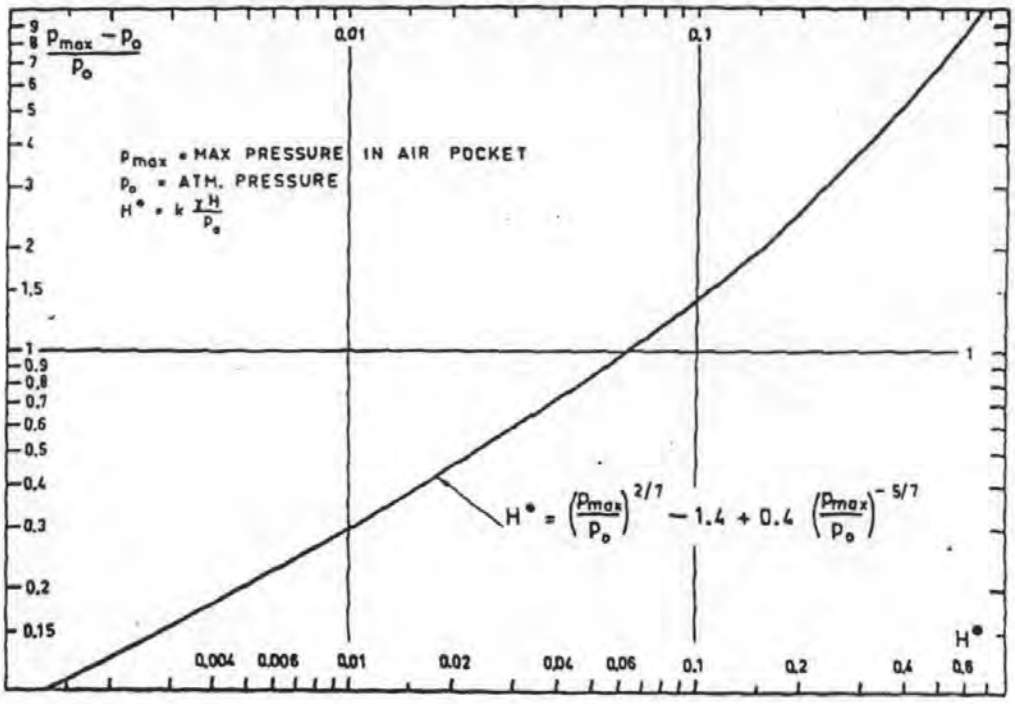

Figure 2.13. Lundgrun's scale relationship for P_{max}.

In Figure 2.13, P_0 is atmospheric pressure and H^* is a dimensionless wave height given by,

$$H^* = k g \rho H / P_0$$

Where k is a dimensionless constant.

The graph is used to first provide the dimensionless 'height' H^*_m from the model scale maximum impact pressure, $P_{max(model)}$. This is multiplied by the length scale to provide H^*_p. The diagram is then reused to provide $P_{max(prototype)}$.

Ramkema (1978) used Bagnold's model to describe the impact of a standing wave and the entrapment of a pocket of air under a protruding structural element. The model was extended to include isothermal compression and to allow for compression of the water, although the latter modification was found to be unnecessary. Good agreement was found between the model predictions for frequency of oscillation and experimental measurements.

Oumeraci and Partenscky (1991), Hattori *et al*, (1992), and Topliss *et al*, (1992) have all developed models to describe the oscillation of entrapped air pockets. Hattori *et al*, (1992) compared predictions based on all three with laboratory measurements. Video images of various breaker types were recorded at 200 Hz with simultaneous pressure records at 5 kHz. The dimensions of the air pocket and surrounding wave were obtained from the video images. It was found that the model due to Topliss provided the most accurate estimate. This solved the Laplace and Bernoulli equations to provide frequencies of oscillation and internal pressures of the pocket from its size, its relative depth, and the velocity of the enclosing wave. It was assumed that the air pocket compressed adiabatically and that the deformation of the wave during compression was insignificant.

2.3.2 Entrained air

The presence of entrained air in a water wave affects its density, compressibility and the speed at which pressure waves propagate through it. Because the air is mixed into the water it is possible to describe it in terms of a percentage or void fraction. This has been measured in both marine and laboratory waves (Lamarre and Melville 1992, Thorpe, 1982, Hwung *et al,* 1992, Fuhrboter, 1986, Graham *et al*, 1993, and Griffiths, 1994, Crawford *et al*, 1997, Crawford 1999), only the studies of Graham, Griffiths, and Crawford, *et al* have included measurements in the presence of a vertical wall. Despite the lack of quantitative data several models have been proposed to describe its effect on impact pressures.

Von Karman (1928) studied the impact of sea plane floats during landing and derived the expression for water hammer pressure (P_{WH}) by considering the compressibility of the water.

$$P_{WH} = \rho C V$$

Where C is the sound speed of the fluid, and V is the impact velocity.

Since the level of entrained air strongly effects the sound speed in water, (1 % aeration reduces C by 90 %) it also has a strong influence on water hammer pressures. Although

some researchers believe that water hammer pressures result from the impact of a steep fronted wave no one has recorded loads of such high magnitude.

Fuhrboter (1969) studied the impacts of high speed water jets and derived an expression for the maximum pressure as a function of the elasticity of both air and water. This was intended to be analogous to a wave jet. Fuhrboter (1986) later showed that the expression failed to predict wave impact pressures during measurements on a sloping revetment in a large wave flume. It was in this study that the first measurements of aeration in laboratory breaking waves were attempted. A spar instrumented with 300 open electrical contacts at 10 mm spacings were installed on the revetment. The contacts were closed as the wave submerged the spar except in the presence of large amounts of air. This allowed the presence of large air pockets to be registered although void fractions could not be obtained. Fuhrboter was not able to quantify the effects of aeration but did conclude that it is the most important factor influencing the magnitude of impact pressures.

Lamarre and Melville (1992) developed a resistance based aeration gauge and used it to measure entrained aeration in (non-similar) marine and laboratory offshore breakers. Typical aeration measurements ranged from 0 to 30 % in the laboratory and up to 12 % in the sea. A more detailed description of the equipment and techniques used can be found in Chapter 4.

Graham *et al* (1993) measured aeration in model scale waves breaking onto a vertical wall. Aeration levels was compared to simultaneous measurements of P_{max} and predictions of water hammer pressures, see Figure 2.14.

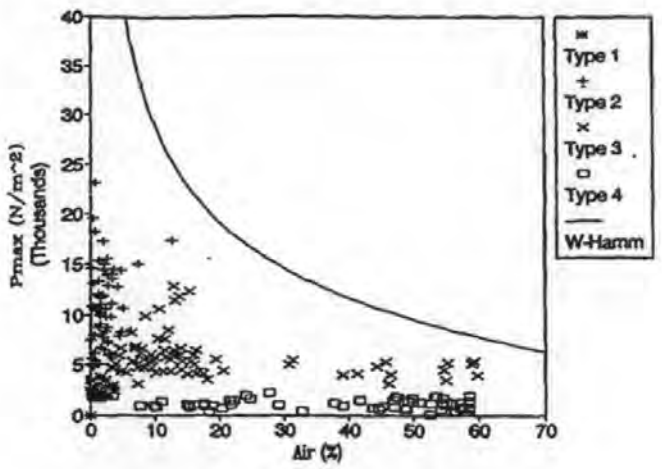

Figure 2.14. Aeration levels, pressure maxima and water hammer pressures, Graham *et al*, (1993), types 1 to 4 are different impacting wave shapes.

The trend of the results was correctly predicted although the magnitude of the pressures were not. This discrepancy was attributed to irregularities in the surface of the breaking wave. It should be noted in this figure that levels of aeration of around 65 % are quoted which are higher than the working range of the instruments which was 0 to 20 %. The 65 % values represent the 'in air' output of the gauges. It seems that the probe output was occasionally being dominated by entrapped air or else subject to three dimensional effects. A more detailed discussion of the equipment is given in section 4.3.

Kamel (1970) gave an analytical solution for shock waves propagating through an elastic solid and a compressible liquid. P_{max} is given in terms of the impact velocity (u), sound speed and density of both solid and liquid.

$$P_{max} = \rho_s C_s [(\rho_w C_w u)/(\rho_w C_w + \rho_s C_s)]$$

Where ρ_s and ρ_w are the densities of the solid and liquid respectively and C_s and C_w are the sound speeds in the solid and liquid.

The duration of the shock pressure was given by the time taken for either of the shock waves to propagate to a free surface and reflect back to the contact point as an expansion

wave. Data recorded by Denny (1951), Rouville (1938), Ross (1955) and Hayashi and Hattori (1958) were used for the comparison as well as the results of drop tests. It was found that the model over predicted pressures by at least a factor of eight. Despite the inclusion of the density and sound speed the discrepancy was still attributed to the presence of entrained and entrapped air. It may also be that the pressure fronts measured in the experiments were not fully developed shock waves.

Weggel and Maxwell (1970) modelled temporal and spatial distributions of impact pressure including the compressibility effects of entrained air. They found, as Bagnold did, that the magnitude of the pressure decreased with increasing thickness of the region of air. Random variations in impact pressure were attributed to variations in air content and thus sound speed.

Partenscky (1988) stated that the impact pressure was highly dependent on aeration as,

$$P_{dyn} = Kl\, \rho\, g\, H_b$$

Where *Kl* is an air content coefficient given by;

$$Kl = 5.4((\,1 / kl\,) - 1)$$

where *kl* is the 'relative' air content which varies between 0.1 and 0.8 depending on site and structure in a similar manner to Blackmore and Hewson's λ term. It seems that *Kl* acts as a coefficient to account for all stochastic variation since the air content can be set to any value to suit the measured data. Partenscky then goes on to develop an effective length model in which the rise time is assumed to be linear and the momentum exchange ends at the maximum impact pressure.

Allsop *et al*, (1996) proposed that the effect of differences in entrained aeration between model and marine waves be accounted for by applying a reduction factor of 0.45 to the impact pressure maxima. This value arose from comparison between laboratory and prototype measurements of wave impacts on a permeable sloping breakwater composed of 'Shed' units.

Peregrine and Thais (1996) also suggested that pressure reduction factors be used to account for differences in aeration. They highlighted the similarity between a flip through impact and the filling flow of a jet in a narrow crack. A compressible model was derived to describe this filling flow and several series of pressure reduction factors were calculated as functions of void fraction.

One possible source of errors in physical models of impacting waves is the use of fresh water to model the sea water of prototype waves. Bubbles in fresh water tend to be larger and less numerous than in sea water, they also have a greater tendency to coalesce because the dissolved salts, organic matter and other contaminants in sea water act to stabilise the bubbles (Scott, 1975). This is illustrated in Figure 2.15.

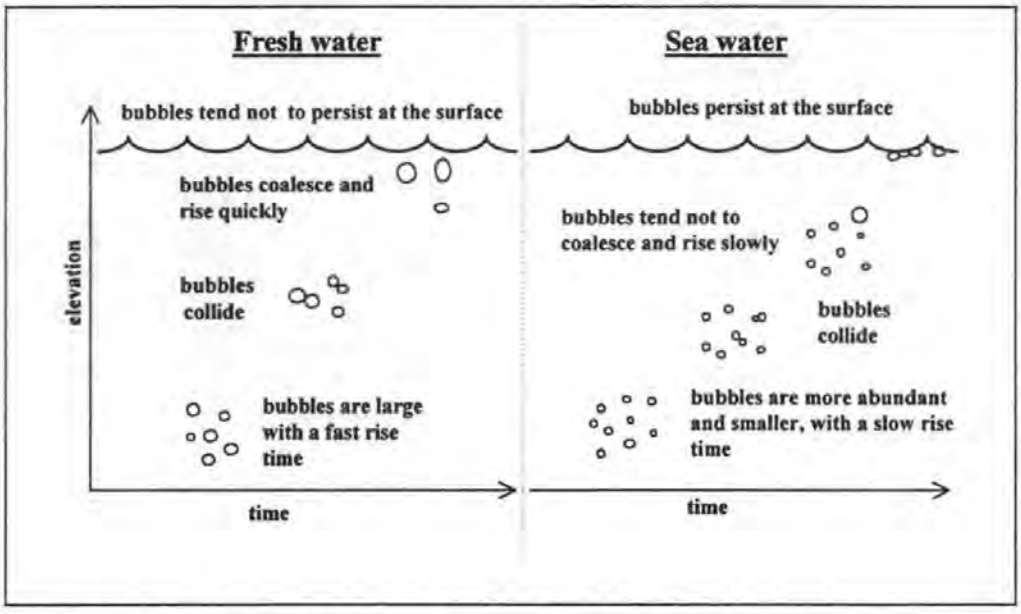

Figure 2.15. Differences between fresh and sea water aeration.

Crawford *et al*, (1997) investigated differences in the aeration characteristics of fresh and sea water impacting waves and the effects they had on impact pressures. They found that the sea water bubbles were smaller and were more likely to remain in the water between impact events. The resulting difference in compressibility meant that only the fresh water impacts exhibited 'well defined short duration impulsive peaks'. Generally it was found that the sea water impacts caused impulses which had longer rise times and total durations, but lower pressure maxima.

2.3.3 Summary

There is general agreement that entrained air plays an important role in determining wave impact loads. Several models have been proposed to describe this effect although none have been validated. This must be at least partly due to the lack of measured data. Differences in the entrained aeration characteristics of fresh and sea water waves have been observed, and shown to have an effect on impact loads.

In order to discuss the significance of air on wave impact pressures it is necessary to consider at least three different forms of aeration, expelled air, entrapped pockets or bubbles and entrained bubbles. The pressures associated with the expelled air in front of a breaker have been discussed but never measured. Various models exist to describe the compression of entrapped air including the Bagnold-Mitsuasu-Lundgren-Ramkema models which consider the momentum or energy transfer in the pocket and the Topliss model. Although these might be used to predict prototype air pocket compression, they still require testing against large scale laboratory data.

2.4 Scaling of physical model wave impact tests

In an ideal physical model of a hydrodynamic process, such as an impacting wave, all the forces would have the same relative importance as in the prototype. This dynamic similarity is required in order that kinematic similarity can emerge. It is therefore necessary to consider all the relevant forces when planning a physical model and when interpreting its results.

Newton's second law describes the motion of a particle when acted on by external forces. Hughes (1993) states that for fluid mechanics problems this law can be written as;

$$\hat{F}_i = \hat{F}g + \hat{F}\mu + \hat{F}e + \hat{F}\sigma + \hat{F}_{pr} \tag{2.2}$$

Where F_i, F_g, F_μ, F_e, F_σ, and F_{pr} are the inertial, gravitational, viscous, elastic, surface tension and pressure forces respectively and the hat symbol denotes vector quantities.

Perfect similitude requires that the ratios of all the forces at the two scales be the same;

$$\frac{(\hat{F}_i)_p}{(\hat{F}_i)_m} = \frac{(\hat{F}g)_p}{(\hat{F}g)_m} = \frac{(\hat{F}\mu)_p}{(\hat{F}\mu)_m} = \frac{(\hat{F}\sigma)_p}{(\hat{F}\sigma)_m} = \frac{(\hat{F}e)_p}{(\hat{F}e)_m} = \frac{(\hat{F}_{pr})_p}{(\hat{F}_{pr})_m}$$

Where the subscripts p and m denote prototype and model respectively. The same thing can be written as an equality of scale ratios, each denoted by the letter N;

$$N_{\hat{F}_i} = N_{\hat{F}g} = N_{\hat{F}\mu} = N_{\hat{F}\sigma} = N_{\hat{F}e} = N_{\hat{F}_{pr}}$$

Such equality is an ideal which can not normally be achieved. Typically all but the most important forces have to be neglected. The most important force acting on a water wave greater than a few millimetres in length is gravity. Its magnitude relative to the inertia force is expressed by the Froude number (Fr);

$$Fr = \sqrt{\frac{Inertial\ force}{Gravity\ force}}$$

or

$$Fr = \sqrt{\frac{ma}{mg}}$$

Taking the acceleration to be convective (V^2/L, following Hughes, 1993) and expanding and expressing in terms of characteristic quantities provides;

$$Fr = \sqrt{\frac{\rho L^3 \frac{V^2}{L}}{\rho L^3 g}}$$

Which simplifies to;

$$Fr = \frac{V}{\sqrt{Lg}}$$

Equality of the Froude number at both model and prototype scale means;

$$\left(\frac{V}{\sqrt{Lg}}\right)_m = \left(\frac{V}{\sqrt{Lg}}\right)_p$$

Which, when rearranged gives;

$$\frac{V_p}{V_m} = \sqrt{\frac{L_p g}{L_m g}}$$

Or expressed with scale ratios ($N_g = 1$);

$$N_V = \sqrt{N_L}$$

To achieve similarity of the gravity forces (Froude scaling), the scale ratio of the velocities must be equal to the root of the length scale.

The relative importance of the viscous forces in equation 2.2 is expressed by the Reynolds number (Re);

$$Re = \frac{Inertial\ forces}{Viscous\ forces}$$

or;

$$Re = \frac{ma}{A\mu\frac{du}{dL}}$$

Where A is the area of shear, μ is the coefficient of absolute viscosity and du/dL is the rate of shear strain. Expressing this in characteristic quantities;

$$Re = \frac{\rho L^3 \frac{V^2}{L}}{L^2 \mu \frac{V}{L}}$$

Allows reduction to;

$$Re = \frac{\rho LV}{\mu}$$

In order to achieve scale similarity of the viscous forces, the Reynolds numbers must be the same.

$$Re_p = Re_m$$

Therefore;

$$\left[\frac{\rho LV}{\mu}\right]_p = \left[\frac{\rho LV}{\mu}\right]_m$$

And;

$$N_\rho \times N_L \times N_V = N_\mu$$

Generally, when $N_\rho = N_\mu = 1$,

$$N_L \times N_V = 1$$

Which contradicts the Froude relationship.

This contradiction is normally avoided by applying the Froude scaling law and assuming that the viscous forces are so small that they can be neglected.

The relative importance of elastic forces is described by the Cauchy number (*Ca*);

$$Ca = \frac{Inertial\ force}{Elastic\ force} = \frac{\rho V^2}{E}$$

Where E is the modulus of elasticity. In order to achieve similarity of elastic forces between model and prototype, the Cauchy numbers must be the same at both scales;

$$\left(\frac{\rho V^2}{E}\right)_p = \left(\frac{\rho V^2}{E}\right)_m$$

Or;

$$N_\rho N_V^2 = N_E$$

If N_ρ=1 and, following Froude, $N_v^2 = N_L$ then;

$$N_E = N_L$$

So the scale ratio of the modulus of elasticity should be equal to the length scale. However, the entrapped and entrained air will have the same E at both scales so will be too 'stiff' in the model. This is compounded by other scale effects which arise due to a lack of scale similarity in the surface tension forces.

Surface tension forces have some influence on the form of the breaking wave, but can also effect impact loads indirectly through their influence on bubble size. The time required for

a bubble to rise to surface and escape to the atmosphere is a strong function of its volume. Consequently, high surface tension, which causes large bubbles, tends to cause short rise times and therefore decreased bubble retention and lower void fractions. As a result, in hydrodynamic situations involving air entrainment, higher surface tension can cause higher density and lower compressibility. Fresh water is typically used in wave flumes and this has a higher surface tension than the sea water which it models. The resulting low levels of aeration, combined with the relatively high modulus of elasticity of air at the small scale, means that small scale flume waves are not compressible enough to correctly model prototype marine waves.

Studies which have investigated scale effects through physical measurements can be grouped into four categories; investigations into particular scale effects, comparisons between marine measurements and flume tests, comparisons between different small scale tests and comparison between small and large scale flume tests.

2.4.1 Investigations into particular scale effects

Stive (1984) discussed the possibility of using special atmospheric conditions to correctly scale the compression of an entrapped air pocket. He argued that by measuring model wave impacts in an enclosed tank in which the air had been replaced with a heavy gas, similarity of the compression characteristics could be achieved. By assuming that impact pressures are simply stagnation pressures the condition for similarity was defined as;

$$N(P_0/\rho V^2) = 1$$

where P_0 is the ambient air pressure, or, with Froude,

$$N_{Po} = N_\rho N_V^2 = N_L$$

and with Euler (the ratio of pressure force to inertial force, $N_\rho N_V^2/N_P = 1$),

$$N_P = N_{Po} = N_L$$

This implies that the ambient air pressure should be scaled with the length scale. This approach was tried by de Boom and Oudshoorn (1975, see Stive, 1984). Wave impact tests were conducted in a vacuum tank using a heavy gas atmosphere at a pressure correctly

scaled below atmospheric. The results were still proportionally larger than prototype levels. This was attributed to the lower levels of entrained gas at smaller scales.

The effect of surface tension on breaker shape was investigated by Miller (1972) who used detergents and anti-foaming agents to modify the surface tension of wave flume water. Different breaker shapes were created using regular, solitary and standing waves in waters of both normal and reduced surface tension. The waves broke due to shoaling over a sloping bottom and the distance of the break point from the paddle was measured. Surface tension was found to have a stabilising effect; when it was reduced, breaking occurred closer to the paddle.

2.4.2 Comparison between marine measurements and flume tests

Bagnold (1939) compared the pressures and pressure rise impulses measured in the flume to field measurements of Rouville *et al*, (1938). The length scale was 1:12. Peak pressures were found to be an order of magnitude smaller in the field data than would have been predicted by Froude scaling the model results. In contrast, Froude scaling the model pressure rise impulses provided a reasonable upper limit to the marine measurements. The discrepancy in peak pressure was attributed to the presence of entrained air and whitecaps increasing compressibility at prototype scale, and random variation in wave shape.

Blackmore and Hewson (1984) considered both model and prototype data when preparing their sea wall design method. Their field data were compared to the small scale results of Mitsuyasu (1962), Hayashi and Hattori (1958) and others in addition to the marine measurements of Rouville *et al*, (1938), Molitor (1935) and Galliard (1904). It was also found that the pressure maxima were relatively small in the marine waves compared to the model data and attributed this to increased aeration. Using Bagnold's observation of a consistent pressure rise impulse a simple relationship was found to fit the data using an 'aeration' term λ which represented effects of aeration, scale, rise time and bed roughness.

2.4.3 Comparison between different small scale tests

In 1951 Denny compared measurements from similar waves of heights 170 mm, 290 mm, and 340 mm. A Froude relationship was found between the statistical distributions of both

peak pressure and force impulse. Despite this result Denny speculates that entrained air in the sea might act to cushion marine wave impacts and reduce pressures.

Chan and Melville (1988) obtained pressure measurements at 20 kHz from laboratory representations of offshore impacting breakers. Two wave heights were used the largest of which was 130 mm. The breaker location and frequency bandwidth were apparently scaled according to Froude although the water depth was not. There also appears to be a discrepancy in the scaling of the wave length and period since N_L (0.868) does not match the square of N_T (0.664). For these reasons and also because the two scales were very close, they were not able to draw quantitative conclusions. They however were able to show that the smaller impacts were qualitatively similar and had all the features of the larger waves, with the exception of some low frequency air pocket oscillations.

2.4.4 Comparison between small and large scale model tests

Comparison between wave impacts significantly different in size and both created under the controlled wave flume conditions are valuable sources of scale information. Such tests have not been conducted for the case of waves breaking on vertical walls but have for related impact conditions.

Skladnev and Popov (1969) conducted a series of model tests of wave impacts on sloping sea walls. Wave steepness was kept constant, whilst wave heights were varied from 0.03 m to 1.2 m. It was found that for $H > 0.5$ m the average wave impact pressure increased linearly with wave height. Smaller waves gave relatively higher pressures and this was attributed to reduced air content. Popov and Ryabyck (In Russian, see Stieve, 1984) continued this work and found the same result for other wave steepnesses. Similar experiments were conducted by Fuhrboter (1986) in two flumes with a scale ratio of 1:10. Impact pressures from regular waves of heights ranging from 0.1 m to 2.1 m were tested. Froude scaling was recommended as a conservative means of estimating prototype pressures. Water running down the slope from the previous test was found to be a major influence on pressure maxima.

Sakakiyama and Ogasawara (1994) showed scale effects in wave impact forces on a vertical caisson. Waves of up to 1.46 m height and 5.48 seconds were tested in a 205 m

long, 6 m deep and 3.4 m wide flume. Smaller waves of from 0.044 to 0.215 m height and 1.2 to 2.19 seconds period were tested in a 55 m by 1.5 m by 2 m flume. The models were similar. Each consisted of a 1:15 impermeable slope, a flat topped impermeable mound, a submerged breakwater and a vertical caisson. Permeable and impermeable submerged breakwaters were tested. Both caissons were instrumented with 12 pressure transducers which had active surface diameters of 12 mm and 5 mm respectively. The pressures of both tests were sampled at 400 Hz.

The primary interests of the tests were the attenuation of wave height as it passed over the submerged breakwater and the maximum force which occurred on the caisson. It was found that relatively larger forces were generated in the smaller scale model for the permeable submerged structure and in the larger scale model for the impermeable submerged breakwater. The former result was attributed to aeration effects whilst the later was thought to result from a scale effect in the permeability of the submerged breakwater which decreased the wave height in the small scale tests. It should be noted that the sample rate was low relative to the typical duration of impulse pressures and was not scaled between tests.

2.4.5 Summary

Because relatively few scale tests have been done the existence of scale effects has not been firmly established although there is evidence that field waves generate relatively smaller pressure maxima. The pressure rise impulse may be effected less strongly. The main cause of the scale effects appears to be differences in aeration characteristics which are due to water type as well as scale. Effects associated with entrapped aeration might be dealt with by either model testing in a sealed flume using a heavy gas atmosphere or by using Lundgren's design chart (Figure 2.13) although neither technique has yet been validated.

No published accounts were found of comparisons between model tests which differ significantly in magnitude for the case of a wave breaking directly onto a vertical wall.

2.5 The dynamics of caisson breakwaters

Caisson breakwaters are often regarded as massive static structures whose resistance to wave loads arises from the friction force which is developed between its base and the rubble mound. Under these conditions the design procedure involves the prediction of the maximum wave load and ensuring that the caisson is heavy enough to provide a greater friction force. In reality, the inertia of the caisson is important and in order to account for this it is necessary to consider the structure as a dynamic system.

Studies have been made of the dynamic behaviour of walls and caissons subject to wave loads. Although it is the latter group which is of principal interest to this work, both share similar concepts so the former will also be considered here.

2.5.1 Dynamic behaviour of a wall subject to impact loads

Kirkgoz & Mengi (1986) used finite elements to model the deformations of an elastic plate due to wave loads. They proposed that dynamic amplification factors (ν) could be used during design as a simple means of accounting for dynamic effects. These relate the maximum force of a dynamic load (F_{max}) to an imaginary effective static load ($F_{stat.}$).

$$\nu = F_{stat.} / F_{max} \tag{2.3}$$

F_{stat} is defined as the static load which would have caused the same deflection (x) as that caused by the dynamic load.

$$F_{stat} = x / k \tag{2.4}$$

Where k is the structure stiffness.

Hattori (1994) measured deflections of a model wall under wave loading and demonstrated that F_{stat} depended on the relationship between impulse duration (T_d) and the natural period (T_n) of the plate. Topliss (1994) numerically modelled an impacting wave and response of a two dimensional plate. Predicted displacements and oscillation frequencies were compared

to the measurements of Kirkgoz and Mengi. Muller (1993) and Muller & Whittaker (1993) used a mass-spring-dashpot model of a beam as an analogy for the front wall of a wave power station. Values of ν were calculated for a range of values of T_n and the importance of the duration and shape of the impulse was shown.

2.5.2 Monolithic caisson motion

The design procedure used in the USSR dealt with caisson motion (see Marinski, *et al*, 1992). It was based on a linear model in which the subsoil was considered as an isotropic, elastic half-space. Marinski compared results from this model to predictions based on simple statics, the Goda formulae, and to a simple non linear dynamic model. It was shown to be less conservative than predictions made using Goda. Marinski recommends the development of non-linear models (in which the soil properties are allowed to vary with time and displacement) to describe the foundation and highlights uncertainties in the impact load histories as a limitation to the method. Marinski, like Kirkgoz & Mengi, recommends that dynamic amplification factors be used during design as a relatively simple means of accounting for dynamic effects.

The design method of Goda (1974, 1994) was also formulated to account for structural dynamics to provide an 'effective' static load. He defined the threshold of sliding as;

$$F_S(t) \leq \mu(W' - U_p)$$

Where $F_s(t)$ is the shear force, μ is the coefficient of friction, W' is the caisson weight in water, and U_p is the wave uplift force. The shear forces are not equal to the hydrodynamic loads; they include a contribution from the inertia of the structure:

$$F_S(t) = F(t) - m\ddot{x} \qquad (2.5)$$

Where m is the involved mass and $\ddot{x}$ is its acceleration. Equation 2.5 shows that the effective shear force for sliding can be greater or less than the real applied hydrodynamic load ($F(t)$) depending upon the direction of acceleration of the structure. In order to understand and predict structural response he modelled the caisson as a mass-spring system with both horizontal and rotational motion and conducted a series of physical model sliding

tests. A 'virtual' mass was included in the numerical model to represent contributions from the rubble mound and sea bed. This prevented the heel and crest moving in opposing horizontal directions. The physical tests involved a model caisson on a rubble foundation that was struck at various elevations and velocities with a weighted pendulum. The resulting peak and residual displacements were measured and compared to predictions made with the theoretical model. A simple hydrodynamic model of wave forces was then used to provide a forcing function for the caisson model. The design method derived by Goda will be discussed further in section 2.6.4.

Takahashi, Tanimoto and Shimosako (1994) used a more complex finite element model to study caisson dynamic behaviour. They used the same impulse form as Goda and calculated a range of effective loads for impulses of different durations. The results were expressed as ratios of F_{stat}/F_{max} (ν), in each case this ratio had a value equal to or less than 1. This contrasts with an earlier prediction made by Lundgrun (1968) that ν could, under resonance conditions, be as great as 1.6.

Oumeraci & Kortenhaus (1994) provided a mass-spring-dashpot model of caisson motion that described both horizontal and rotational motion. This was developed using the results of large scale model tests to provide values for the mass and the stiffness and damping terms. Both the physical and numerical model were then used to investigate structural response to different features of various applied force time histories. A single degree of freedom mass-spring model was then used to obtain values for ν for triangular loads of various relative durations (T_d/T_n) and relative rise times (T_r/T_d). They observed that, (for impulses of equal height) when $T_d/T_n < 0.3$, the value of ν is dominated by the impulse magnitude. Between $T_d/T_n = 0.3$ and $T_d/T_n = 1$, the impulse duration becomes increasingly important and above this region the rise time dominates the dynamic response. They go on to discuss the validity of using these factors for the purposes of design, and identify some limits. The load should not be too spatially focused (i.e. T_d should be greater than $0.1T_n$) and the structure should be simple so that different frequency modes are uncoupled. They conclude that such models are a suitable and rapid means for:

- Comparing dynamic load severaties.
- Identifying the most critical loads and their relevant characteristics.
- Identifying the most relevant items to be further investigated.

- Obtaining a range of the maximum response to be expected.

It has been generally accepted that the degree of simplification inherent in such models is outweighed by their usefulness (Goda, 1994, Oumeraci and Kortenhaus, 1994, de Groot *et al*, 1996).

2.5.3 Summary

Dynamic effects can cause the effective load generated by an impacting wave to be greater or less than the actual hydrodynamic load. Consequently, it is important to consider dynamic behaviour when designing caisson breakwaters. The models which have been used to investigate dynamic effects have been relatively simple. This is at least partly due to large uncertainties associated with wave impact loads as well as the mass, stiffness and damping terms. Dynamic amplification factors have been used to describe dynamic behaviour and have been recommended as a suitable means of predicting dynamic effects. To apply these factors the form of the load time history has to be known, in particular the maximum force, the rise time and the impulse duration.

2.6 Design methods for the prediction of wave impact loads

In preceding sections it has been shown that wave impact loads are very difficult to predict theoretically. In contrast, waves can be physically modelled relatively easily which makes this technique a valuable means of conducting research and assessing the suitability of potential designs. However, the effects of aeration and scale remain almost entirely unquantified. In addition, numerical models which are necessary to account for the influence of structure inertia on the likelihood of failure have only emerged recently.

Despite these significant problems many caisson and masonry vertical breakwaters have been successfully designed, using methods which were themselves based in part on physical model tests. It is instructive to consider these methods and the ways that they have overcome the significant gaps in knowledge.

The first design method proposed this century was very simple, it assumed that the maximum impact load was directly related to hydrostatic pressure.

2.6.1 Hiroi

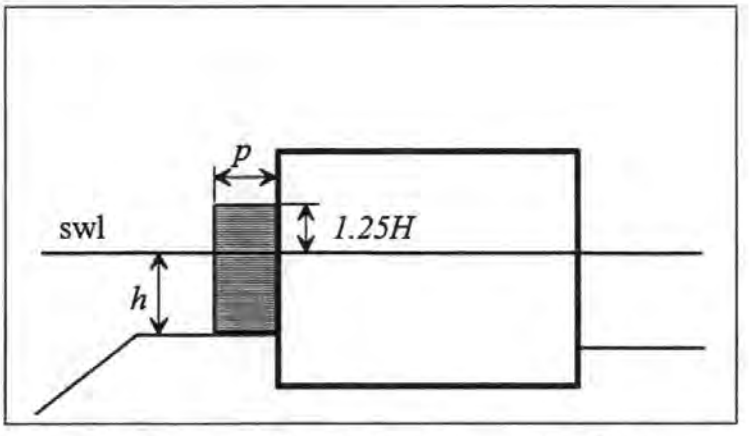

Figure 2.16. Pressure distribution proposed by Hiroi.

Figure 2.16 shows the pressure distribution proposed by Hiroi (1920). It is rectangular and extends from the top of the berm to an elevation of $1.25H$ above the still water level. The load is given by:

$$p = 1.5\, w_o\, H$$

(Later, $p = 1.5\, w_o\, H_{1/3}$)

Where H and $H_{1/3}$ are the wave height and the significant wave height respectively, and w_o is the specific weight of sea water.

This formula was used by Japanese engineers for breakwaters in water depths less than twice the wave height ($h < 2H$). Hiroi knew that much higher pressures occurred during some wave impacts but he considered them to be too transient to cause the structure to move. The constant was therefore set to the low value of 1.5 using engineering judgement in an attempt to predict F_{stat} rather than F_{max}. This equation is clearly very simple and does not account for other important parameters such as angle of wave approach or wavelength.

For greater depths, where breaking due to shoaling was not expected the formulae given by Sainflou (1928) were used.

2.6.2 Sainflou

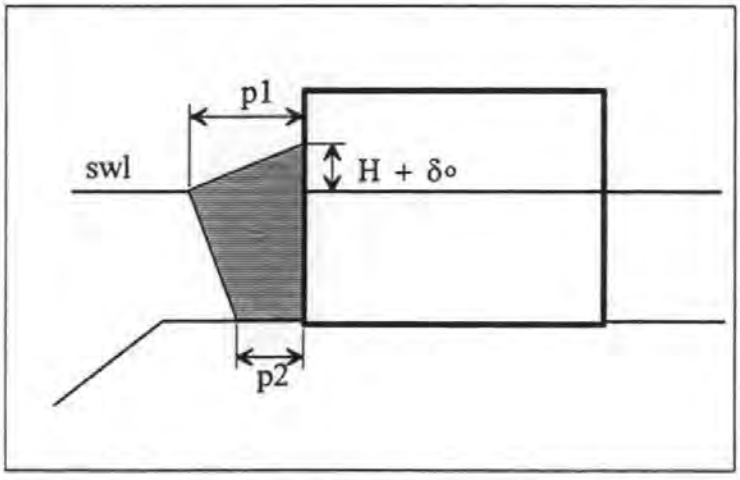

Figure 2.17. Pressure distribution proposed by Sainflou.

The pressure profile on the structure front is given by:

$$\delta_o = (\pi H^2 / L) \coth kh$$

$$p1 = (p2 + w_o h)(H + \delta_o) / (h + H + \delta_o)$$

$$p2 = w_o H / \cosh kh$$

$$k = 2\pi / L \qquad \text{(wave number)}$$

Where L is the wave length and h is the water depth.

Since the waves were assumed to be non-breaking, the load was considered to be slowly varying and the dynamic behaviour of the structure was not considered. This method is more refined than the equation of Hiroi because, in its derivation, the loads on the structure were related to wave kinematics. However, the limitation to non-breaking waves is a considerable simplification.

2.6.3 Minikin

The design method published by Minikin (1950) attempted to use an estimation of wave kinematics to predict wave impact loading.

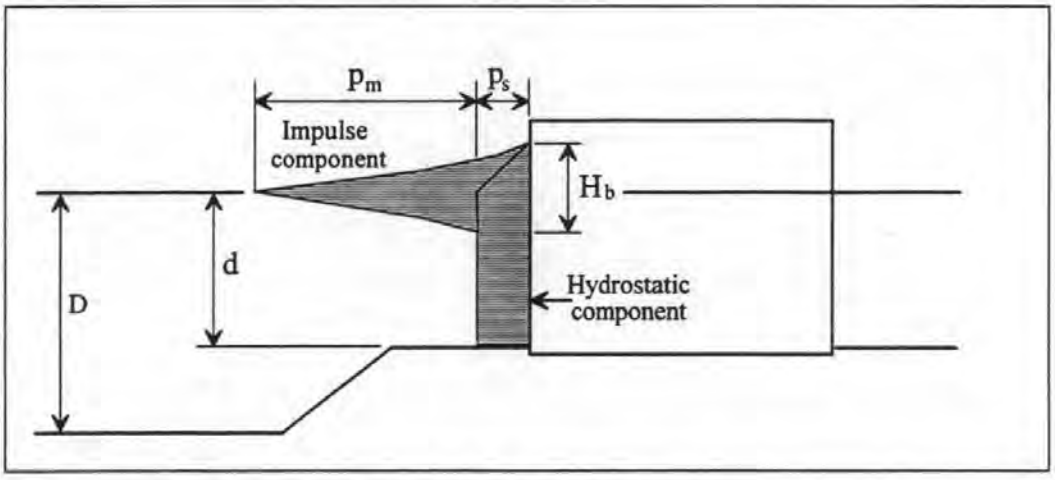

Figure 2.18. Pressure distribution due to Minikin, (1950).

The most often reproduced form of Minikin's equations appear in the Shore Protection Manual:

$$p_m = p_{max} (1 - 2|z|/H)^2 \qquad \text{:where } |z| =< H/2$$

$$p_{max} = 101\, w_o\, (H/L)\, (d/D)\, (D + d)$$

$$p_s = 0.5\, w_o\, H\, (1 - 2z/H) \qquad \text{:where } 0 =< z < H/2$$

or

$$p_s = 0.5\, w_o\, H \qquad :z < 0$$

Where C_{mk} is the wave celerity, L is the wave length, z is elevation relative to still water level, $|z|$ is the magnitude of z and p_s and p_m are static and impulsive components respectively.

The development of this pressure distribution was partly based on the work of Bagnold (1939) and a model of the vertical distribution of energy within a wave. It was calibrated against field measurements of Rouville, *et al* (1938). It can be seen that the foreshore is more comprehensively described than in the method of Hiroi, also the wave length is used as well as the wave height. The characteristics of the water are represented by its specific weight. There are several reasons why this design method might be expected to be conservative and so should be used with caution;

- No consideration is made of the inertia of the structure, therefore the significance of the transient nature of these high pressures is neglected.
- Bagnold investigated one breaker shape which was selected because it generated extremely high impact pressures. In addition he studied solitary waves which are known to propagate at higher velocities than normally occur with a wave train.
- The field data of Rouville *et al* includes the highest impact pressures recorded to date.
- Goda (1974) compared the behaviour of 34 caissons under storm conditions with performance predicted using the Minikin formulae. Failure was predicted for each case including 13 which had not moved. It should be noted however that it is not clear which form of the Minikin equation Goda used and that impact pressures were not measured for any of the caissons which were studied. Therefore no comparison was made between measured and predicted pressures, only between the prediction and occurrence of sliding.
- There is some doubt as to whether the derivation given in Minikin (1950) is dimensionally correct.

2.6.4 Goda

When Japanese engineers used both the Hiroi equation and the method of Sainflou during the design of a single structure they experienced a discontinuity in predicted wave loads and therefore breakwater dimensions at $h = 2H$. Because of this, and the simplistic nature of the Hiroi formula, a new design method was developed by Goda (1974). This was based on model sliding tests, case studies of the sliding failure of prototype structures and relatively simple models of hydrodynamic loads and structural dynamic response.

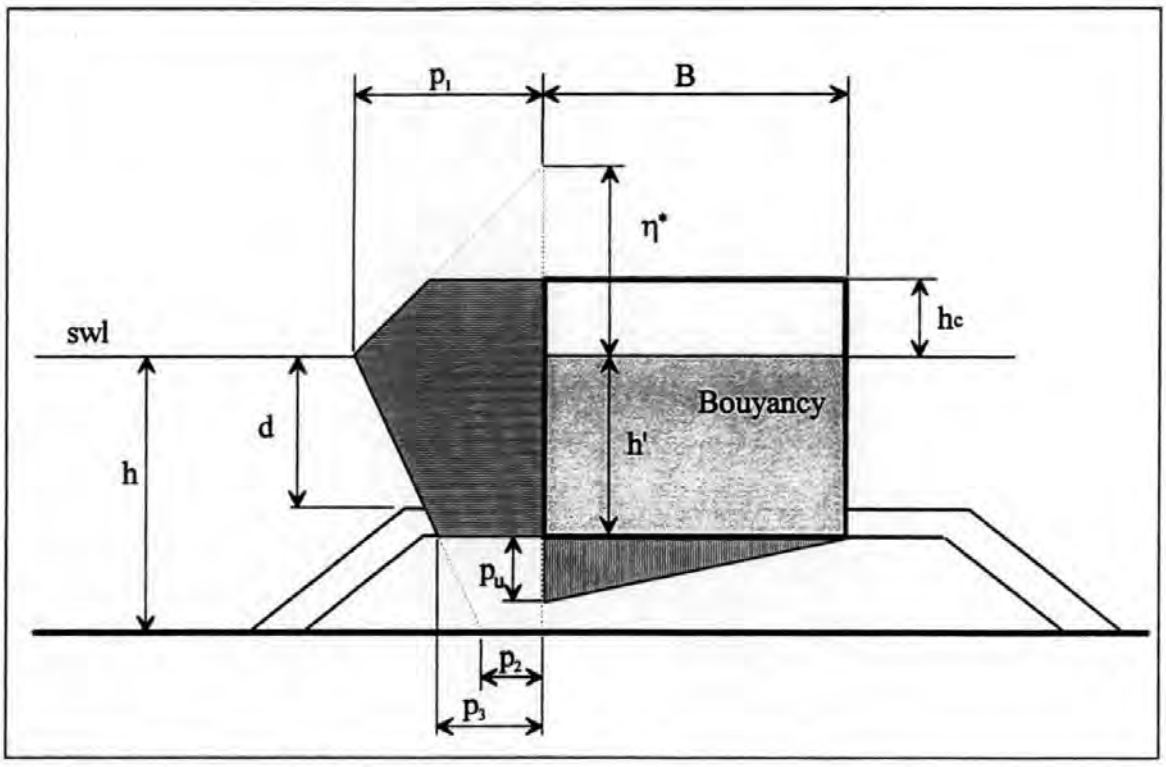

Figure 2.19. Pressures due to Goda, 1974.

The pressure distribution, which is shown in Figure 2.19, is given by:

$$\eta^* = 0.75\,(1 + \cos\beta)\,H_{max}$$

$$p_1 = w_o\,H_{max}\,(\alpha_1 + \alpha_2 \cos^2\beta) \qquad \text{(Goda, 1974)}$$

[Later revised to $p_1 = 1/2\,(1 + \cos\beta)(\alpha_1 + \alpha_2 \cos^2\beta)\,w_o\,H_{max}$, Goda, 1992 and BS 6349, 1984]

$$p_2 = p_1 / (\cosh(2\pi h / L))$$

$$p_3 = \alpha_3 p_1$$

$$p_u = \alpha_1\,\alpha_3\,w_o\,H_{max} \text{ (Goda, 1974)}$$

[Later $p_u = 0.5\,(1 + \cos\beta)\,\alpha_1\,\alpha_3\,w_o\,H_{max}$, Goda, 1992 and BS 6349, 1984]

[Original misprint $\alpha_1 = 0.6 + 1/2\,((4h/L)/(\sinh(4\pi h/L)))^2$, Goda, 1974]

$$\alpha_1 = 0.6 + 1/2\,((2kh)/(\sinh(2kh)))^2, \text{ Goda, 1992}$$

$$\alpha_2 = \min[\{(h_b - d)/(3h_b)\}\,(H_{max}/d)^2, 2d/H_{max}]$$

$$\alpha_3 = 1 - (h'/h)\,[1 - \{1/\cosh(2\pi h/L)\}]$$

$$H_{max} = \min\{1.8\,H_{1/3}, H_b\}$$

$$H_b = 0.17\,L_o\,\{1 - \exp[-1.5\,(h_b/L_o)\,(1 + 15\tan^{4/3}\theta)]\}$$

$$h_b = h + 5\,H_{1/3}\tan\theta$$

$$T_{max} = T_{1/3}$$

Where β is the angle of wave approach and θ is the foreshore slope. β should be rotated by up to 15° toward the line normal to the breakwater to reflect uncertainty in its calculation.

The balance between the impulse and quasi static pressure components is maintained by means of the three α terms. α_1 and α_2 were determined empirically using model experiments and 34 case studies of caisson behaviour under storm conditions. The revision of P_u was made to account for the effect of the wave direction on the uplift pressures. The expression for H_{max} was empirically derived to account for the variations in wave height as it approached the structure due to shoaling and breaking.

The formulae do not explicitly describe the physics of an impacting wave. Instead they map the combined response of a structural dynamic model and a simple model of hydrodynamic loading. In the latter model the magnitude of the force impulse is assumed to be equal to the momentum of a half cylinder of water of diameter H_b moving with the same velocity as the wave (C_b), as illustrated in Figure 2.20.

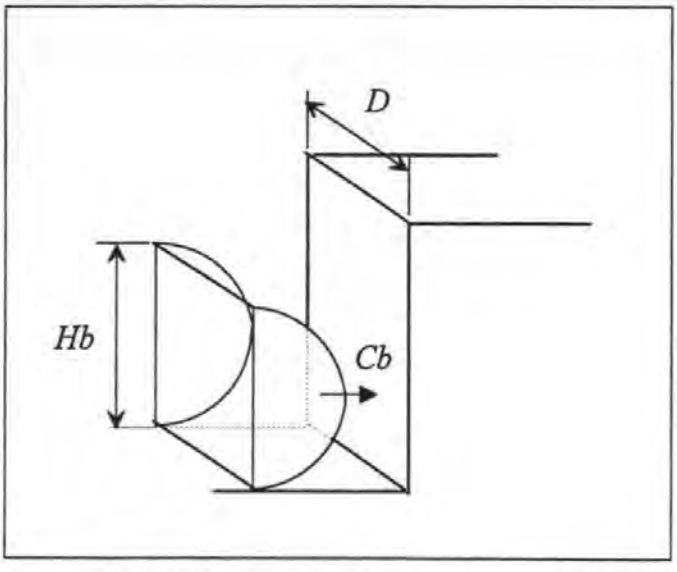

Figure 2.20. Half cylinder of water assumed to cause impulse loads.

This set the magnitude of the force impulse to:

$$I_{Goda} = (\pi/8)\, \rho\, C_b\, D\, H_b^2$$

Which is approximately:

$$I_{Goda} = 0.4\,\rho\,C_b\,H_b^2$$

per unit run of the structure

The form of the impulse was assumed to be a right angled triangle with its peak at the end of its duration, as shown in Figure 2.21.

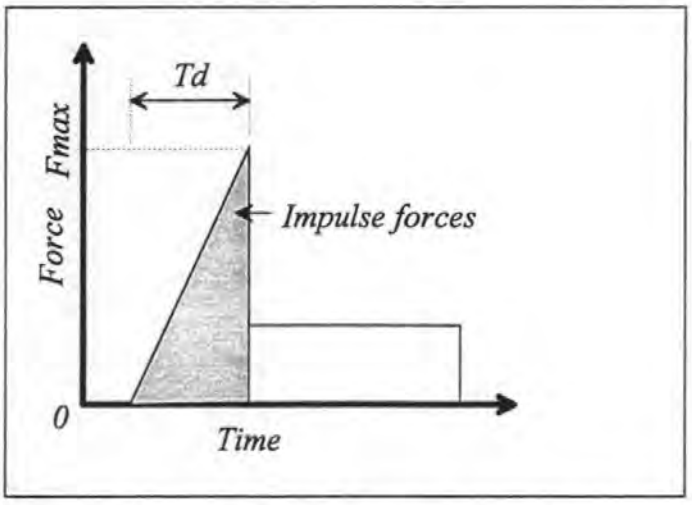

Figure 2.21. Illustration of the form of the force time history assumed by Goda.

Data collected from small scale experiments were then used to determine a minimum value for the impulse duration of:

$$T_{d(min)} = \frac{\pi C_b}{g60}$$

Which set the largest possible value of F_{max} to:

$$F_{max} = 15\,\rho\,g\,H_b^2$$

Per unit length. By combining the hydrodynamic and structural dynamic models Goda predicted that the effective static pressure has a maximum of $3\,\rho\,g\,H_b$ and that such levels are rarely reached.

The Goda method has become the most widely used for caisson breakwaters because;

- It has been tested against the performance of prototype structures (Goda, 1974 and Tanimoto and Takahashi, 1994).
- It avoids structural discontinuities which results from the use of depth limited formulae.
- It includes more of the parameters which affect wave loading than any other method including angle of wave approach, breaker height at the structure (and the means to calculate this), wave period, water depth, depth of berm, buoyancy and berm width.
- Scale effects were partly overcome because the method was calibrated against the performance of prototype structures.
- Allowance has been made for the dynamic response of the structure.

The limitations of this method should also be recognised. Not all the factors known to influence loading are included, such as the berm permeability and roughness, aeration, scale and breaker shape. However it is reasonable to suppose that these have been implicitly accounted for, at least in part. Because the formulae are partly empirical they are relatively inaccessible for development and may be limited in their range of applicability. Another possible limitation is a built in assumption that the worst breaker shape is one which has broken before it arrives at the structure, this may not always be the case.

One of the main advantages of this scheme for the design engineer is that it deals, to some extent, with the dynamic behaviour of the structure. As with the Hiroi method the effect of the load is predicted rather than the actual transient loads. This has also lead to its occasional misuse by designers who will sometimes use it to predict loading on other structure types or structure elements. Also researchers occasionally compare measured wave impact pressure maxima to Goda's effective pressures (see for example Ergin and Abdulla 1993, and the criticism which followed it by Allsop and Muller, 1995).

Tanimoto and Takahashi (1994) reviewed the Goda method and found that it did not properly account for the forces which occur during impulse loads. Using the results of new laboratory sliding tests they suggested that an impulse coefficient α_I should be added: p_1 is replaced by;

$$p_1 = 0.5\,(1 + \cos\beta)\,(\alpha_1 + \alpha^* \cos^2\beta)\, w_o H_D$$

Where

$$\alpha^* = \text{Max}\,[\,\alpha_2,\ \alpha_i\,]$$

$$\alpha_i = \alpha_{io}\,\alpha_{il}$$

a_{io} represents the effect on the wave height of the mound

$$\alpha_{io} = H / d \qquad \text{if} \quad H =< 2d$$

$$a_{io} = 2 \qquad \text{if} \quad H > 2d$$

α_{il} represents the effect of the mound shape

$$\alpha_{il} = \cos\delta_2 / \cosh\delta_1 \qquad \text{if} \quad \delta_2 =< 0$$

$$\alpha_{il} = 1 / [\,\cosh\delta_1\,(\cosh\delta_2)^{1/2}\,] \qquad \text{if} \quad \delta_2 > 0$$

$$\delta_1 = 20\,\delta_{11} \qquad \text{if} \quad \delta_{11} =< 0$$

$$\delta_1 = 15\,\delta_{11} \qquad \text{if} \quad \delta_{11} > 0$$

$$\delta_2 = 4.9\,\delta_{22} \qquad \text{if} \quad \delta_{22} =< 0$$

$$\delta_2 = 3\,\delta_{22} \qquad \text{if} \quad \delta_{22} > 0$$

$$\delta_{11} = 0.93\,(B_M / L - 0.12) + 0.36\,[\,(h - d) / h - 0.6\,]$$

$$\delta_{22} = -0.36\,(B_M / L - 0.12) + 0.93\,[\,(h - d) / h - 0.6\,]$$

Where B_M is the berm width and L is the wave length.

2.6.5 Blackmore and Hewson

Another relevant wave impact formula that is used in the design of sea walls was proposed by Blackmore and Hewson, (1984) and included in BS 6349, (1984). It is of particular interest because it is the only approach which deals explicitly with the level of entrained air in the wave.

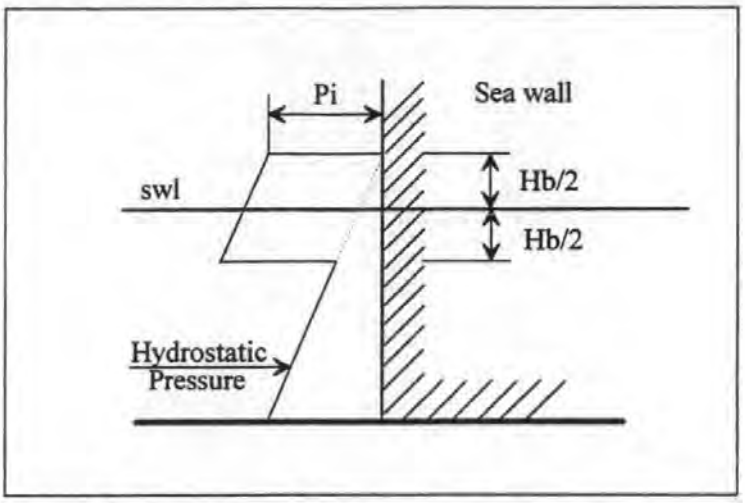

Figure 2.5. Pressure distribution of Blackmore and Hewson (1984).

$$Pi = \lambda \rho T C_b^2$$

Where λ is the aeration term which has units of s^{-1} and is also a function of wave steepness, rise time, foreshore roughness and scale. Recommended values were derived from laboratory tests and marine measurements on sea walls in the south-west of England. They range between 0.1 and 0.5 with decreasing foreshore roughness at prototype scale and 1 and 10 at model scale. The equation was developed from the compression model of Bagnold and was shown to provide a good fit to the field and model data.

Muller and Walkden (1998) proposed new values for λ pointing out that this method does not account for the importance of foreshore slope. They proposed the extended range of values for λ shown in Table 2.1. This was based on a review of field measurements and model tests.

Sea bed	Seabed slope		
	1/5 - 1/10	1/30 - 1/50	1/100
Very smooth	1.5	0.9	0.7
Rough, rocky	0.5	0.3	0.24
Very rough, surfacing rocks	0.31	0.18	0.14

Table 2.1. Extended aeration factors, from Muller and Walkden (1998)

2.6.6 Summary

During this century the design methods available to breakwater engineers have been increasingly sophisticated and have included more of the parameters known to affect impact loads. Despite this evolution they have always had to employ empiricism to overcome gaps in knowledge and, to date, none of them deal with all of the relevant parameters. Some have tried to relate wave kinematics to the load, although Goda successfully used a very simple model of an impacting cylinder which moved with the celerity of the wave. It has proved to be important for those methods intended to predict impulsive loads on breakwaters that they account for the high structural inertia. Hiroi did this using engineering judgement. Goda took a more advanced approach and modelled dynamic behaviour. Minikin neglected dynamic effects and this is probably a major reason why his method is not widely used. In fact Goda (1992) stated that he knew of no structures which had been designed to withstand 'Minikin' loads.

Chapter 3

The interpretation of wave impact loads

3.0 Introduction

This chapter will provide a context for both the experiments conducted during the study and the way in which the results are interpreted. Justification for the types of experiment is drawn from gaps in knowledge, which were identified in the preceding chapter. Chapter 2 also revealed a need for development in the philosophy used to interpret the results of model tests. A new approach is suggested. This is developed from ideas that have evolved from Bagnold's 'effective length' concept.

3.1 Experiments

Chapter 2 identified a clear need for a laboratory based comparison between wave impact tests that differ in size by at least an order of magnitude. To meet this need both small and large scale tests were conducted. The former tests were made in the flumes of the University of Plymouth's School of Civil Engineering, and the University of Edinburgh's department of Mechanical Engineering. Very few large scale facilities exist, so this project was fortunate to benefit from a short period of access to the Large Wave Flume, or Grosser Wellen Kanal (GWK) in Hanover, through collaboration with the Franzius Institute and the University of Hanover. These experiments and the others conducted during this study are described in Chapter 5. A comparison between their results is made in Chapter 9.

There has been a great deal of interest in the effects of air on wave impacts. This has lead to some recent developments in apparatus that can be used to obtain measurements of aeration in impacting breaking waves. This study builds on these developments in order to obtain aeration measurements during the scale tests. Due to the newness of the work, Chapter 4 is devoted to the development of aeration measurement apparatus and

techniques. Because of the large number of parameters known to complicate wave impact loads, it was decided to compliment the aeration tests with a series of aerated 'Drop' tests. These involved the impact of a falling plate, instrumented with pressure transducers, onto the surface of a body of water into which controlled quantities of aeration were introduced. This allowed an investigation of aerated liquid / solid impacts under closely controlled conditions. The aeration results are presented in Chapter 6.

3.2 Interpretation of wave impact loads.

The review of literature revealed a general form that has emerged in the methods used for the design of caisson breakwaters. This can be summarised as; establish a maximum force impulse, predict its form and account for the dynamic response it induces in the structure. It seems reasonable that a similar approach be adopted when interpreting the results of physical model tests. It is therefore surprising that the force impulse has received relatively little attention in the literature. Some studies have looked at individual measured impulses but none could be found that had investigated its variation over multiple events or for a range of test conditions. Several studies had dealt with a part of the force impulse, namely the pressure rise impulse. This was first observed by Bagnold (1939), who found that it tended towards a definite upper limit; he expressed this as an 'effective length'.

3.3 The effective length concept

The 'effective length' is the length of an imaginary horizontal column of water travelling with the wave and located behind its air pocket. As has already been described in section 2.3.1, this length of water was assumed to act like a piston compressing the pocket to generate an impulse. Bagnold obtained values for this length from measurements of pressure rise impulse by assuming that the height of the air pocket was a fixed proportion of the wave height and that the pressures on the wall were equal within the air pocket and hydrostatic beyond it. This allowed him to assume that his single pressure transducer provided him with a measurement of force. He was therefore able to relate the time integral of the measured rise in pressure (the shaded area in Figure 3.1) to the momentum of the conceptual piston.

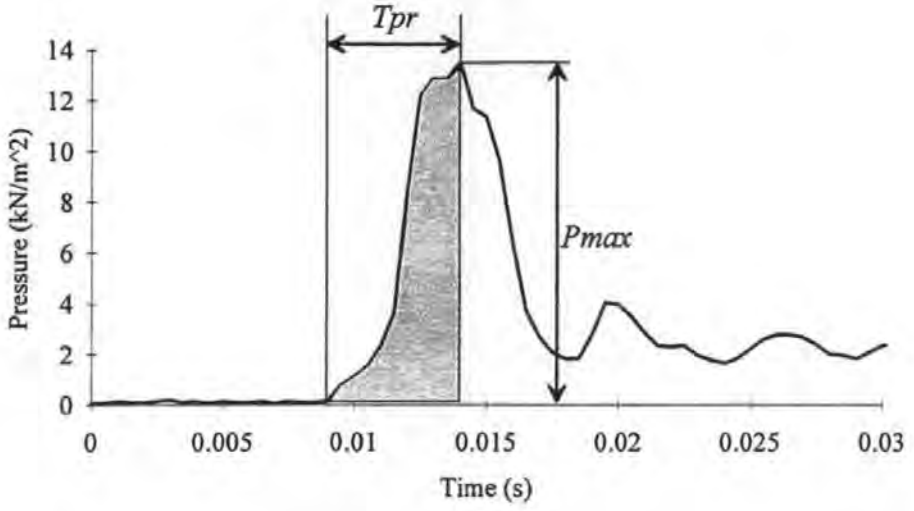

Figure 3.1. Example of the temporal variation of an impact pressure time history recorded at still water level, the shaded area represents the pressure rise impulse.

Through his assumptions and measurements Bagnold obtained the following description of the impulse momentum;

$$I_{Bagnold} = 0.08\,\rho\,H_b^2\,C_b \qquad (3.1)$$

A similar description was used by Lundgren (1968) to model 'ventilated shock' impacts. In this case the momentum assumed to be involved in the impulse was much larger:

$$I_{Lundgren} = 0.5\,\rho\,H_b^2\,C_b \qquad (3.2)$$

In section 2.6.4 it was shown that Goda assumed a similar level of momentum in the hydrodynamic model at the centre of his design method.

$$I_{Goda} = 0.4\,\rho\,H_b^2\,C_b \qquad (3.3)$$

Comparison of equations 3.1 to 3.3 show that both Lundgren and Goda believed the effective length to be much greater than the value found by Bagnold. This may be partly explained by the fact that Bagnold defined his impulse as ending at the load maxima, whereas Goda and Lundgren proposed that the impulse lasted until the forces had dropped

back to quasi-hydrostatic levels. However, neither Goda nor Lundgren provided experimental data to support their values.

Other results can be found which support the idea of an upper limit to the magnitude of the pressure rise impulse; these have been expressed in the form of relationships between the pressure maxima and the rise time.

3.4 P_{max} T_{pr} relationships

When regular waves impact tests are conducted upper limits tend to emerge in the P_{max} T_{pr} domain, when P_{max} is large T_{pr} tends to be small and *vice versa*. Weggel *et al*, (1970) found,

$$P_{max} = 232\, T_{pr}^{-1} \tag{3.4}$$

To be an upper limit to the results of 12 laboratory 2D measurements with a beach slope 1/20 and a discontinuous wave wall. Regular waves were used to form one breaker type and although the heights and periods are not specified, the steepness is given as 70 mm/sec. Six pressure transducers were used which were located 19 mm apart. No information was provided on their characteristics or sample rate or the measures taken to ensure a calm water surface. They also found:

$$P_{max} = 485 T_{pr}^{-1} \tag{3.5}$$

for waves of 17.9 mm/sec steepness.

In 1990 Kirkgoz found:

$$P_{max} = 250 T_{pr}^{-0.9} \tag{3.6}$$

Which was the best fit line to 70 laboratory 2D measurements with a beach slope of 1/10 and a continuous wave wall. Regular waves were used in still water depth of 0.61 m with an average height of 0.259 m and a 2 second period, these conditions produced plunging

breakers. 10 pressure transducers with a 19 mm active surface diameter at 30 mm centres were sampled at 40 kHz. 1 hour was left between each test to allow the water surface to calm.

Hattori *et al,* (1994) obtained:

$$P_{max} = 400T_{pr}^{-0.75} \tag{3.7}$$

As the upper limit function to a large number of laboratory events which included a range of breaker shapes. The beach slope was 1:20 and the water depth at the wall was 50 mm. Regular wave trains were generated with an energy absorbing paddle with heights which varied from 40 to 120 mm and periods of 1.5, 1.7 and 2.0 seconds. Six pressure transducers were sampled at 5 kHz and located at 10 mm centres around still water level.

An example obtained from marine waves was shown by Blackmore and Hewson (1984):

$$P_{max} = 3100T_{pr}^{-1} \tag{3.8}$$

This is the upper limit function to approximately 80 full scale marine wave impacts measured on a sea wall. The wave heights ranged from 0.8 to 1.3 m with periods of from 2.67 to 8.5 seconds. The waves had mostly broken at impact. Seven 25 mm diameter pressure transducers were positioned at around 1 m intervals.

These results are illustrated in Figure 3.2.

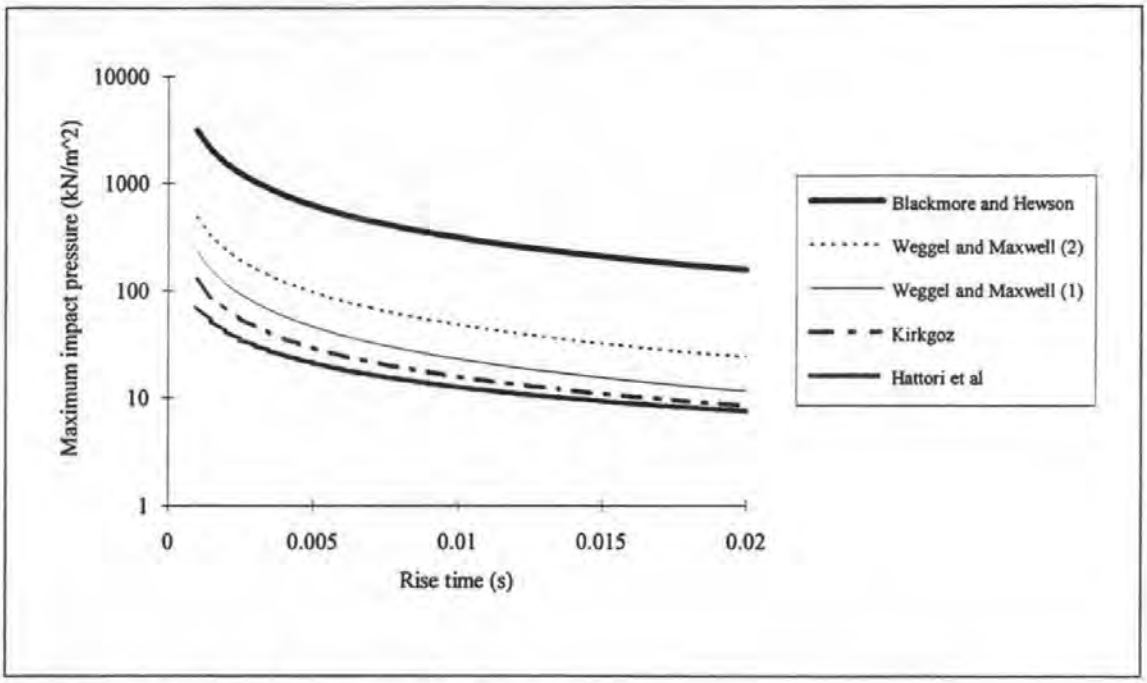

Figure 3.2. Published P_{max} T_{pr} relationships.

These examples are given to show both the variation in the forms of the relationships (the constant varies between 232 and 3100 and has various different units) and to demonstrate the great number of differences between the test conditions which make them difficult to compare.

These relationships emerge because the pressure rise impulse is basically triangular, is evidently limited in magnitude and highly variable in form. Several explanations have been proposed to explain this variability.

3.5 Scatter below the P_{max} T_{pr} lines

It has been generally assumed that the variability in the form of the pressure rise impulse is due to a variation in aeration. This may be in the form of entrained air, as assumed in the formulae of von Karmen, Partenscky and Kamel (see section 2.3.2), expelled air, (Lundgren 1968) or entrapped air as proposed by Bagnold;

$$P_{max} - P_0 = 2.7\ (\rho\ U^2\ K/D) \qquad (3.9)$$

so that for similar waves the pressure maxima and rise time depended on the thickness of the air pocket (D). Minikin (1950) approached the problem by trying to fit a spatial pressure variation to a theoretical temporal variation to identify a maximum. Goda (1994) dealt with forces and simply assumed:

$$F_{max} = 15\,\rho\,g\,H_b^2 \tag{3.10}$$

and that

$$T_d = 2\,I_{Goda} / F_{max} \tag{3.11}$$

3.6 Scaling of the impulse

Bagnold compared his model results for effective length with field data recorded by Rouville *et al* (1938). He found that they were quite well related by the Froude law. This was in contrast to the comparison of impact pressure maxima which showed that Froude scaling the model measurements over-predicted the prototype pressure maxima. It follows that prototype rise times must have been relatively larger for the prototype events. This may be visualised using Figure 3.2 as a general shift in location along the P_{max} T_{pr} lines towards the right hand side with an increase in scale.

3.7 Summary

Measurements of wave impacts will be made at different scales which will be complimented with simultaneous measurements of aeration. One of the objectives of the project is to provide a methodology for the prediction of design loads for caisson breakwaters from model results. Guidance has been found in the emergent form of textbook design methods, i.e. those which do not make use of physical model tests. This is to predict the form and magnitude of the force impulse and then use it to assess structural response. Recent developments in understanding of caisson dynamics have provided the means of predicting structural behaviour including relatively simple dynamic models and dynamic amplification factors. Relatively little data has been generated, to date, on the force impulse. Some attention has been given to the pressure rise impulse; its magnitude

has been shown to tend towards an upper limit. There is some evidence to suggest that this upper limit may be free of scale effects. The form of the pressure rise impulse has been shown to be basically triangular but highly scattered around or under a boundary described by;

$$P_{max} = A\, T_{pr}^{-B} \qquad (3.12)$$

Where A and B are constants that have not yet been related to the physics of impacting waves. Some models have been proposed to explain the scatter, but these have not been validated against experimental data. It is generally believed that it is related to the presence of aeration.

In addition to conducting scale tests and measuring wave aeration this project will investigate properties of the force impulse and the meaning behind equation 3.12. By these means it is hoped to develop a new methodology for predicting design wave loads for caisson breakwaters using the results of physical model tests.

Chapter 4

Development of aeration probes

4.0 Introduction

Resistance based aeration probes were developed for both large and small scale measurements. The design of the large scale apparatus was based on instruments previously used by Griffiths (1994) during field measurements. The difficulties associated with such measurements increase as the size of the wave decreases, consequently entirely new apparatus was designed, developed and tested for the small scale tests.

4.1 Resistance based aeration measurements

Griffiths (1994) reviewed various methods which could be applied to the measurement of void fractions in water including optical back-scatter, acoustic recordings as well as localised measurements of capacitance and resistance. She concluded that the last of these was the most appropriate and went on to conduct field measurements using sensitive instruments developed by Bird *et al*, (1999). These operated by generating a high frequency alternating electrical field between two electrodes, and measuring its resistance. The resistances were converted into percentages of aeration using an equation of Maxwell (1873) that was derived to give the void fraction (β) of a conducting medium containing small spheres of zero conductivity:

$$\beta = \frac{R_{p1} - R_{po}}{R_{p1} + (R_{p0}/2)} \qquad (4.1)$$

where R_{pi} and R_{p0} are the electrical resistances of voided and unvoided medium respectively.

This equation was first used for the measurement of air in water by Lamb and Killen (1950) who examined the self aeration of fast flowing streams. They needed spatially focused readings, so generated a small field of influence (measurement region) by positioning their electrodes close together. The small gap meant that the measured resistance was strongly affected by individual bubbles so the output signal showed large fluctuations. This was overcome by observing the signal with a needle voltmeter with a poor frequency response and recording an estimated mean value. This provided a simple form of time averaging. The results for void fraction varied from around 2 % at the channel base to around 90 % at the frothy air water boundary. Results were distorted to some degree by motion of the probes which deflected in the fast moving flow. Lamarre and Meville (1992) used a similar approach to produce contour maps of air plumes below laboratory and field offshore breakers. Since the void fraction varied periodically with the process of wave breaking, time averaging was not desirable, so a large field of influence was needed to minimise the sensitivity of the output to individual bubbles. The field size increases with the gap between the probes, but this could not be made too large because of the close proximity of the water surfaces in the small scale breaking waves. A long field of influence was therefore created using thin wire electrodes aligned perpendicular to the essentially two dimensional flow. The output of this probe may have been sensitive to the direction of the flow and might have caused some air entrainment when located near the still water level although this was not discussed. Graham *et al*, (1993) developed similar wire electrodes for use with the resistance meters of Bird *et al*. These were used to obtain measurements of void fraction in small scale fresh water impacting waves to compliment simultaneous measurements of pressure. These instruments suffered from problems inherent in their design, in particular they were sensitive to the direction of bubble motion and errors arose due to a lateral offset between them and the pressure transducers. Walkden *et al,* (1995) used a process of ensemble averaging to improve the confidence in the output of these instruments in order to examine the relationship between entrapped air and the motion of regions of high pressure on the wall. These instruments will be discussed below in greater detail. Crawford *et al,* (1997) took measurements of aeration in both fresh and sea water small scale impacting waves, as previously described in section 2.3.2. The instruments they used were copies of the new probes developed in this chapter.

4.2 Design of large scale electrodes

Due to collaboration with the universities of Hannover and Braunschweig aeration measurements were conducted as part of this study in Europe's largest wave flume, the Grosser Wellen Kanal (GWK). The time available to prepare for these tests was too short to allow testing and development of new instruments before deployment so the design was based on one previously used in field measurements by Griffiths (1994). Her probes were made from two bolts protruding from a metal housing that contained a pressure transducer positioned between the bolts. They were aligned perpendicular to the plane of the sea wall upon which they were mounted and were partially insulated so that only the ends of the bolts acted as the electrodes.

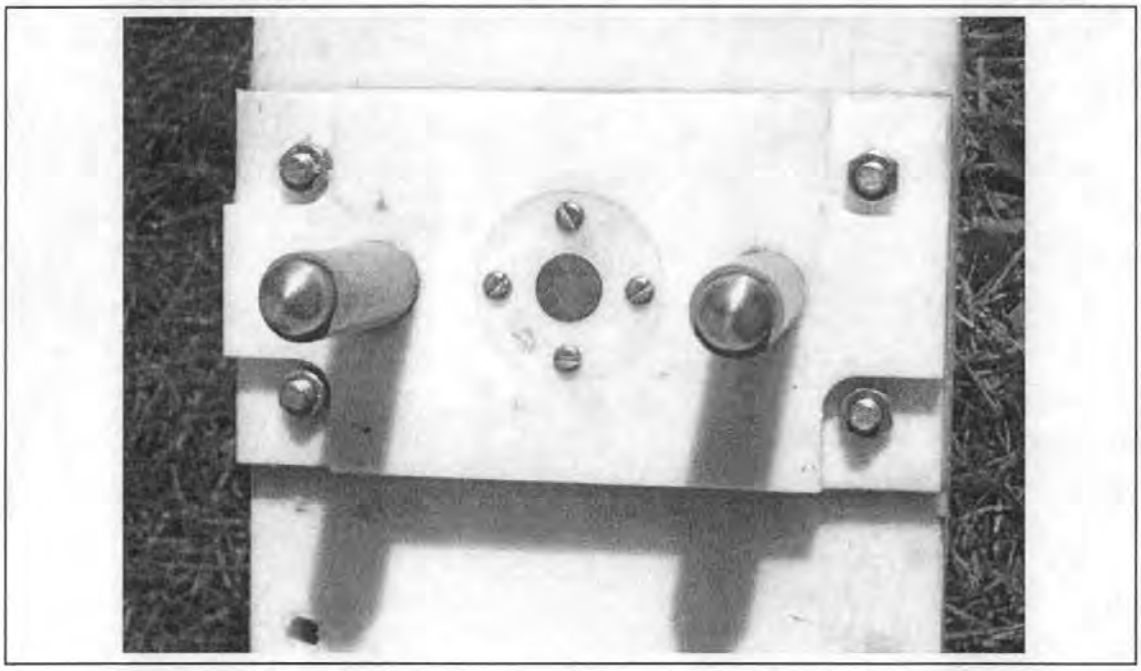

Figure 4.1. Pressure transducer and aeration probes mounted in the GWK spar.

The GWK aeration probes were made from 15 mm diameter stainless steel bar which was 140 mm long. Most of the bar was insulated with ABS pipe and sealed with two 'O' rings, the conducting ends were turned to hemispheres. The electrode pairs were fixed into a mounting plate so that each projected by 60 mm with a gap between them of 85 mm. Details of the electrodes and mounting plates are shown in Figures 4.1 and 4.2.

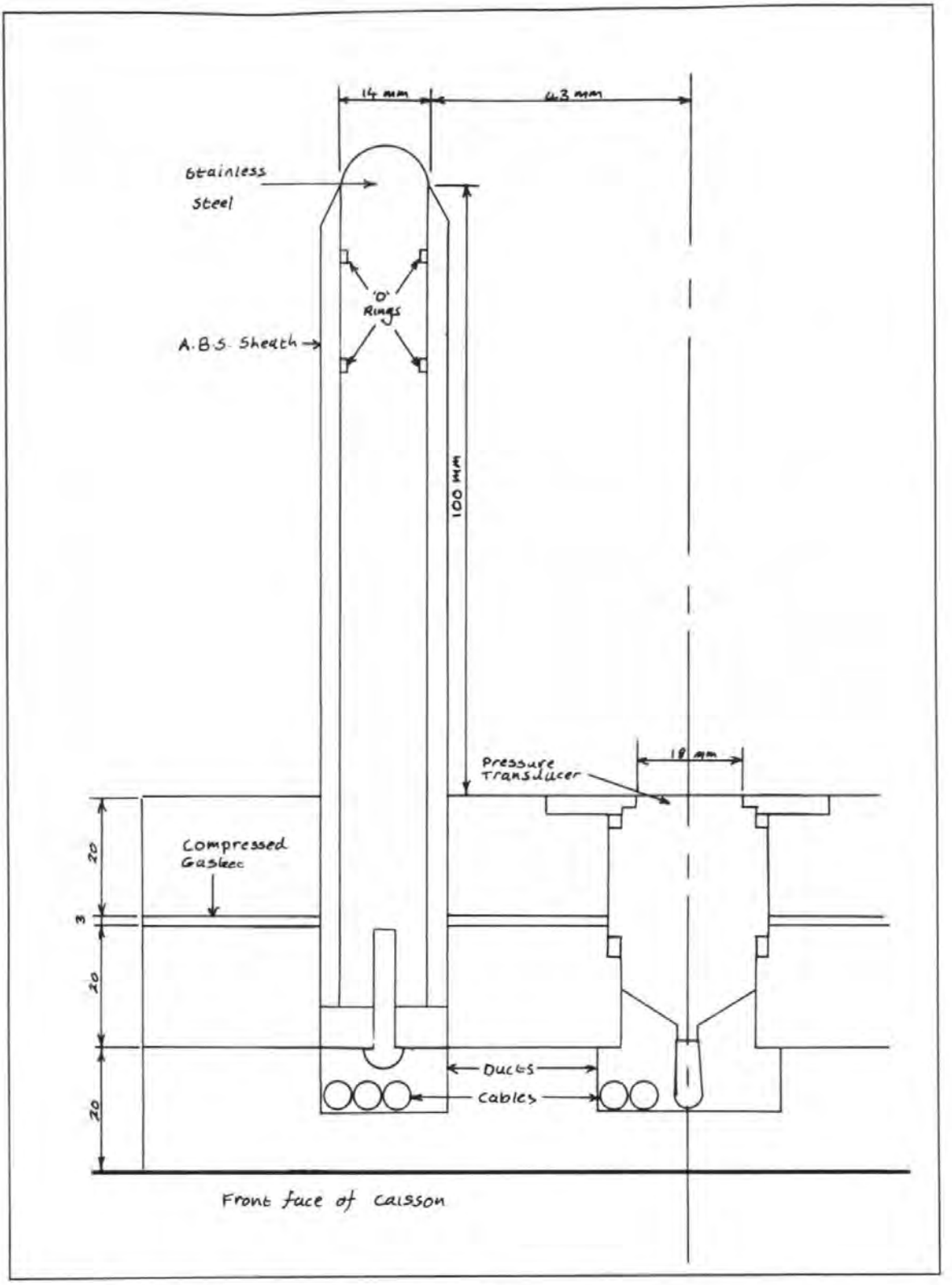

Figure 4.2. Details of the GWK aeration probes.

4.3 Small scale wire electrodes

Before developing new aeration probes for use at small scale, the thin wire electrodes developed by Graham *et al*, (1993) were used to make preliminary observations and to test

their performance. They were mounted perpendicular to the plane of water motion, 10 mm from the face of the wall as shown in Figure 4.3. Results which are typical of those obtained with these instruments can be seen in Figures 4.4 and 4.5.

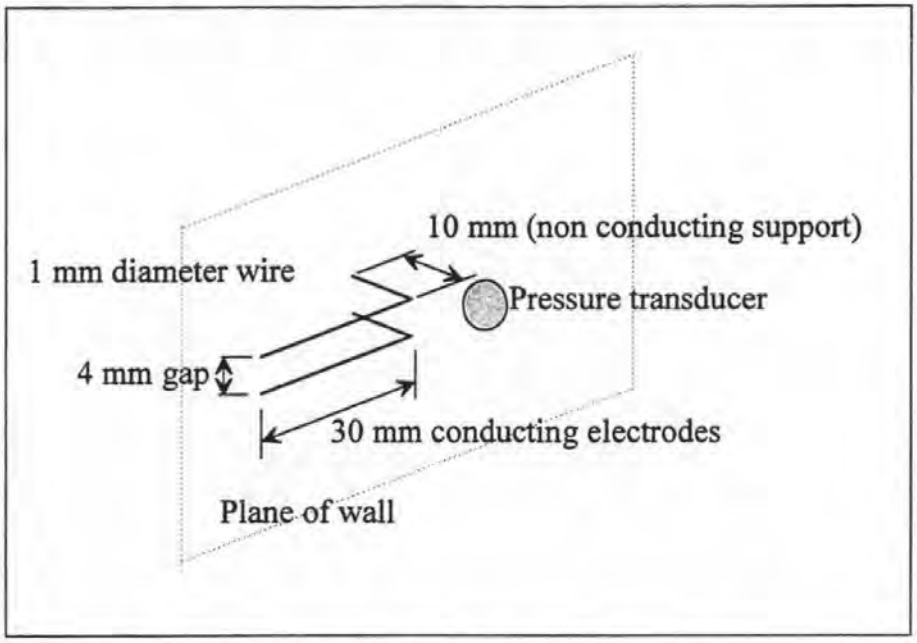

Figure 4.3. Configuration of thin wire aeration electrodes.

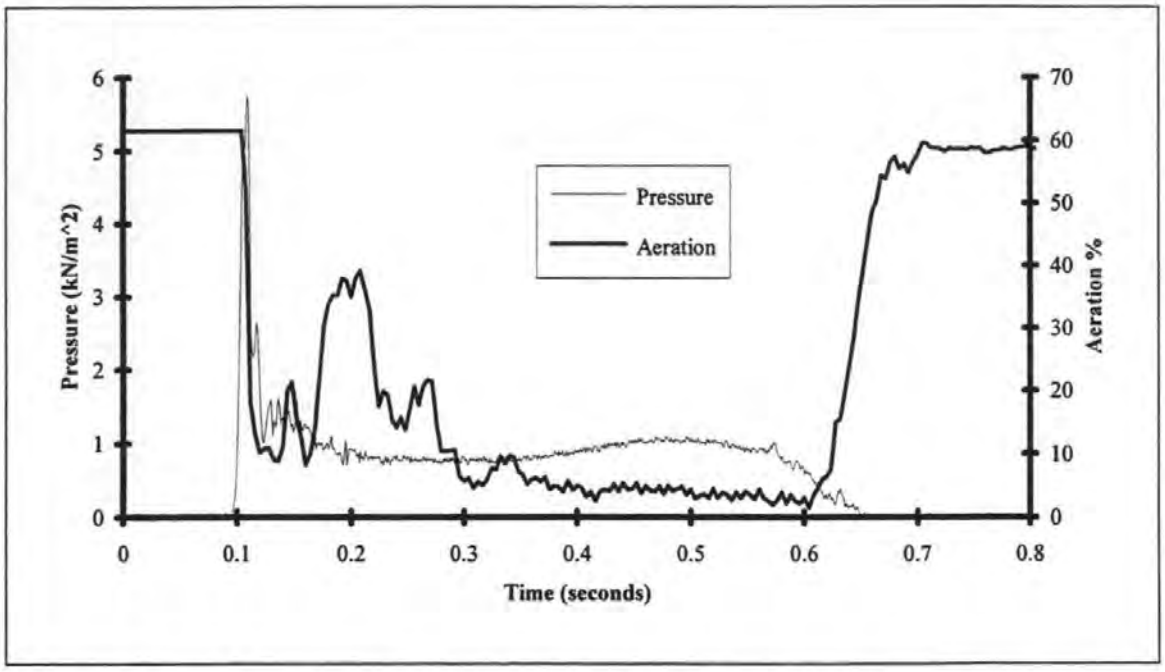

Figure 4.4. Typical aeration time history recorded with thin wire electrodes, with a synchronous pressure record.

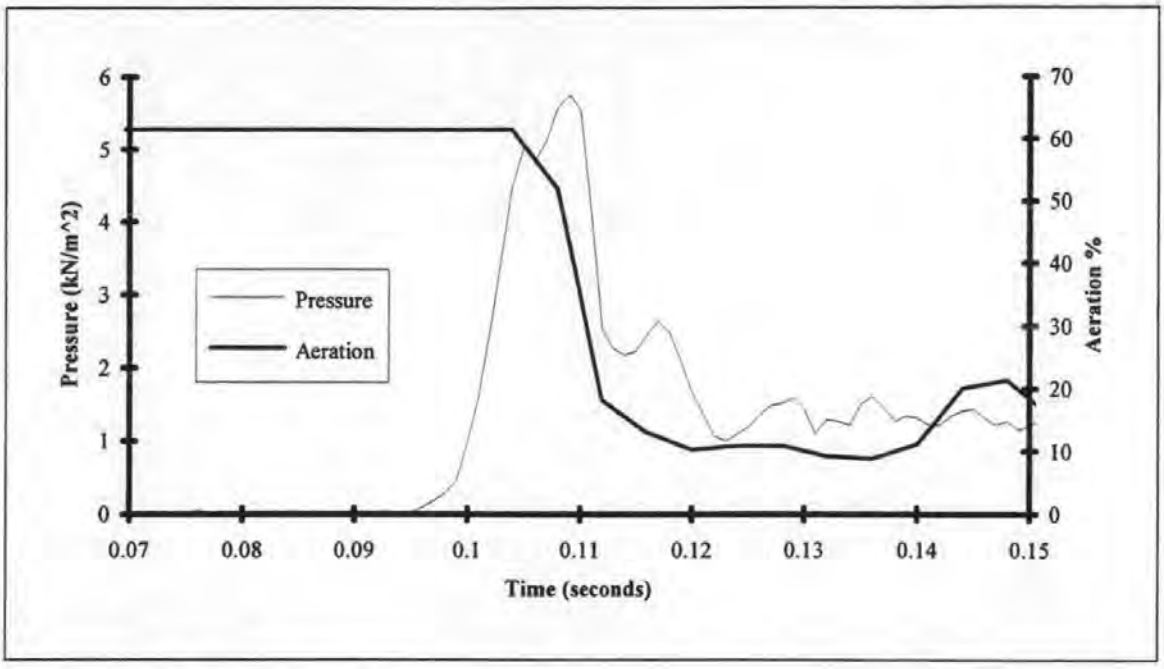

Figure 4.5. Enlarged section of Figure 4.4.

A problem experienced with these instruments was that many tests showed impact pressures occurring before the aeration gauges showed any response or else showed very high void fractions as can be seen in Figure 4.5. Two possible explanations for this are that either three dimensional effects caused the wave to arrive at the pressure transducers (which were horizontally offset) before the aeration probes, or the high output indicated the presence of a large air pocket or a partially submerged field of influence. Further problems occurred because of the construction and orientation of the electrodes.

Because each was slender and only supported at one end with its principle axis perpendicular to the plane of water motion, there was a danger of the electrodes deflecting. They may also have caused some air entrainment by obstructing the flow. Graham *et al*, (1992) also observed, during calibration, that the output of the instruments was sensitive to the relative direction of the moving bubbles. This was because the field of influence was concentrated at the electrodes so that the measured resistance depended upon the location of the bubble within the field. If a bubble moved vertically past both electrodes (Figure 4.6a) then the overall measured resistance was greater than if the same bubble passes horizontally through the field (Figure 4.6b).

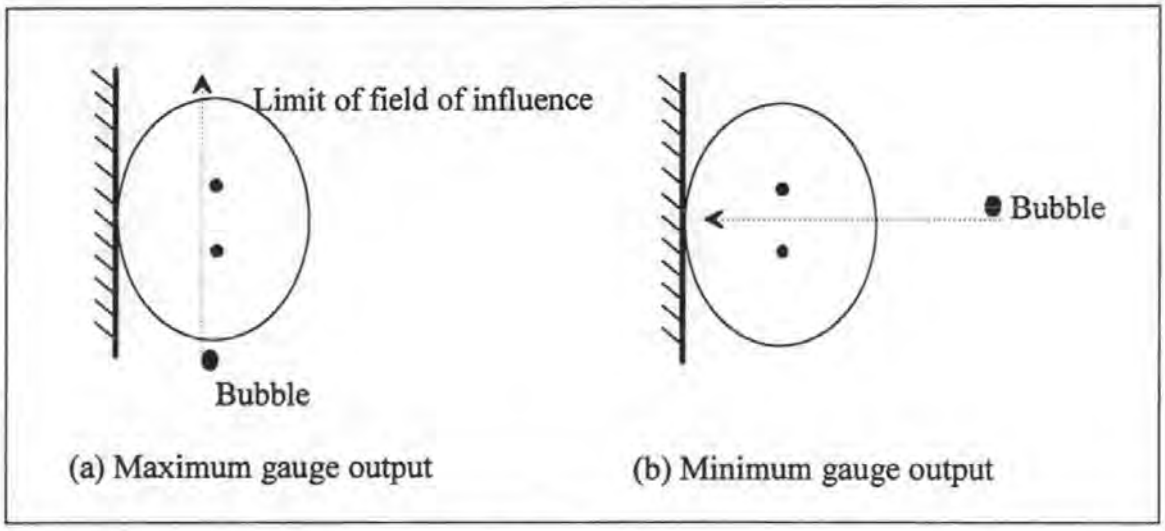

Figure 4.6. Illustration of the reason for the directional sensitivity of Graham's electrodes in the plane of flow.

Consequently the relationship between void fraction and measured resistance during the, mainly horizontal, arrival of the wave at the wall is different to that which exists during the uprush directly after impact. Since measurements could only be obtained when the electrical field was full the system was only accurate during the small time interval between the arrival of the water at the wall and before the development of the uprush. This moment could only be identified from the pressure records which, as was shown above, were at risk from lateral offset errors.

4.4 Development of new probes

New probes were designed after considering the nature of aeration in waves and the problems experienced with the wire electrodes. An ideal probe would be able to discern expelled air, entrapped pockets and entrained bubbles, in addition its construction should be rigid and cause minimal flow separation. One arrangement which was considered was to use non-protruding flat plates embedded in the wall, but this option was rejected because of the expected high sensitivity to entrapped air. For this reason it was decided to use protruding electrodes and the means by which they might be supported were considered. These included a free-standing column on the foreshore, wires tensioned from the foreshore to a structure above the wall and simple mounts projecting from the wall face. The last of these was chosen because it was believed they would be the least prone to deflection and least likely to cause flow separation. It was decided that the electrodes

should face towards each other rather than towards the approaching wave to maximise the electrode gap and so reduce flow disruption between the probes. The electrode size (4.5 mm diameter circular plates) was selected to match the working range of the existing resistance meters.

Circuitry for only four probes was available so the array configuration had to be carefully selected. A main requirement was the ability to identify when the field of influence was fully submerged and whether entrained, entrapped or expelled air was being measured.

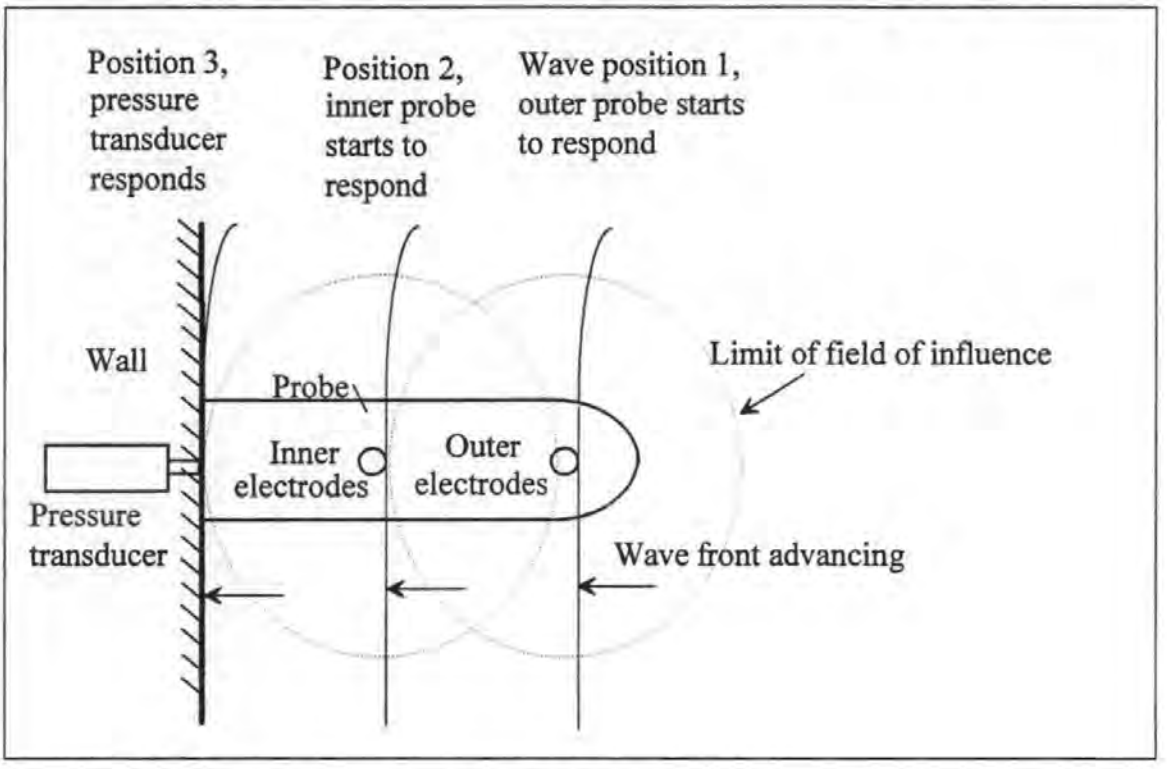

Figure 4.7. New electrode configuration showing different stages of submersion.

The electrode arrangement in Figure 4.7 was chosen so that the submersion of the field of influence of the outer electrodes could be determined when the wave arrived at position 2 (i.e. the moment the inner electrodes first responded). Similarly the response of the pressure transducer could indicate the complete submersion of the field of the inner electrodes. When the wave front is at position two, any aeration measured by the outer gauge would be due to entrained air. After the wave arrives at the wall the field of influence of the inner electrodes may contain entrained and entrapped air. Subtraction of the entrained air component measured by the outer gauge enables the entrapped air component measured by the inner gauge to be estimated. It was expected that the observation of expelled air would be more difficult but might be achieved by calculating a

horizontal velocity from the time delay between the submersion of the outer and inner electrodes, and then predicting an arrival time at the wall. Expelled air causes a rise in pressure at the wall before the wave impinges. Thus it was thought that it may be possible to observe a pressure rise before the predicted arrival of the wave at the wall.

Having selected this probe form, experiments were carried out to determine the optimum electrode gap, temperature effects, calibration, the effects of bubble size and whether the probes themselves caused air entrainment.

4.5 Electrode gap

The size of the field of influence varies with the gap between the electrodes. The best gap / field size had to be chosen to meet the conflicting requirements for a spatially focused reading and for a large ratio of field size to bubble size. After considering the scale of the waves in which measurements would be taken (of the order of 100 mm) it was decided that a maximum field dimension of 20 mm was desirable. A variety of gaps were investigated by submerging the probes in a container which was being filled with water at a known rate. It is difficult to determine an absolute value for the size of an electrical field but clearly the field weakens with increasing distance from the electrodes. The distance from the electrodes at which the free surface begins to have an effect was defined as the radius at which the instruments output voltage dropped by 1 % of its full range. With an electrode gap of 13 mm this limit was found to be approximately 9.5 mm. A typical result is shown in Figure 4.8.

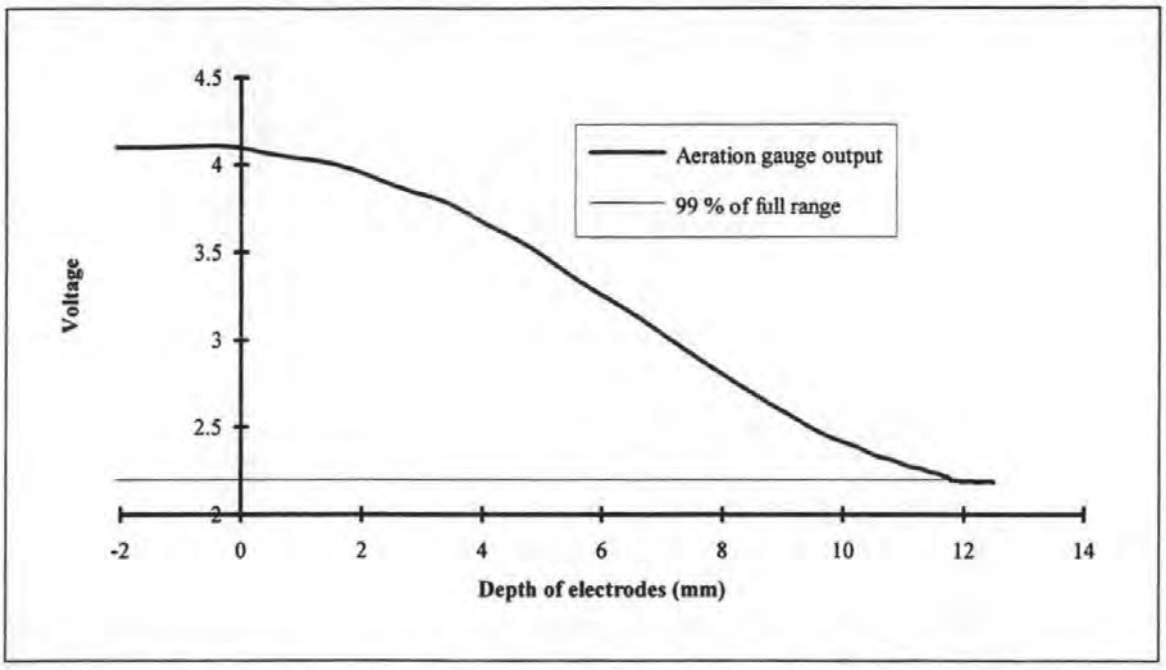

Figure 4.8. Variation of aeration gauge output in a filling tank with an electrode gap of 13 mm.

In this graph the depth has been measured from the edge of the electrodes. The field dimensions are illustrated in Figure 4.9 and the chosen probe arrangement is shown in Figure 4.10.

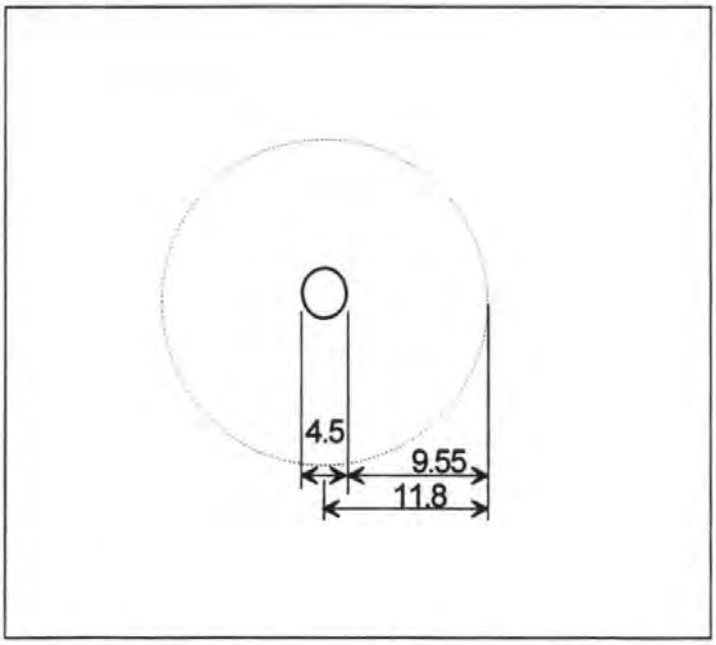

Figure 4.9. Electrode and field dimensions in millimetres.

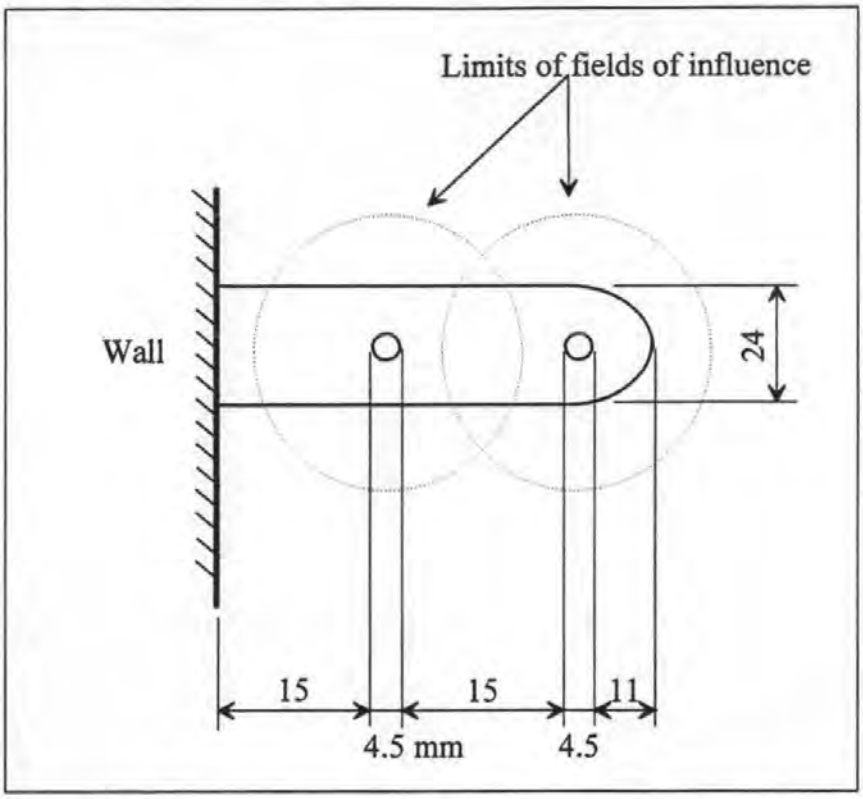

Figure 4.10. Location of electrodes in the probes showing the limits of the fields of influence.

Four probes were made, each containing two electrodes. They were 50 mm long, 24 mm wide and 6 mm deep. The electrodes were small stainless steel cylinders, 4.5 mm in diameter, 4 mm long, with a small screw inserted into the rear face so that a wire could be attached. Each electrode was connected to the controlling circuitry via short low impedance cables.

4.6 Temperature effects

The relationship between the gauge output and the temperature of the water was found to be strong and linear, as shown in Figure 4.11.

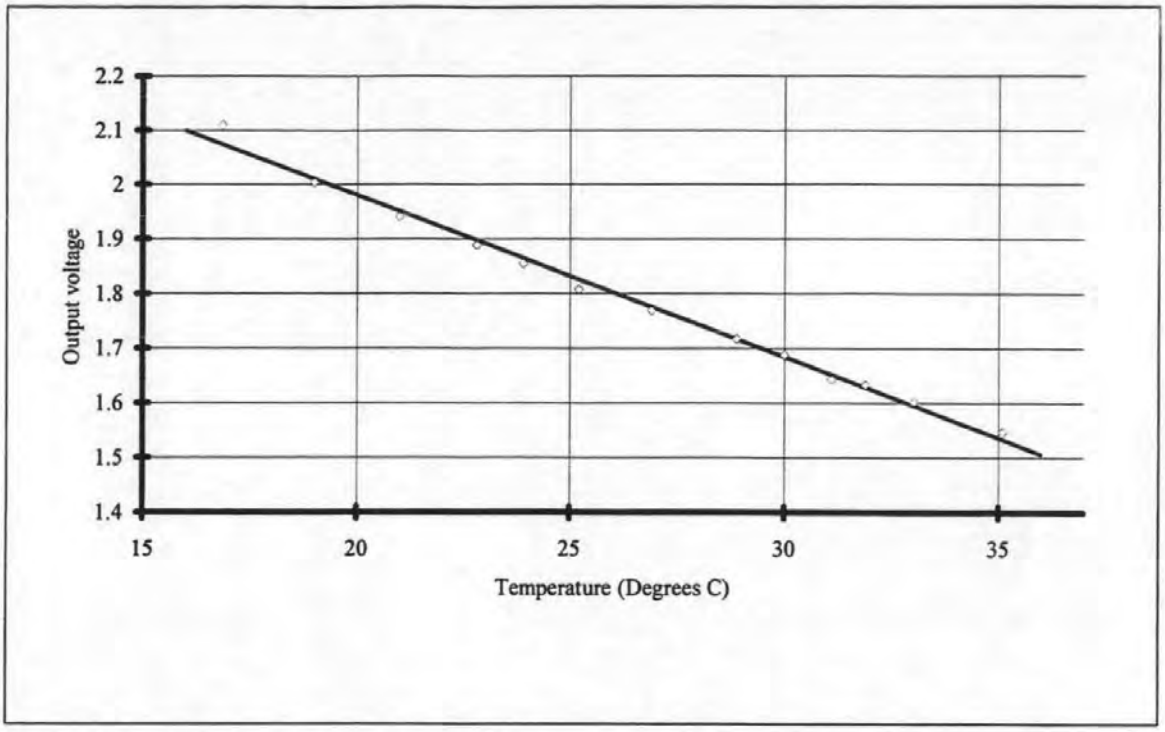

Figure 4.11. Variation of unaerated voltage output with changing temperature.

The effect was considered significant enough to require the monitoring of the temperature of the flume water during the tests.

4.7 Calibration

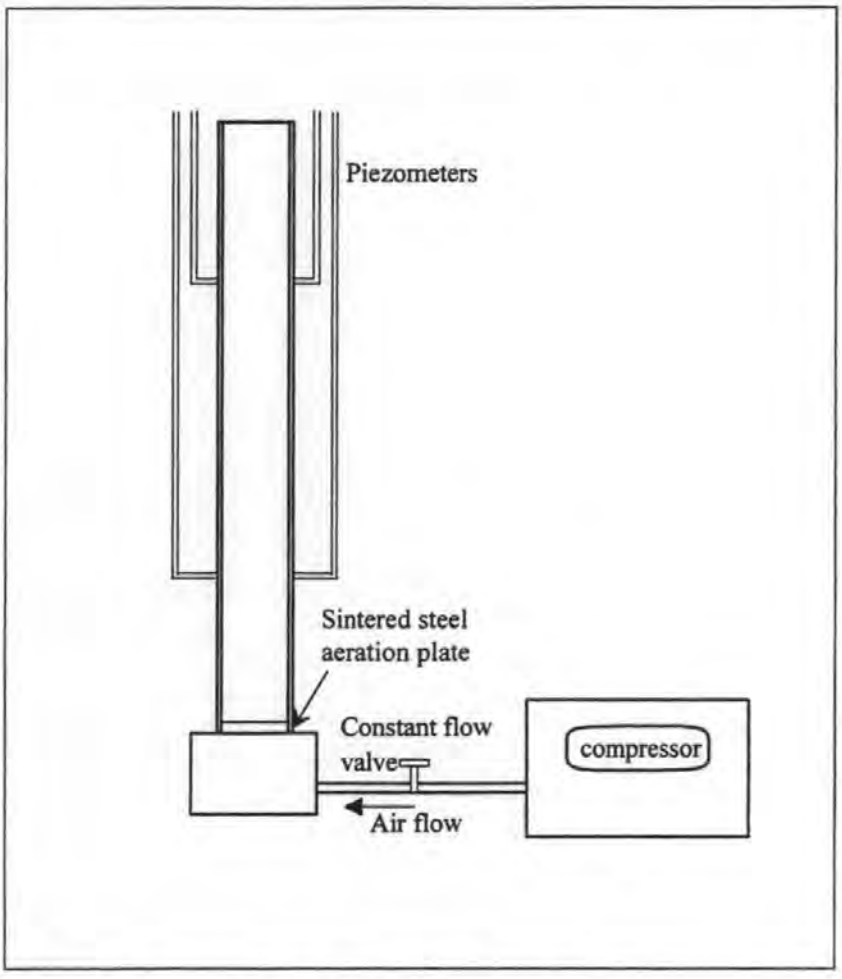

Figure 4.12. Illustration of calibration water column.

The probes were calibrated within a vertical 1.34 m long clear acrylic tube with an internal diameter of 100 mm and a wall thickness of 5 mm. Air could be introduced at the base of the tube (see Figure 4.12) through a sintered steel filter with a pore size of 6 microns. This enabled various levels of aeration to be established. Four piezometer tubes were arranged to provide measurements of hydrostatic pressure at two depths 0.8 m apart from which the aeration levels were calculated. The water used in the calibration was drawn from the wave tank to ensure that it had similar electrical and chemical properties.

The resistance meters were first calibrated and their response was established as being invariant with time. The electrodes were then submerged in the calibration rig and short 10 second time series were recorded from each probe at each aeration level. Each series was averaged and the associated resistance calculated. Initially the probe output was found to

exhibit intermittent variable offsets caused by small bubbles which occasionally stuck to the electrodes. Cleaning and polishing the electrodes solved this problem although it was still necessary to inspect the electrodes during calibration. Bubble attachment was not expected to be a problem during wave impact tests because of the high inertia of the surrounding water (during calibration the flow of air was driven by its buoyancy but during wave impacts it is driven by the water). By relating each aerated resistance value to the unaerated resistance using equation 4.1, a predicted aeration level was obtained. This was compared to the measurements made with the piezometers. The results from one probe are presented in Figure 4.13.

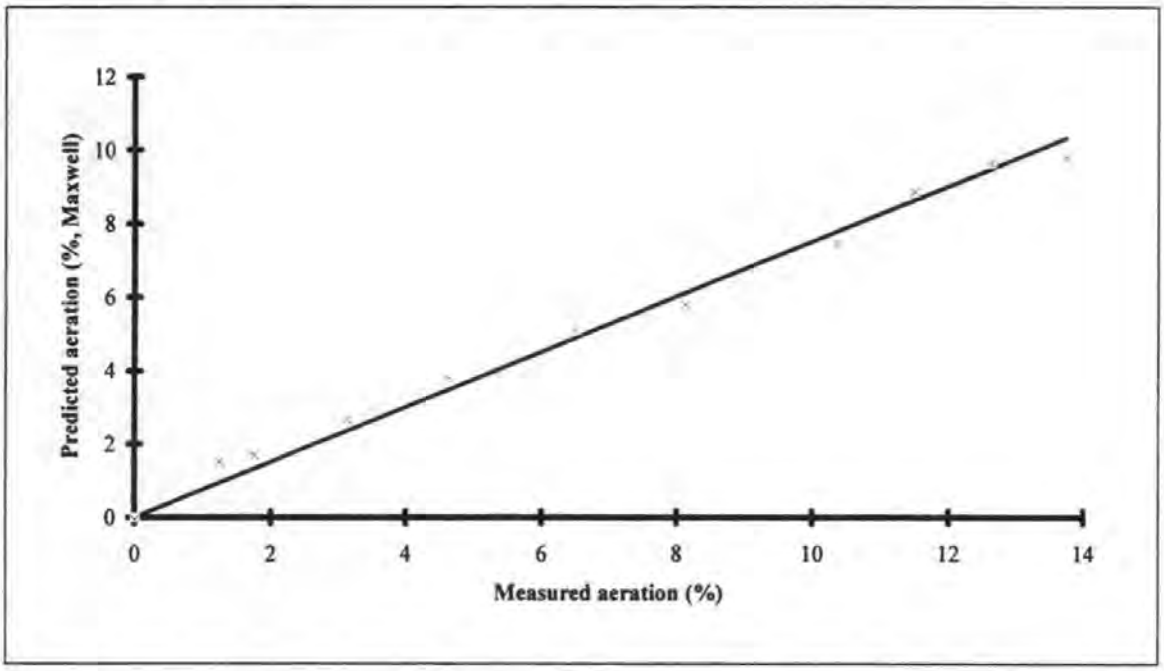

Figure 4.13. Comparison between levels of aeration measured using piezometers and air gauge 1.

It can be seen that although the relationship is linear it does not have a gradient of 1. This indicates that Maxwell's theory can be used to predict aeration from the measured resistance but only if a constant multiplier is introduced.

4.8 Minimisation of self aeration

Because the selected probes were intrusive to the flow it was necessary to establish whether they affected impact pressures or caused additional aeration. Drop test equipment was used to investigate the behaviour of the probes under highly repeatable and completely unaerated impacts. The probes were attached to the underside of a horizontal plate which was allowed

to drop from a variety of heights onto a water surface (Figure 4.14, see also section 5.3). A miniature pressure transducer (also described in section 5.2.2) was mounted in the centre of the plate between the probes. Pressures were measured with and without the probes and no significant difference was observed. However, the aeration results were poor since the gauge outputs did not indicate 0 % aeration after each impact. A typical result is shown in Figure 4.15.

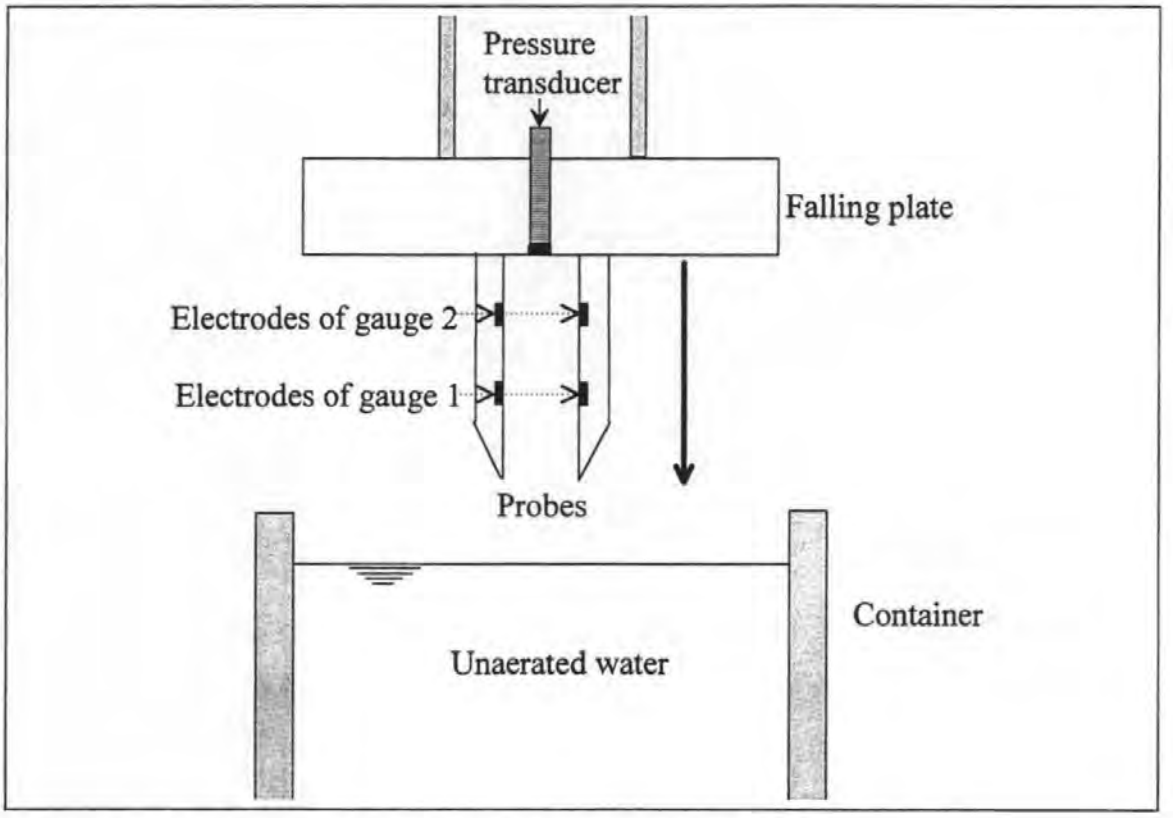

Figure 4.14. Drop apparatus for checking self aeration by probes.

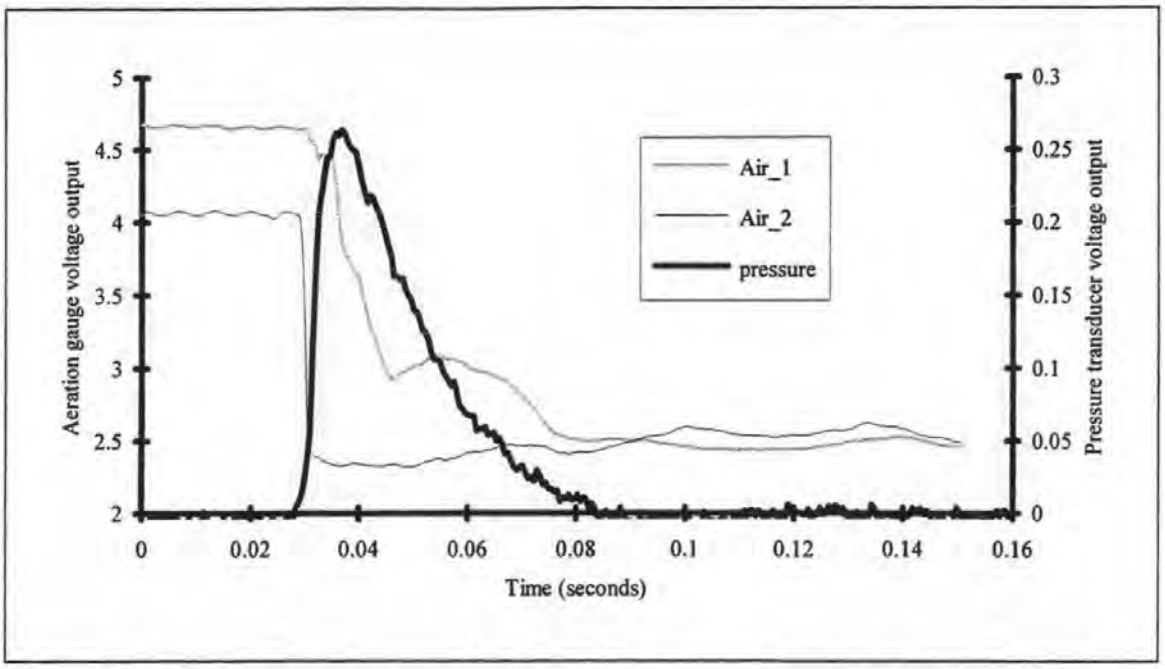

Figure 4.15. Outputs from the aeration and pressure transducers during a drop test in which the horizontal plate struck the surface of unaerated water at a velocity of 2 m/s.

Although the outputs from both aeration gauges fell rapidly from their 'free air' values (>4V) upon impact, neither falls to the zero aeration value of 2V. This suggests that the probe arrangement was either causing flow separation or otherwise causing air to be entrained in the water. On a more positive note, the relative timings of the first aeration electrodes reaching the water, the second aeration electrodes reaching the water and maximum impact pressures being achieved, can clearly be seen.

Tests with various other probe shapes eventually resulted in the development of the streamlined form shown in Figure 4.16. Use of this type of probe repeatedly lead to zero or near zero post impact levels of aeration as illustrated by the typical set of results presented in Figure 4.17.

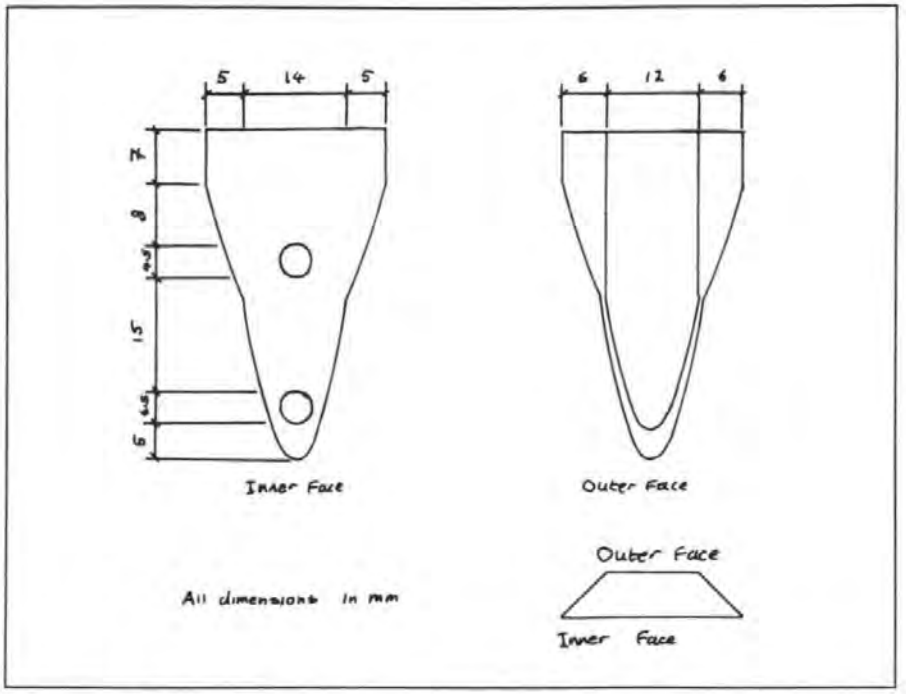

Figure 4.16. Details of the new streamlined probes.

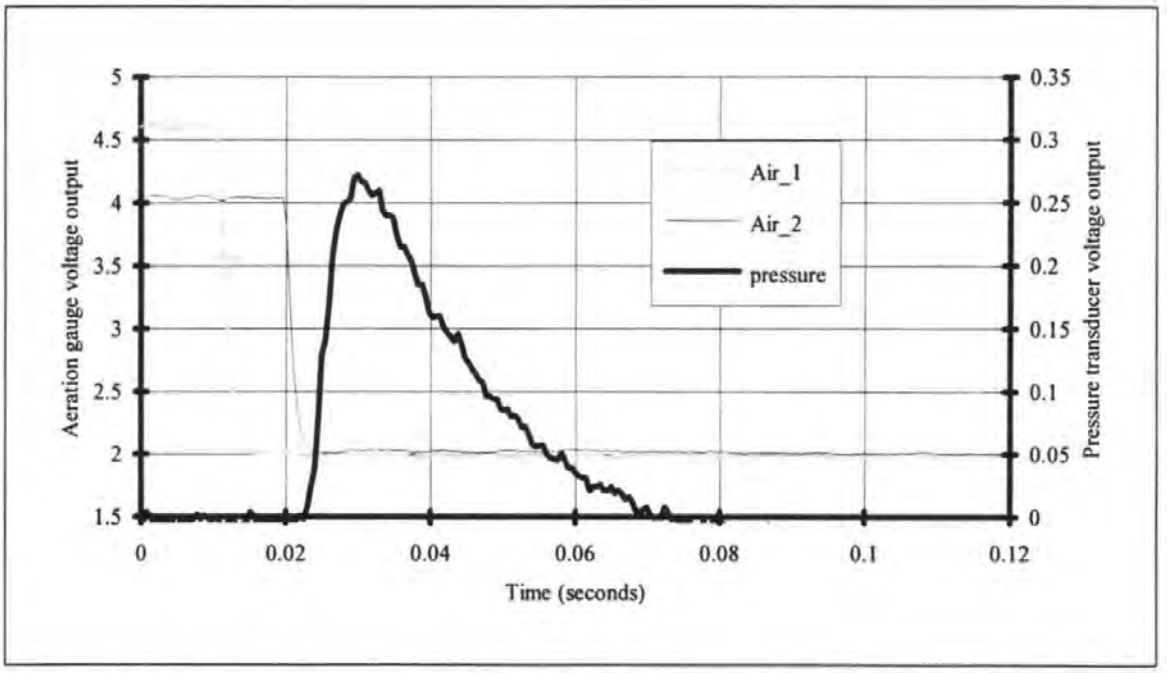

Figure 4.17. Minimal air entrainment caused by the streamlined probes during a 2 m/s impact.

4.9 Signal analysis

Because of the need for a spatially focused reading, the output of the instruments was strongly affected by the passage of individual bubbles. These caused spikes such as those shown in Figure 4.18.

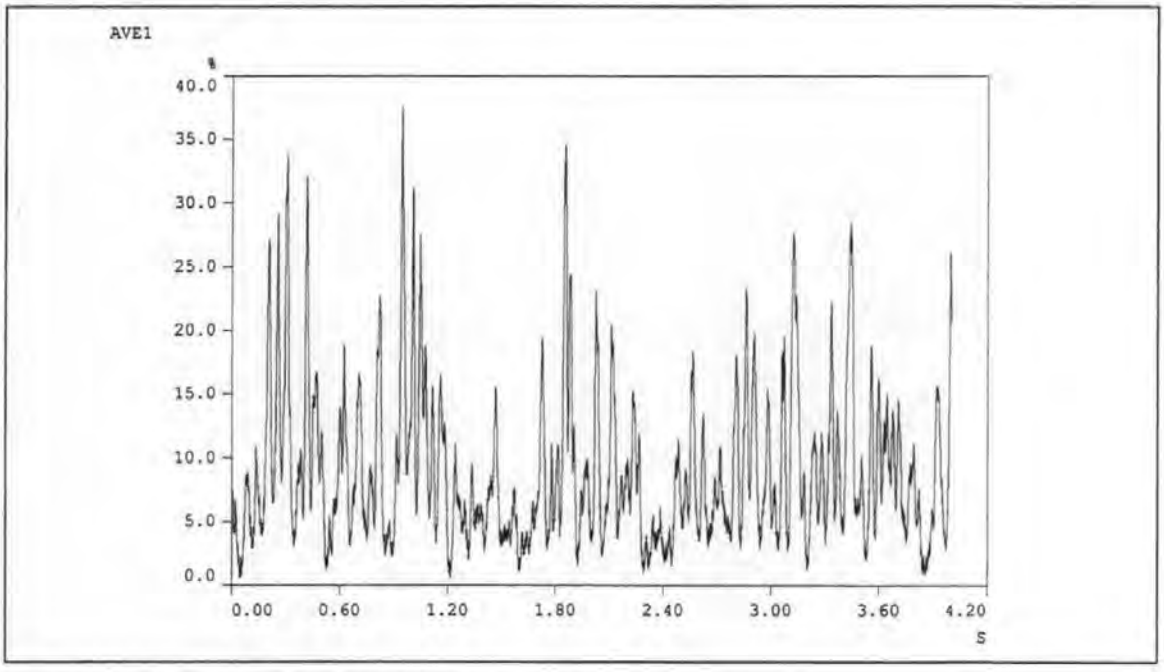

Figure 4.18. Typical 2 kHz aeration record of 8 % aeration.

Clearly, some form of signal smoothing was required in order to provide an 'average' aeration level. Two types were considered, moving point and ensemble averaging. The former method involves the selection of a small time window which is moved incrementally along the time series. At each location the value in the centre of the window is replaced by the average of all the points within the window. Samples of aeration records were smoothed in this way but it was found that large window sizes were required to produce only moderate reductions in the signal fluctuation. It was decided that the resulting loss of temporal resolution made this approach unsuitable for the fast changing phenomena associated with impacting waves. The effect of ensemble averaging the signal was then investigated.

Ensemble averaging involves the creation of a new time series through the addition and averaging of whole time series of equal length. For example three time series A_i, B_i, and C_i each of length n units could be ensemble averaged to create a fourth time series D_i in the following way:

$$D_1 = (A_1 + B_1 + C_1) / 3$$
$$D_2 = (A_2 + B_2 + C_2) / 3$$
$$D_3 = (A_3 + B_3 + C_3) / 3$$
...
$$D_n = (A_n + B_n + C_n) / 3$$

To investigate the effect of ensemble averaging the aeration records, one hundred records were obtained from each of the four instruments (*rec*1 to *rec*100). Each was four seconds long and recorded at 2 kHz. The standard deviation *rec*1 was found and compared to the standard deviation of the ensemble average of *rec*1 and *rec*2. This in turn was compared to the standard deviation of the ensemble average of *rec*1, *rec*2 and *rec*3. By continuing this procedure, 99 ensemble averages were calculated for each probe and the standard deviation of each was found.

The results from the four instruments (labelled *Air* 1 to *Air* 4) can be seen in Figures 4.19 to 4.26. For each instrument the maximum, minimum, mean, mean plus standard deviation and mean minus standard deviation are shown as functions of the extent of ensemble averaging, i.e. the number of segments included in the ensemble averaging process.

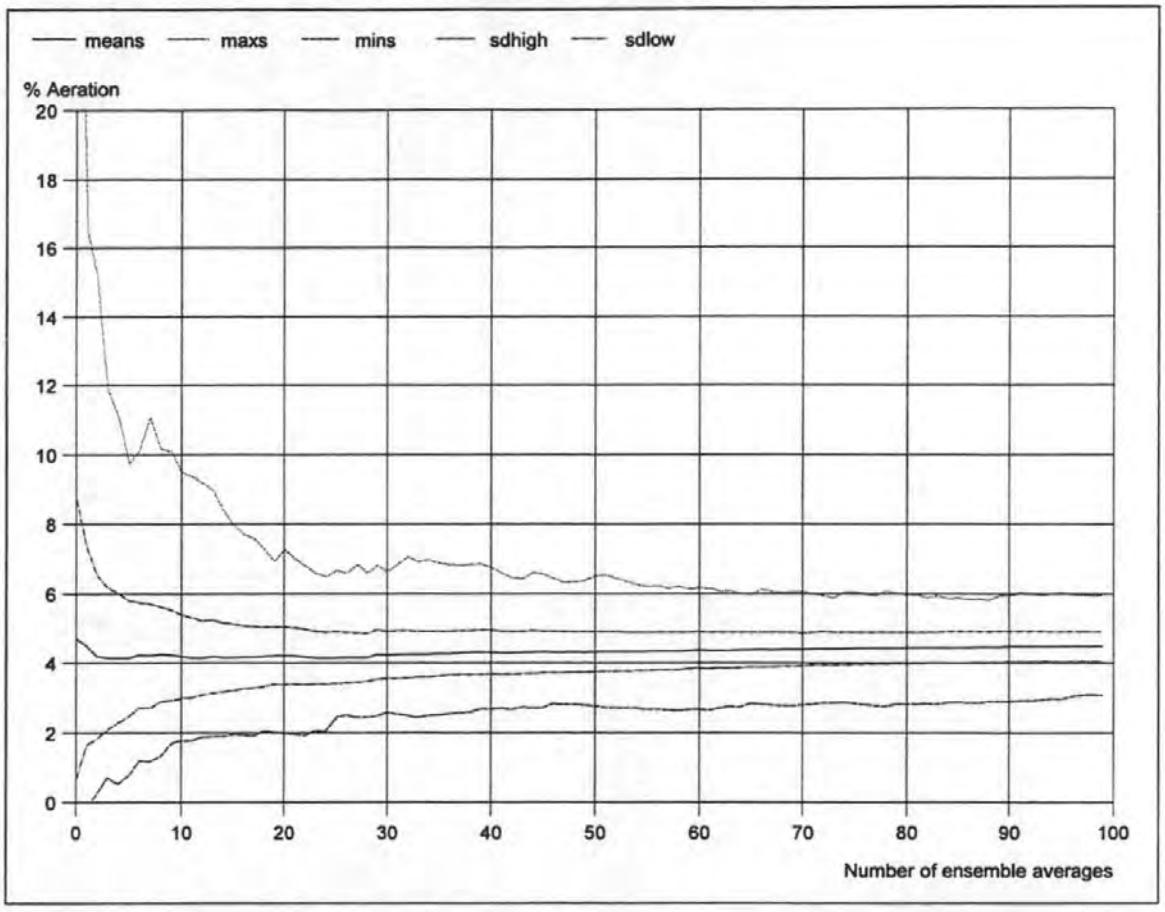

Figure 4.19. The effect of ensemble averaging on signal confidence, maximum, minimum, mean, mean plus standard deviation (*sdhigh*) and mean minus standard deviation (*sdlow*), for *Air* 1.

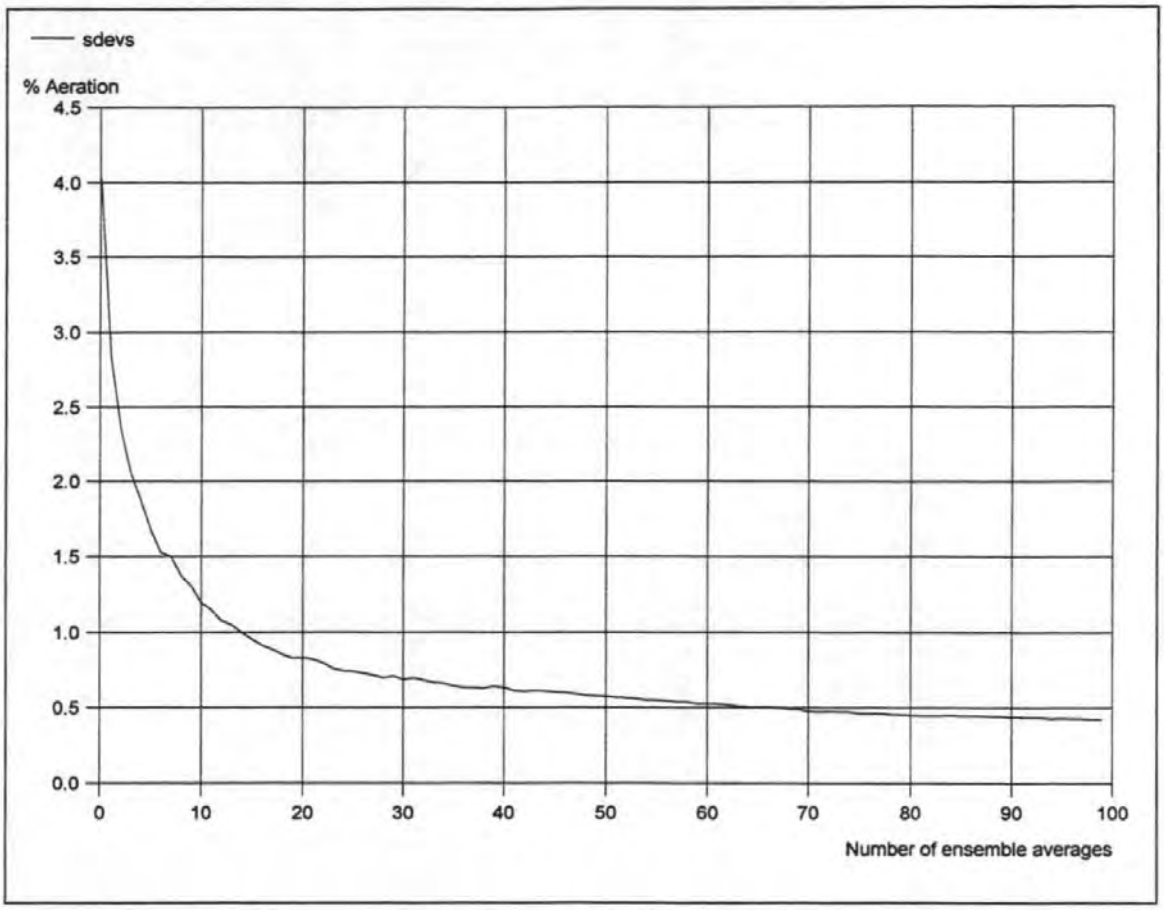

Figure 4.20. The effect of ensemble averaging on standard deviation of aeration signal, *Air* 1.

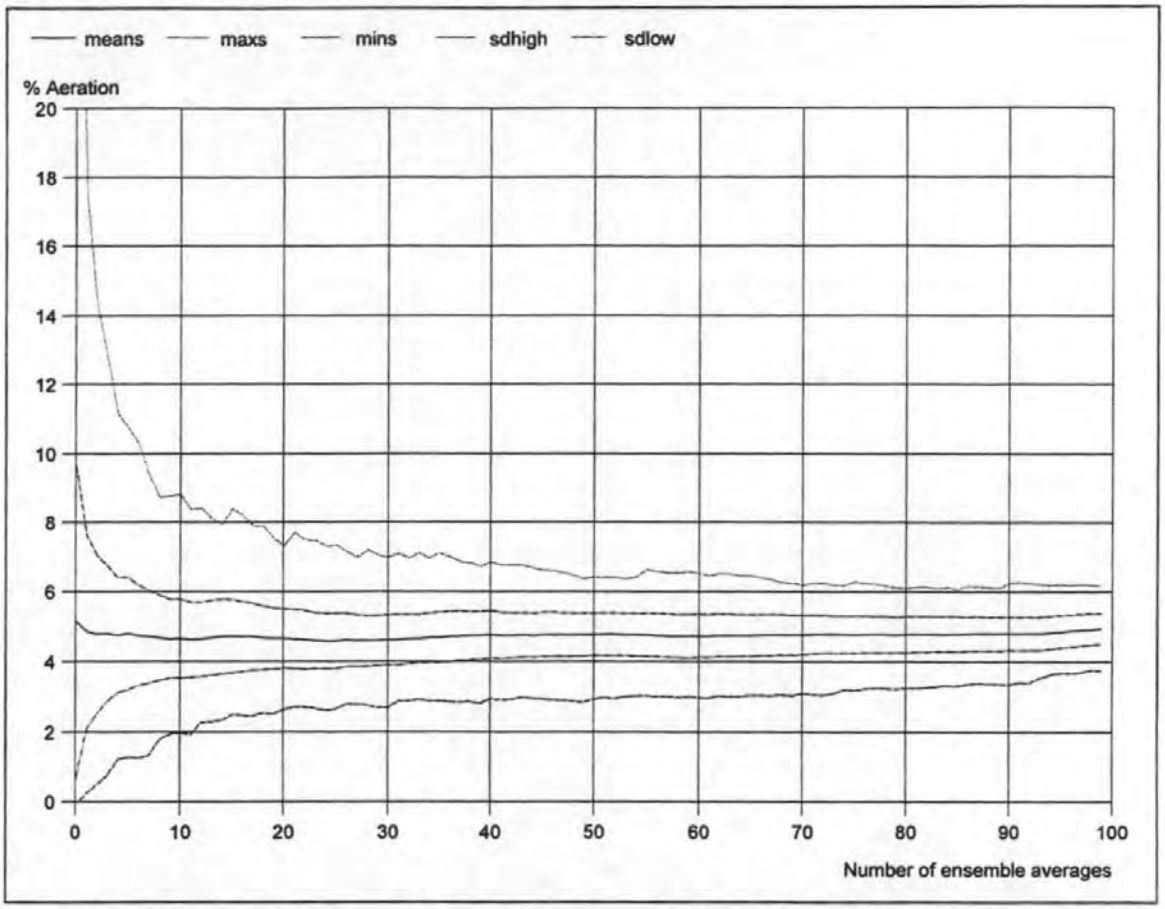

Figure 4.21. The effect of ensemble averaging on signal confidence, maximum, minimum, mean, mean plus standard deviation (*sdhigh*) and mean minus standard deviation (*sdlow*), for *Air* 2.

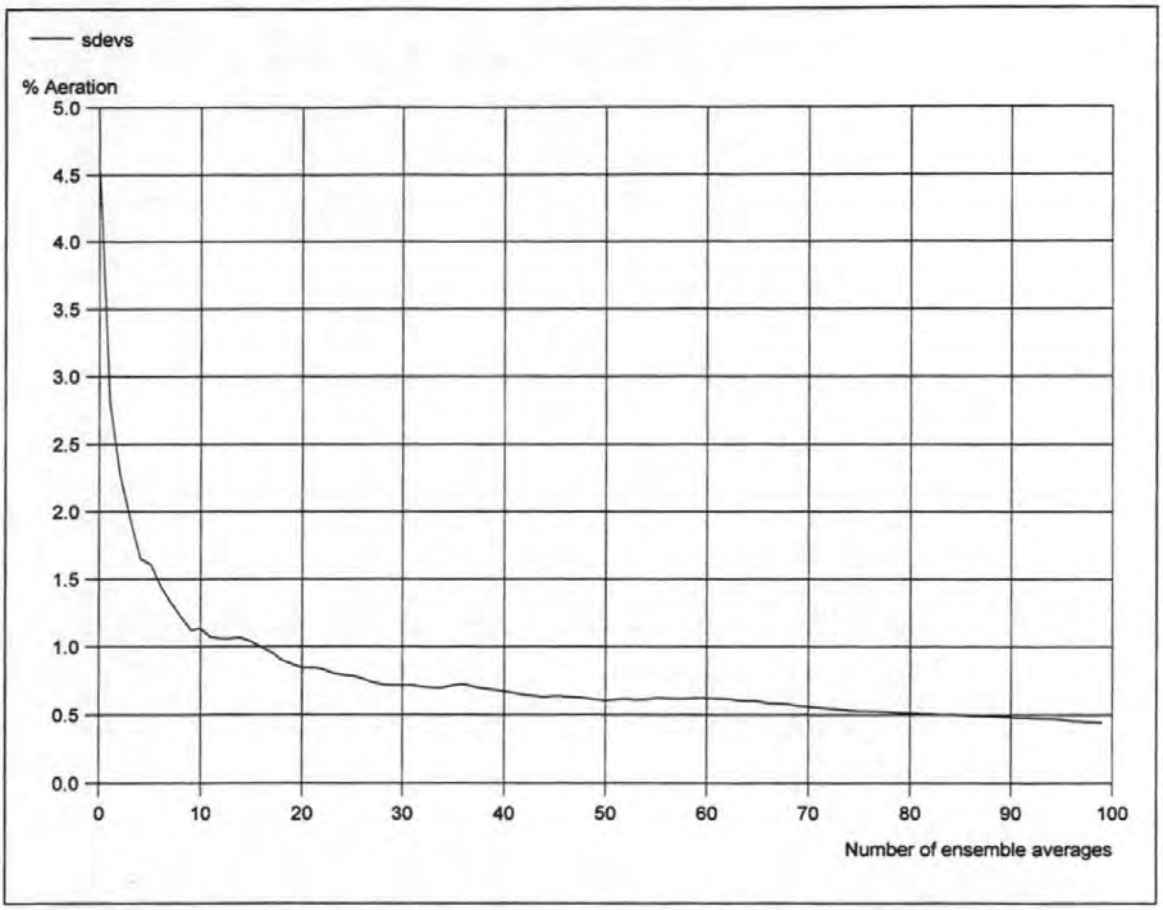

Figure 4.22. The effect of ensemble averaging on standard deviation of aeration signal, *Air 2*.

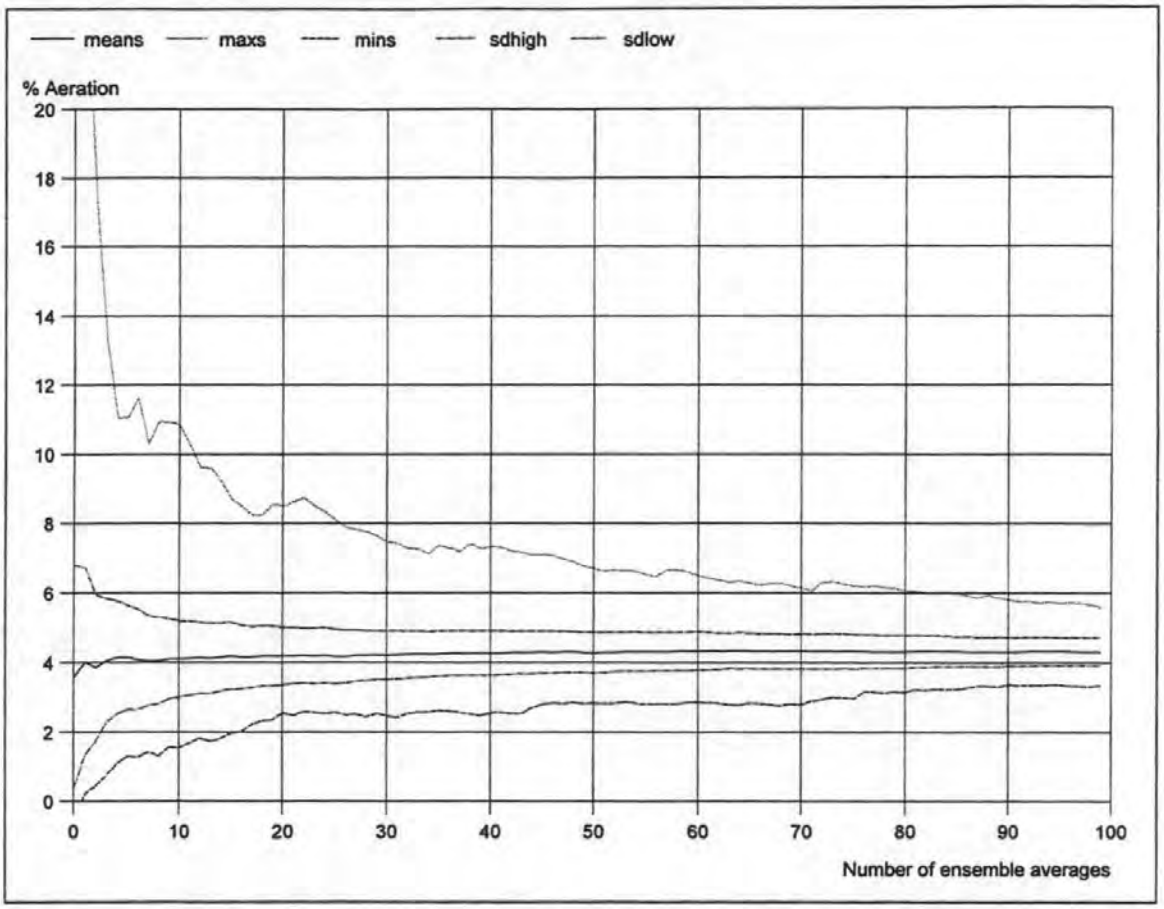

Figure 4.23. The effect of ensemble averaging on signal confidence, maximum, minimum, mean, mean plus standard deviation (*sdhigh*) and mean minus standard deviation (*sdlow*), for *Air* 3.

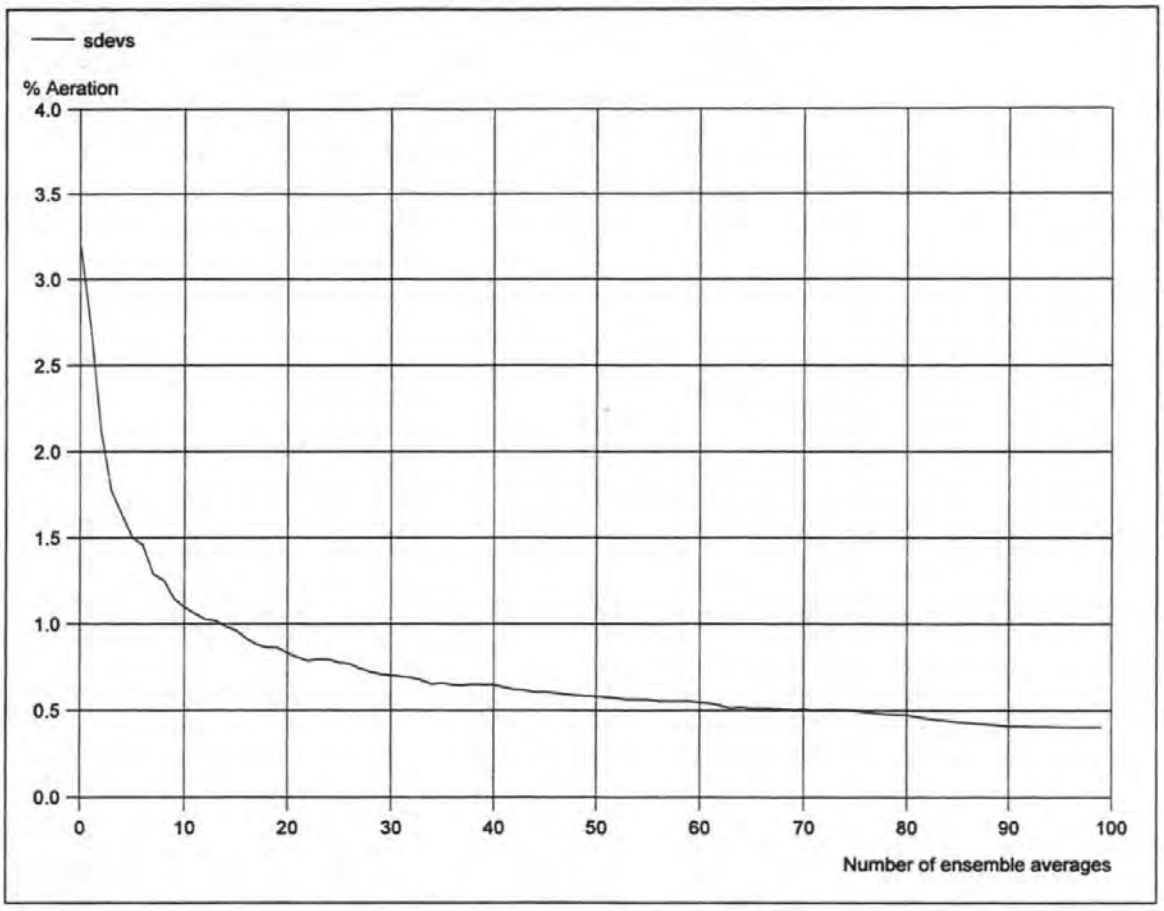

Figure 4.24. The effect of ensemble averaging on standard deviation of aeration signal, *Air 3*.

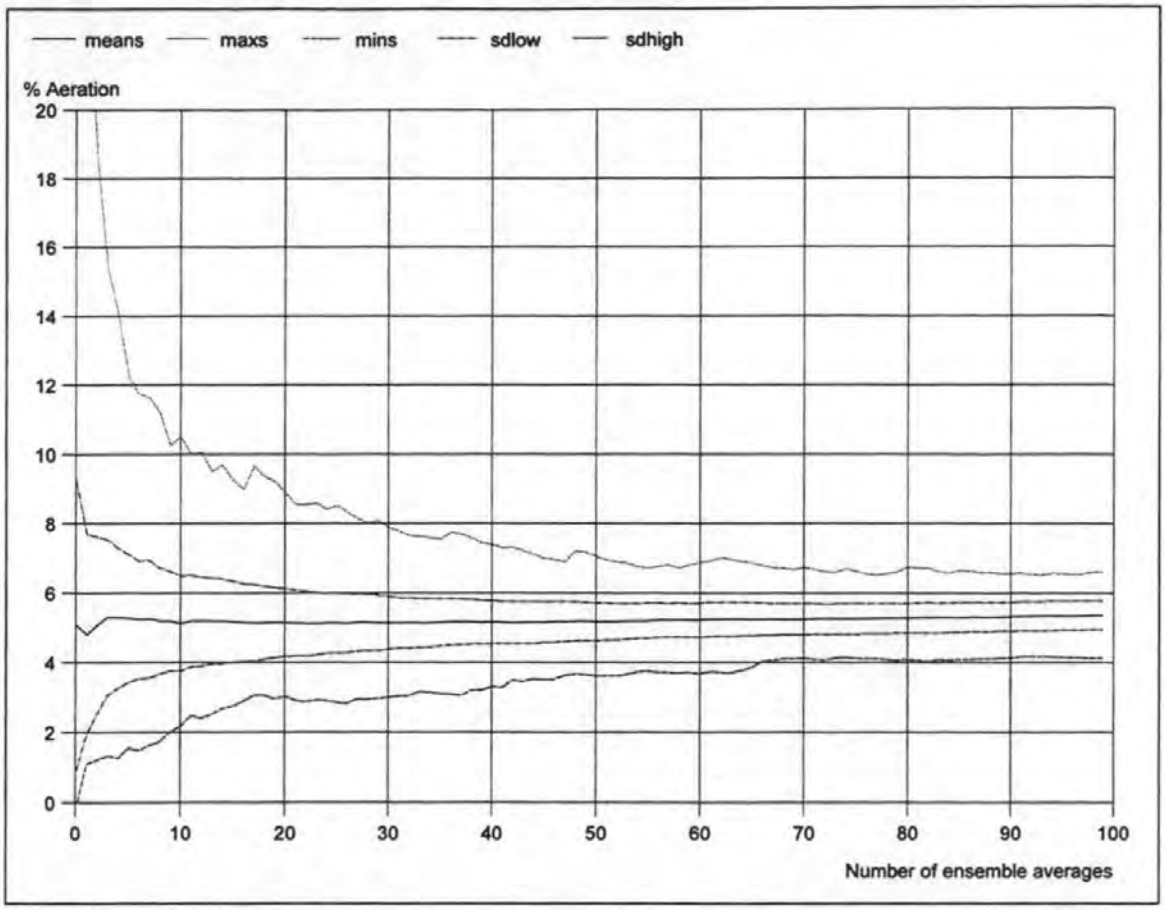

Figure 4.25. The effect of ensemble averaging on signal confidence, maximum, minimum, mean, mean plus standard deviation (*sdhigh*) and mean minus standard deviation (*sdlow*), for *Air* 4.

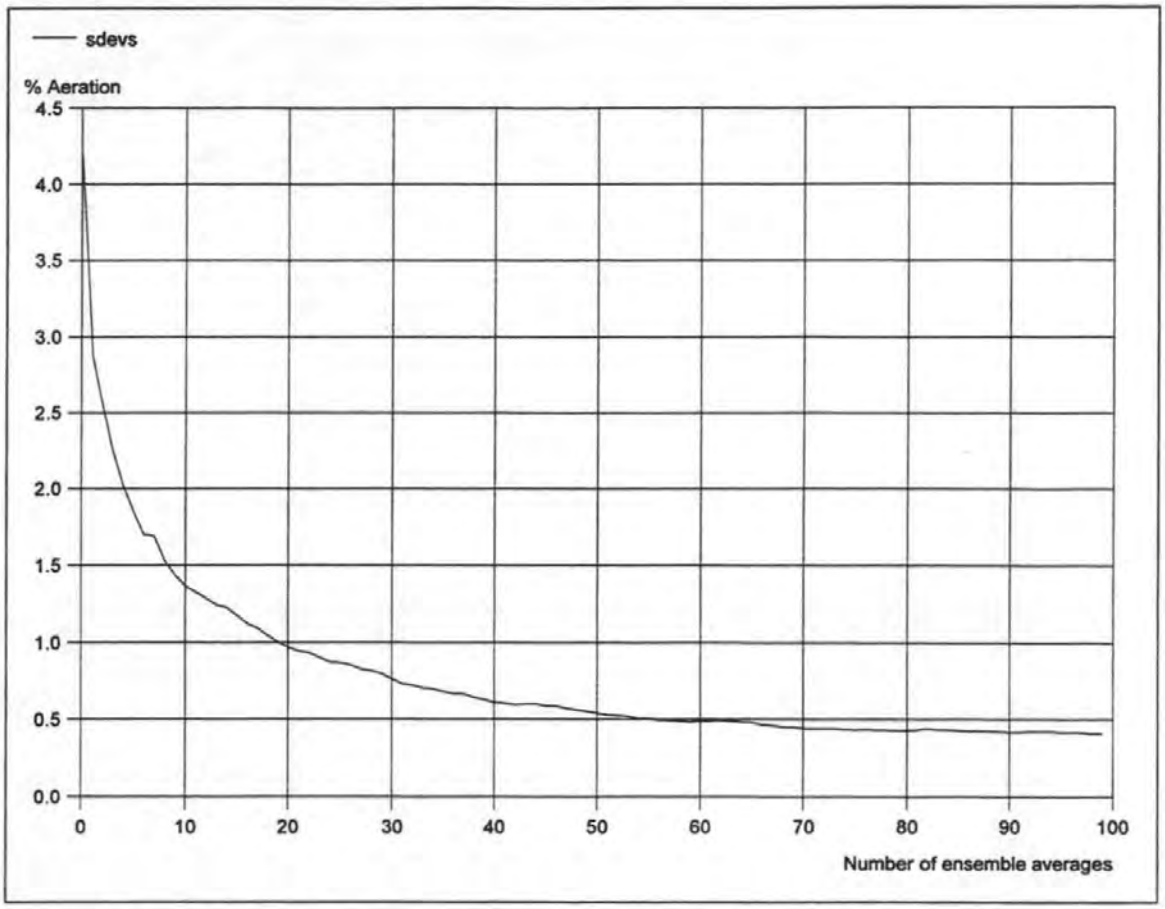

Figure 4.26. The effect of ensemble averaging on standard deviation of aeration signal, *Air* 4.

It was found that when 50 segments were averaged in this way the standard deviation of the signal reduced to between 0.6 and 0.7 %, which, assuming a normal distribution in the signal, related to a 95 % confidence range of +/- 1.37 % aeration. It was therefore decided to employ ensemble averaging to provide a high confidence in the output of aeration gauges without the loss of temporal resolution. The cost of adopting this approach was that the results of individual waves could not be compared. Instead at least 50 regular waves were required for the averaging process to produce one 'typical' aeration time history.

4.10 Summary

Probes and analysis techniques were developed to allow the measurement of aeration in small scale breaking waves. Simpler large scale probes were also designed. The devices were resistance based and allowed calculation of percentages of aeration (void fraction). The electrodes of the small scale devices were arranged in a square array perpendicular to the wave wall to promote the discernment of expelled, entrapped and entrained air. They were built into probes which were streamlined to prevent self aeration. During drop tests it was found that the presence of the probes did not affect the magnitude of the impact pressures between them. The instruments were sensitive to individual bubbles but signal confidence was increased, without the loss of temporal resolution through ensemble averaging.

Chapter 5

Experimentation

5.0 Introduction

Approximately 4000 regular and solitary wave impact events were recorded. Some of these were thought to be unsuitable for analysis, usually due to three dimensional motion in the flumes, and are not described here. From the rest approximately 23000 pressure time histories, 11000 aeration time histories and 3300 force time histories were analysed, the vast majority using specially developed semi-visual, semi-automatic techniques. Not all of these were needed to support this thesis.

Measurements were made in collaboration with the University of Hannover and the Technical University of Braunschweig, in the Grosser Wellen Kanal (GWK), which is Europe's largest wave flume. They were also obtained at small scale in the wave flume of the University of Edinburgh's (UoE) department of mechanical engineering, and in the University of Plymouth (UoP) wave flume. Drop tests were also conducted using aerated sea and fresh water, these were supplemented with measurements of bubble size.

5.1 Large scale tests

The GWK is a large concrete 'U' channel 324 m long, 5 m wide and 7 m deep with a 1 MW energy absorbing paddle. At the time of the tests described here, waves shoaled over a 1:50 sloping sand bed and a rubble berm before arriving at a sand filled concrete caisson. Images and details of the flume and model are shown in Figures 5.1 to 5.3. Further information on the flume and model caisson can be found in Oumeraci and Kortenhaus (1994).

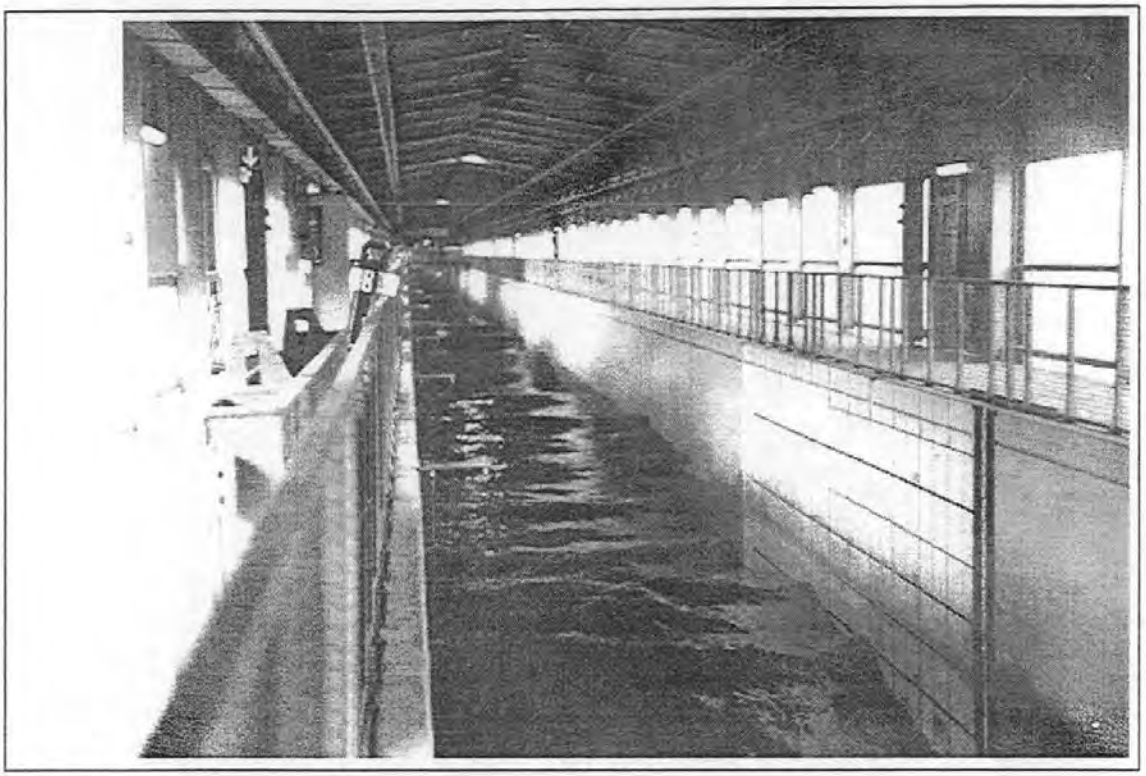

Figure 5.1. The Grosser Wellen Kanal.

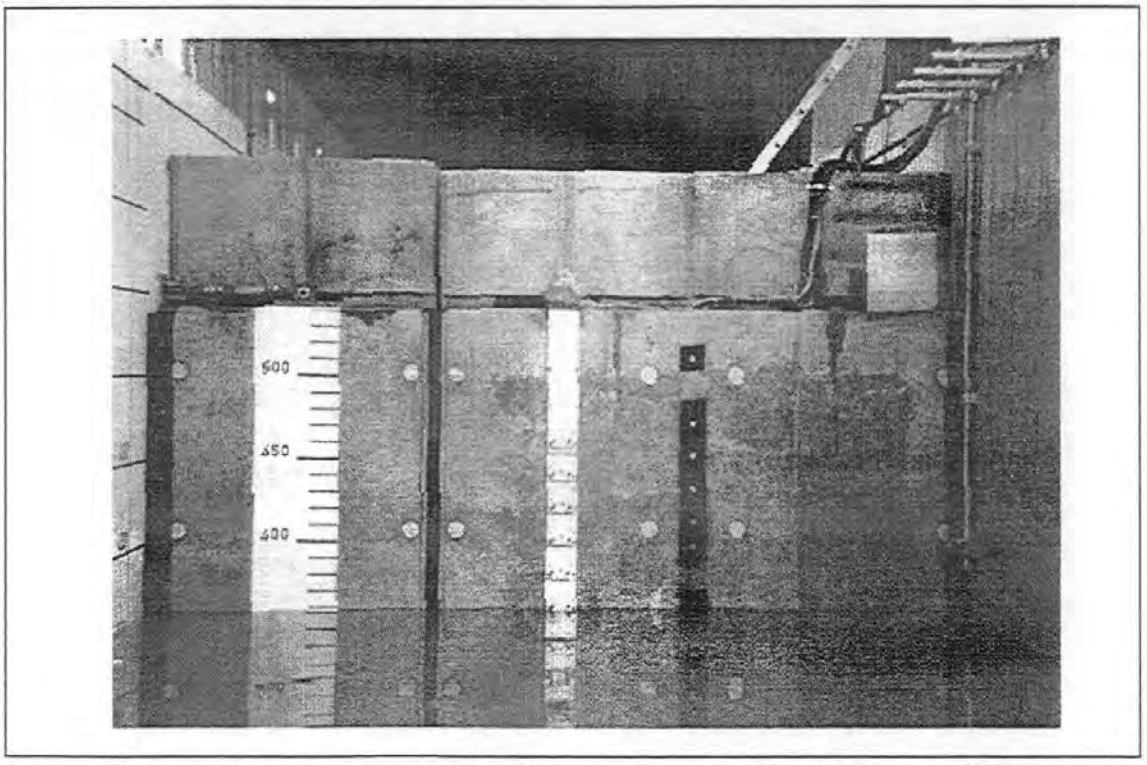

Figure 5.2. The GWK model caisson with the instrumented spar fixed to its centre.

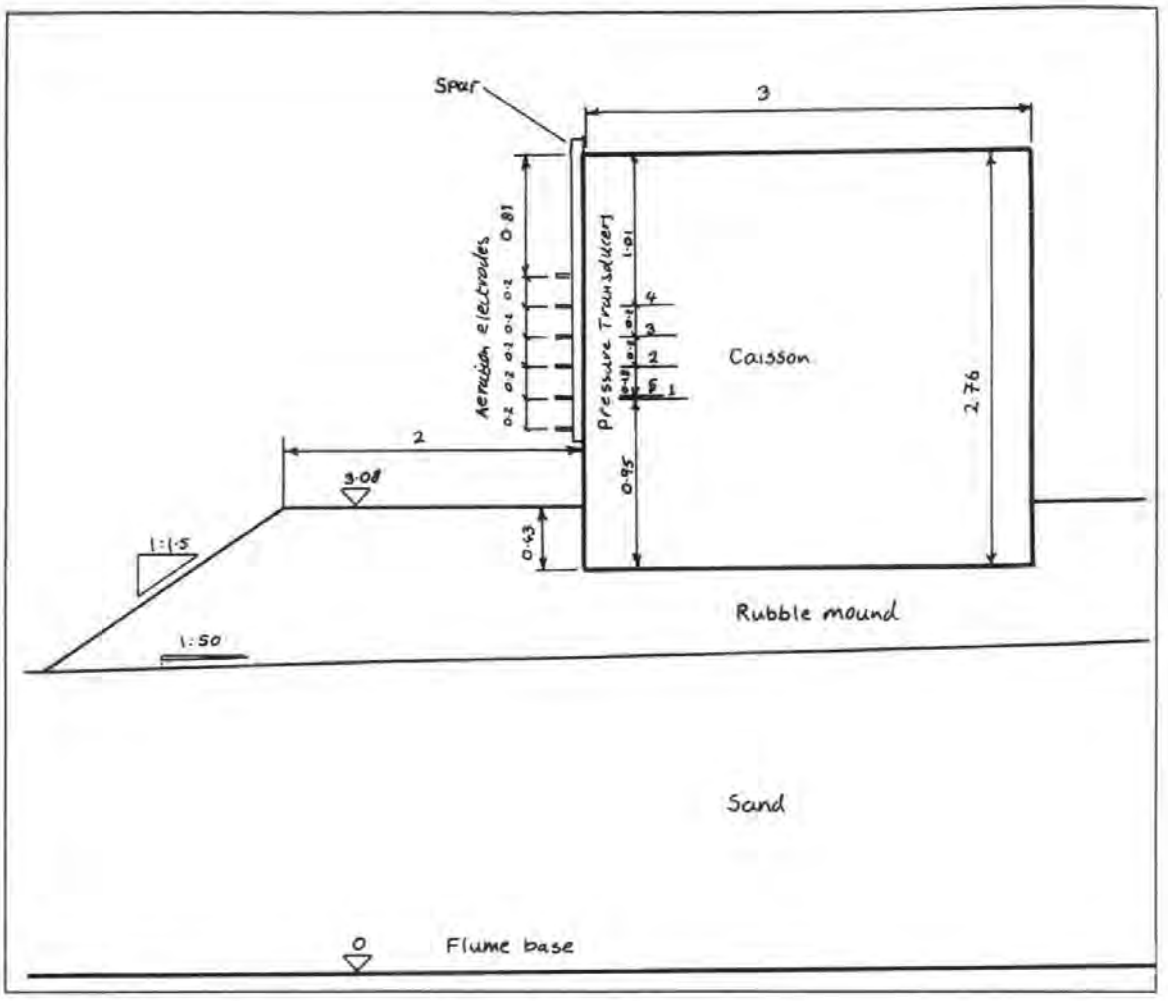

Figure 5.3. General arrangement of the GWK model.

A spar instrumented with aeration and pressure transducers was designed, built and installed on the caisson front. This can be seen as the central vertical white strip in Figure 5.2. Dimensions of the aeration probes and a cross section of the spar has been shown above in Figure 4.2. Four Kulite type 219 pressure transducers with working ranges of 0 to 400 kN/m^2 were built into it at the elevations shown in Figure 5.3. This type of transducer has a natural frequency of 30 kHz when submerged in water and is temperature compensated from -10 to 50° C.

The distance between the transducers and the data logging equipment was approximately 55m which introduced the danger of signal attenuation and a reduction in the signal to noise ratio. The amplifiers were therefore positioned as close as possible to the caisson in a protective aluminium box and coaxial cable was used to reduce electrical interference. The box was wrapped in damp proof membrane to protect it from the large quantities of uprushing water. To protect the transducers and connections from the fast flowing high

pressure water the spar was designed to be waterproof with internal ducts through which the cables could rise up the caisson face before passing out through watertight glands.

Some modifications were made to the spar on site to provide additional protection to the instruments. A plate which had been used to protect the cable glands from uprushing water was removed, reshaped and replaced so that it was more firmly mounted, and provided less disturbance to water flow. The cables were then wrapped in 10 mm thick sponge gasket material to attenuate the pressures caused by falling water and then rolled in a sheet of damp proof membrane, held together with tape and cable ties. To further waterproof the spar all the joints of the ABS body were resealed with ABS cement and the flange gaskets were compressed to 3 mm and sealed with silicone (see Figure 4.2).

The mounting of the spar had to be completed rapidly and be secure against high impact loads. This was achieved by drilling holes into the caisson face, using the spar as a template, inserting a threaded bar into each of the holes and fixing it with resin. The Hilti HITC-100 system resin injecting gun was chosen with 8 mm stainless steel threaded bar in a 10 mm diameter hole, nominally 100 mm deep.

Mobile data logging equipment, consisting of a Microlink logger controlled with 'Windspeed' software on a 486 DX PC, was transported to the GWK. The data was stored on the PC's hard disc, and was backed up daily using a Core tape streamer. The data was viewed and analysed with FAMOS software. Video images of each test were recorded using two static, and one mobile camera. These provided images of the wave profile and the whole caisson front elevation.

18 regular and 14 solitary wave tests were conducted. Pressure and aeration were monitored at 1 or 2 kHz at four levels on the spar with an additional pressure record being provided by one of the GWK built in transducers. The breaker types were varied from steep non-breaking waves to well developed plunging breakers by changing the water depths, wave heights and periods. The aeration amplifiers were calibrated each day and the water temperature, conductivity and salinity were recorded. The test details are shown in Tables 5.1 and 5.2. The file codes record the date and number of each test, so that, for example, 01029406 refers to the sixth test conducted on the first of February, 1994.

Test Code	Wave Height	Wave Period	Water Depth	Pressure sample rate	Aeration sample rate
	(m)	(Seconds)	(m)	(kHz)	(kHz)
O1029401	0.7	3.5	3.7	1	1
O1029402	0.8	3.5	3.7	1	1
O1029403	0.9	3.5	3.7	1	1
O1029404	1	3.5	3.7	2	2
O1029405	0.7	4.5	3.7	2	2
O1029406	0.8	4.5	3.7	2	2
O1029407	0.9	4.5	3.7	2	2
O1029408	1	4.5	3.7	2	2
O2029401	1.1	4.5	3.69	2	2
O2029402	1	5.5	3.69	2	2
O2029403	0.9	5.5	3.69	2	2
O2029404	1	5.5	3.69	2	2
O2029405	0.8	5.5	3.69	2	2
O2029406	1	4.5	3.9	2	2
O2029407	0.8	4.5	3.9	2	2
O2029408	1.1	3.5	3.9	2	2
O2029409	1	3.5	3.9	2	2
O2029410	0.9	3.5	3.9	2	2

Table 5.1. Details of the regular wave tests conducted in the GWK.

Test Code	Wave Height	Water Depth	Pressure sample rate	Aeration sample rate
	(m)	(m)	(kHz)	(kHz)
O3029407	0.8	3.3	2	2
O3029409	1	3.3	2	2
O3029408	0.9	3.3	2	2
O3029410	1.1	3.3	2	2
O4029401	1	3.1	2	2
O4029402	0.95	3.1	2	2
O4029403	0.9	3.1	2	2
O4029404	0.85	3.1	2	2
O4029405	0.8	3.1	2	2
O4029406	0.75	3.1	2	2
O4029407	0.7	3.1	2	2
O4029408	0.65	3.1	2	2
O4029410	0.85	3.1	2	2
O4029411	0.85	3.1	2	2

Table 5.2. Details of the solitary wave tests conducted in the GWK.

5.2 Small scale wave impact tests

The UoP flume is 20 m long, 1.2 m deep and 0.9 m wide. Waves impinged on a vertical wall assembly which had a rigid construction of 25 mm thick marine plywood and a front face of 25 mm clear acrylic. The wall face was attached by four large gussets to a base plate. The wall and base assembly was weighted and screwed to a 1:4.5 sloping foreshore which was also made from 25 mm thick marine plywood. This was fixed to the walls of the tank by two aluminium angles which ran down each side and were bolted at 300 mm centres. Additional rigidity was provided by plywood supports under the beach which ran across the width of the tank. Sandbags were packed behind the wall to reduce vibrations. The flume layout is shown in Figures 5.4 and 5.5.

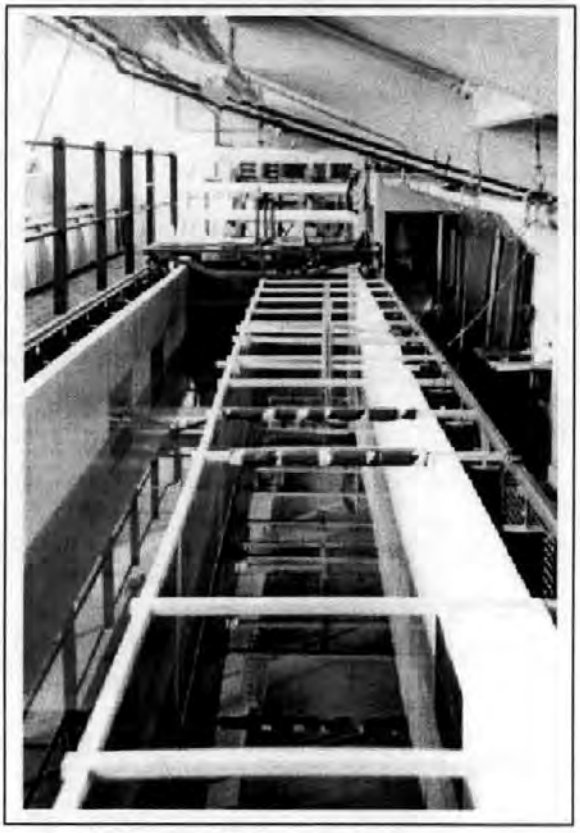

Figure 5.4. The UoP wave flume.

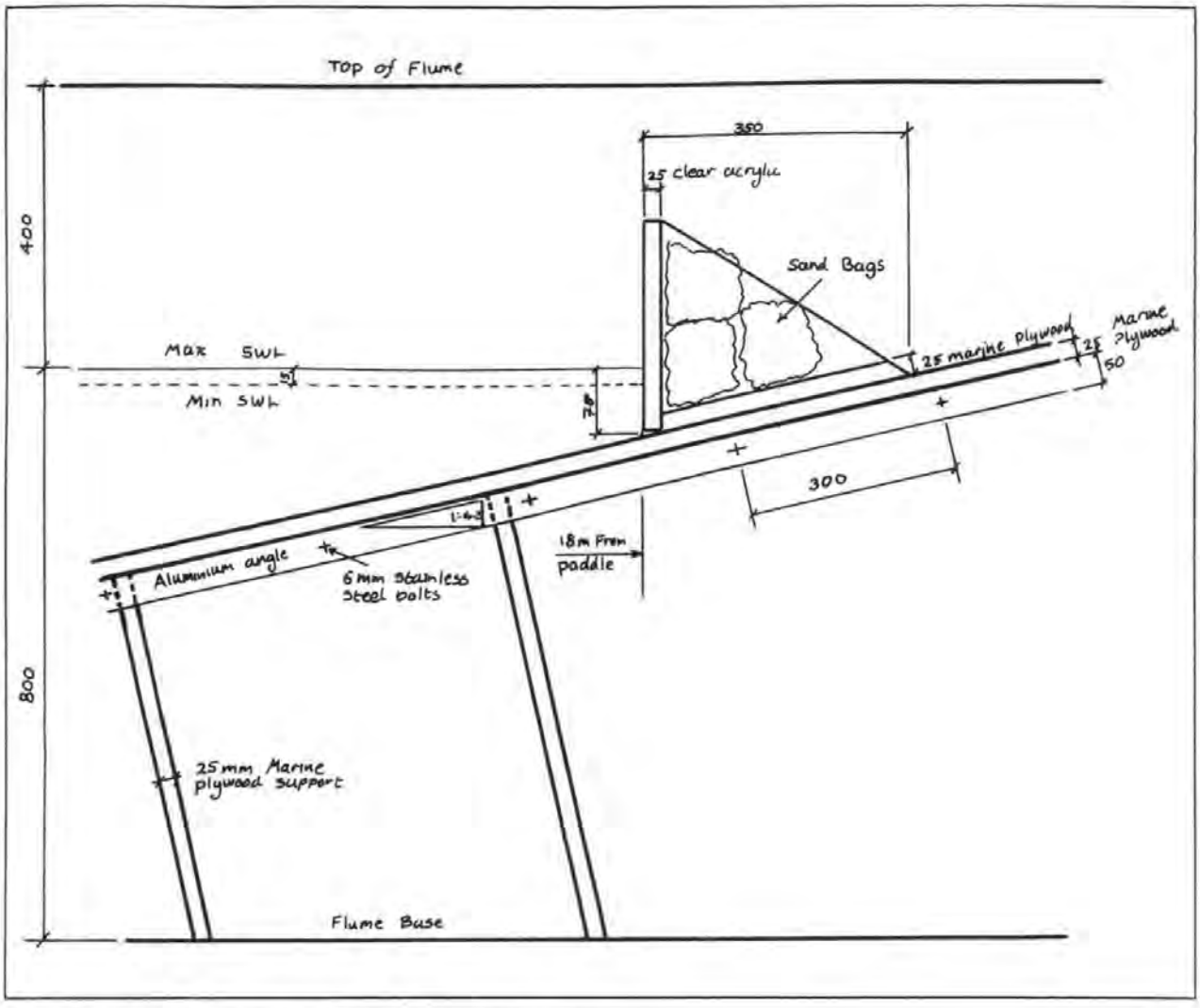

Figure 5.5. Diagram of the UoP wave flume.

The paddle was of the 'wedge' type so had the advantage of avoiding the generation of reverse waves on the return strokes. The wedge was moved by hydraulic rams and controlled by software supplied by H.R. Wallingford, running on a BBC microcomputer. A wave absorption system, which is described in Bullock and Murton, (1989) prevented re-reflection of wave energy.

Wave heights were initially measured with a resistance type wave gauge fitted to a motorised trolley. The gauge moved down the length of the channel recording the water surface elevation and linear wave theory was used to resolve the recorded elevations into incident and reflected wave heights. For later experiments a new wave measurement system was installed which resolved the incident and reflected wave energy spectra using the signals of three wave probes. A minimum of 20 points were recorded per gauge per wave for at least 300 waves, (see Davidson, *et al*, 1994).

Six sealed gauge Kulite type 219 pressure transducers were used to record pressures on the wall, although some were damaged during tests. They had an active surface diameter of 18 mm, a frequency response in water of 30 kHz and a pressure range of 100 kN/m^2. The top three transducers were separated vertically by 20 mm whilst the bottom four were spaced at 15 mm (see Figures 5.6 and 5.7). For the majority of tests two additional miniature transducers were used; these are described below in section 5.2.2.

Video recordings of the tests were made through a transparent viewing panel. This allowed identification of the breaker type and provided information on the presence of any air pockets. It was also possible to see entrained air although this was more difficult to assess due to edge effects.

The UoE flume is 20 m long, 0.4 m wide and has a working depth of 0.7 m. The wavemaker is of the 'flap' type and uses force feedback to monitor and absorb reflected waves. The waves shoaled over a 1:7 sloping foreshore before breaking on a clear acrylic wave wall. This wall was instrumented with 8 Druck PDCR 8310 pressure transducers, each having a natural frequency of 28 kHz. They were placed in the centre of the wall with their centres at elevations of 30, 55, 81, 87, 121, 141, 161, and 214 mm above the toe. One regular wave test was conducted (test 29099801) the conditions of which are described in Table 5.3. The impacting waves entrapped thin pockets of air. Wave heights were measured in the absence of the structure using resistance type wire gauges.

5.2.1 Artificial aeration test

A comparison was made between the impacts of two similar wave trains (19059301 and 20059301), one of which had air artificially injected into it. This was introduced via an 800 mm long 6 mm diameter polythene tube perforated with twin lines of pin holes on opposite sides which were spaced at 3 mm centres. This tube was fixed to the plywood foreshore to minimise disruption of the wave and was parallel to the wave wall. The gap between aerator tube and wave wall was optimised at 100 mm after several trial runs with different locations, to allow the bubbles to rise into the crest without escaping before impact.

Test Code	Flume	Aeration source	Wave Height	Wave Period	Number of waves	Water Depth at wall	Pressure sample rate	Aeration sample rate
			(mm)	(Seconds)		(mm)	(kHz)	(kHz)
19O593O1	UoP	Natural	90	1.33	75	70	1	0.25
2OO593O1	UoP	Artificial	90	1.33	75	70	1	0.25
O8O896O2	UoP	Natural	111	1.25	280	78	2	2
O8O896O3	UoP	Natural	127	1.25	280	78	2	2
O8O896O4	UoP	Natural	97	1.25	280	78	2	2
O8O896O5	UoP	Natural	112	1.33	263	64	2	2
O8O896O6	UoP	Natural	81	1.33	263	65	2	2
29O998O1	UoE	Natural	135	1.23	140	87	2	-

Table 5.3. Small scale regular wave test details.

5.2.2 Natural aeration tests

Five tests were conducted using the new aeration probes described in sections 4.3 to 4.7. Pressures were recorded at the locations used in the artificial aeration tests with additional measurements being made between each probe pair by means of Kulite XTM-190 miniature transducers. These had an active surface diameter of 3.9 mm and a pressure range of 69 kN/m^2, a natural frequency of 15 KHz in water and temperature compensation from 0 to 50° C. At least 250 wave impacts were measured during each of the tests during which the pressures and aeration instruments were sampled at 2 kHz. The arrangement of transducers and aeration probes can be seen in Figures 5.6 and 5.7.

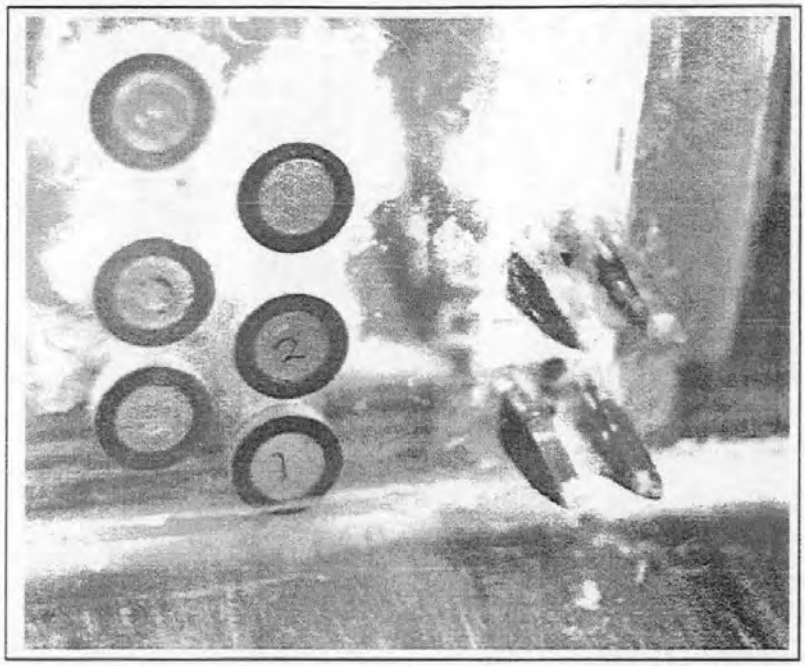

Figure 5.6. Instrumentation used during the natural aeration tests.

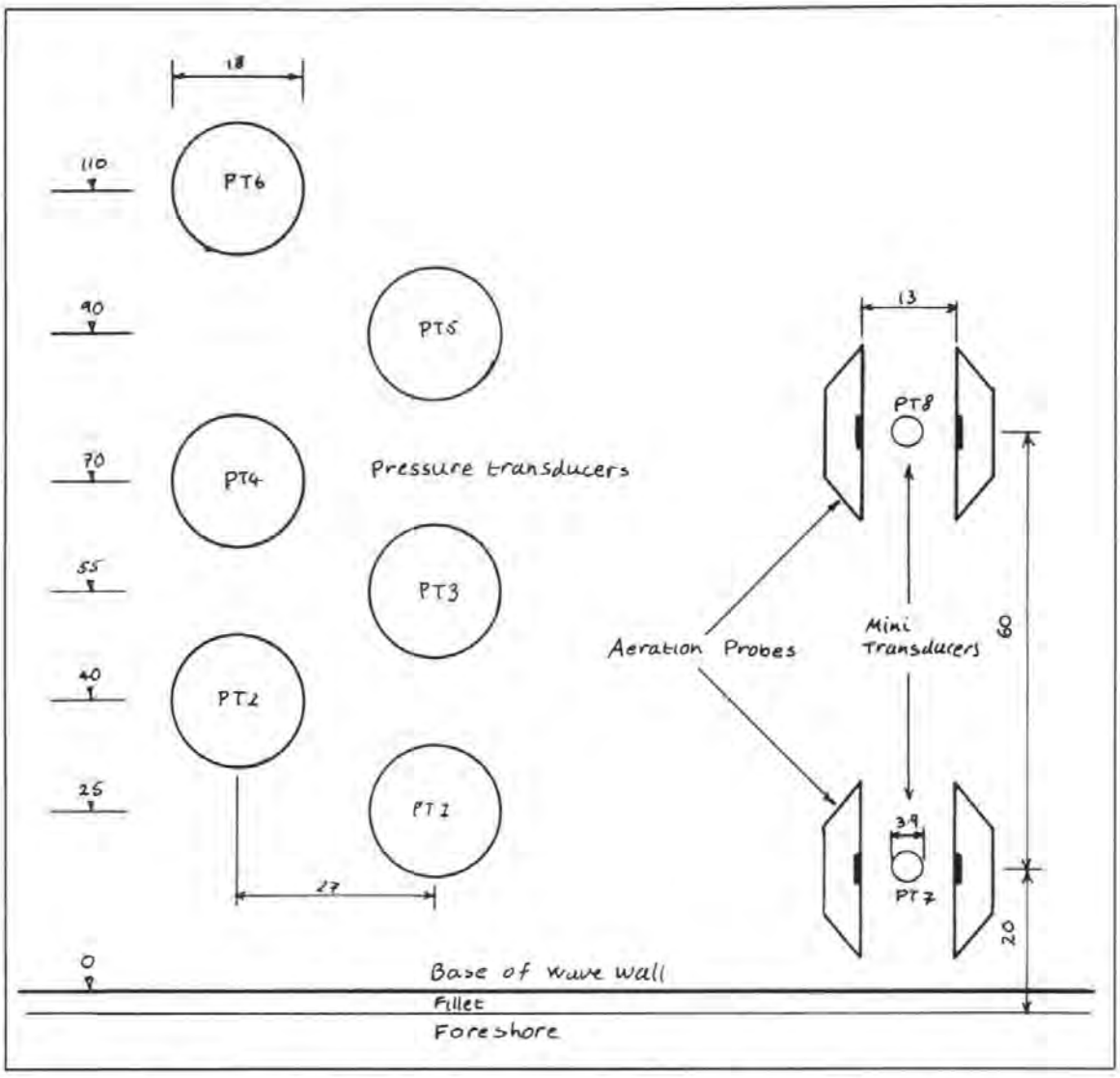

Figure 5.7. General arrangement of instrumentation during the natural aeration tests.

5.3 Drop tests

A series of drop tests were conducted in which a plate which was instrumented with pressure transducers was dropped onto the surface of a body of water into which various levels of aeration were introduced. These drop tests were used to investigate the effect of entrained aeration and water type on impact loads under more controlled conditions than were possible with breaking waves. The measured parameters were the plate mass, its impact velocity and the percentage of air entrained in the water. In order to ensure repeatability, the plate had to be plane and parallel to the water surface at the moment of impact and the parameters of interest had to be well controlled.

The apparatus consisted of a rigid 'traveller' which was allowed to free fall down two guide bars and strike the surface of a body of water contained in a vertical tube, see Figures 5.8 to 5.10. The traveller, which is illustrated in Figure 5.8, consisted of an 18 mm thick ABS circular impact plate and two 20 mm thick ABS guide plates joined by seven 8 mm diameter steel bars. It was guided by two 20 mm diameter stainless steel bars, each hanging by a pin joint from a steel suspension frame. The water was contained by a 1.34 m long 100 mm internal diameter clear acrylic tube with a wall thickness of 5 mm at the base of which was an aerator. Holes for miniature pressure transducers were drilled into the drop plate and the tube, which was also fitted with four peizometers.

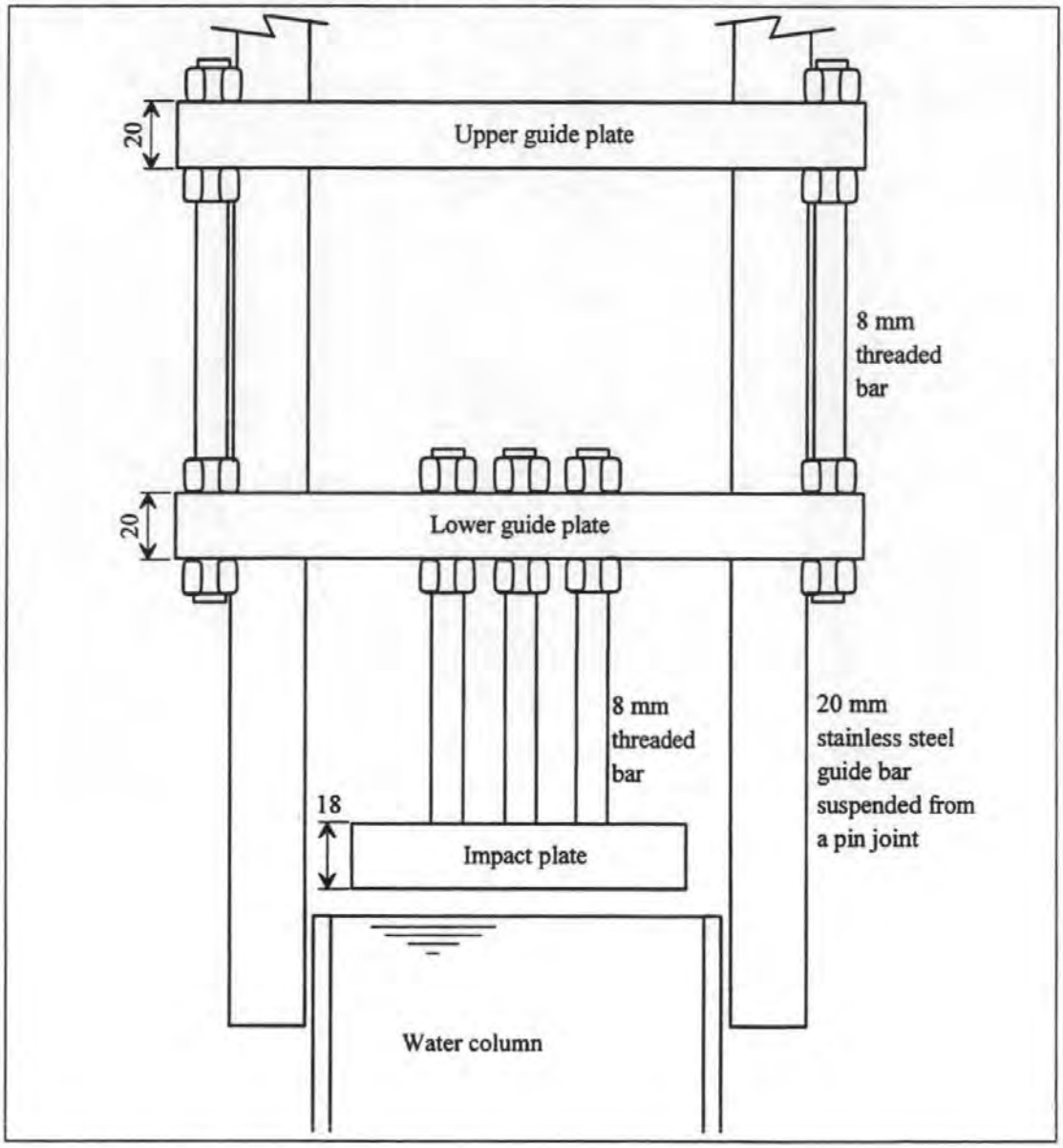

Figure 5.8. Drop test 'traveller'.

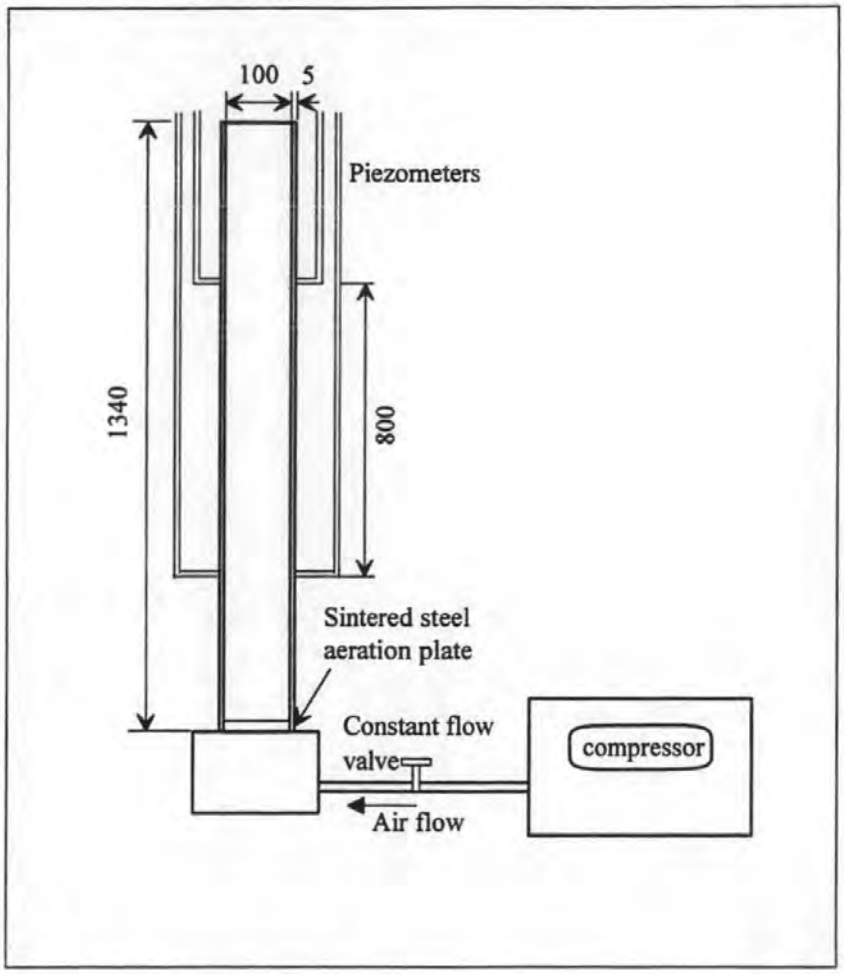

Figure 5.9. Aeration column.

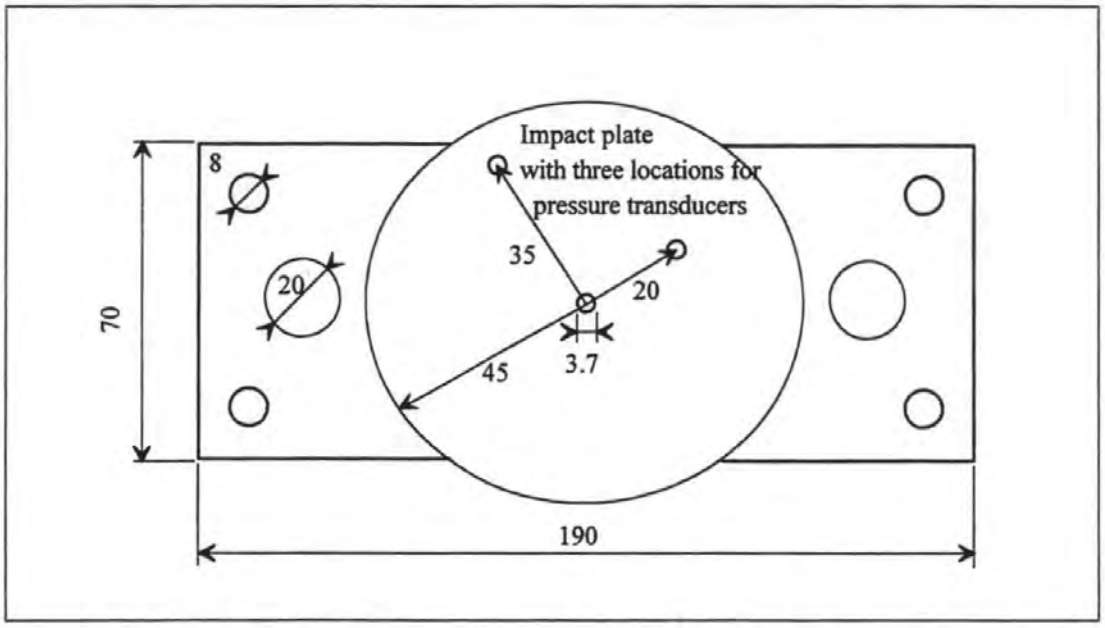

Figure 5.10. Detail of impact plate showing the locations for the pressure transducers.

This apparatus allowed close control over the angle between the plate and the horizontal water surface. The guide bars hung vertically from their pin joints so it was only necessary to ensure that the traveller was 'square' in order for the plate to be plane parallel to the water at impact. Fine adjustment was allowed by varying the distance between the impact plate and the lower guide plate along each of the three support bars. The mass of the traveller was simply controlled by the addition of extra weights when required, and by cleaning off any small quantities of pooled water.

Attempts were made to incorporate a means of measuring the velocity at impact using video images and proximity sensors. Such techniques were found to be difficult to incorporate with accuracy and time consuming to analyse. It was decided to produce repeatable impact velocities by releasing the traveller from set heights. A staff was made which had protruding bars at incremental heights. By supporting the traveller on a selected bar, then removing the staff, an instantaneous release was achieved and the traveller fell from a known elevation. The height of the water surface was controlled between each test by refilling the tube until it overflowed. Having the water surface at the top of its container prevented a build up of air pressure within the tube during the moments before impact.

The main series of tests included three impact velocities, (2.0, 2.8 and 3.4 m/s) two water types, (sea water and fresh water) two traveller masses (1.35 and 1.85 kg), and aeration levels ranging from 0 to 18 % as described in Table 5.4. Each test condition was repeated three times. Other tests were conducted to investigate the effect of reducing the plate size, the pressure distribution across the plate, and the effect of recessing the pressure transducers. Pressures were measured at 5 kHz using the miniature transducers described in section 5.2.2 at up to 3 locations on the surface of the plate (see Figure 5.10).

Aeration level (%)	Velocities (m/s)	Mass (kg)	Water type
0	2.0, 2.8, 3.4	1.85	Sea water
0.3	2.0, 2.8, 3.4	1.85	Sea water
0.9	2.0, 2.8, 3.4	1.85	Sea water
2.4	2.0, 2.8, 3.4	1.85	Sea water
7.8	2.0, 2.8, 3.4	1.85	Sea water
13	2.0, 2.8, 3.4	1.85	Sea water
15.6	2.0, 2.8, 3.4	1.85	Sea water
0	2.0, 2.8, 3.4	1.35	Sea water
0.9	2.0, 2.8, 3.4	1.35	Sea water
2.6	2.0, 2.8, 3.4	1.35	Sea water
5.4	2.0, 2.8, 3.4	1.35	Sea water
11.1	2.0, 2.8, 3.4	1.35	Sea water
8	2.0, 2.8, 3.4	1.35	Sea water
16.8	2.0, 2.8, 3.4	1.35	Sea water
0	2.0, 2.8, 3.4	1.35	Fresh water
0.4	2.0, 2.8, 3.4	1.35	Fresh water
1.6	2.0, 2.8, 3.4	1.35	Fresh water
6.1	2.0, 2.8, 3.4	1.35	Fresh water
8.9	2.0, 2.8, 3.4	1.35	Fresh water
13.5	2.0, 2.8, 3.4	1.35	Fresh water
17.5	2.0, 2.8, 3.4	1.35	Fresh water
0	2.0, 2.8, 3.4	1.85	Fresh water
0.4	2.0, 2.8, 3.4	1.85	Fresh water
1.7	2.0, 2.8, 3.4	1.85	Fresh water
4.7	2.0, 2.8, 3.4	1.85	Fresh water
6.6	2.0, 2.8, 3.4	1.85	Fresh water
9.5	2.0, 2.8, 3.4	1.85	Fresh water
13.1	2.0, 2.8, 3.4	1.85	Fresh water
16.7	2.0, 2.8, 3.4	1.85	Fresh water

Table 5.4. Drop test conditions, each was tested three times.

Air flow was created with a rotary screw compressor which had a reservoir to ensure a constant driving pressure of 750 kN/m^2. The flow rate was adjusted with a constant flow valve. The aeration chamber in the base of the water column was circular in plan with a 90 mm diameter roof made of sintered steel which had a pore size of six microns. It was large

relative to the base of the tube which ensured a uniform distribution of bubbles and produced the smallest possible bubbles for the selected flow rates and water types. It was not possible to directly measure the air flow rate using this apparatus or to ascertain the consistency of the driving pressure, so repeated measurements of aeration in the tube were made during the experiments. Several different techniques of aeration measurement were tried including assessing bulking, measuring sound speed in the air water mixture and obtaining pressure differentials by means of peizometer tubes and pressure transducers. The peizometers were found to be the most accurate indicators.

5.4 Bubble measurements

The aeration column used during the drop tests was employed to measure bubble sizes and distributions. A grid was placed on the wall of the tube and bubbles were photographed using a stills camera with a micro lens and a flash gun. The flash duration and therefore the exposure time was 0.7 ms.

5.5 Accuracy and confidence

The performance of the aeration equipment has already been investigated and described in detail in Chapter 4. Its output during 'live' tests is shown, interpreted and discussed in following chapters. Gross errors in the pressure data were avoided through simple good practice such as appropriate calibration procedures, sampling transducers well below their natural frequencies and following other manufacturers guidelines. Despite these efforts it is still difficult to establish levels of confidence in the results. The level of flume noise, the size of the pressure transducers, their location and sample rate will all affect the measurements. This problem is, at least at present, unavoidable. No limits have yet been found for the brevity of duration of P_{max} or the smallness of the area over which it acts. Consequently, there are no specifications for the lower limit to the size of transducer or an upper limit for its sample rate. No special attempt was made in these tests to pursue extremes pressures. This is justified in the context of a study into the stability of a structure with high inertia such as a vertical breakwater (this is discussed in greater detail in Chapter 10). Forces are more significant to the problem of overall stability than localised pressures and large pressure transducers record forces more accurately because of their greater spatial

coverage. In these tests it was more important to record the magnitude of the force impulse (I_{mp}) accurately rather than P_{max}. Figure 2.10 indicates that, for a given sample frequency, the percentage inaccuracy in I_{mp} may be two orders of magnitude less than in P_{max}.

This study attempted to achieve high confidence in results, but this was not pursued by recording pressures with improved precision but by changing the way they were processed and interpreted. The significance of structure inertia was recognised, therefore spatial and temporal integration was used to provide forces and impulses. In the process of integration transient and localised variation is averaged out.

Chapter 6

The influence of aeration on wave impact pressures

6.0 Introduction

Although it is widely believed that air has important effects on wave impact loads, there is no general agreement on its role. It is known that entrained aeration is intrinsically linked with wave energy dissipation and compressibility. It is also clear that the volume and location of entrapped air depends upon the shape of the wave at impact and that it can form a compressible boundary at the wall. The fact that these roles have not been fully described either quantitatively or qualitatively is partly due to a lack of laboratory measurements.

Because the unknowns associated with aeration and wave impact pressures are so numerous, not all of them could be answered within this study. Investigations were limited to the following problems;

- The relationship between entrapped air, breaker shape and impact load.
- Quantification of entrained aeration at small scale.
- The relationship between entrapped air and impact pressure maxima.
- The effect of artificially entrained air on impact loads.
- The effect of entrained air on drop test impact force maxima.

Firstly, the interrelationship between aeration, pressure and breaker shape was observed using large scale solitary waves in the GWK. The air pocket impact produced particularly high loads on the caisson so this type was selected for further investigation at small scale. Air pocket impacts were generated in a series of tests during which the new probes were used to measure the aeration. A relationship was found between the peak impact loads and the quantity of entrapped air. Artificial aeration tests were then conducted which appeared to indicate an inverse relationship between entrained aeration and impact pressure although

there were concerns that the injection of air may have affected the breaker shape. A series of aerated drop tests involving both fresh and sea water were then used to derive an empirical relationship between impact forces and aeration and to investigate the importance of water type.

The new aeration probes designed for the small scale tests performed well but the large scale equipment failed during experiments. The spar upon which the electrodes were mounted leaked despite being designed against the ingress of water. This caused the electrodes to short-circuit and this made calibration impossible. Consequently the large scale aeration results could only be used as rough indicators of the presence of air.

6.1 The relationship between breaker shape, entrapped air and impact pressures for large scale solitary waves

The large scale solitary wave tests (04029401 to 04029410, see Table 5.2) were used to investigate the relationship between entrapped air and breaker shape and its effect on impact pressure time histories. These solitary waves were used rather than regular waves because the long period of time between breaker events (approximately 20 minutes) minimised both the presence of ambient entrained air and 'noise' on the water surface. The water depth was held at a constant 3.1 m whilst the wave heights were increased from 0.65 to 1.00 m in 0.05 m increments. Pressure time histories recorded with transducer 5, which was located 0.97 m above the caisson toe are shown for each of these waves in Figures 6.2 to 6.9 together with sketches of the approximate form of the breakers.

Each of the pressure time histories shown here are similar in that they can be divided into two characteristic regions. First, there is an essentially triangular region associated with the impulse as the wave arrives at the wall, which is followed by a region of slowly varying pressure associated with the underlying quasi-hydrostatic load. A schematic diagram is shown in Figure 6.1.

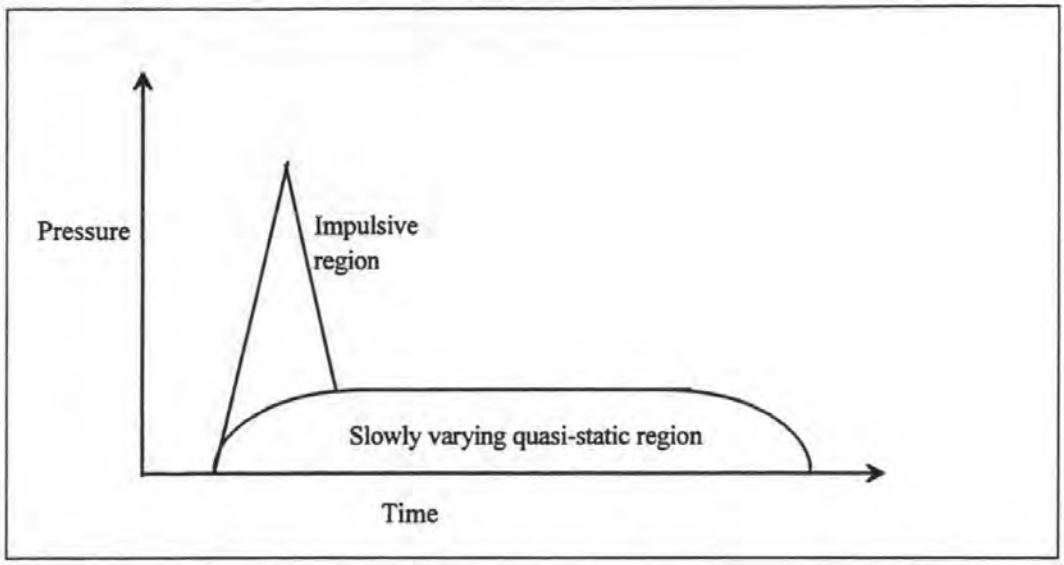

Figure 6.1. Schematic representation of the two characteristic regions of the pressure time history produced by a breaking wave.

6.1.1 Steep wave impact (H = 0.65 m)

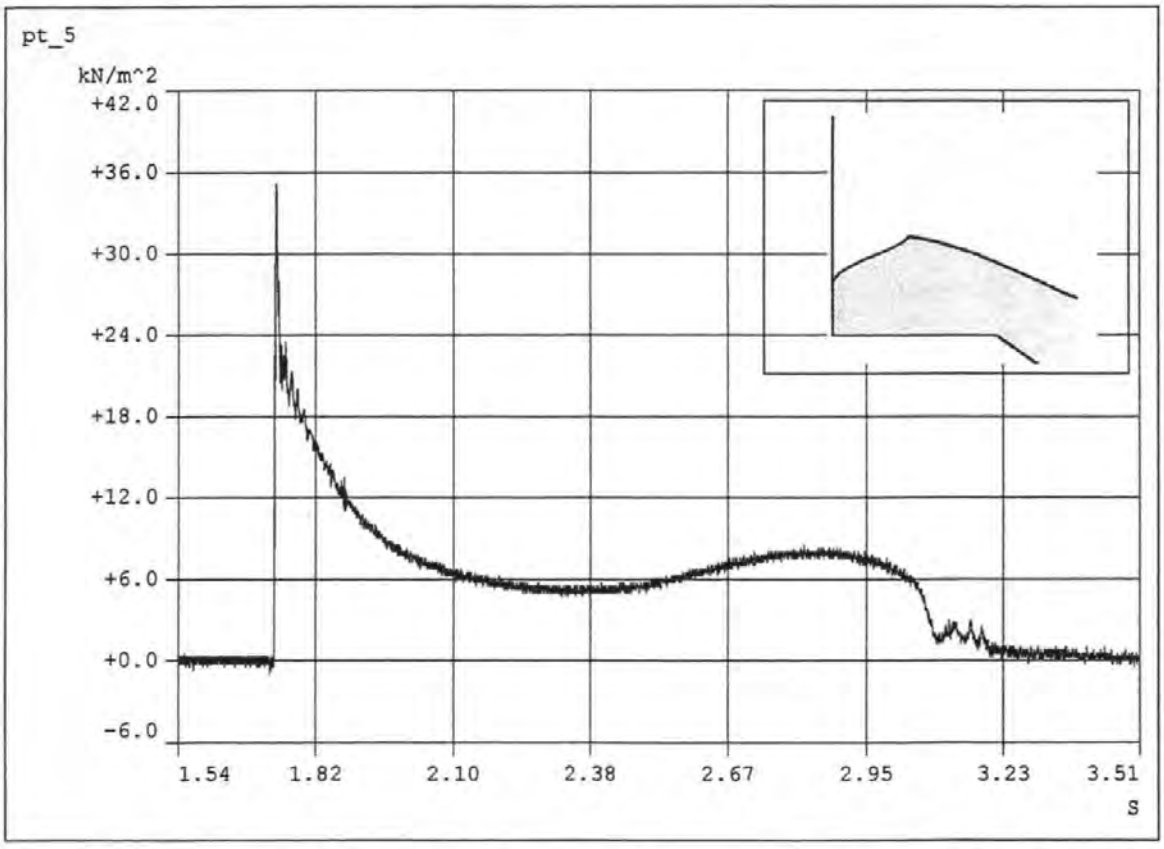

Figure 6.2. Pressure time history for the impact of a steep solitary wave, H = 0.65 m, Test 04029408.

In Figure 6.2 the impulsive region may be estimated to last from approximately 1.73 s to 1.9 s. At approximately half way through the time history (2.3 s in Figure 6.2) the pressure drops to a minimum; this point is probably associated with the moment when the uprush reaches its maximum elevation. This wave was steep but did not have an overhanging crest. The peak pressure and rise time were *5.5* ($P_{max}/\rho.g.H$) and 6 ms respectively. The wave form did not entrap any air and this probably explains the smoothness of the trace.

6.1.2 Steep wave impact (H = 0.70 m)

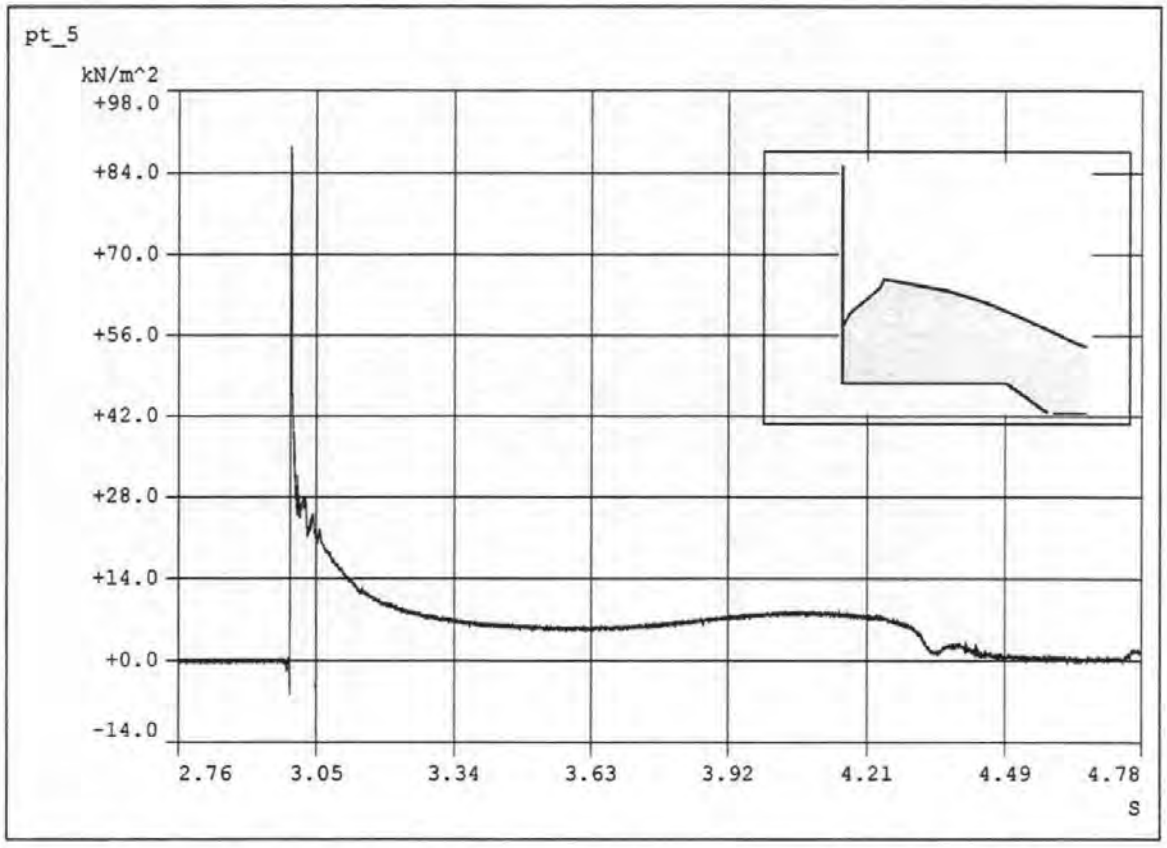

Figure 6.3. Pressure time history of a steeper solitary wave impact, H = 0.70 m, Test 04029407.

The 0.70 m high wave was very similar to the 0.65 m wave except that, being larger, it assumed a more developed form at impact. The profile was steeper which lead to a higher peak pressure ($P_{max}/\rho.g.H$ = 12.8) and a shorter rise time of only 1.5 ms, see Figure 6.3. Negative pressures can be observed at the start of the impact, Hattori *et al*, (1994) suggested that this phenomena may be due to a high velocity jet rising up the wall and generating suction at the face of the pressure transducer. Slight oscillations can be seen just after the peak pressures.

6.1.3 Steep wave impact (H = 0.75 m)

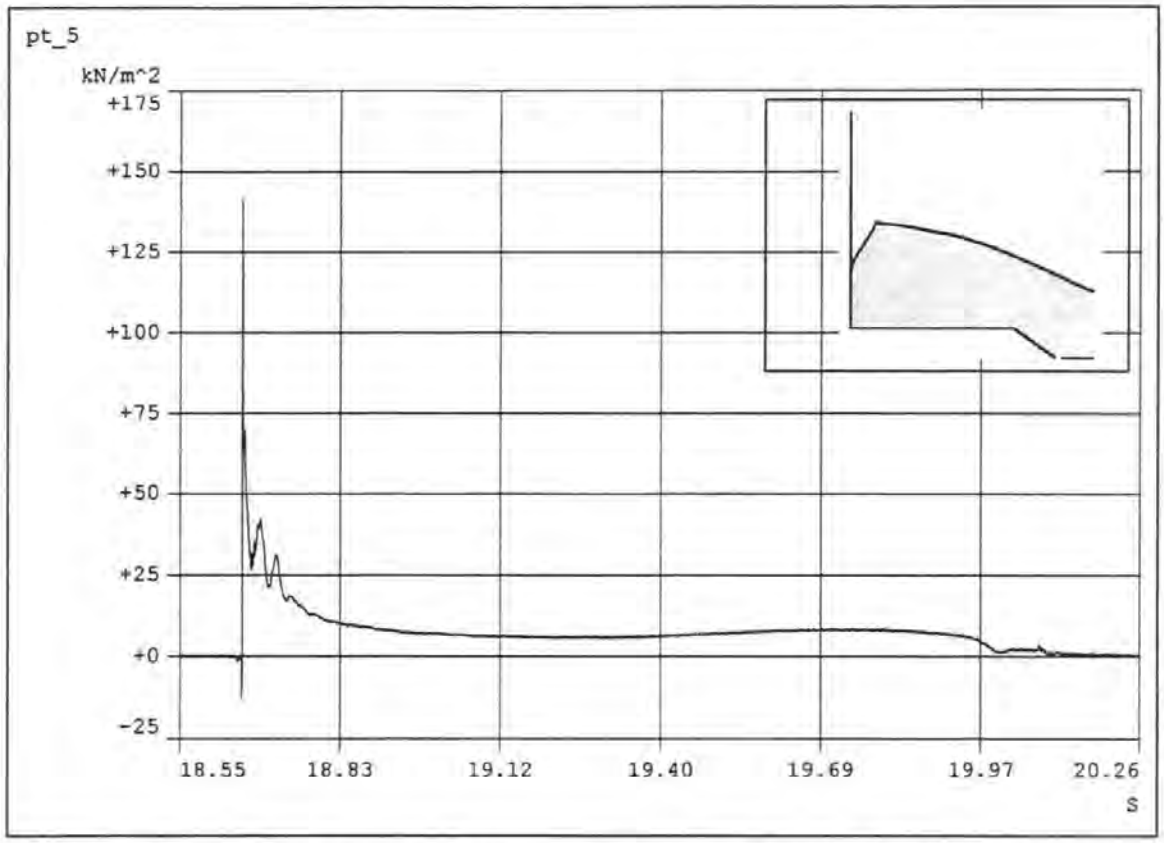

Figure 6.4. Pressure time history of a steeper solitary wave impact, H = 0.75 m, Test 04029406.

The impact of the 0.75 m high wave shown in Figure 6.4 is similar to the previous two. The peak pressure has increased again to $P_{max}/\rho.g.H$ = 19.2 and the rise time has reduced to 0.5 ms which was the sample frequency. The initial negative pressures have increased in magnitude, presumably indicative of higher vertical velocities. It is interesting to observe that the small oscillations seen in the previous impact are also present and that their magnitude has increased, which is a trend that continues with the 0.80 m wave. Visual and video inspection of these waves did not reveal any air entrapment which might have explained their presence. The period of these oscillations is approximately 0.04 seconds, which is slightly less than the natural period (T_n) of the structure that is calculated below in Chapter 8 as 0.056 seconds. Given uncertainties associated with the calculation of T_n and the low water level during the solitary wave tests which would decrease the added hydrodynamic mass and therefore decrease T_n, it seems probable that these observed oscillations arise from motion of the caisson in response to the impact.

6.1.5 Small air pocket wave impact (H = 0.85 m)

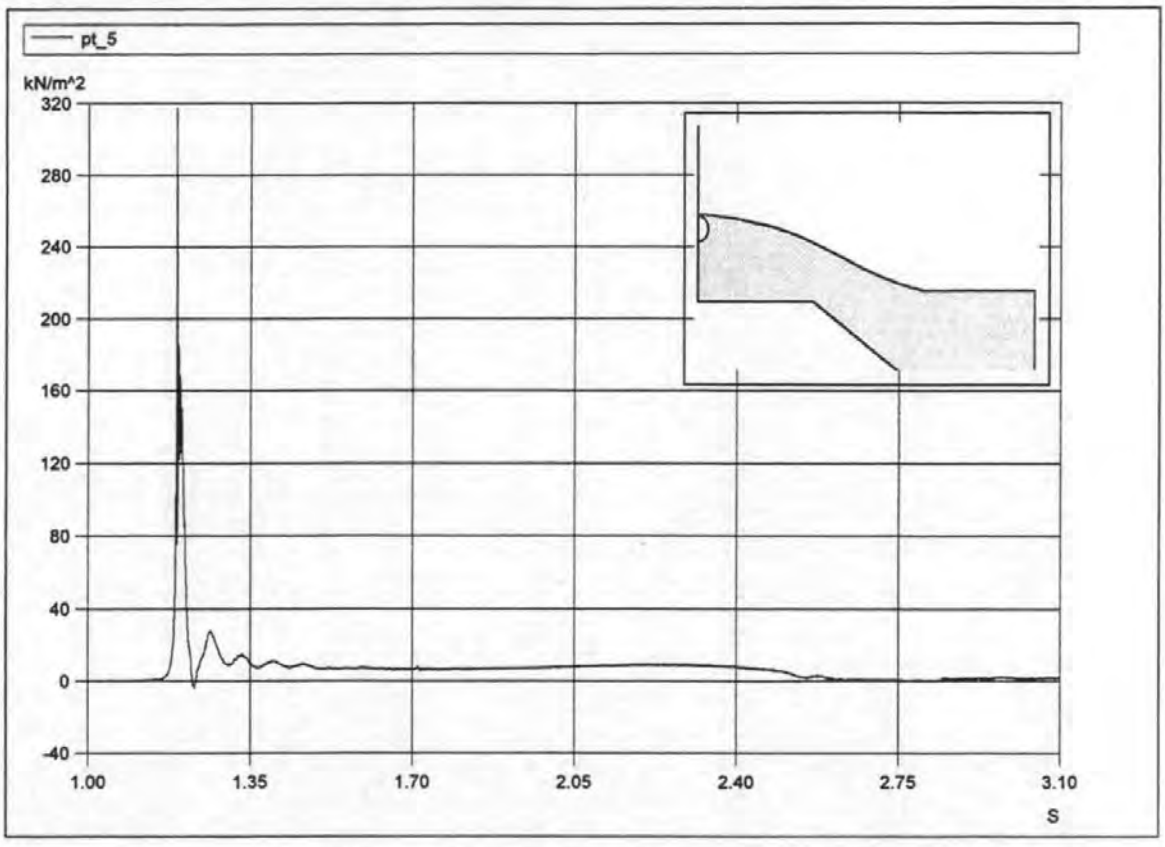

Figure 6.6. Pressure time history of a small air pocket solitary wave impact, H = 0.85, Test 04029404.

The 0.85 m high wave assumed a shape at breaking which entrapped a small air pocket (Figure 6.6) and caused a pressure maxima of $P_{max} / \rho.g.H = 38.1$ which was the highest of the series and had a rise time of 25 ms. The pressure time history appears to be similar to the one shown in Figure 6.5 except that the rise time is much longer and the oscillation after the peak include values which fall below zero. Both of these observations can be attributed to the entrapment of the air pocket.

6.1.4 Flip-through wave impact (H = 0.80 m)

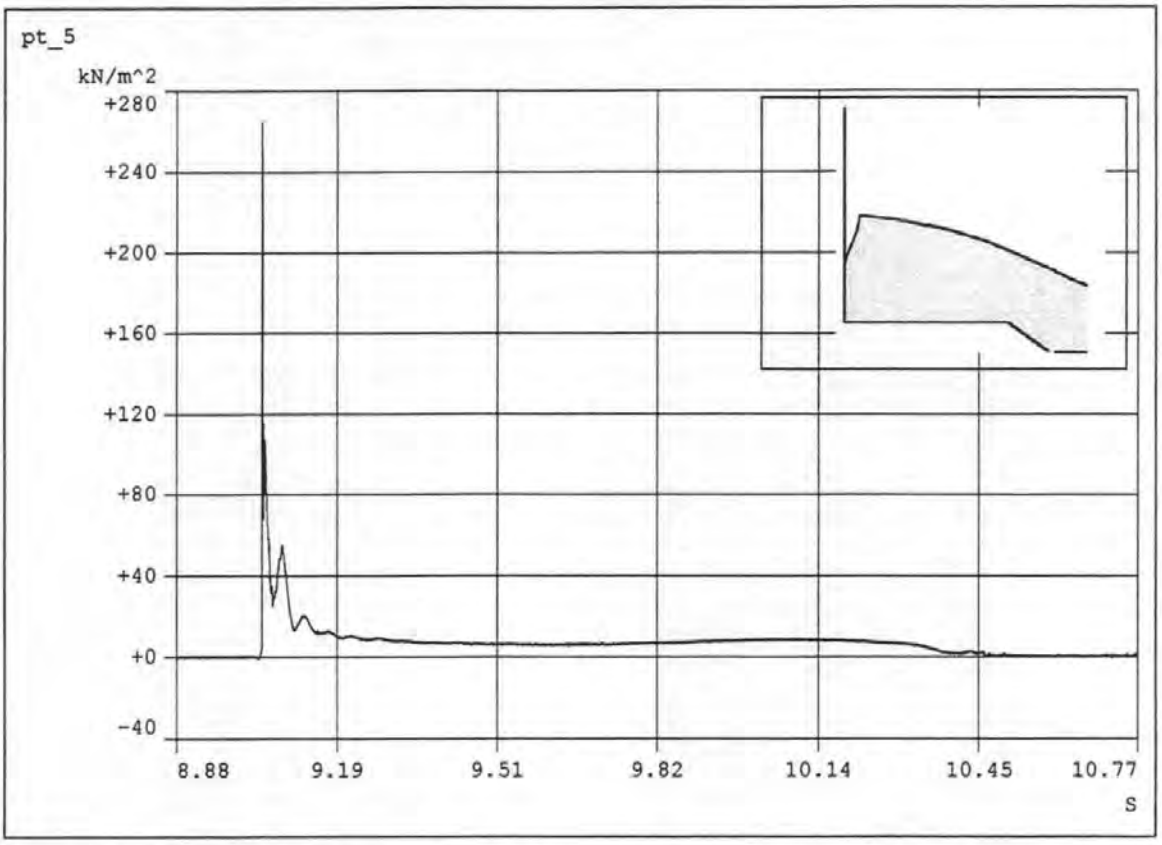

Figure 6.5. Pressure time history of a flip-through solitary wave impact, H = 0.80 m, Test 04029405.

The 0.8 m high (Figure 6.5) wave produced a flip-through impact. In this type of impact the water surface rises very quickly at the wall preventing the wave from entrapping any aeration. This impact produced the second largest peak pressure in this series ($P_{max} / \rho.g.H$ = 33.8) with a rise time of only 0.5 ms. This is equal to the sample rate so it is reasonable to suppose that the actual maximum pressure was not recorded.

6.1.5 Small air pocket wave impact (H = 0.85 m)

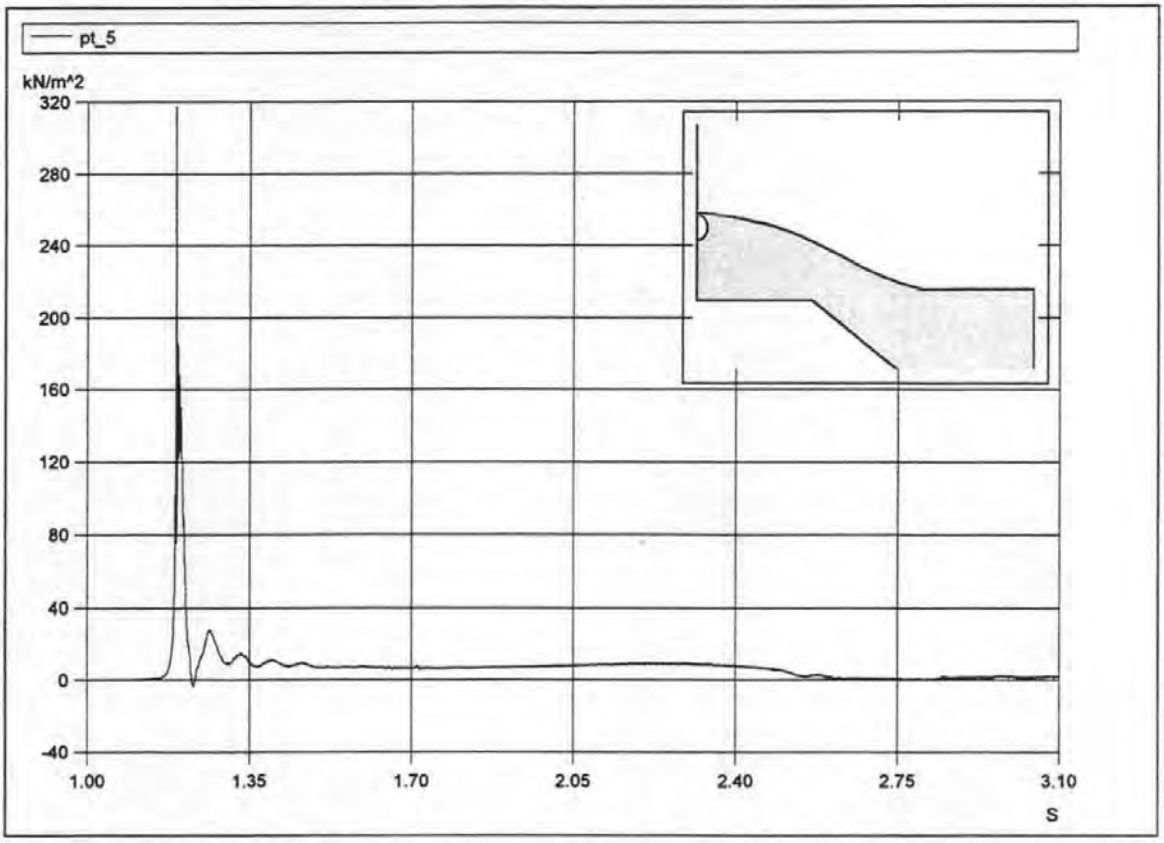

Figure 6.6. Pressure time history of a small air pocket solitary wave impact, H = 0.85, Test 04029404.

The 0.85 m high wave assumed a shape at breaking which entrapped a small air pocket (Figure 6.6) and caused a pressure maxima of $P_{max}/\rho.g.H = 38.1$ which was the highest of the series and had a rise time of 25 ms. The pressure time history appears to be similar to the one shown in Figure 6.5 except that the rise time is much longer and the oscillation after the peak include values which fall below zero. Both of these observations can be attributed to the entrapment of the air pocket.

6.1.6 Large air pocket wave impact (H = 0.90 m)

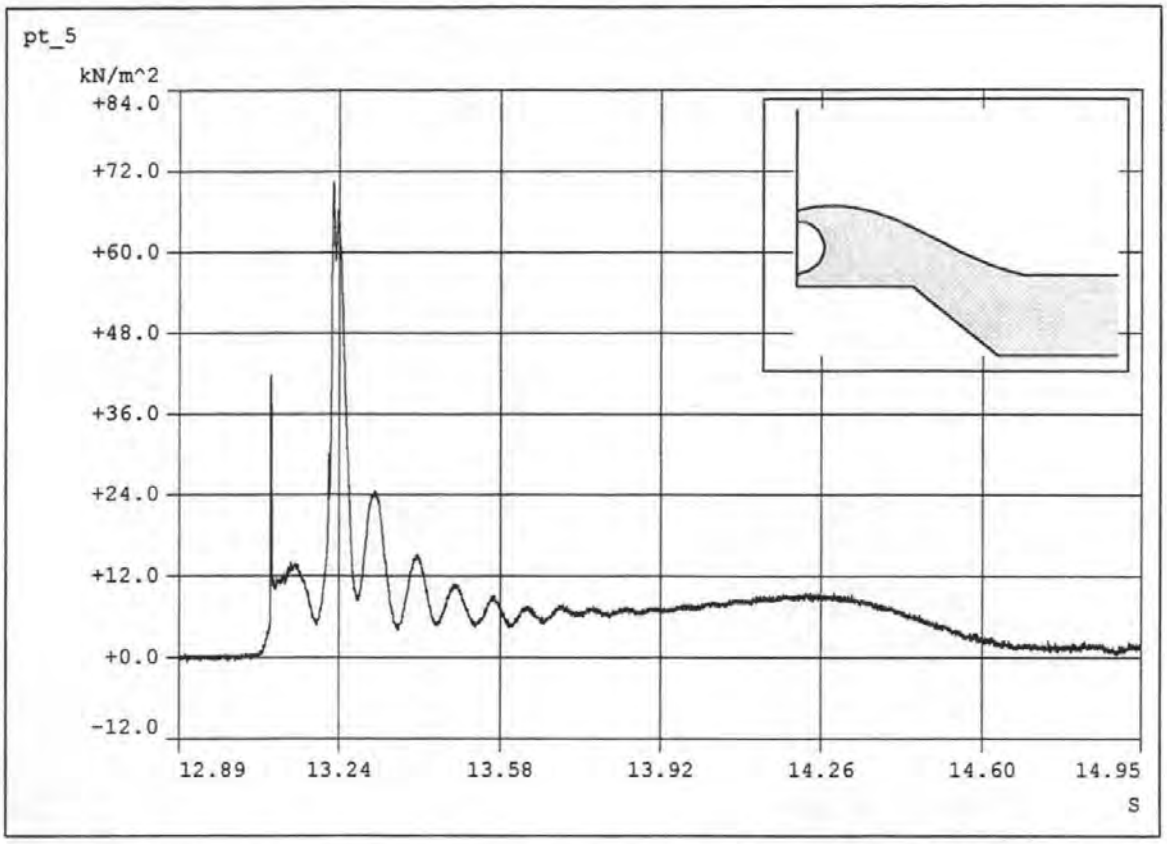

Figure 6.7. Pressure time history of large solitary air pocket impact, H = 0.90 m, Test 04029403.

The air pocket trapped by the 0.90 m wave was larger than that of the 0.85 m wave, as illustrated in Figure 6.7. Two pressure peaks occurred with a region of low pressure between them. These were followed by a period of damped oscillation.

6.1.7 Toe breaker wave impact (H = 0.95 m)

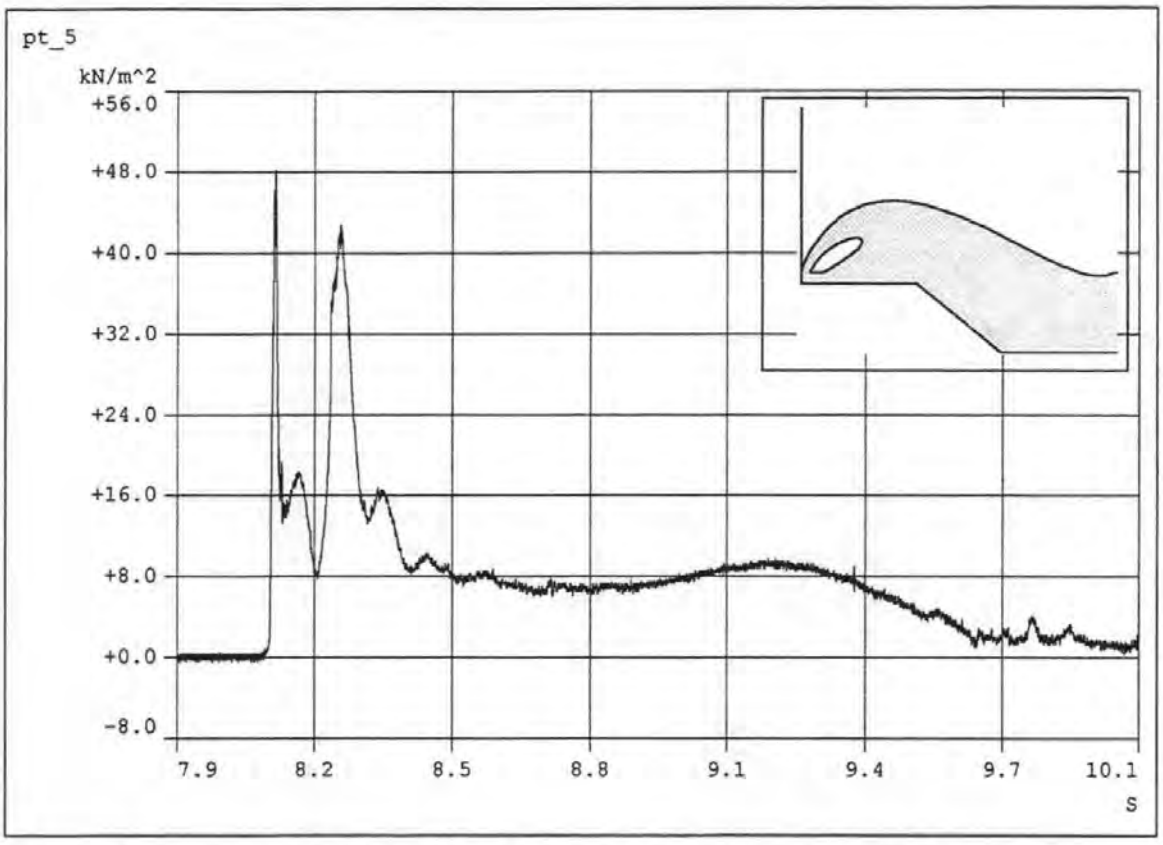

Figure 6.8. Pressure time history of a solitary toe breaker impact, H = 0.95 m, Test 04029402.

The crest of the 0.95 m high wave plunged on the toe of the caisson and created a similar force time history to the large air pocket impact. It can be seen in Figure 6.8 that the first peak is more pronounced and reaches a greater maxima than the second peak. The rise time is only 15 ms and there are no significant pressure oscillations.

6.1.8 Beach breaker impact (H = 1.00 m)

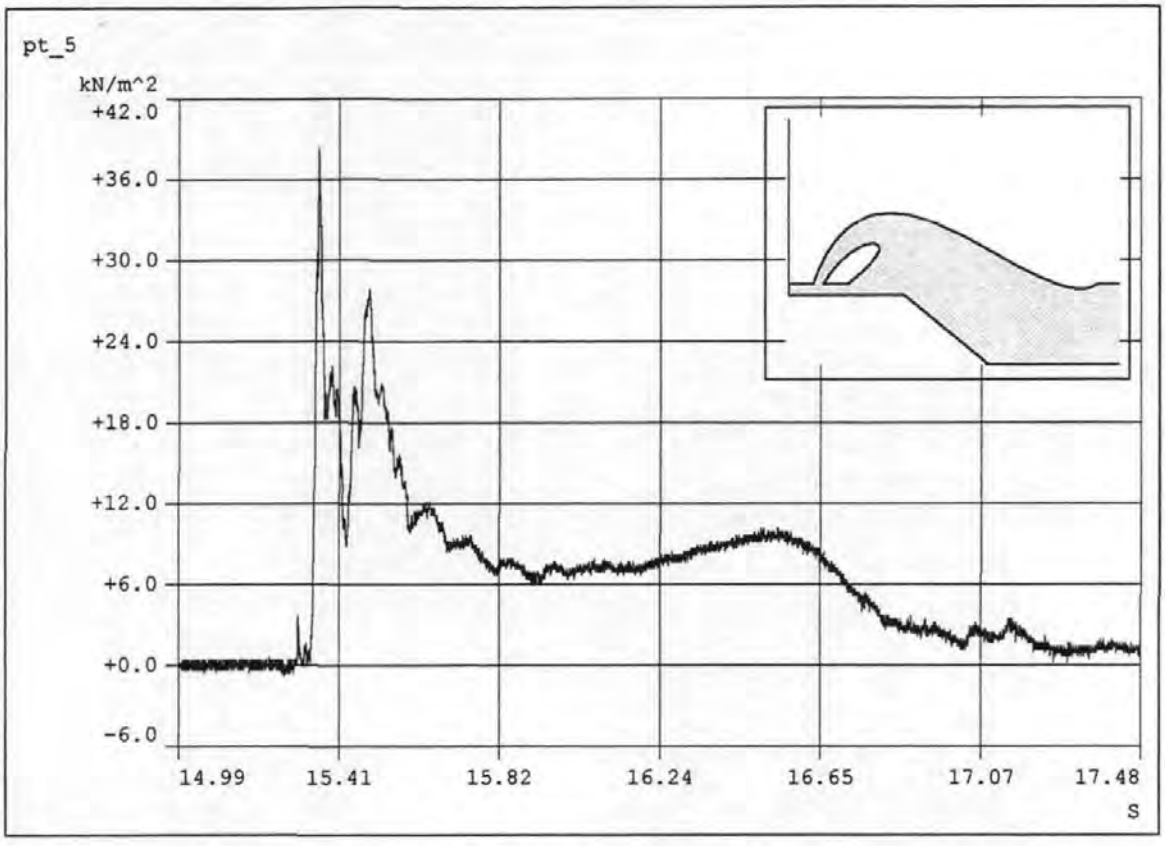

Figure 6.9. Pressure time history of a solitary beach breaker impact, H = 1.0 m, Test 04029401.

Like the toe breaker and large air pocket impact, the 1.0 m beach breaker also produced a double peak in the pressure record, as can be seen in Figure 6.9. The first peak is more pronounced than it was in the previous waves. It appears that the double peaks and pressure oscillations are due to the entrapment of air. Similar oscillations have been seen by several other researchers and have been attributed to fluctuations in size of the air pocket (see for example Oumeraci and Partenscky, 1991, Hattori *et al*, 1992 and Topless *et al*, 1992). More understanding of the presence of the double peaks can be gained by examining the aeration time histories.

6.1.9 The relationship between entrapped air and double peak impacts

Figure 6.10 shows a pressure and aeration time history recorded at the same location during the beach breaker impact. The pressure record shows the double peak form. The first peak is clearly associated with the arrival of the wave at the wall which can be seen by the rapid drop in the output of the aeration instrument as it becomes submerged. The occurrence of the second peak is usually attributed to compression of the air pocket (see for example Oumeraci and Partenscky, 1991), however the data from the aeration gauges show that this may not be the case.

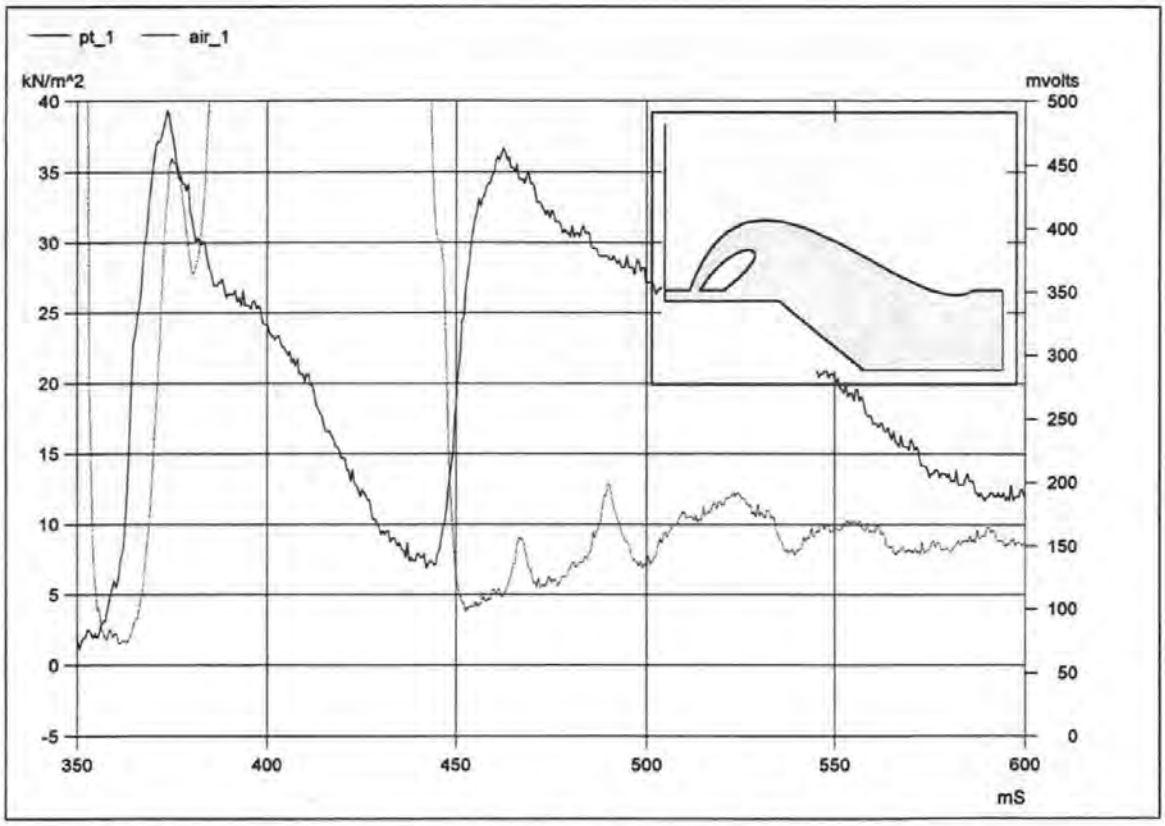

Figure 6.10. Expanded pressure time history and aeration time history recorded at level 1 during the beach breaker of Test 04029401.

It can be seen in Figure 6.10 that between the double peaks the aeration level is very high, indicating the presence of the pocket. During this time the pressure is low or falling. The second peak occurs as the output of the aeration gauge drops, indicating the arrival of the water behind the pocket. These results show a decompressing, or low pressure air pocket rather than one which is being compressed. The same patterns can be found in results recorded at other elevations during this event, which are shown in Figures 6.11 to 6.13.

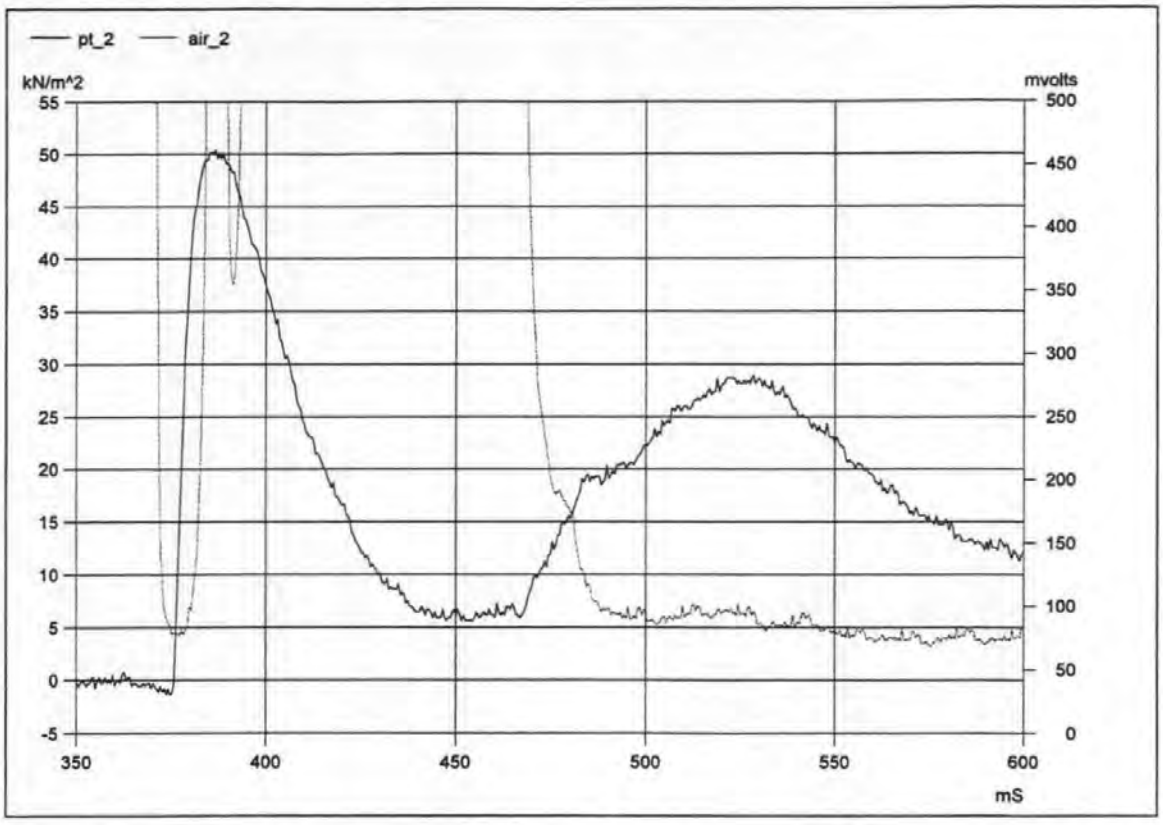

Figure 6.11. Expanded pressure time history and aeration time history recorded at level 2 during the beach breaker of Test 04029401.

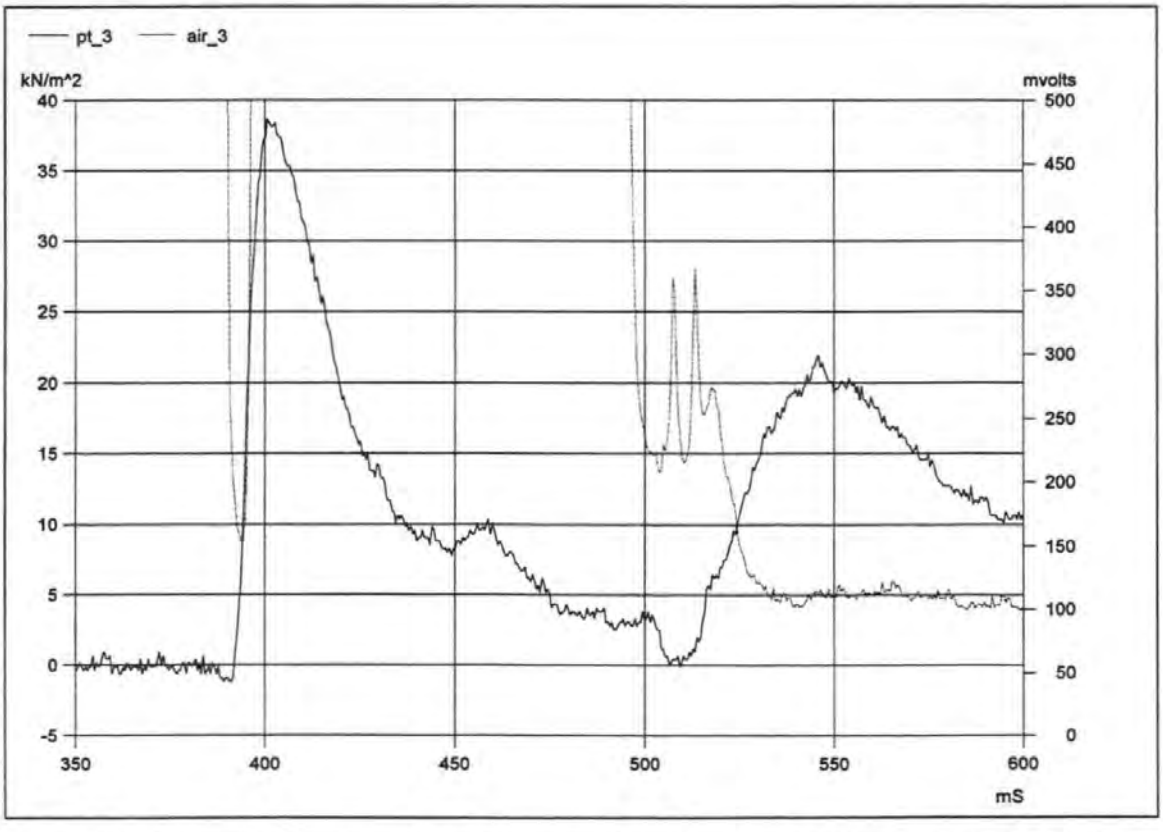

Figure 6.12. Expanded pressure time history and aeration time history recorded at level 3 during the beach breaker of Test 04029401.

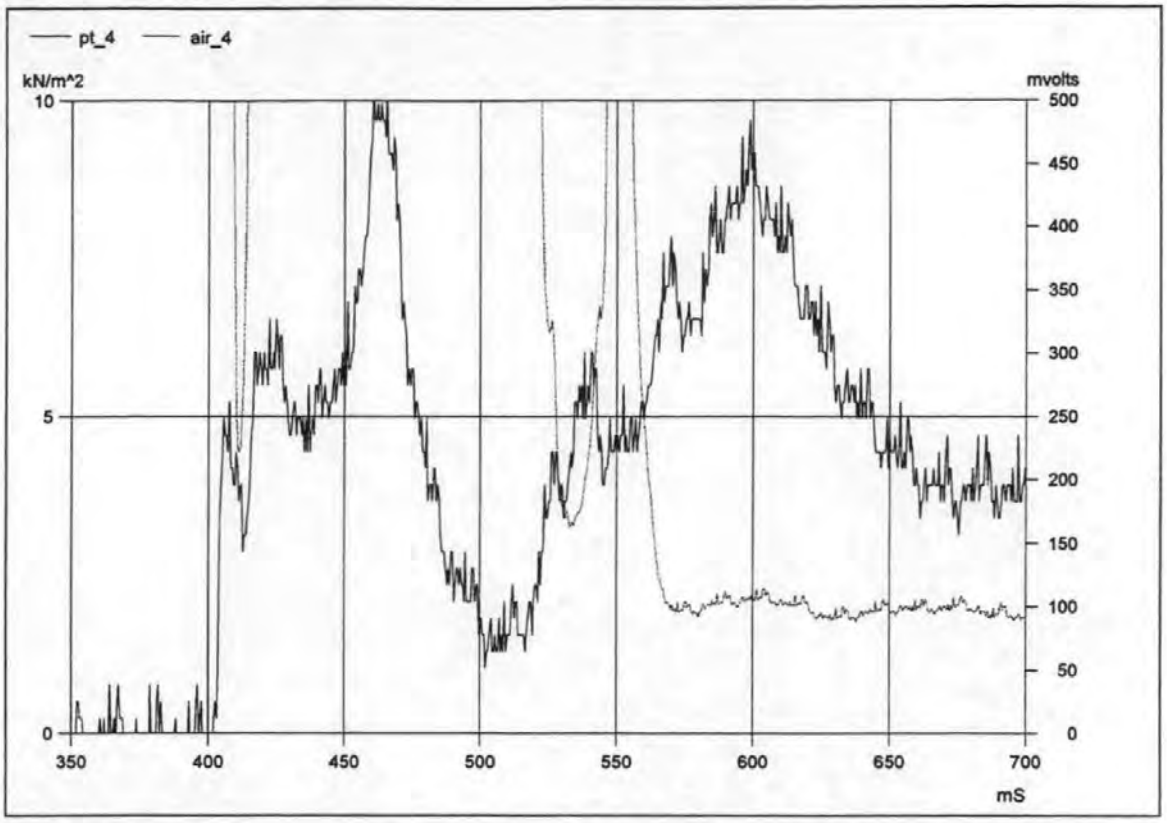

Figure 6.13. Expanded pressure time history and aeration time history recorded at level 4 during the beach breaker of Test 04029401.

The results of the toe breaker and large air pocket impacts show the same relationship between high aeration and low pressure. Single representative pressure and aeration time history from these events are shown in Figures 6.14 and 6.15, other data are shown in Appendix A.

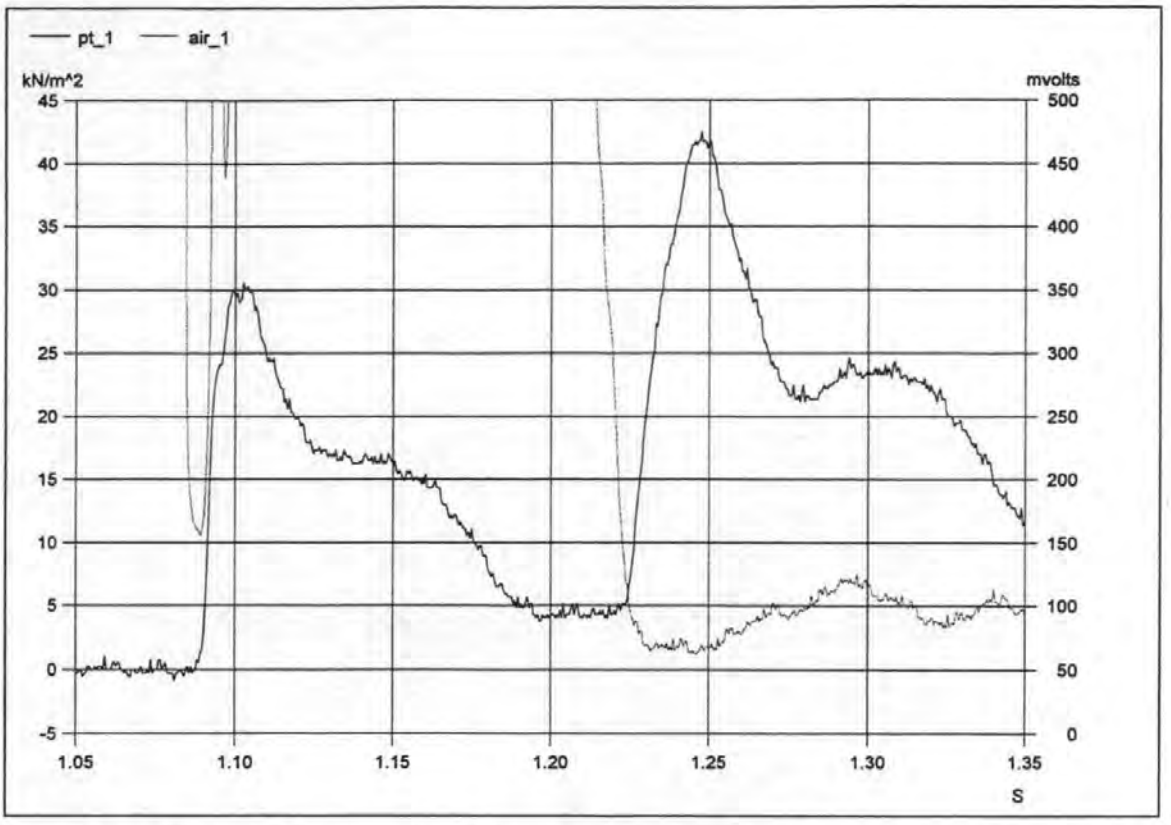

Figure 6.14. Expanded pressure time history and aeration time history recorded at level 1 during the large air pocket impact of Test 04029403.

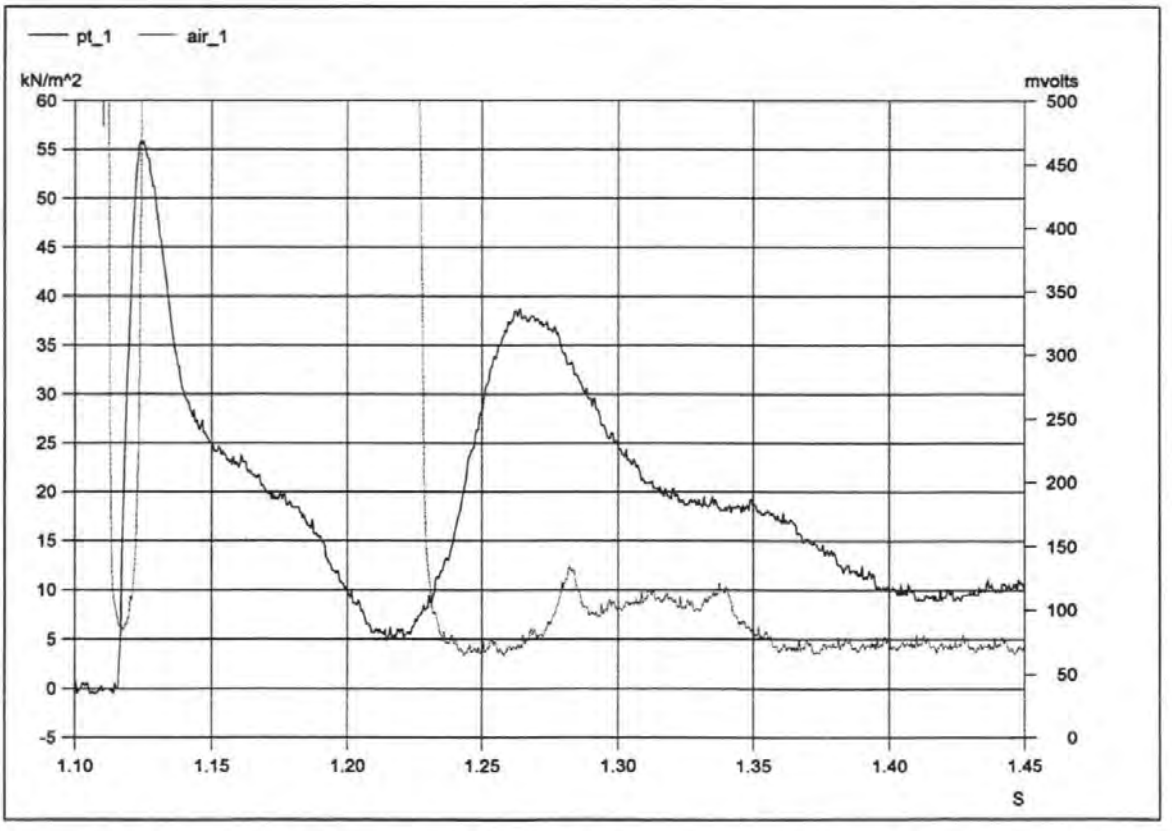

Figure 6.15. Expanded pressure time history and aeration time history recorded at level 1 during the toe breaker impact of Test 04029402.

6.1.10 Summary

The large scale solitary waves were used to investigate the relationship between breaker shape, the form of the load time history and entrapped air. Solitary waves were used rather than regular wave trains because they were less likely to contain entrained air and were naturally less 'noisy' because the water in the flume had at least 20 minutes to calm between impact events. In addition, the aeration results from the solitary waves were least affected by the problem of short circuiting because of the low still water level and time available for the water to drain out of the spar between impacts. It was found that entrapped air, the shape of the breaker and the load time history are intrinsically linked. The shape of the breaker determines the volume and location of the entrapped air and both of these affect the form of the load time history. The entrapped air is clearly associated with double peaks and oscillations in the pressure time histories. In these results the trough between the double pressure peaks is associated with low pressure or decompression of the entrapped air rather than compressed air as had previously been believed. Some oscillations were seen in the absence of entrapped air as in the case of the flip through impact. This appears to indicate monolithic vibration of the caisson.

In addition, these results show that very short rise times can occur in the absence of entrained air. Tests 04029406 and 04029405 both showed rise times of 0.5 ms which was the frequency at which the pressure transducers were sampled. It is therefore reasonable to suppose that the actual rise time may have been even shorter.

6.2 Aeration measurements in small scale waves

The highest loads produced by the range of solitary waves occurred with the air pocket impact. This breaker type was therefore selected for further investigation at small scale during tests 08089602 to 0808906. The new small scale aeration probes were used to measure aeration within the waves as they impacted on the wall. No waves were generated during test 08089601 which was conducted to obtain an unaerated reference voltage for equation 4.1. The electrodes of *Air* 1 and *Air* 2 were positioned 20 mm above the surface of the foreshore, *Air* 3 and *Air* 4 were 60 mm above them in the arrangement illustrated in Figures 6.16 and 5.7.

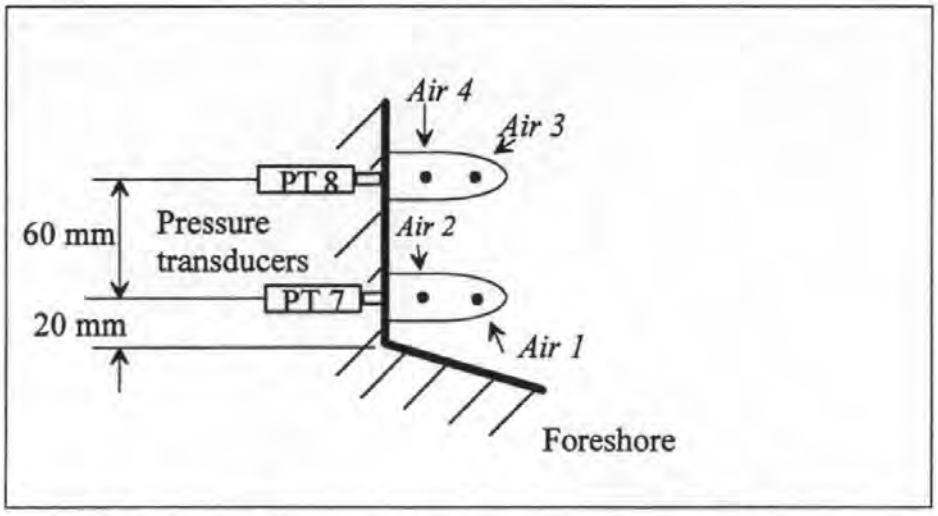

Figure 6.16. General arrangement of aeration electrodes and pressure transducers.

In this section some aeration time histories are shown to illustrate how the aeration characteristics varied from wave to wave. In order to reduce scatter due to the effects of individual bubbles (see section 4.9) the results are also shown in the form of ensemble averages. This provides general information about the aeration characteristics of each test.

The time reference chosen for the ensemble averages was the moment of maximum impact pressure (*TPmax*), as illustrated in Figure 6.17.

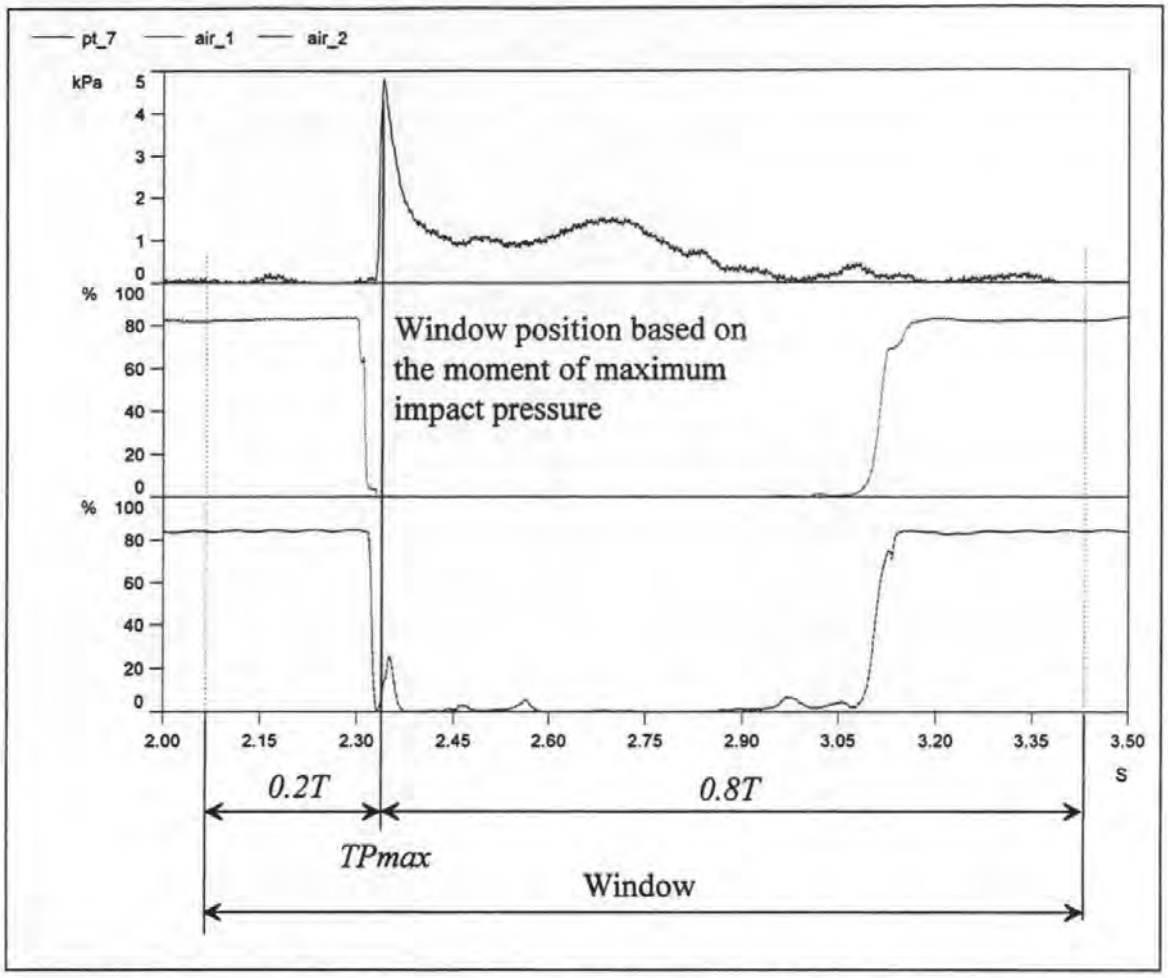

Figure 6.17. Section of the data recorded with PT 7, *Air* 1 and *Air* 2 during test 08089602, showing the location of the 'window' used during the ensemble averaging process.

During the ensemble averaging process *Air* 1 and *Air* 2 were associated with PT 7 because they were co-located. Similarly, *Air* 3 and *Air* 4 were associated with PT 8. For each impact event the record of PT 7 was processed to identify a value for *TPmax*, the start time of a window with a duration of one wave period *T* was then established at *TPmax* - 0.2*T*, as illustrated in Figure 6.17. The output of PT 7, *Air* 1 and *Air* 2 during this window of time were then stored. This process was repeated for all the events in the test (280 waves in the case of test 08089602) and for PT 8, *Air* 3 and *Air* 4. Any number of the segments from an individual instrument could then be combined to create an ensemble average aeration or pressure time history using the process described in section 4.9.

6.2.1 Test 08089602, H = 111 mm, T = 1.25 s.

The majority of the waves that were generated during test 08089602 developed the form shown in Figure 6.18.

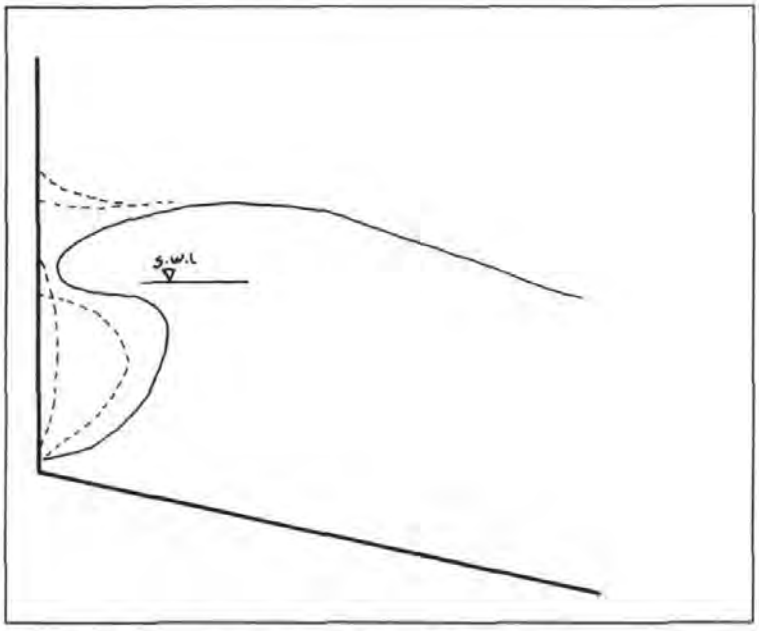

Figure 6.18. Breaker shape for test 08089602.

Air pockets were trapped against the wall and flattened during the impact and uprush. These pockets rapidly broke down into bubble clouds. Some of the aeration time histories recorded during this test are shown in Figures 6.19 to 6.22.

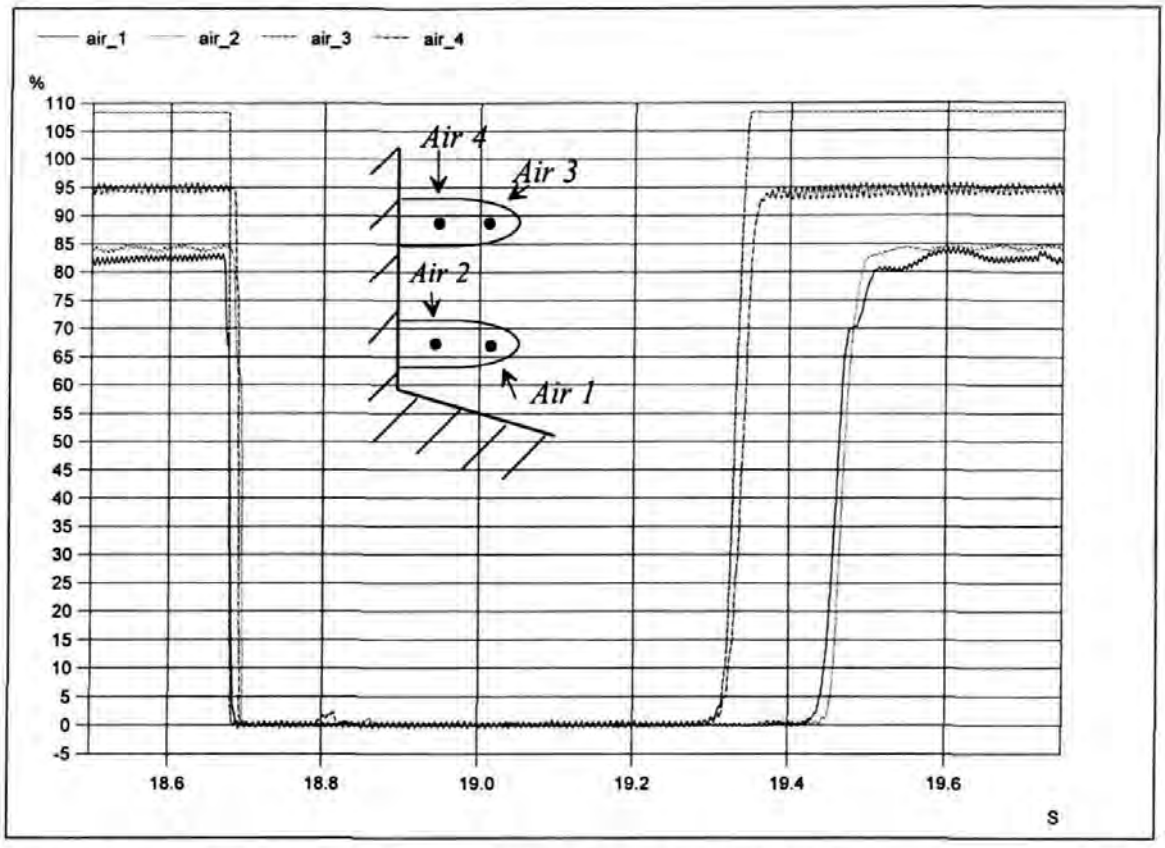

Figure 6.19. Aeration time histories recorded during test 08089602.

These show some of the variation in entrapped air and therefore breaker shape from wave to wave. Figure 6.19 is an example of an event in which aeration was almost entirely absent. Following the submersion of the instruments, which is indicated by the rapid drop from the initial high 'atmosphere' readings (< 80 %) all four records drop to zero aeration. There is no evidence from these readings of entrapped or entrained aeration.

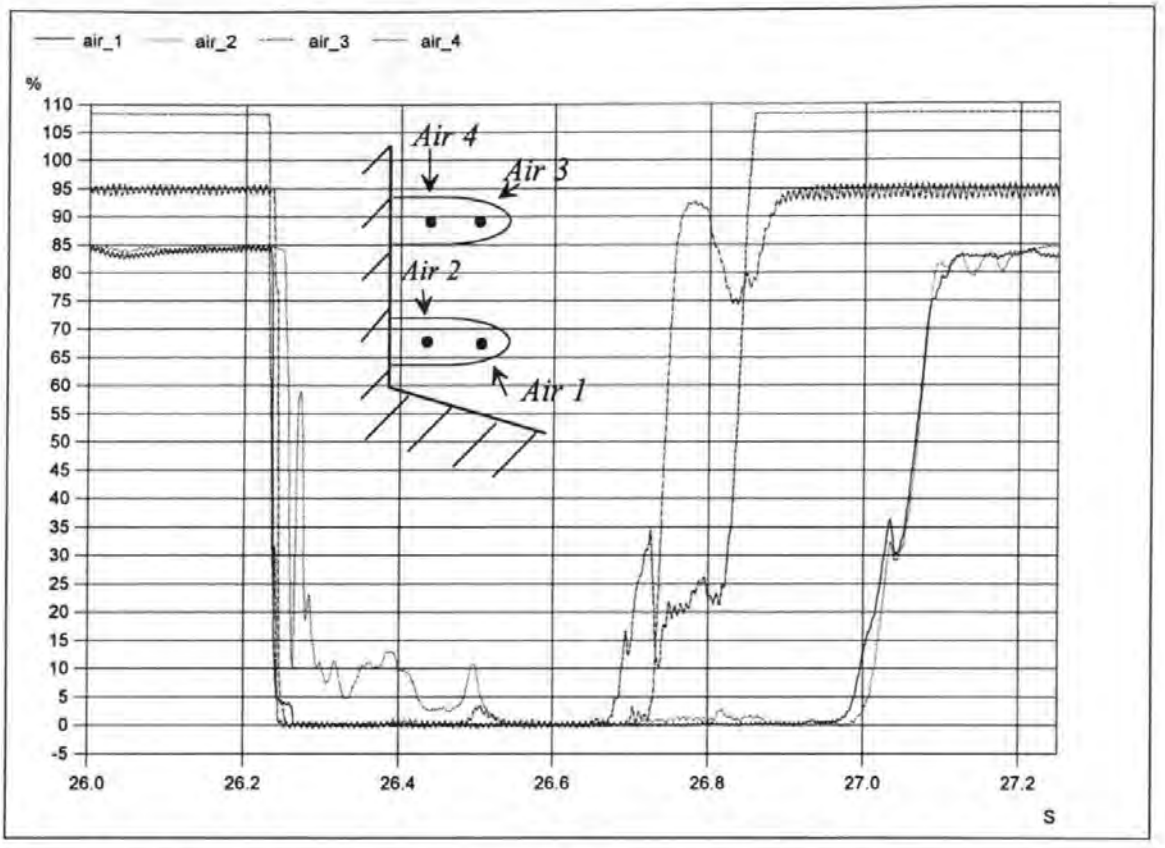

Figure 6.20. Aeration time histories recorded during test 08089602.

However, air was entrapped during the majority of the impacts in this test. The example shown in Figure 6.20 is more typical and shows entrapped air fairly low at the wall. Only *Air* 2 shows aeration, the output of the other instruments drop rapidly to zero, indicating that although entrapped air is present, entrained air is not.

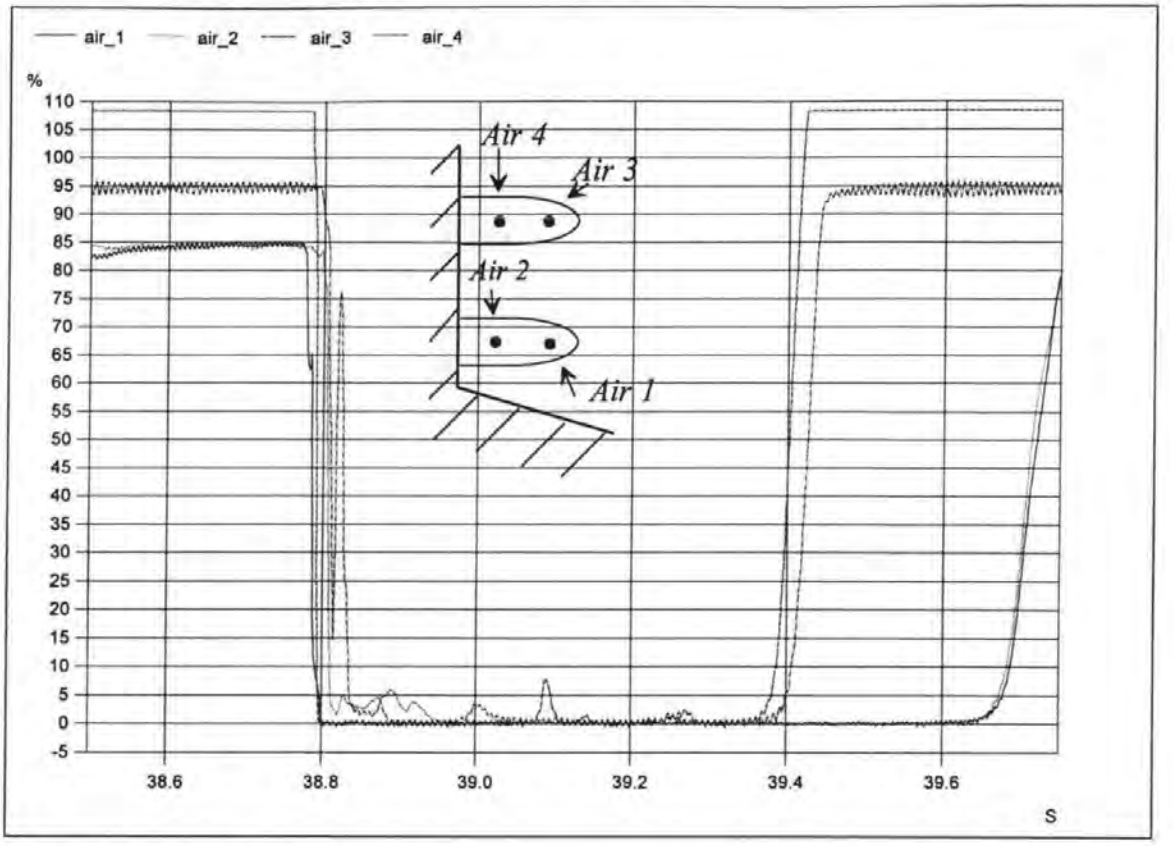

Figure 6.21. Aeration time histories recorded during test 08089602.

During some impacts the entrapped air was measured by *Air* 4 as well as *Air* 2, an example is shown in Figure 6.21, with an expanded view given in Figure 6.22. There is still no indication of entrained air in the output of *Air* 1 and *Air* 3.

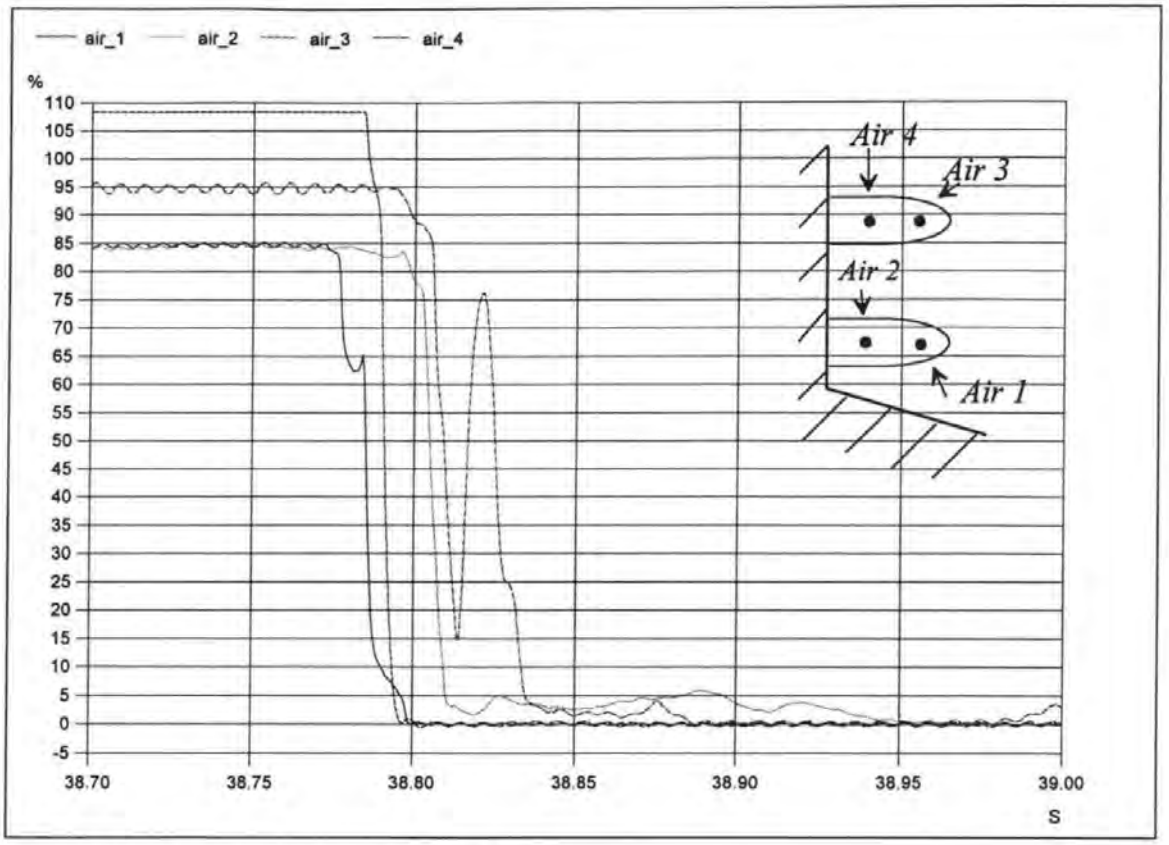

Figure 6.22. Expanded view of Figure 6.21.

These aeration characteristics can be seen when all the 280 impacts are combined into one ensemble average.

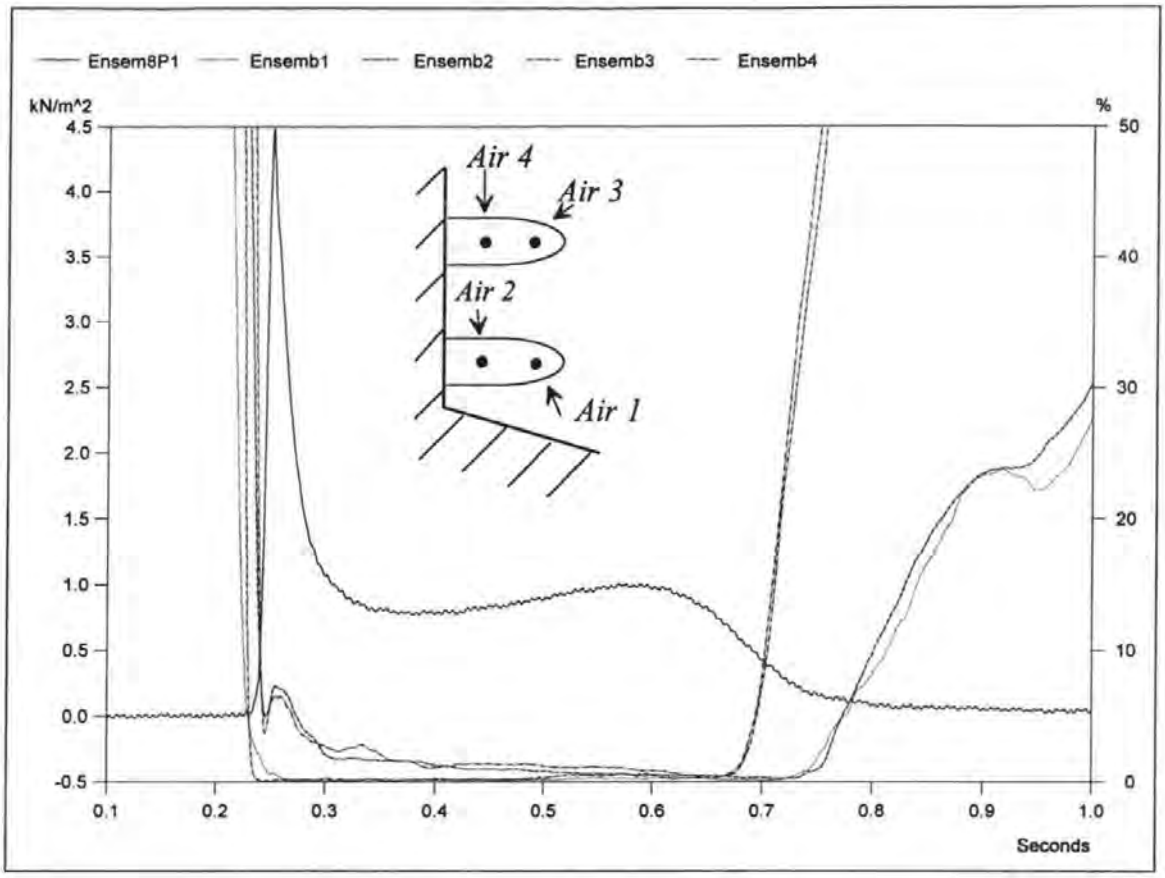

Figure 6.23. Ensemble averaged pressure and aeration time histories calculated from all 280 impact events recorded during Test 08089602.

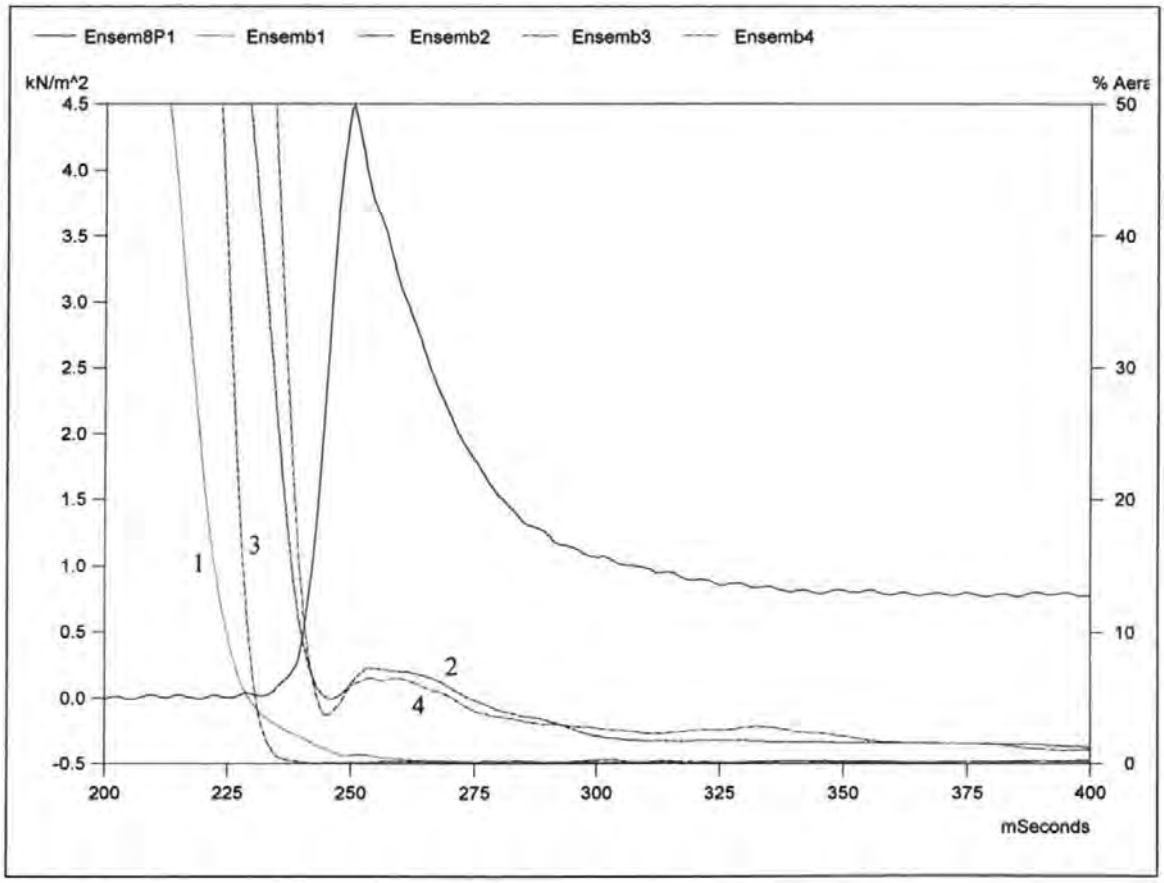

Figure 6.24. Expanded view of Figure 6.23.

In Figures 6.23 and 6.24 an ensemble averaged pressure time series has been included to give an indication of the time at which the peak pressure occurred. It can be seen that *Air* 1 and *Air* 3 became submerged before *Air* 2 and *Air* 4 because they projected further from the wall. *Air* 1 and *Air* 2 were submerged longer than *Air* 3 and *Air* 4 because they were at a lower elevation. At the start of submersion *Air* 1 and *Air* 3 show very low levels of aeration indicating, as was seen in Figures 6.19 to 6.22 that for most events there is minimal or zero ambient aeration entrained in the water. This is supported by the observation that at the end of the submersion time all four instruments record very low aeration levels. *Air* 2 and *Air* 4 both show higher aeration levels shortly after submersion caused by air trapped at the wall.

6.2.1 Test 08089603, H = 127 mm, T = 1.25 s.

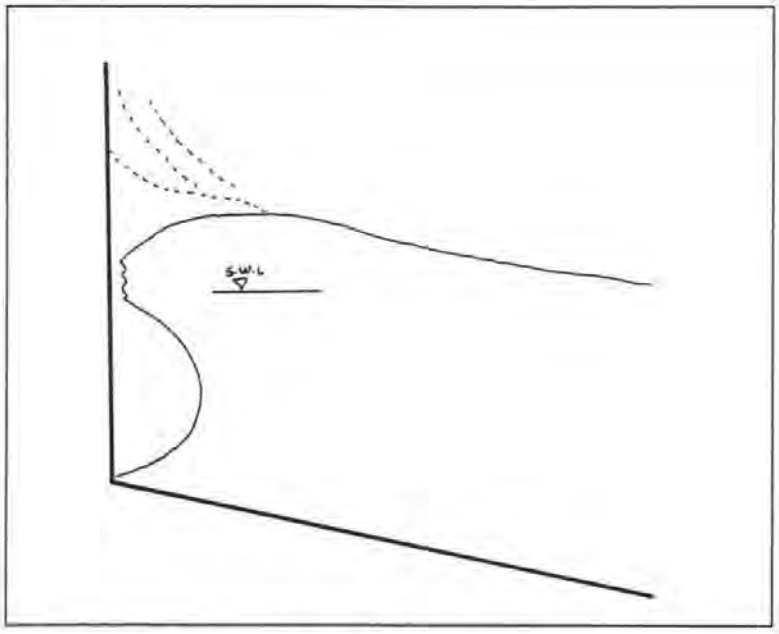

Figure 6.25. Breaker shape for test 08089603.

The characteristic breaker shape for test 08089603, which is shown in Figure 6.25, was similar to that of the previous test. The aeration records indicated that the air pocket was large. In Figure 6.26 *Air* 1, *Air* 2 and later *Air* 4 all show high levels of air during the early stages of the impact.

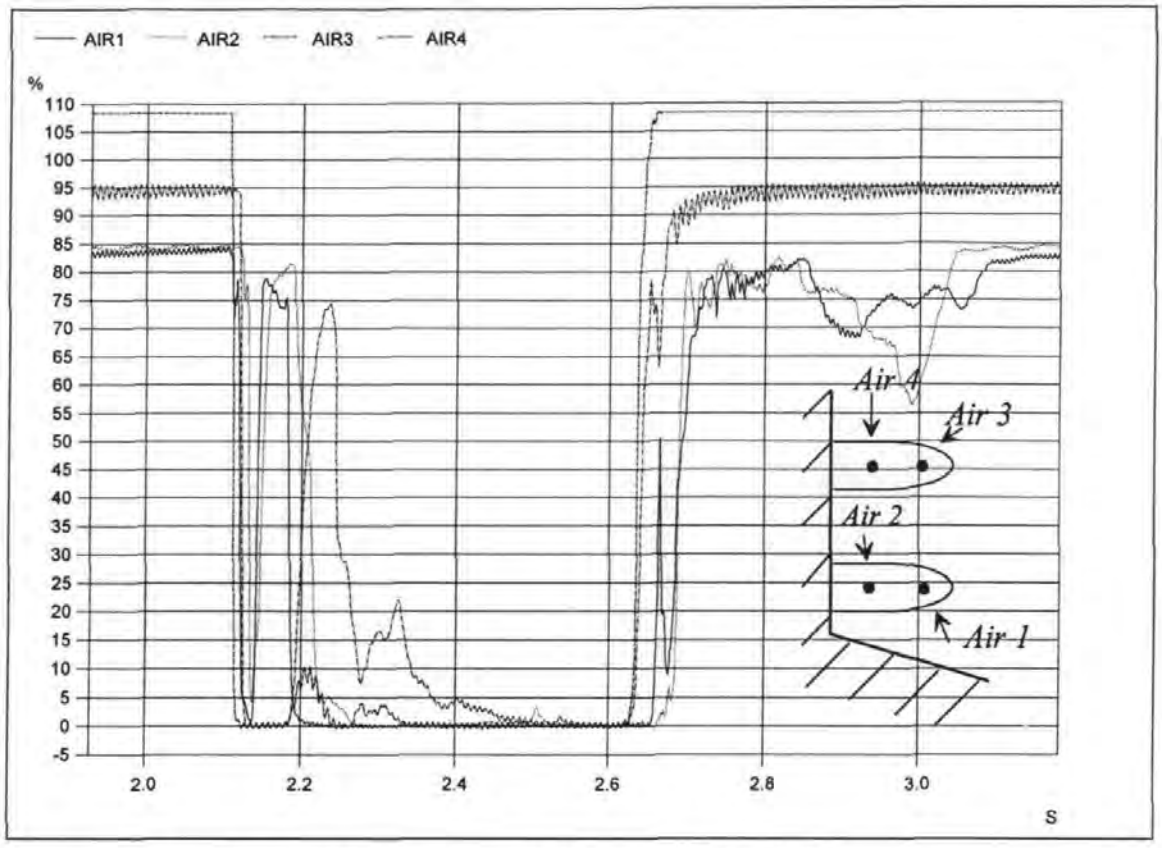

Figure 6.26. Aeration time histories recorded during test 08089603.

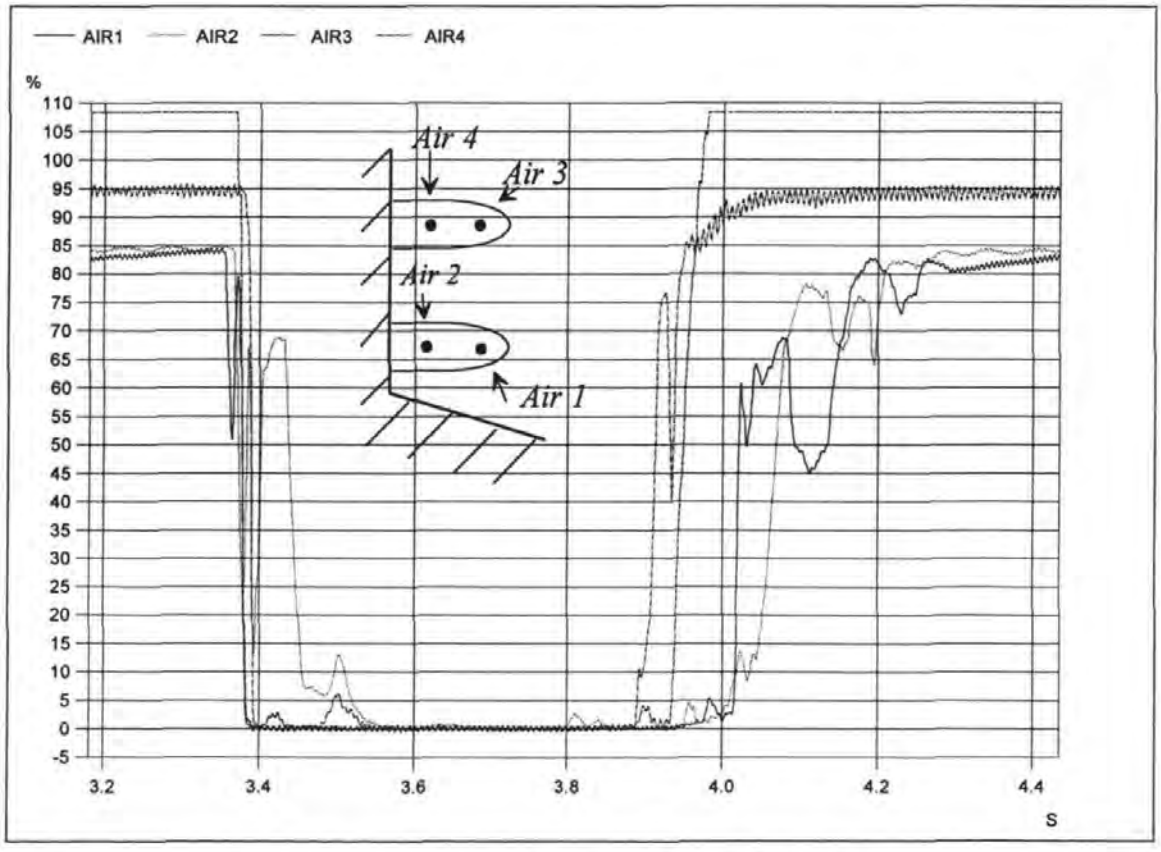

Figure 6.27. Aeration time histories recorded during test 08089603

Natural scatter in the size of the air pocket meant that during some impacts it was so small that it only affected the output of *Air* 2, as can be seen in Figure 6.27.

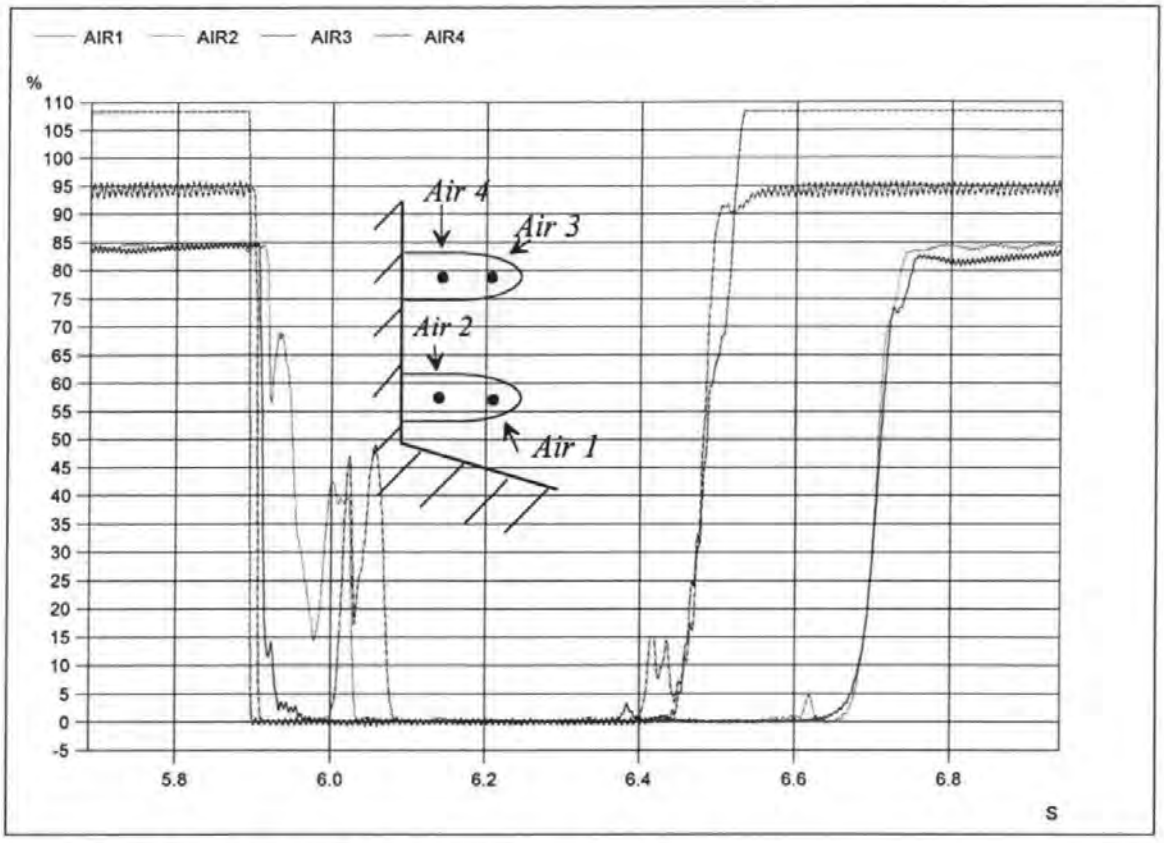

Figure 6.28. Aeration time histories recorded during test 08089603.

Figure 6.28 shows evidence of an air pocket that impinges on the field of influence of *Air* 2 and, as it rises up the wall, *Air* 4. *Air* 1 is also slightly affected but quickly returns to a zero reading. *Air* 3 and the early stages of *Air* 4 both clearly show that no entrained air is present.

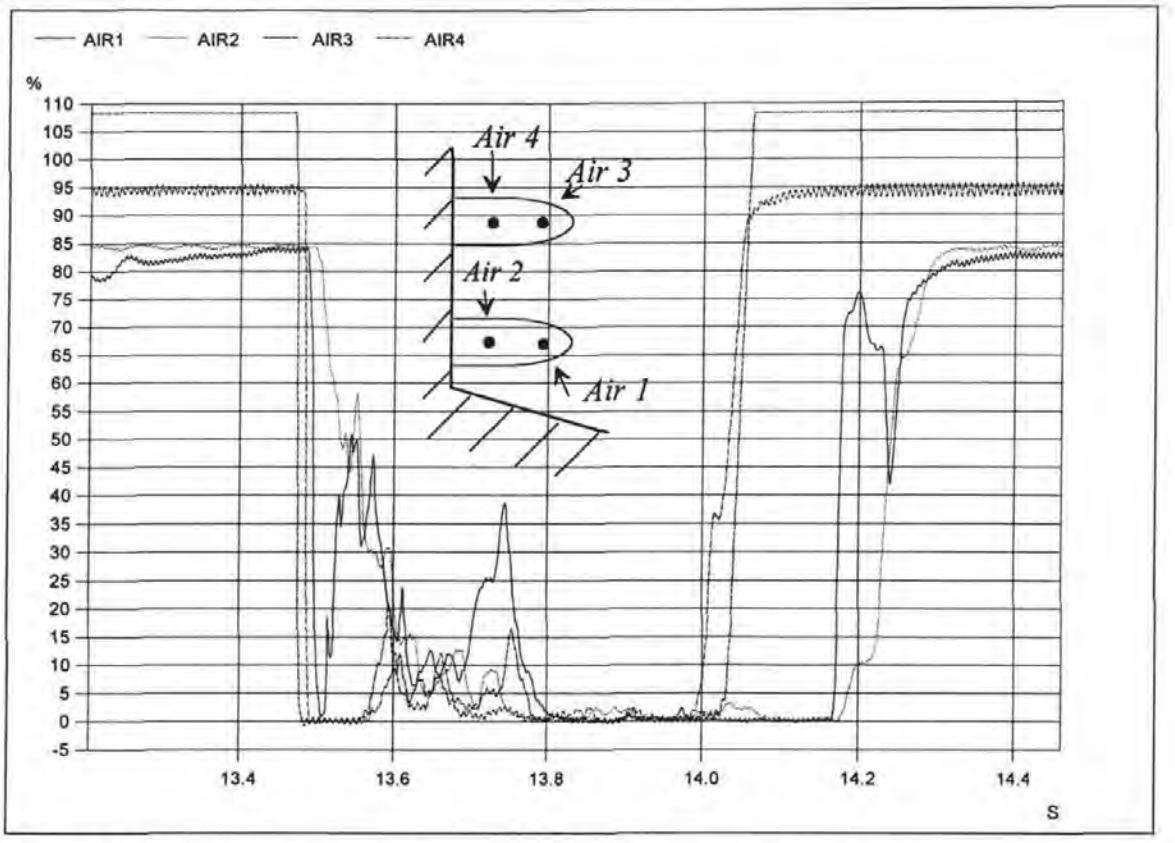

Figure 6.29. Aeration time histories recorded during test 08089603

Much more aeration is evident in Figure 6.29. During the early stages of the impact, at around 13.55 seconds, *Air* 1 and *Air* 2 register high levels of air whilst *Air* 3 and *Air* 4 indicate zero aeration. This implies a low wide air pocket with no entrained air above it. At approximately 13.6 seconds the air pocket appears to migrate up to influence *Air* 3 and *Air* 4.

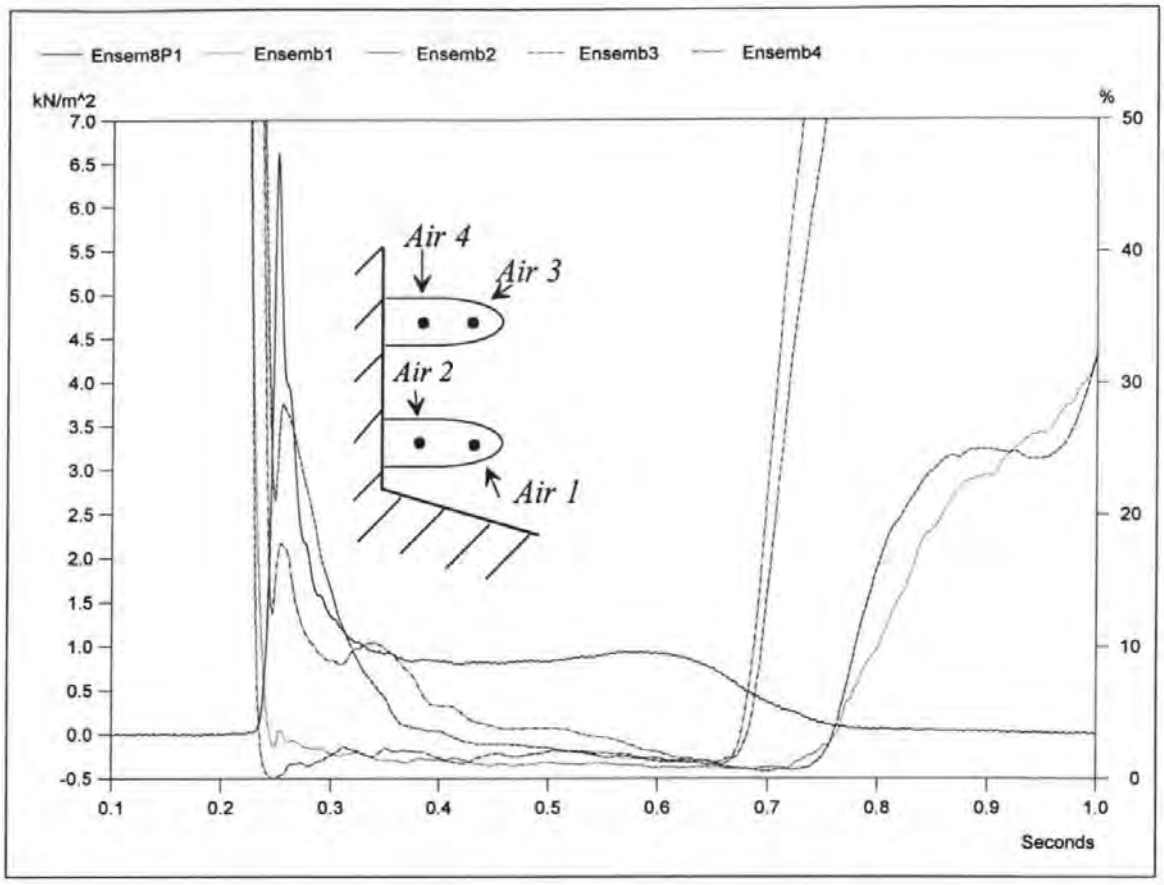

Figure 6.30. Ensemble averaged pressure and aeration time histories calculated from all 280 impact events recorded during Test 08089603.

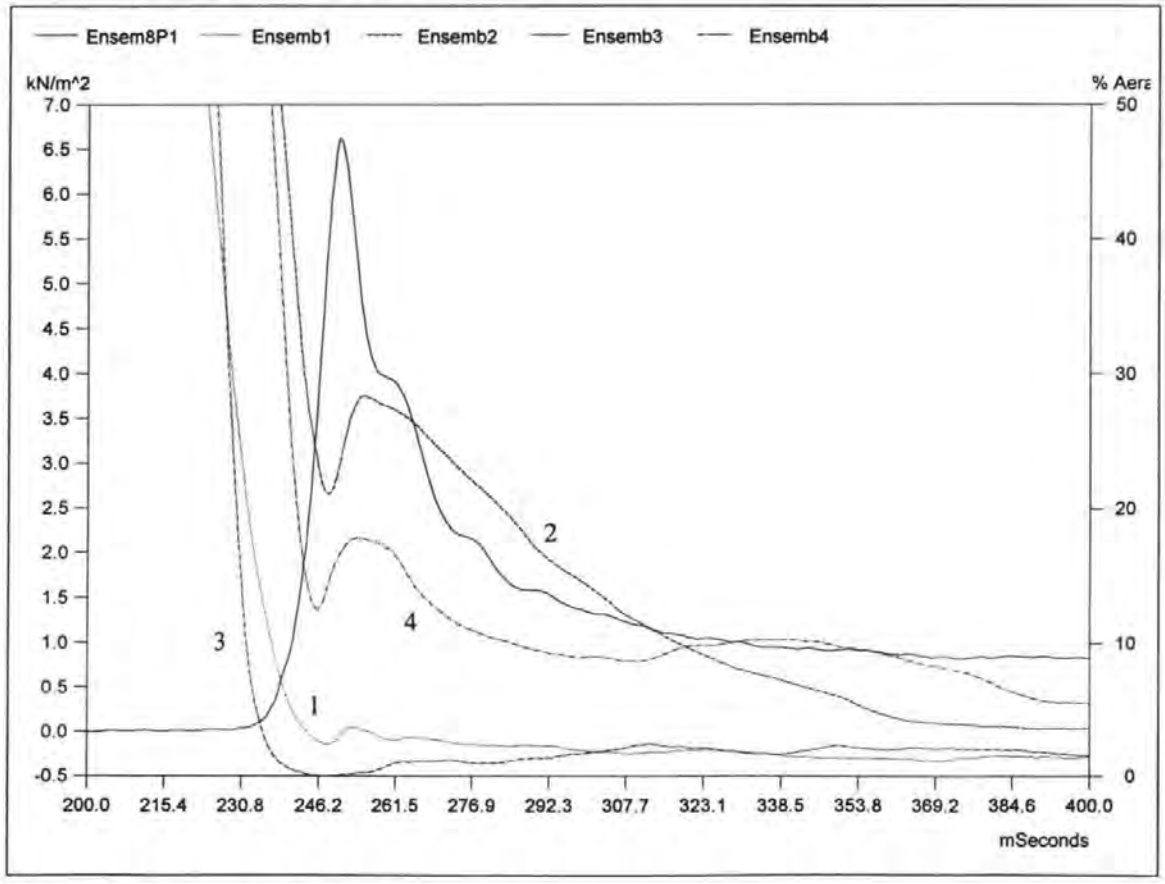

Figure 6.31. Expanded view of Figure 6.30.

The ensemble averaged results from test 08089603 (Figures 6.30 and 6.31) show high aeration levels at the wall recorded by *Air* 2 and *Air* 4 (Ensemb2 and Ensemb4). Aeration is also indicated by *Air* 1 and *Air* 3 (Ensemb1 and Ensemb3) although the results shown in Figures 6.26 to 6.29 suggest that this is entrapped rather than entrained, at least during the generation of the impulse.

6.2.3 Test 08089604, H = 97 mm, T = 1.25 s

The majority of the breakers that occurred during test 4 trapped a thin pocket of air at the wall. Occasionally the wave did not quite develop this shape and instead became more like a flip through event. Both these shapes are illustrated in Figure 6.32.

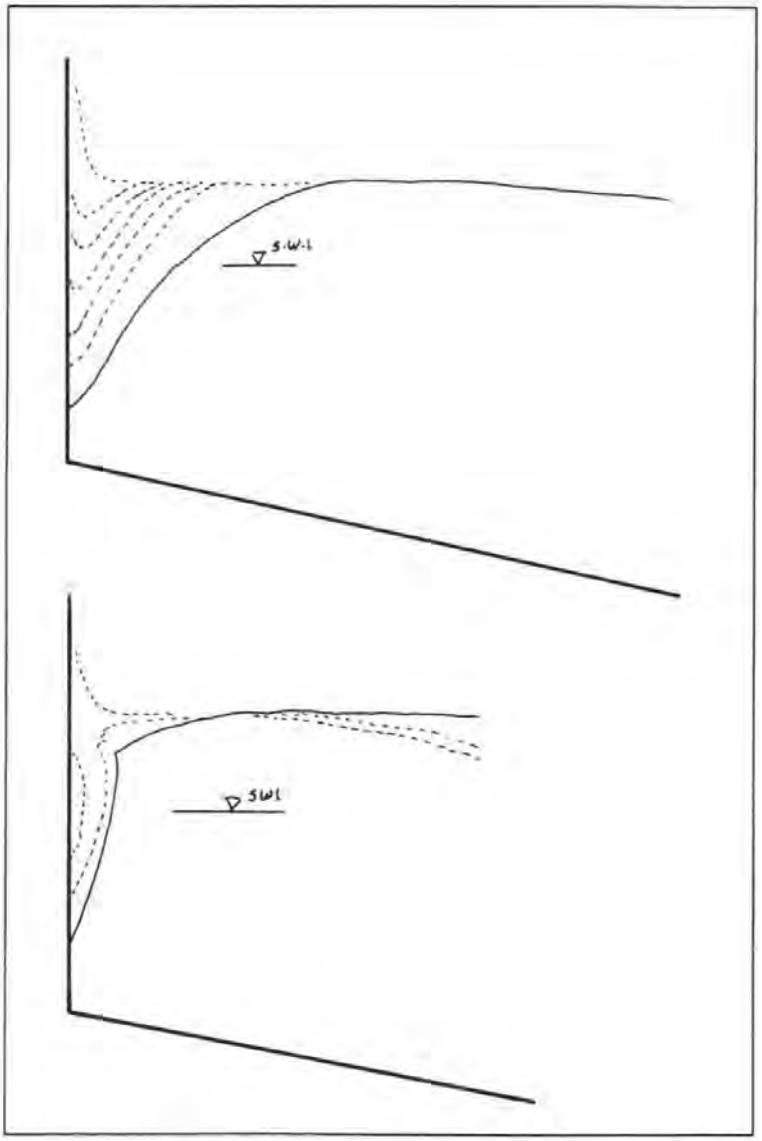

Figure 6.32. Two breaker shapes formed during test 08089604.

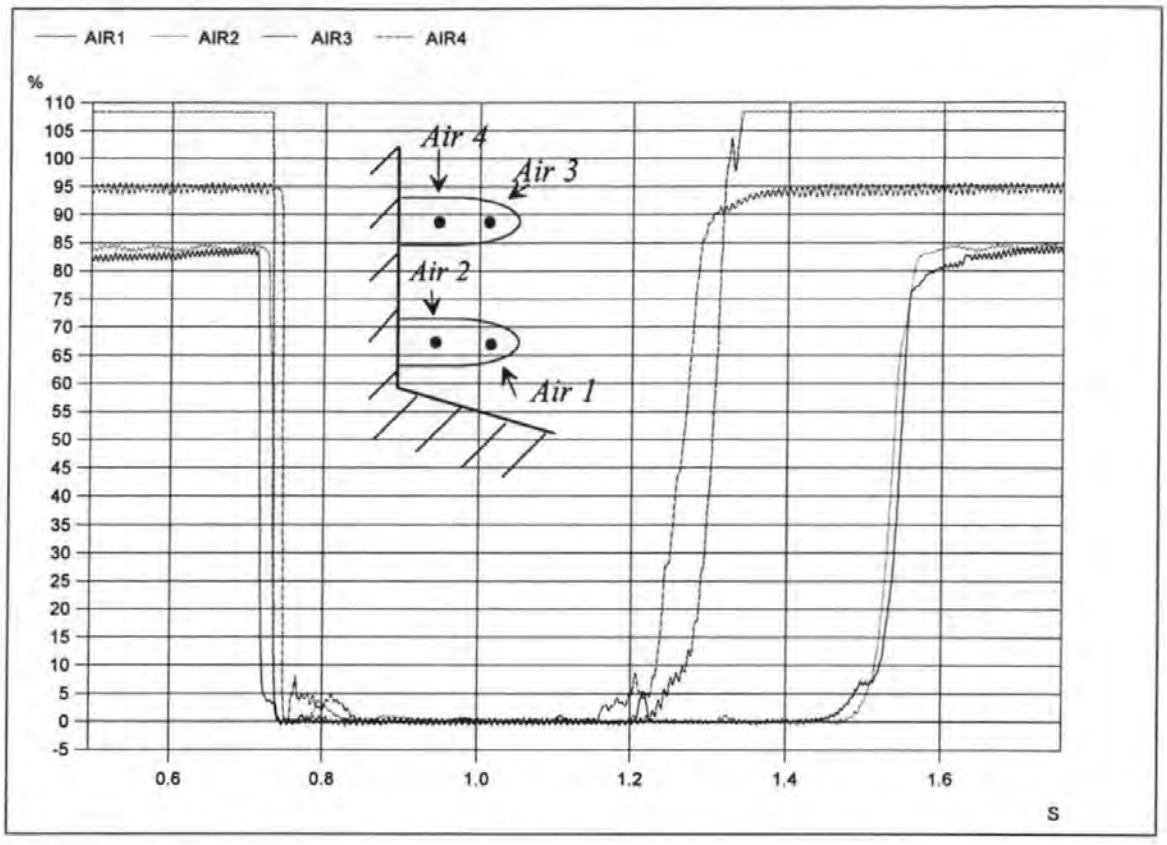

Figure 6.33. Aeration time histories recorded during test 08089604.

The near flip-through type trapped very little air. Figure 6.33 shows an example in which *Air* 4 and, to a lesser extent *Air* 2 show small amounts of air.

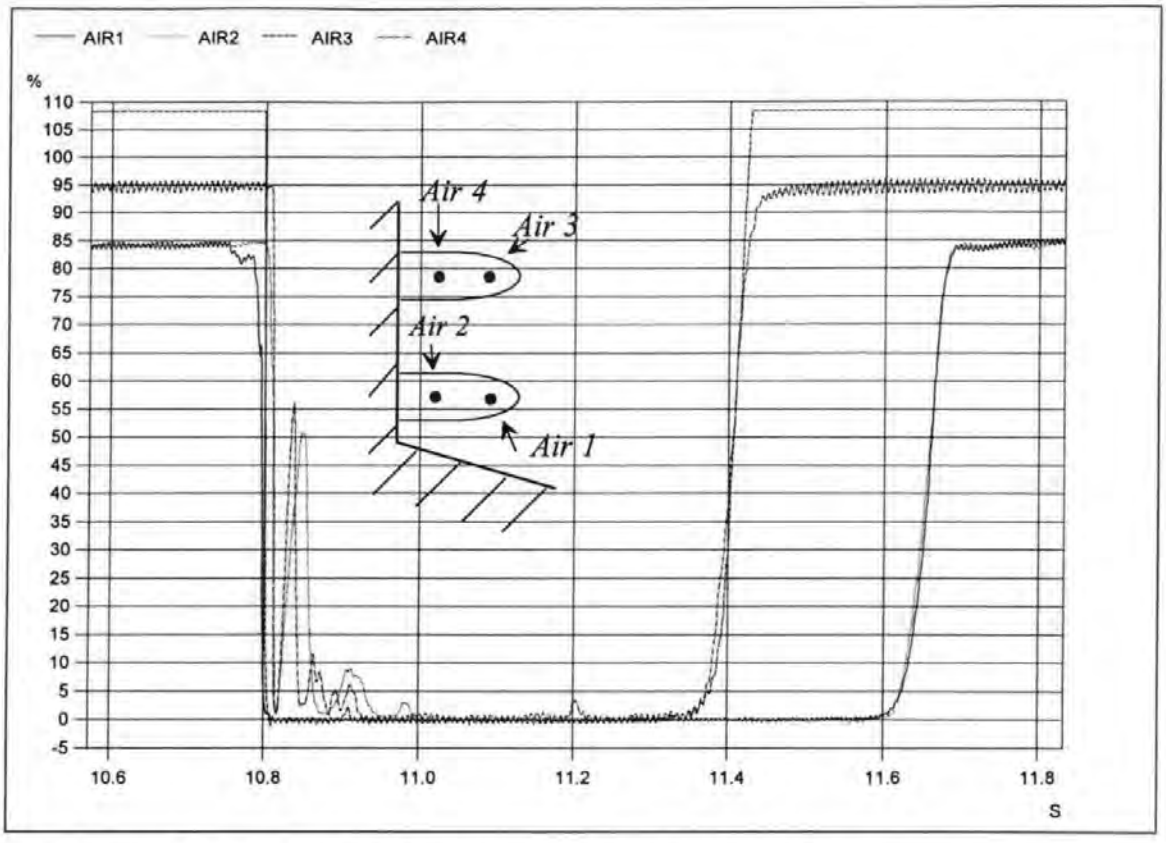

Figure 6.34. Aeration time histories recorded during test 08089604.

The thin air pocket impacts showed characteristic transient peaks in aeration that were recorded by both *Air* 2 and *Air* 4, as can be seen in Figures 6.34 and 6.35. As with the other impacts, no entrained air is evident during the impulsive region of the impact.

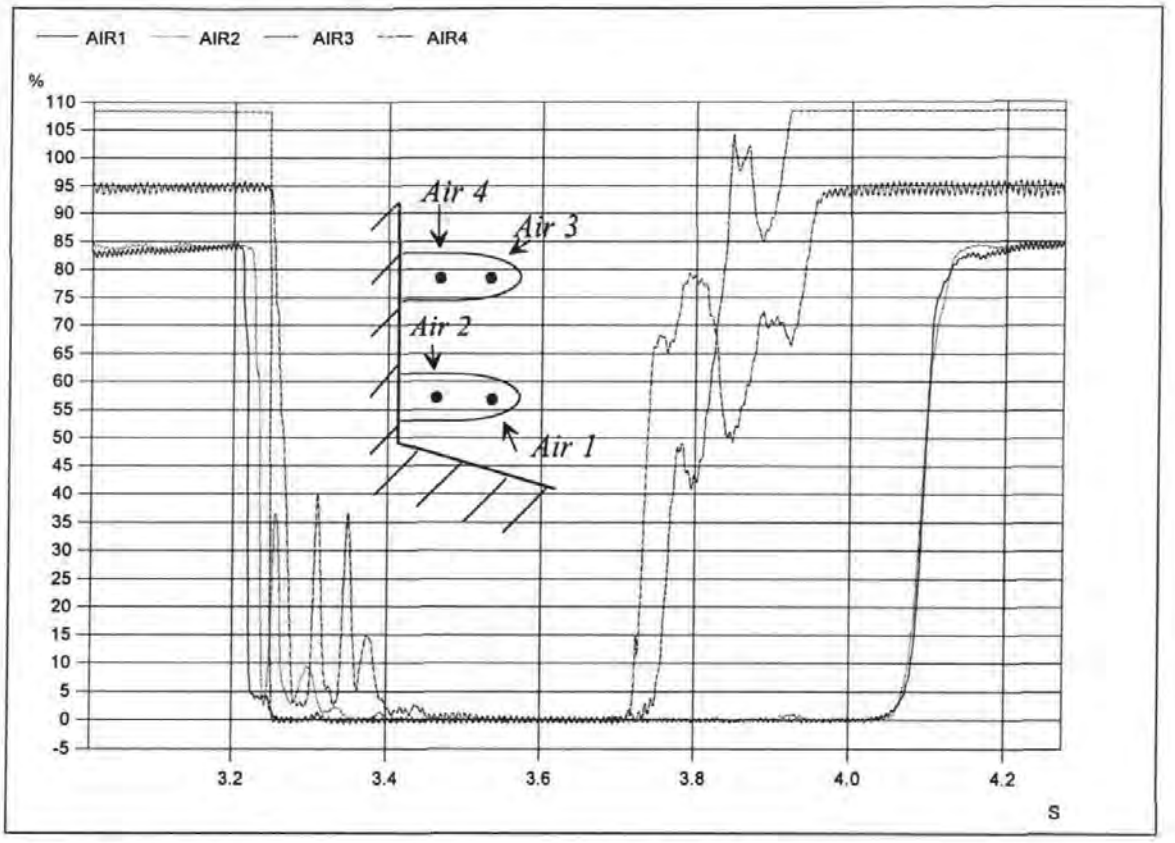

Figure 6.35. Aeration time histories recorded during test 08089604.

These characteristics are also shown by the ensemble averaged aeration time histories in Figures 6.36 and 6.37. Small amounts of air trapped at the wall are shown by *Air* 2 and *Air* 4 (Ensemb2 and Ensemb4), whilst no entrained air is recorded by *Air* 1 and *Air* 3 (Ensemb1 and Ensemb3).

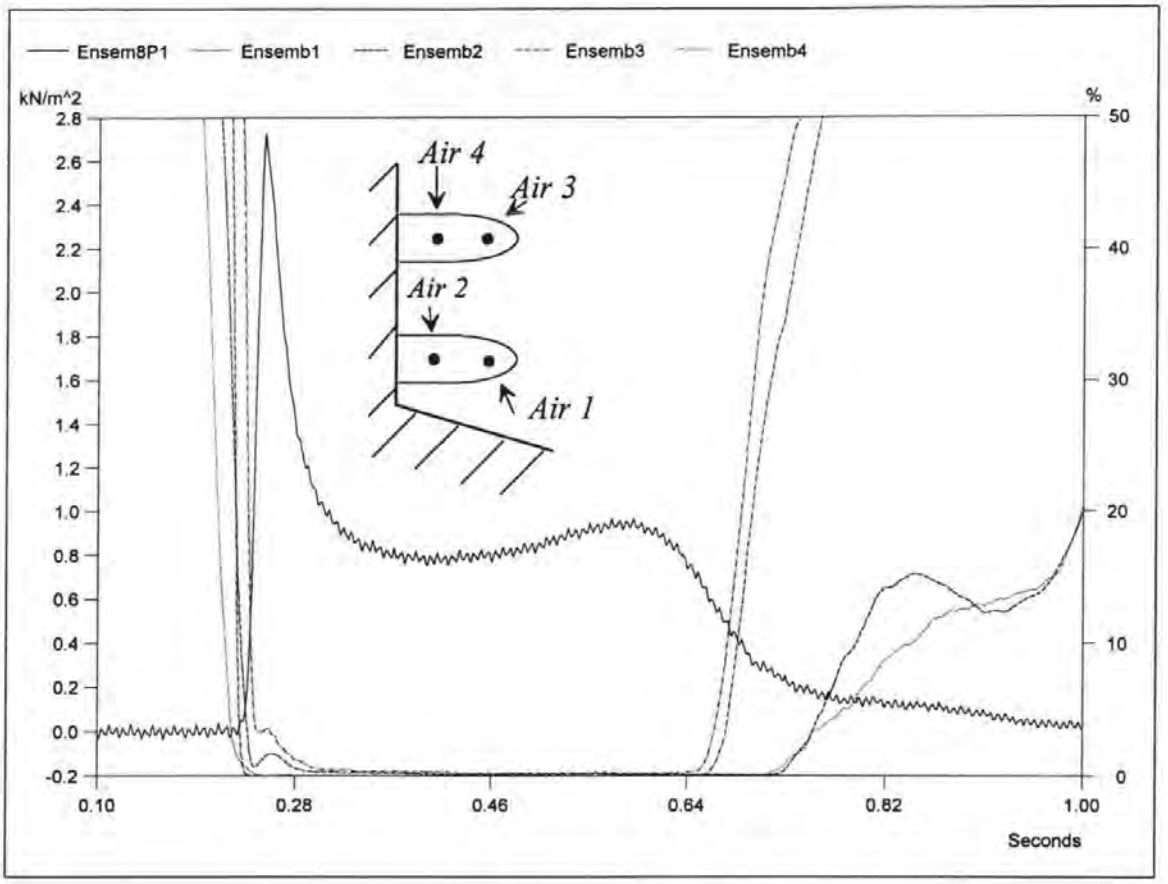

Figure 6.36. Ensemble averaged pressure and aeration time histories calculated from all 280 impact events recorded during Test 08089604.

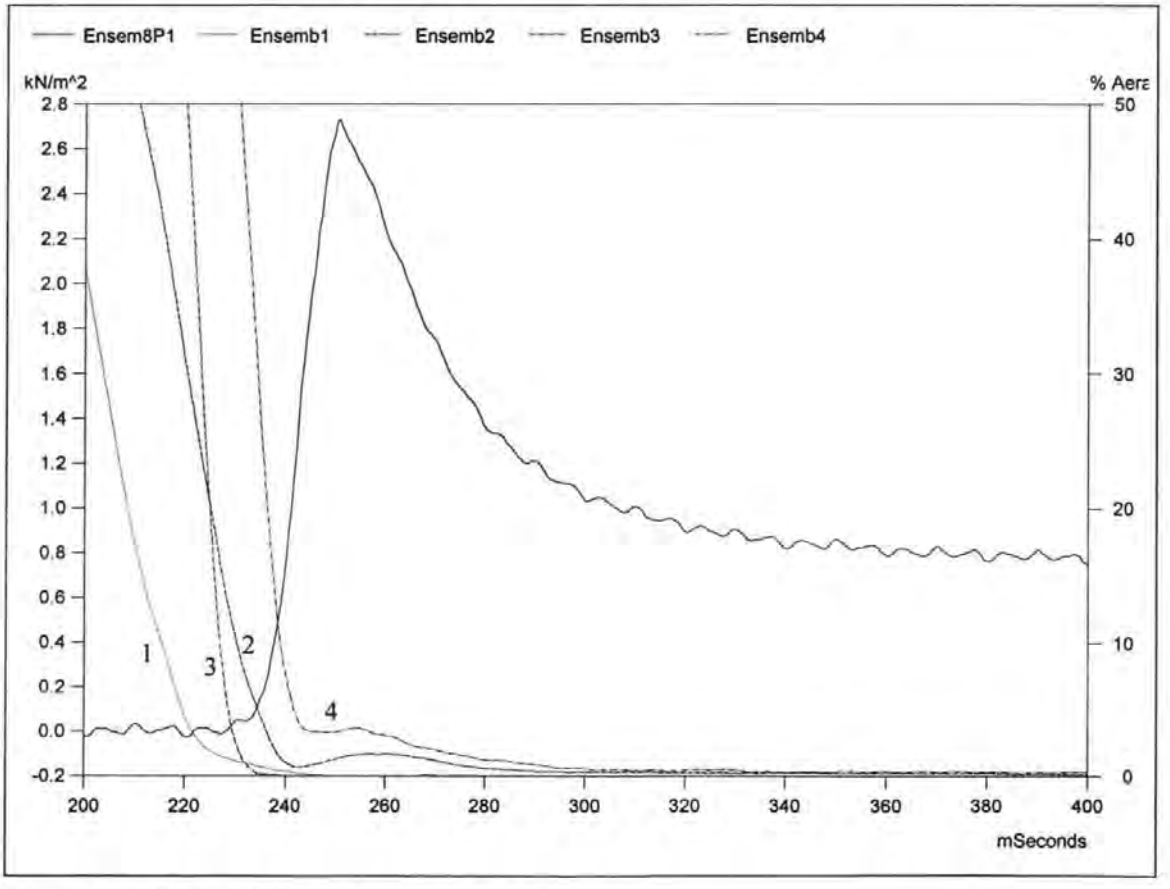

Figure 6.37. Expanded view of Figure 6.36.

6.2.4 Test 08089605, H = 112 mm, T = 1.33 s

The breaker shape produced during test 08089605 is shown in Figure 6.38.

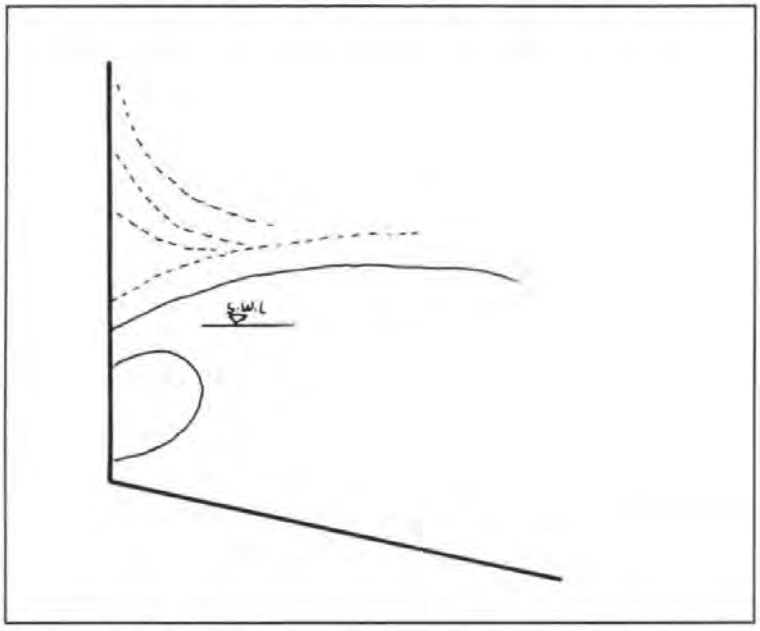

Figure 6.38. Breaker shape formed during test 08089605.

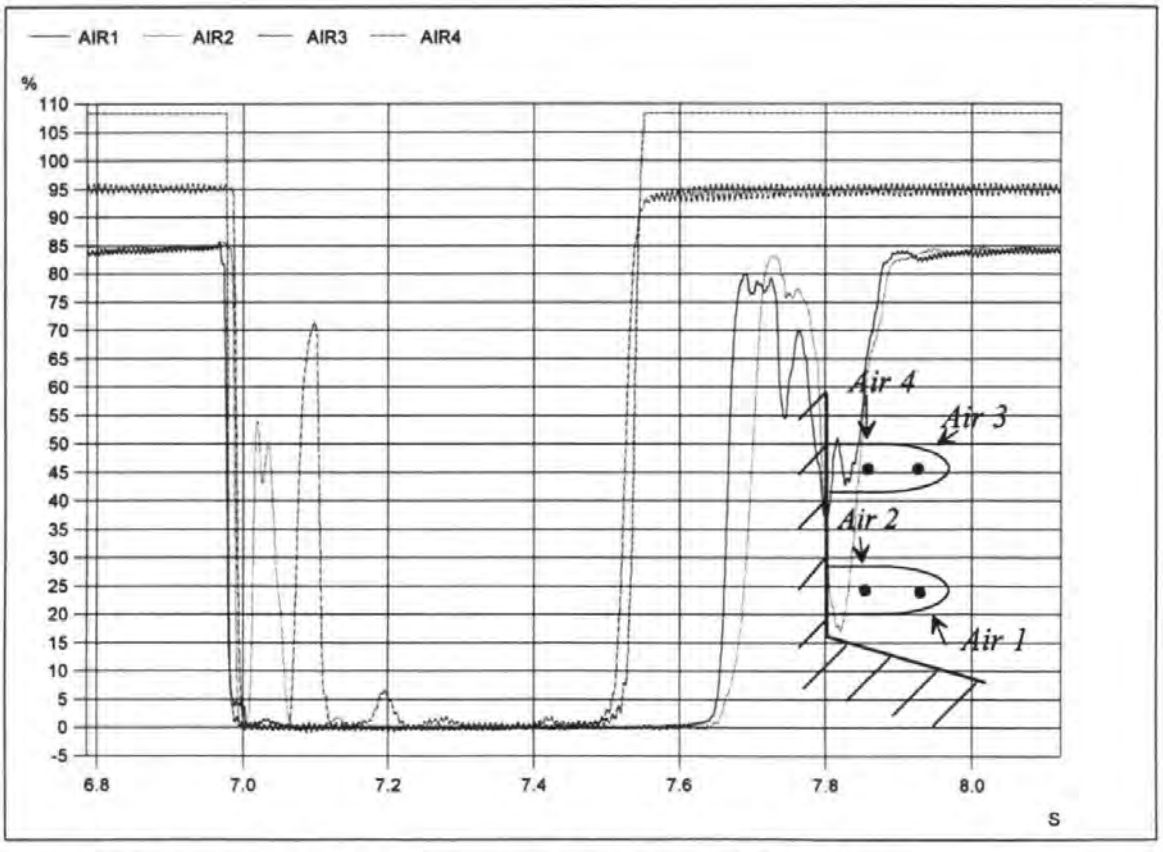

Figure 6.39. Aeration time histories recorded during test 08089605.

The location and movement of air indicated by the results in Figure 6.39 correspond well to the low air pocket breaker drawn in Figure 6.38. The crest seals the air pocket at the toe causing *Air* 2 to record a peak. The pocket then migrated up the wall causing *Air* 2 to fall back to zero and *Air* 4 to peak. During some impacts the pocket was pulled away from the wall rather than rising up it. An example of this can be seen in Figure 6.40. In this case the initial peak in *Air* 2 can be seen without any response from *Air* 4.

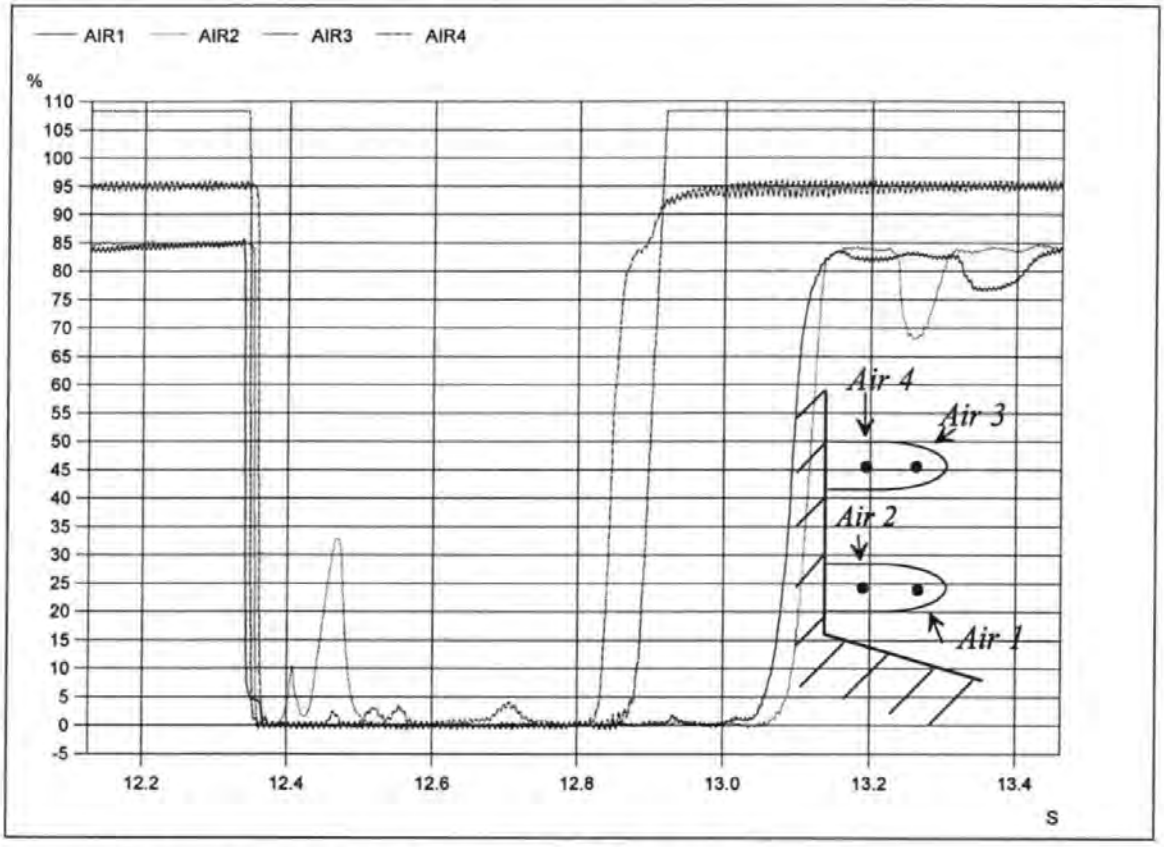

Figure 6.40. Aeration time histories recorded during test 08089605.

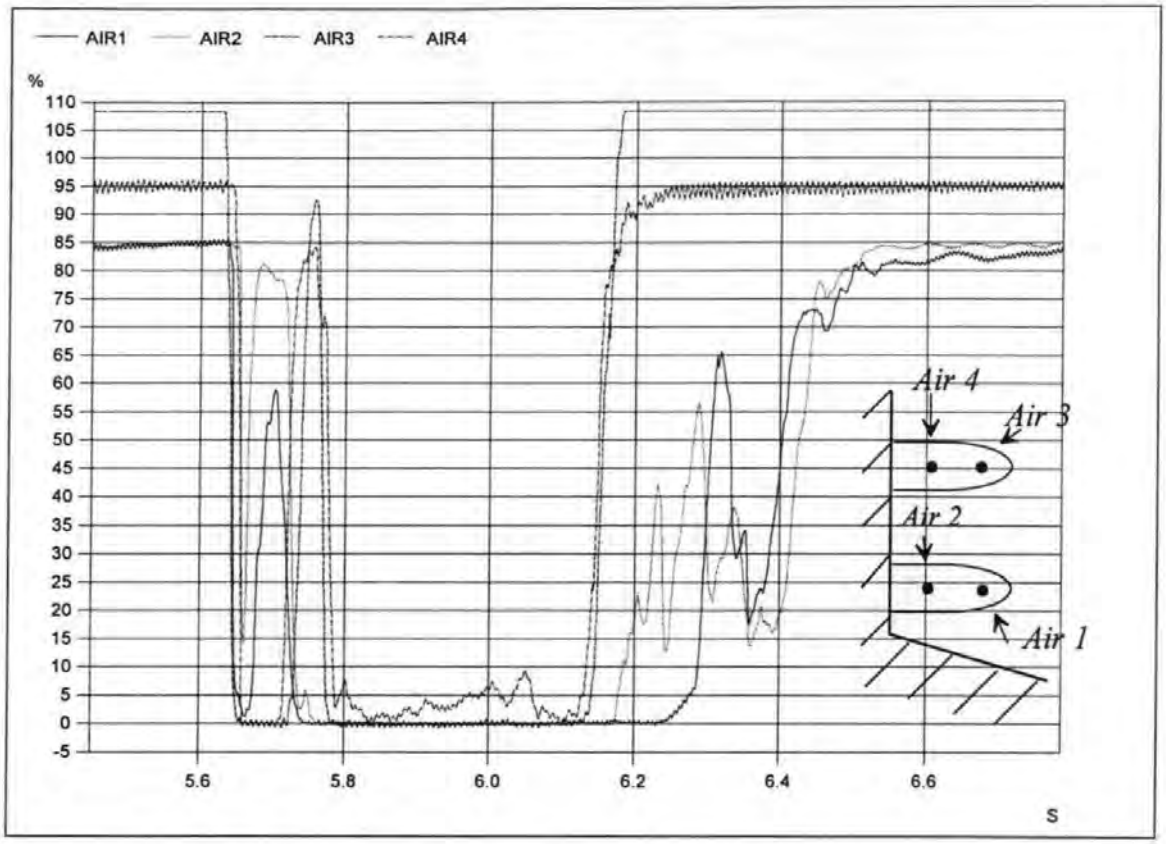

Figure 6.41. Aeration time histories recorded during test 08089605.

During some events the air pocket was relatively wide and extended from the wall to the outer electrodes. In Figure 6.41 *Air* 1 and *Air* 2 both respond initially, whilst *Air* 3 and *Air* 4, which are within the crest, show no entrained air. *Air* 1 and *Air* 2 drop to zero aeration as the pocket rises and begins to affect *Air* 3 and *Air* 4.

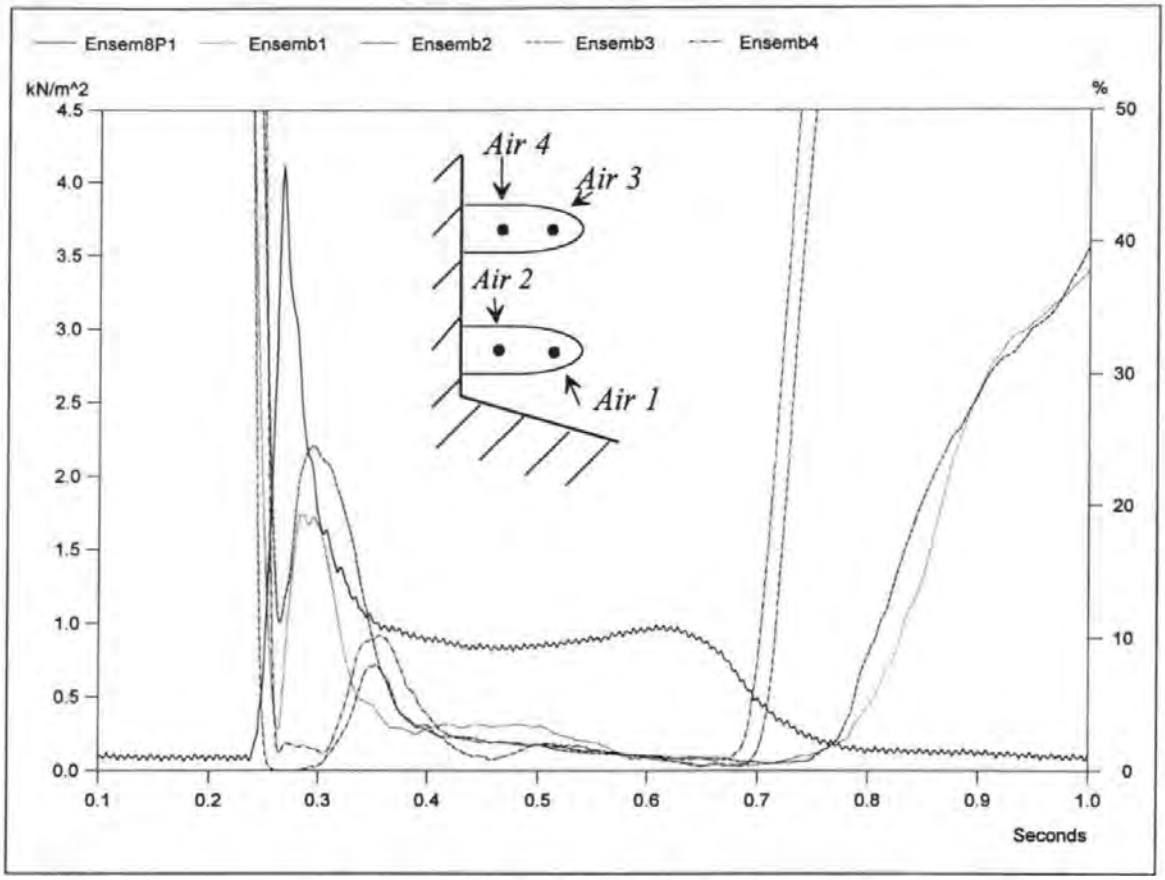

Figure 6.42. Ensemble averaged pressure and aeration time histories calculated from all 263 impact events recorded during Test 08089605.

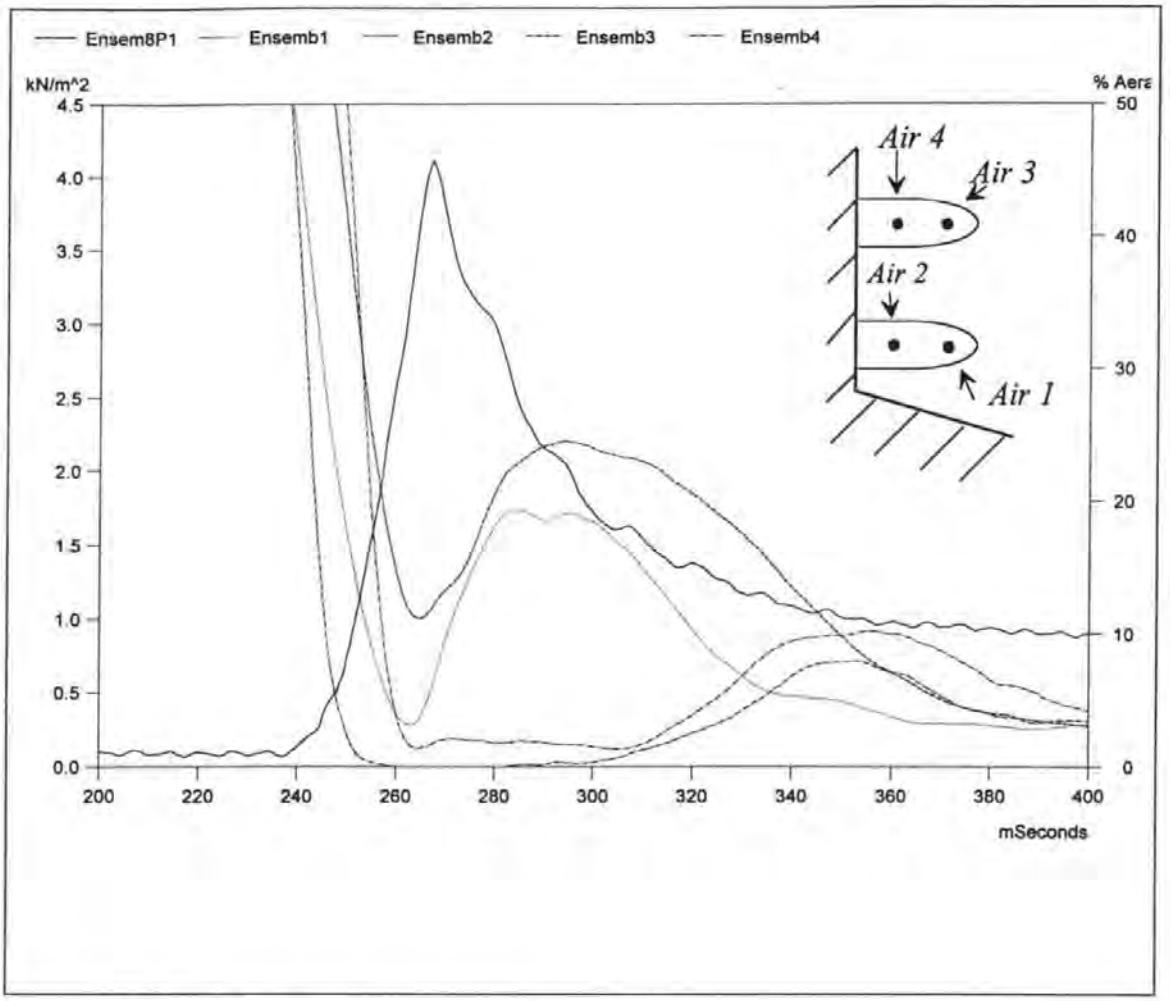

Figure 6.43. Expanded view of Figure 6.42.

The same overall pattern emerges in the ensemble averaged aeration time histories, peaks in *Air* 1 and *Air* 4 followed by later smaller peaks in *Air* 3 and *Air* 4 (Figures 6.42 and 6.43). It should be noted that, as with the other tests, the aeration indicated by *Air* 3 and *Air* 4 during the time interval of from 0.25 to 0.3 seconds probably indicate a slight influence of entrapped air rather than entrained air.

6.2.5 Test 08089606, H = 81 mm, T = 1.33 s

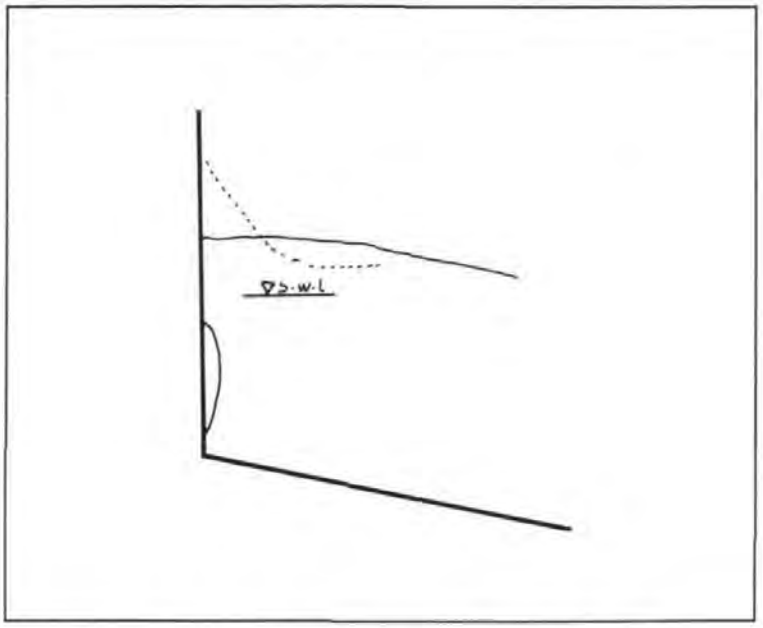

Figure 6.44. Breaker shape from test 08089606.

Figure 6.44 shows a drawing of the breaker shape that was formed during test 08089606. The impacts were similar to those which occurred in the other tests in that little evidence was found of entrained air, as can be seen in the records of *Air* 1 and *Air* 3 in Figures 6.45 to 6.47.

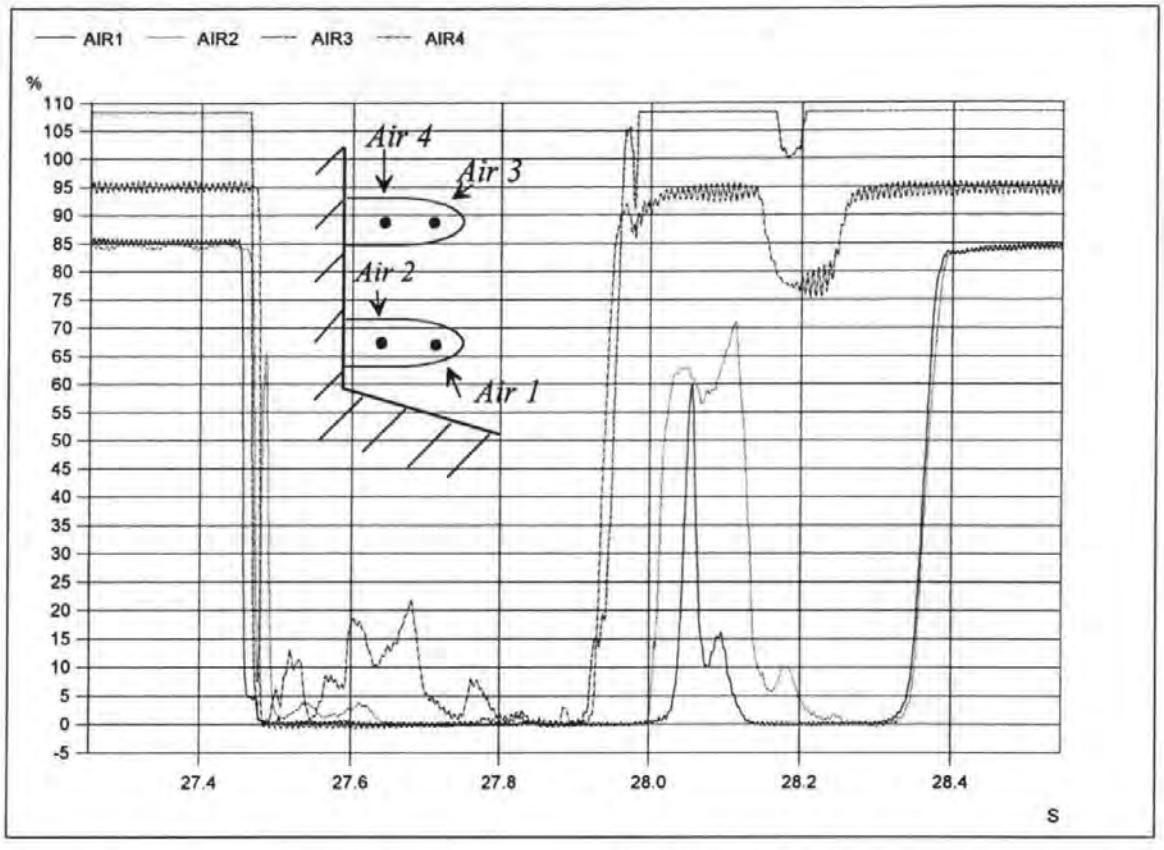

Figure 6.45. Aeration time histories recorded during test 08089606.

The quantity of entrapped air is relatively small, as can be seen in the records of *Air* 2 and *Air* 4. Occasionally, as in the example shown in Figure 6.45, this entrapped air was retained at the wall for a long period of time.

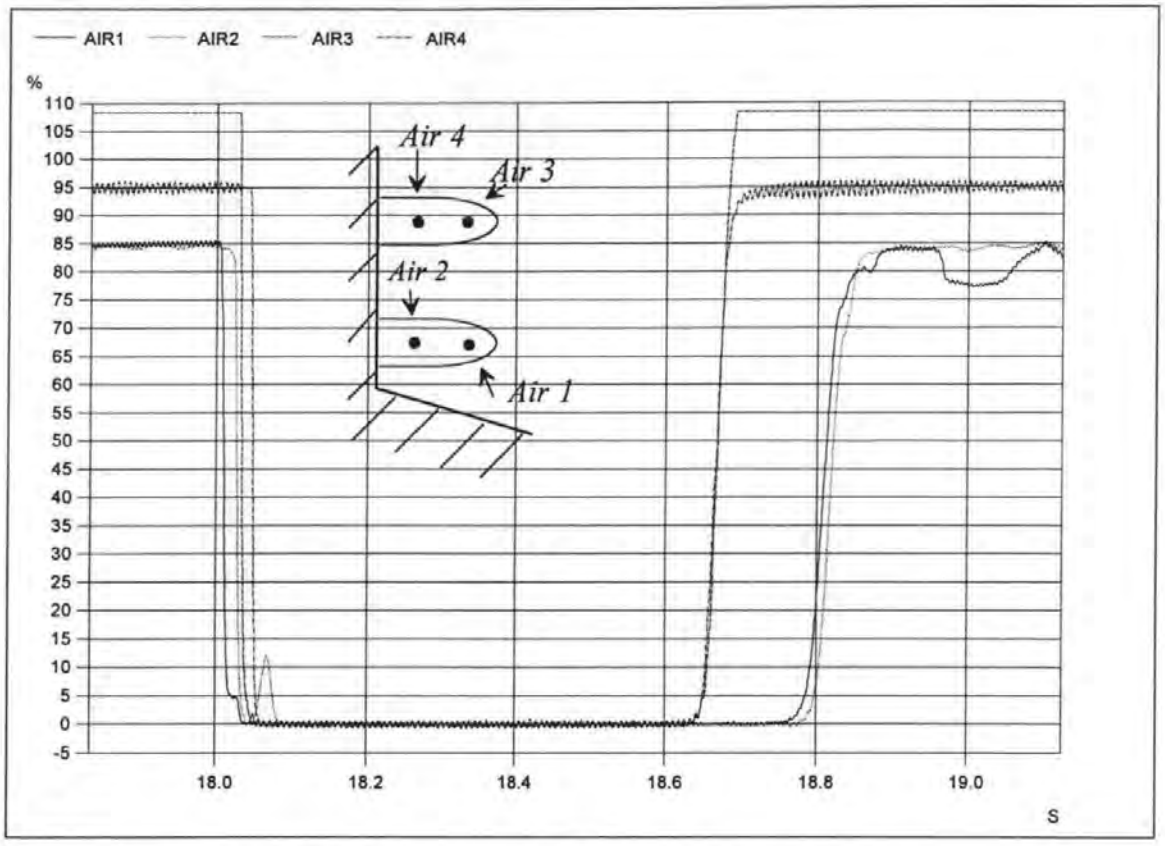

Figure 6.46. Aeration time histories recorded during test 08089606.

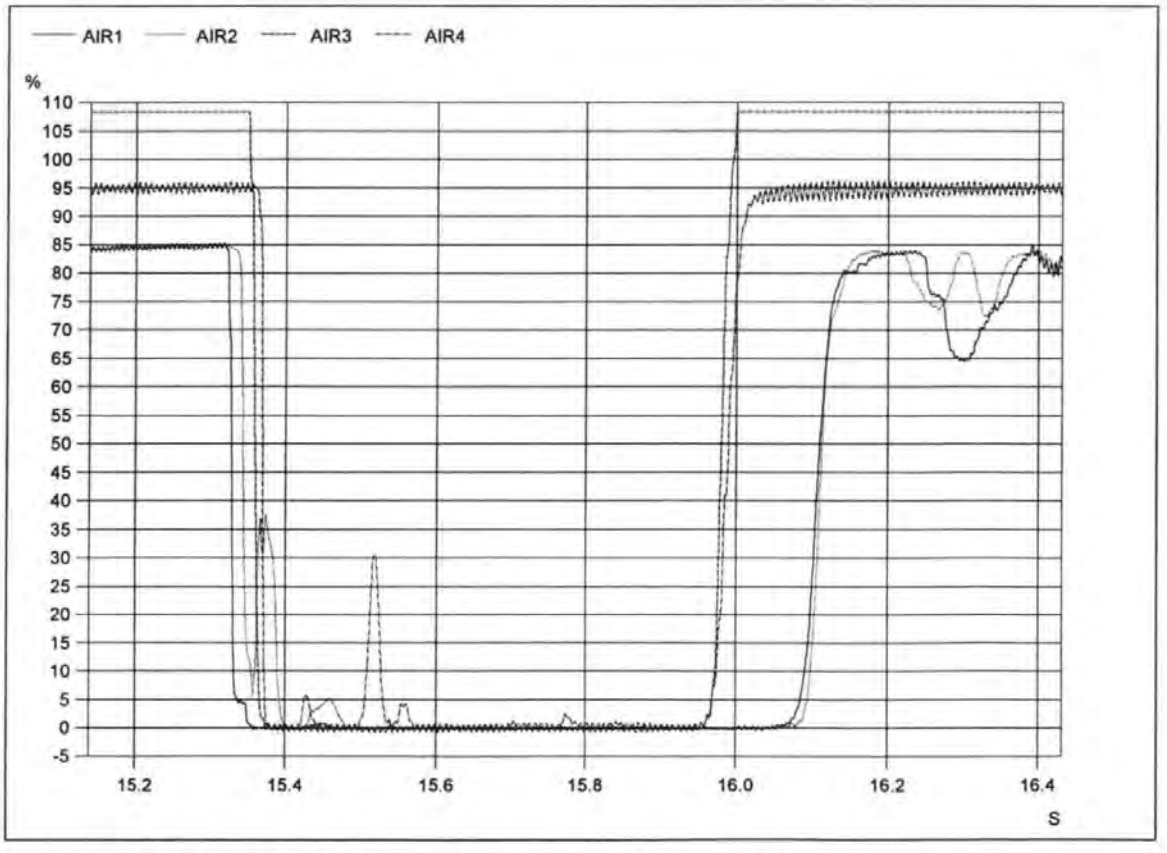

Figure 6.47. Aeration time histories recorded during test 08089606.

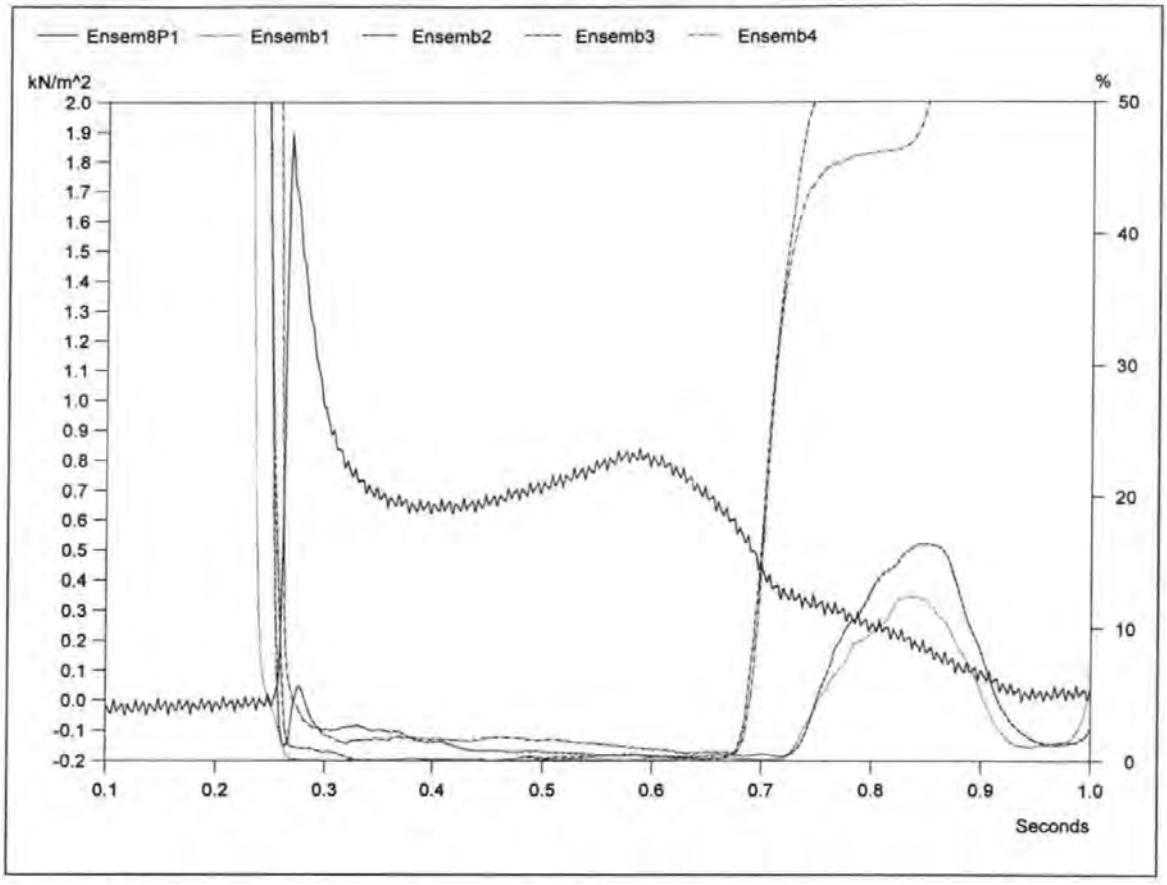

Figure 6.48: Ensemble averaged pressure and aeration time histories calculated from all 280 impact events recorded during Test 08089606.

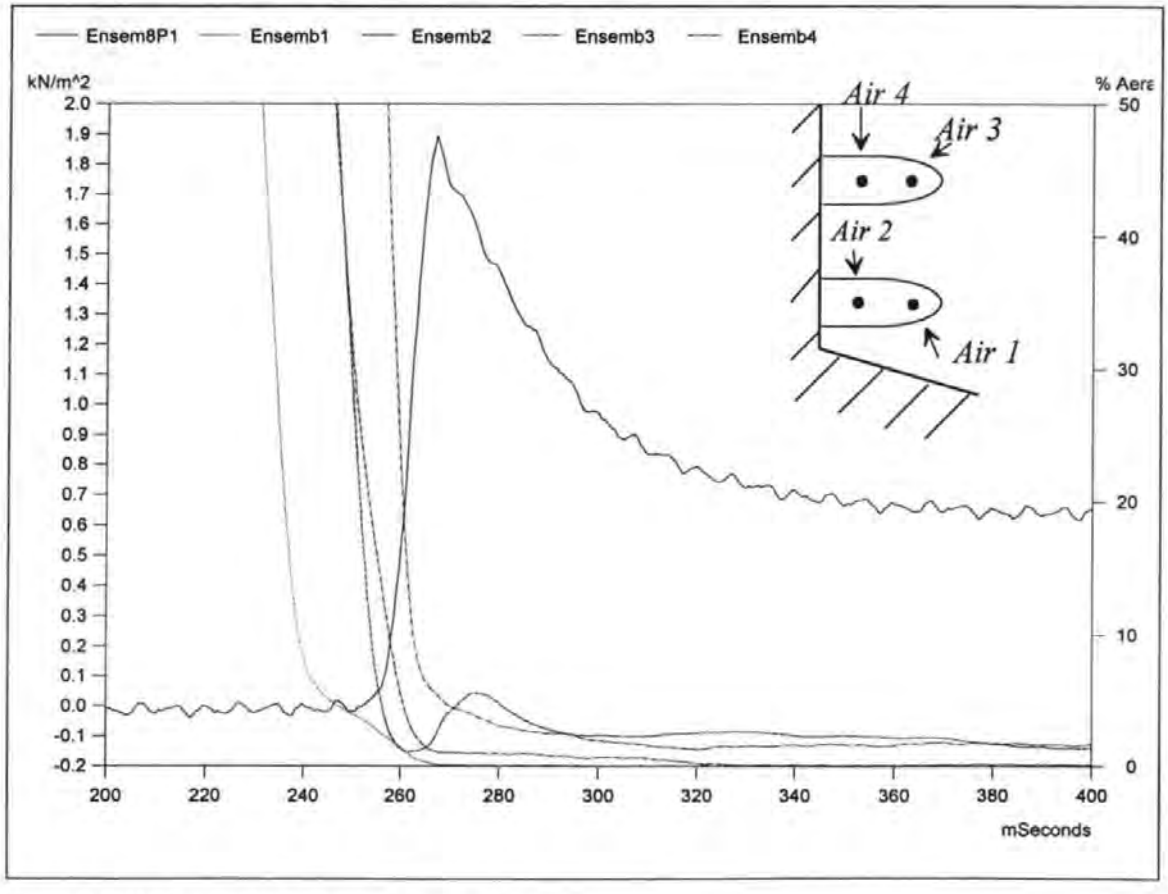

Figure 6.49. Expanded view of Figure 6.48.

It can be seen from the aeration measurements shown in this section that although aeration is sealed between the wave and the wall during impact, little or no air is present in the form of a cloud of ambient bubbles. Consequently, these tests could be used to study the relationship between entrapped air and impact load, but not the importance of entrained air.

6.2.6 The influence of entrapped air on pressure maxima

In order to investigate whether any relationship existed between entrapped air and the magnitude of the maximum impact pressure, the impacts occurring in each test were ranked by P_{max} and divided into five groups of at least 50. One ensemble average was then calculated per gauge for each of these five groups. This provided five aeration time histories per gauge for each test, with Ensemble 1 representing the 50 events which generated the highest values of P_{max}, and Ensemble 5 representing the time histories of the 50 impact events with the lowest values of P_{max}.

Since each ensemble average aeration time history represented at least 50 original aeration time histories, the level of accuracy could be estimated to be +/- 1.4 % (see section 4.9). Details of the results obtained in this way from test 08089602 can be seen in Figures 6.50, 6.51, 6.53 and 6.54.

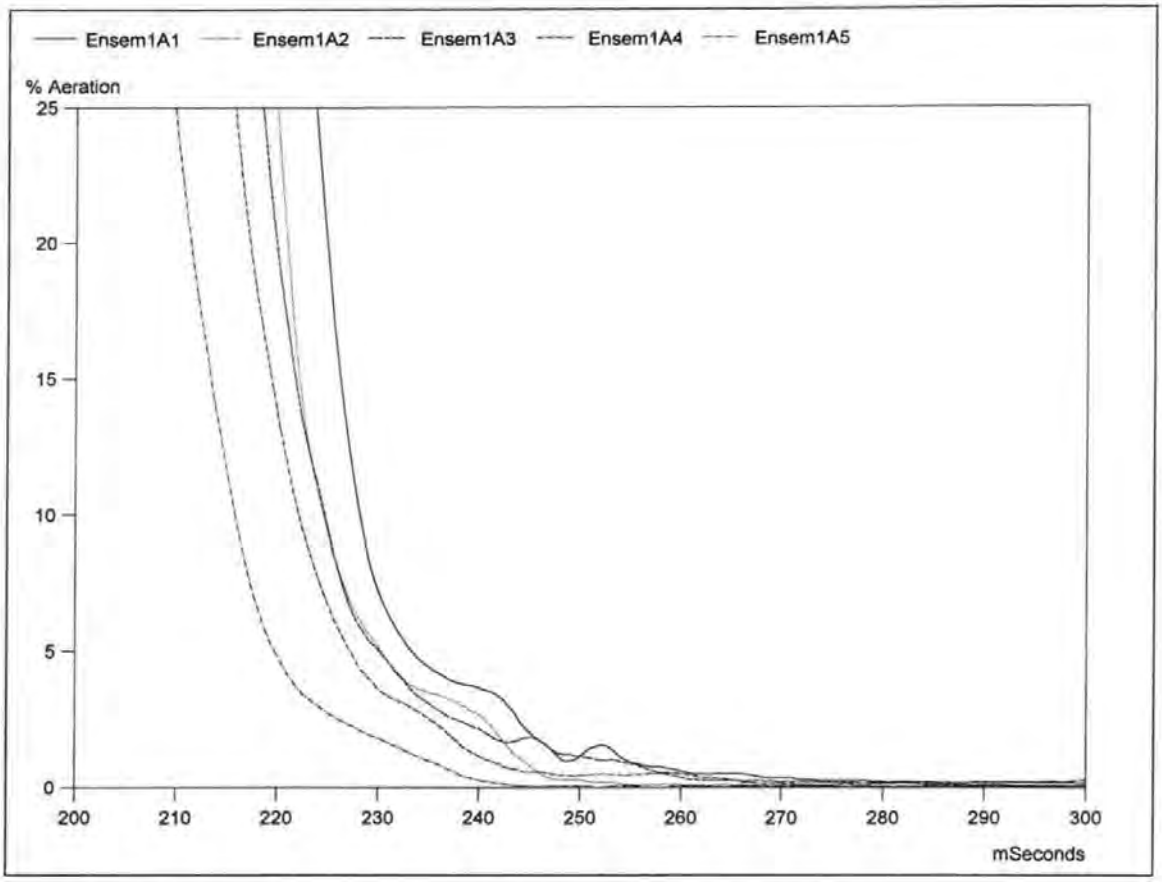

Figure 6.50. Ensemble averaged records from *Air* 1, Test 08089602.

In these Figures each ensemble average represents data from 56 events; *Ensem1A1* is obtained from the records of *Air* 1 using the 56 events with the highest values of *Pmax*, as measured by *PT 7, Ensem1A5* relates to the 56 events with the lowest values of *Pmax*.

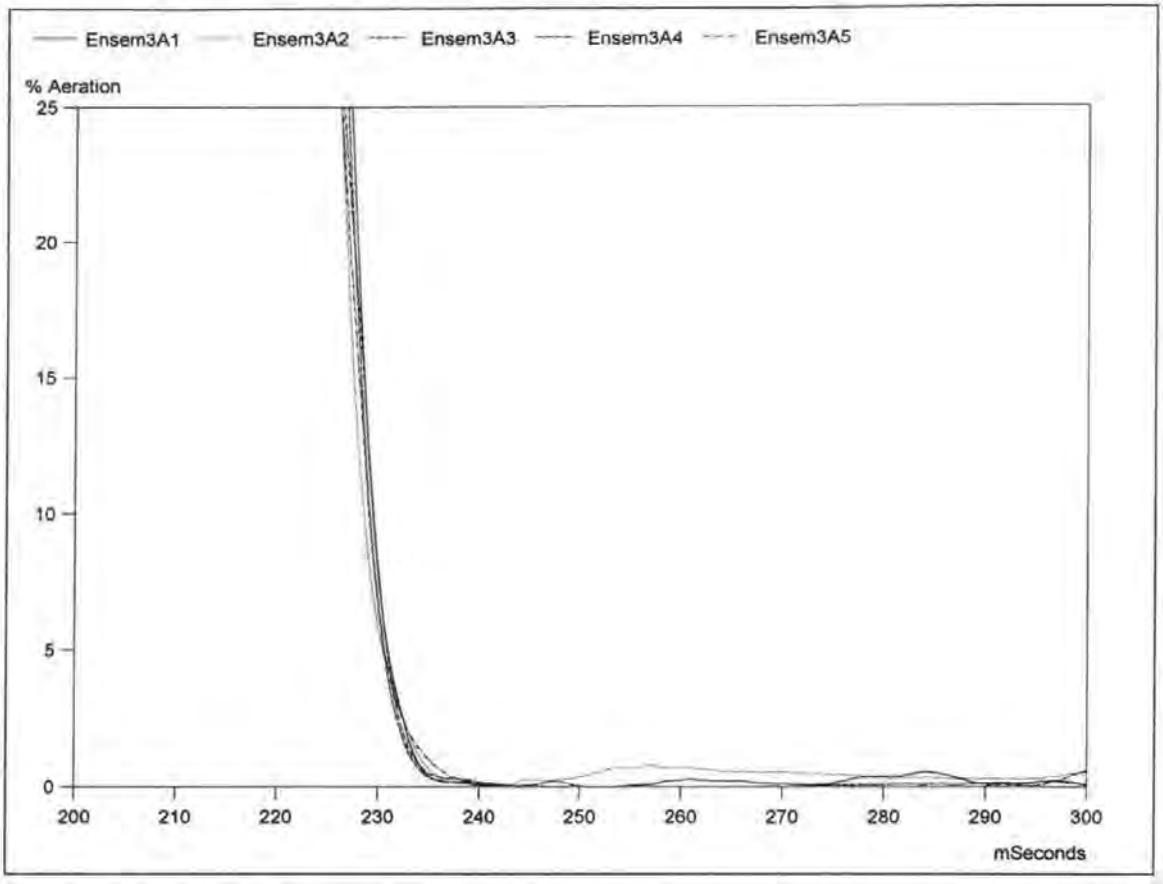

Figure 6.51. Five ensemble averaged records with *Air* 3, Test 08089602.

The five ensemble averages calculated from *Air* 1 all show very similar forms, as do the five calculated from *Air* 3. The only difference appears to be that for *Air* 1, the times at which the aeration time histories show submersion are staggered. Ensemble 5 is the first to fall followed by 4,3,2 and 1 in that order. This happens because an increase in P_{max} is associated with a decrease in the rise time T_{pr} so TP_{max} occurs relatively later in the impact. Because all of the ensemble averaged aeration time histories are aligned by TP_{max} those with low peak pressures appear to drop to submerged levels of aeration before the others. The relationship between P_{max} and T_{pr} can be seen in Figure 6.52 which includes all the data from all the transducers used in test 08089602.

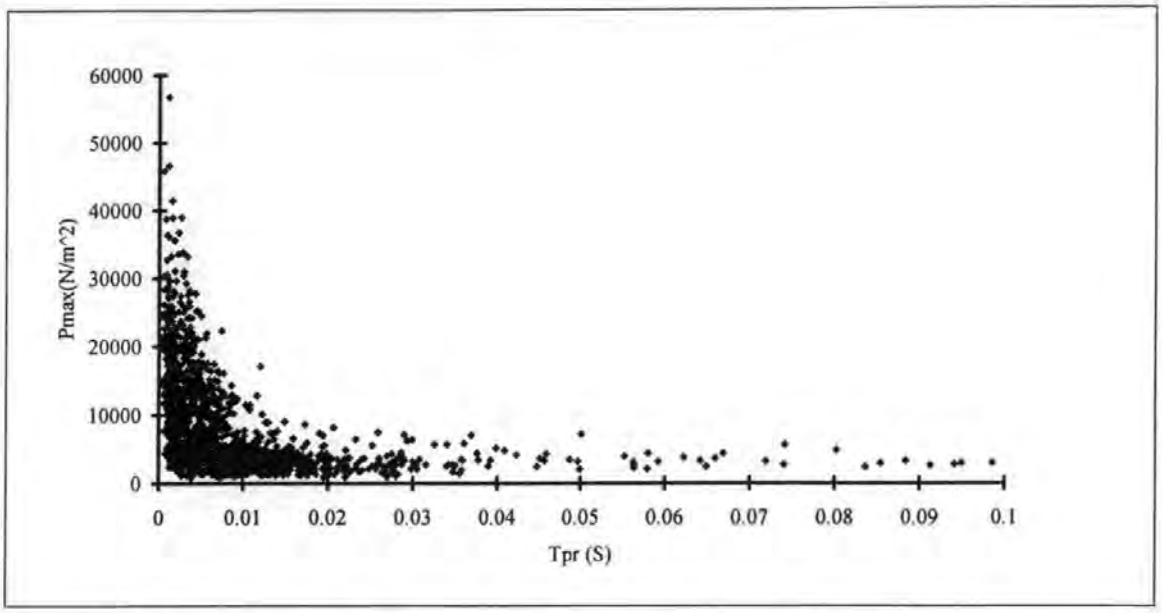

Figure 6.52. Scatter diagram of P_{max} and T_{pr} for test 08089602, all transducers.

Similar figures from other tests are given in Appendix B.

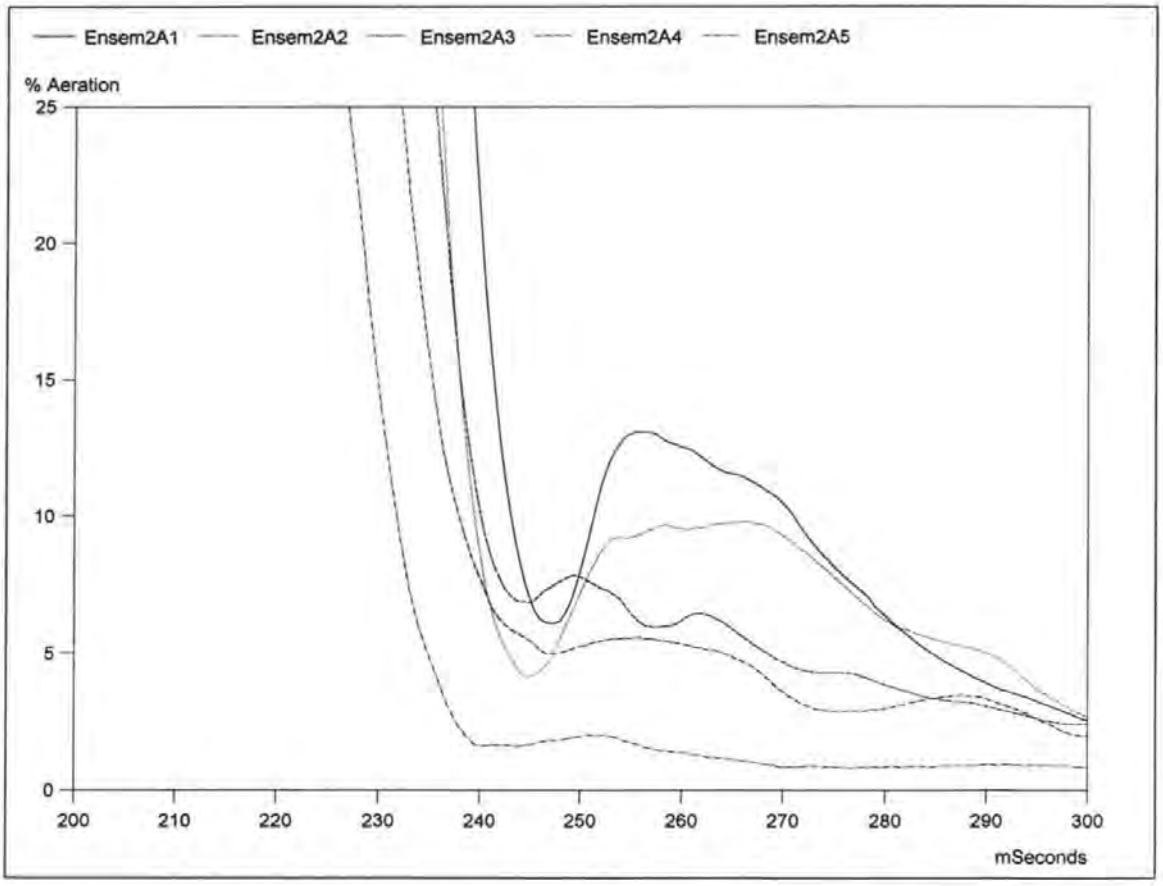

Figure 6.53. Five ensemble averaged records from *Air* 2, Test 08089602.

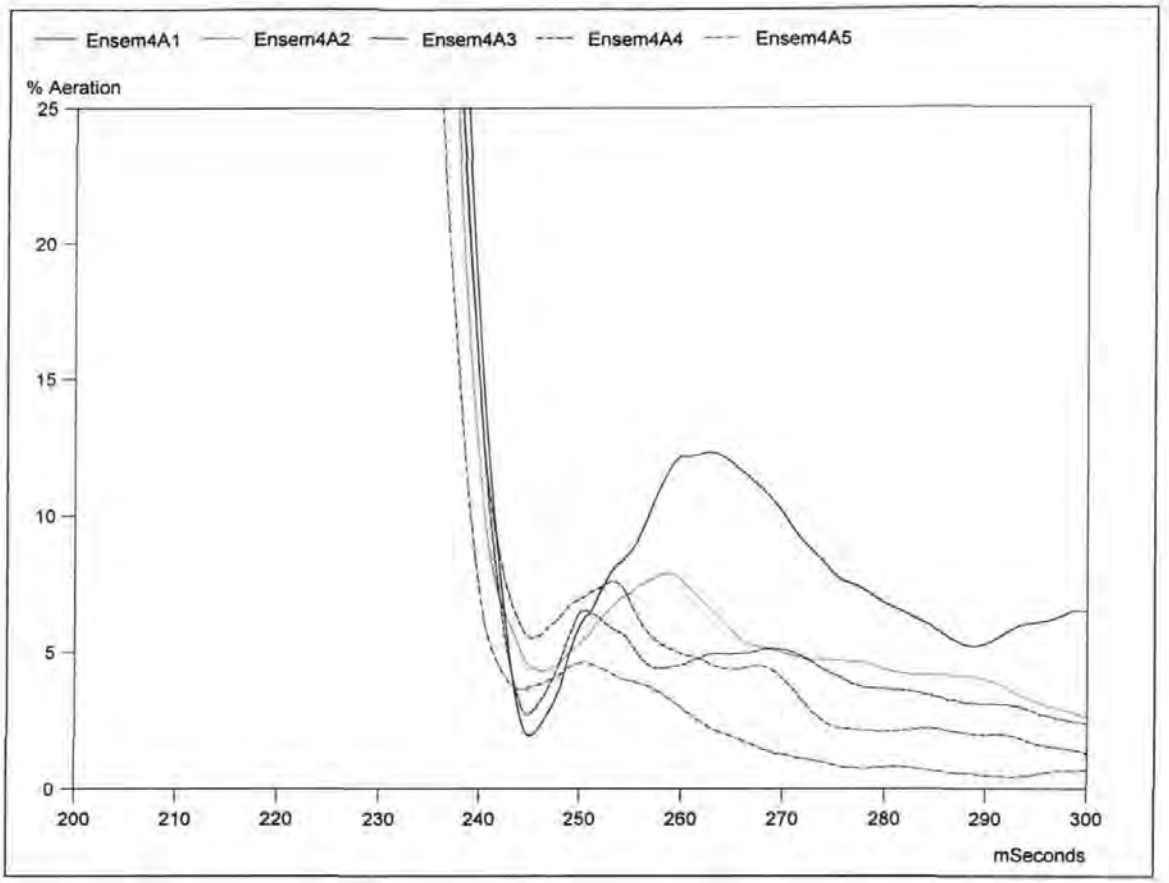

Figure 6.54. Five ensemble averaged records from *Air* 4, Test 08089602.

The effects of entrapped air can be seen in the aeration time histories calculated from probes 2 and 4 in Figures 6.53 and 6.54. All show a rapid drop from emerged to submerged levels followed by a point of inflection when the gradients change from negative to positive. There is then a rise to maxima of up to 13 %. As discussed above these peaks indicate the entrapment of air between the wave and the wall. Both figures show a correlation between the size of these peaks and the magnitude of the peak pressure. Ensemble one shows the most aeration followed by ensemble 2, 3, 4 and 5 in that order.

An attempt was made to quantify this observation by calculating an aeration flux during the early stages of the impact. This flux was defined as the integral of the ensemble averaged time history from the point of inflection for a duration of $T / 20$, where T was the wave period. This fraction of the wave period was selected as it approximated the duration of the longest wave impulse. In Figure 6.55 values of aeration flux calculated in this way have been compared to a dimensionless P_{max}.

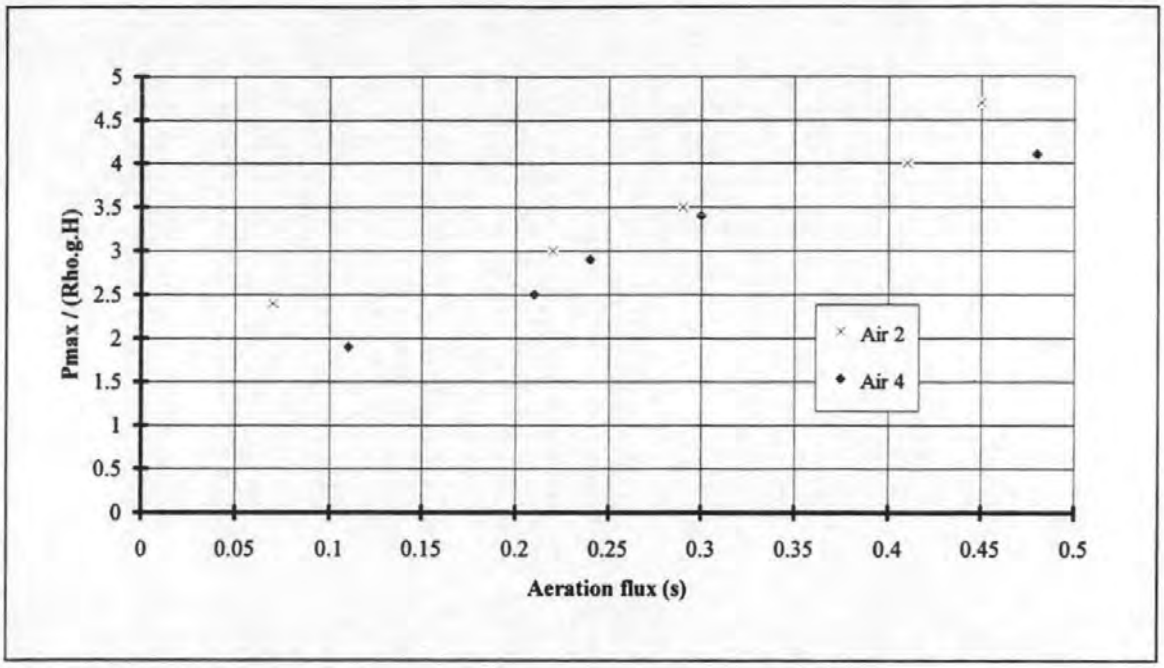

Figure 6.55. Aeration flux recorded at the wall during Test 08089602.

Each point in Figure 6.55 relates to one of the ensemble averaged aeration time histories shown in Figures 6.50, 6.51, 6.53 and 6.54. The values of P_{max} were taken from the ensemble averaged pressure time histories and normalised by $\rho g H$. It can be seen that higher levels of aeration flux are associated with higher pressure maxima.

This trend can be shown another way using the measurements of aeration flux from each of the wave impacts as in Figure 6.56.

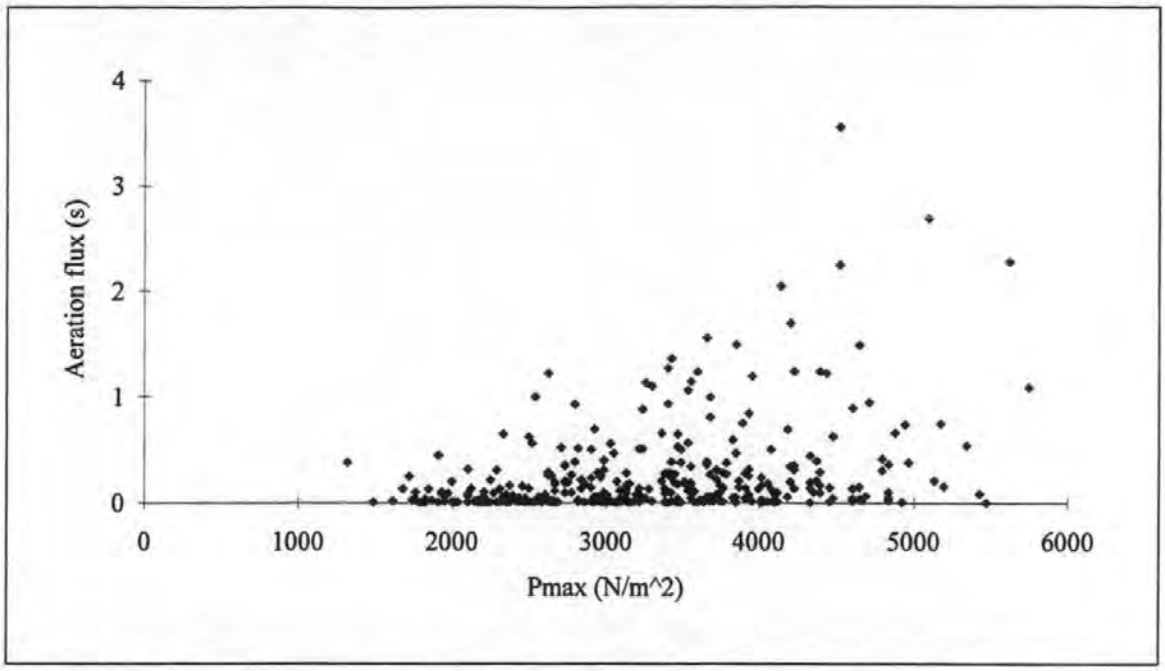

Figure 6.56. Scatter diagram of aeration flux and maximum impact pressure, pressure transducer 8 and *Air* 4.

This trend was investigated further using results from all five tests. In Figure 6.57 all the calculated values of aeration flux which were obtained from the records of *Air* 2 are shown. This instrument was selected because it was the lowest of the two at the wall and was therefore the most suitably located for the measurement of entrapped air.

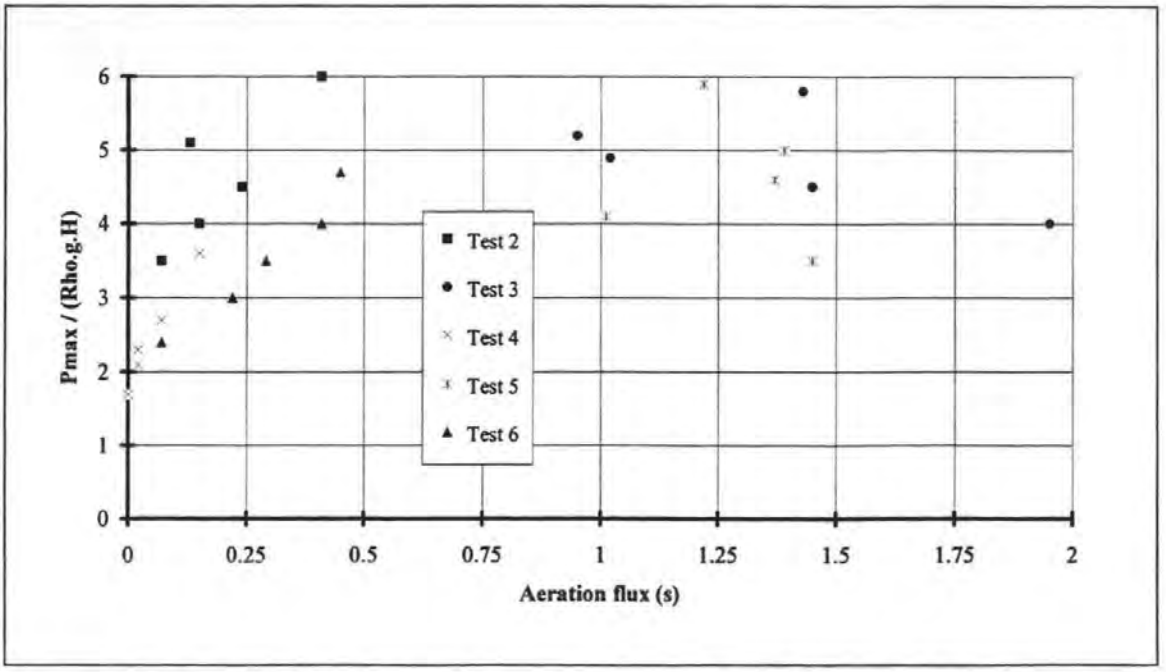

Figure 6.57. Aeration flux calculated from the results of *Air* 2 during all five tests.

The results in Figure 6.57 can be grouped into two regions, those associated with small air pockets (below about 0.5 s) and those associated with large pockets (above about 1 s). The small air pocket results all show the previously mentioned correlation between higher aeration and higher pressures. For the larger pockets the trend is less clear but appears to be reversed. This can be seen qualitatively in the original ensemble averaged aeration time histories obtained from *Air* 1, test 08089605, shown in Figure 6.58.

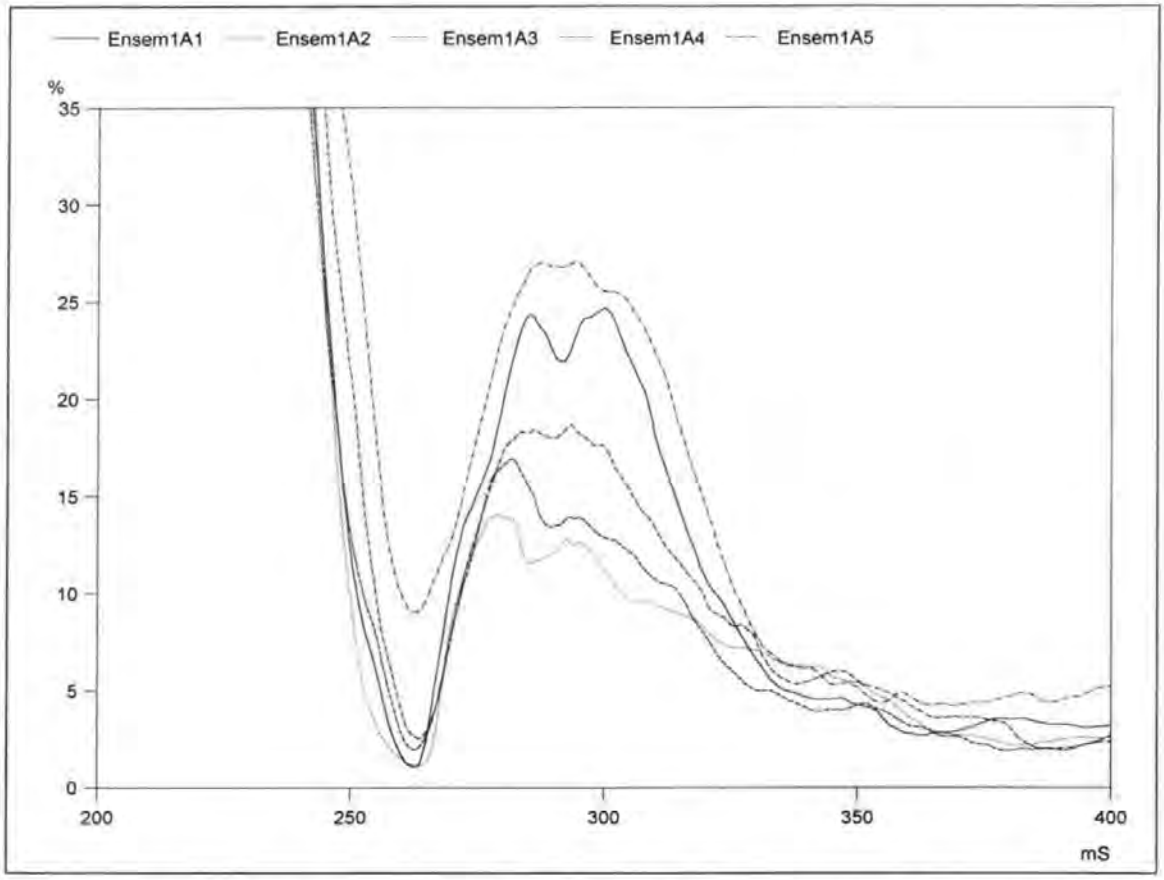

Figure 6.58. 5 ensemble averaged aeration time histories obtained from Air 1, Test 08089605.

These results indicate that entrapped aeration can be associated with both increases and decreases in impact pressure maxima, depending on whether it is trapped as a large or small air pocket.

6.2.7 Summary

The new probes were found to be a viable means of measuring aeration in small scale impacting waves. The results showed very little evidence of entrained air during the

impulsive part of the wave impacts. For the majority of the impacts air was only recorded by the electrodes that were close to the wall. When air was recorded further from the wall this could usually be attributed to the occurrence of a particularly wide air pocket. A relationship was found to exist between the presence and quantity of entrapped air and the magnitude of the pressure maxima. Since air trapped between the wave and the wall exists as a distinct and separate phase, it can not be defined simply as a void fraction or percentage. An 'aeration 'flux' was therefore defined, based on the volume and duration of the entrapped pocket. Clear relationships were found between this aeration flux and impact pressure maxima. When a relatively large pocket of air was formed it acted to reduce peak pressures, as would be expected from the models of Bagnold (1939), Mitsuyasu (1966), Lundgren (1968) and others. However such models would fail to predict the result for the smaller air pockets which appeared to increase pressure maxima, or at least be associated with higher peak pressures. This unexpected, and counterintuitive result will be discussed further in Chapter 10.

The lack of natural entrained air within these small scale waves prompted an experiment in which air was artificially introduced into impacting waves.

6.3 Artificial aeration test

The wave train used in test 20059301 had the same period and height as that used in test 19059302 but had air artificially introduced using the techniques described in section 5.2.1. The pressure transducer which recorded the highest impact pressures for the two tests was identified and its records were analysed to extract each maximum pressure per wave impact. The results are shown in Figure 6.59.

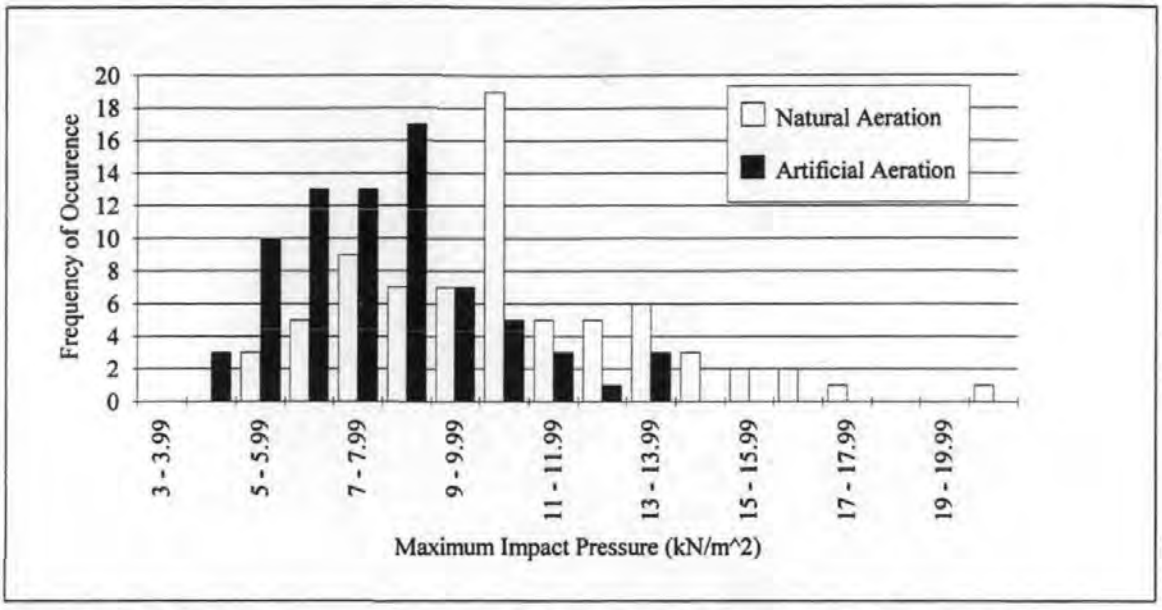

Figure 6.59. Maximum impact pressures of tests 19059301 (naturally aerated waves) and 20059301 (artificially aerated waves).

It can be seen that the addition of air reduced the maximum and average values and the range of pressure maxima. However, temporal and spatial integration of the pressure impulses showed that on average, the force impulses generated by the two tests were similar. This can be seen in the histogram in Figure 6.60, where each value of the impulse has been normalised to the area of force time history in which it occurred (see section 7.3 for a full description of this process). Although the distribution of values has been affected, with the impulses of the artificially aerated waves having a smaller range, the average value of the two tests are very similar, 0.255 for the naturally aerated waves, and 0.251 for the artificially aerated waves.

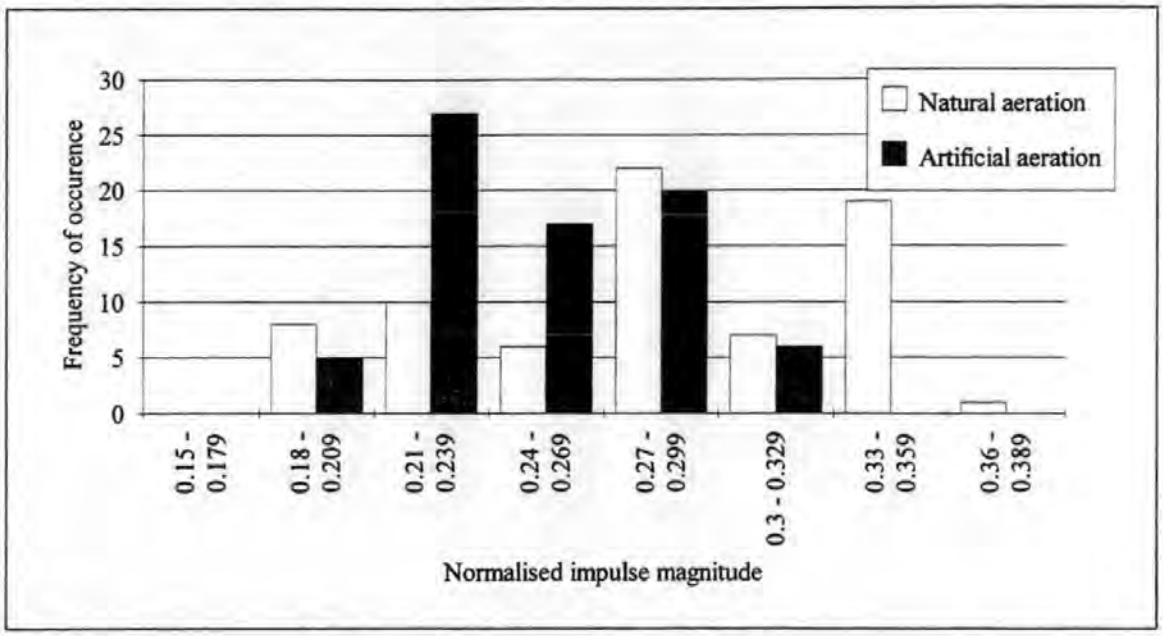

Figure 6.60. Histogram of the normalised magnitudes of the force impulses of tests 19059301 and 20059301.

This result suggests that the additional aeration has changed the shape of the impulse but not its magnitude. Unfortunately this type of test was found to have an inherent uncertainty, the injection of air must affect the shape of the wave to some degree. The shape of the wave strongly influences the impact load, therefore any observed change in load may be due to the additional air or the change in wave shape. Because of this ambiguity this type of test was not repeated.

6.4 The effect of entrained air on drop test impact pressures

The small scale wave impact tests were found to contain little or no entrained air so they could not be used to investigate the relationship between entrained air and impact pressures. A series of aerated drop tests were therefore conducted and used to examine the importance of both the quantity and bubble size distribution of entrained air.

The drop test equipment included a clear acrylic vertical cylinder that was filled with water, an aerator fixed into the base of the tube and a 'traveller' which was allowed to fall onto the surface of the water. In the bottom of the traveller was a circular plate which was instrumented with pressure transducers. A detailed description of this equipment can be found in section 5.3. Both fresh and sea water were used to produce different bubble size

distributions. A brief investigation was first made of these distributions.

Fixed mass flow rates of air were introduced into columns of both fresh and sea water. The bubbles were photographed and measured. Figure 6.61 shows the result of one comparison.

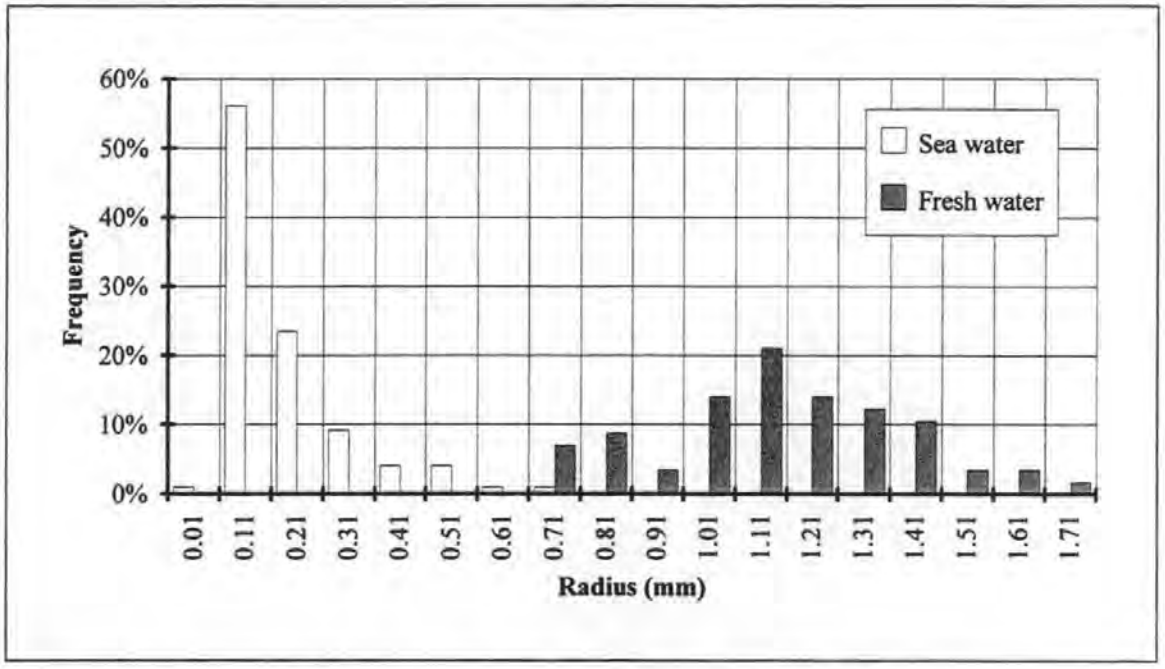

Figure 6.61. Frequency distributions of sea and fresh water bubble diameters.

It can be seen that the bubbles in the sea water were much smaller than those in the fresh water. As a consequence the sea water bubbles took longer to rise to the water surface. This meant that although equal mass flow rates of air were introduced to both water types, the sea water always contained more. For the tests from which the data in Figure 6.26 is taken, the sea water contained 2.0 % air whilst the fresh water contained only 1.75 %.

This observation may have an important implication for wave impact tests conducted in large scale flumes. The advantage of conducting experiments in large flumes is perceived to be that the waves are less prone to scale effects. Scale effects are usually attributed to differences in aeration and it is generally expected that large flume waves will have similar aeration characteristics to prototype waves because of their size. The bubble observations show that, due to differences in the aeration retention characteristics between fresh and sea water, for the same entrainment rate sea water will contain more air. Consequently large scale fresh water waves should not be expected to have the same aeration characteristics as sea water waves of equal height.

When the 'traveller' was allowed to drop onto the water the results were found to be highly repeatable, particularly for the tests which involved low levels of air. This can be seen in Figure 6.62 in which three impact pressure time histories are shown which have peak values which vary by less than 0.5 %.

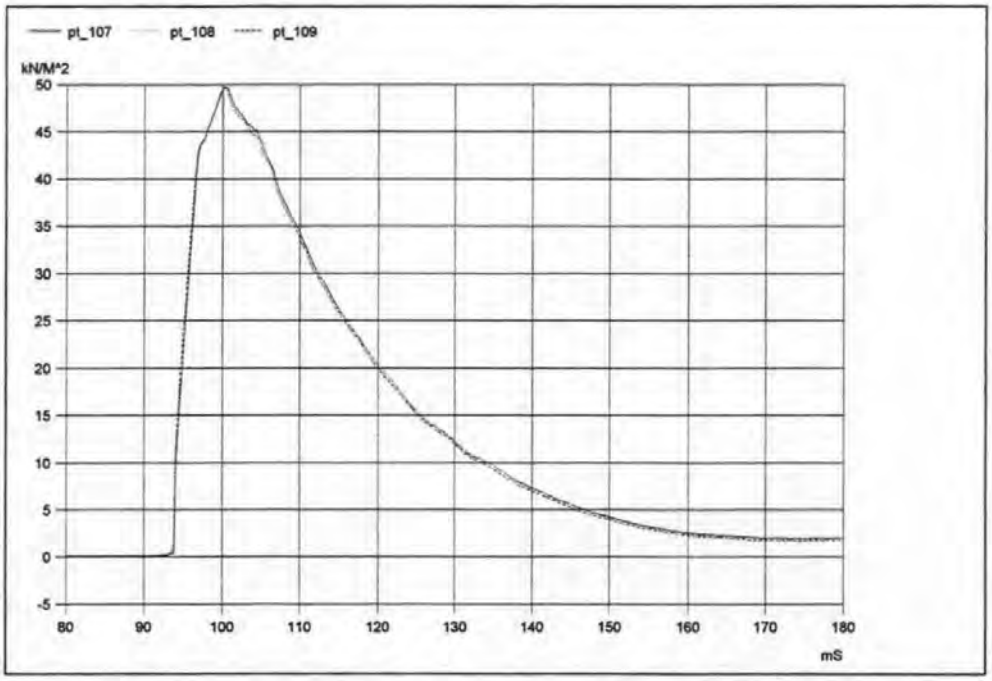

Figure 6.62. Repeatability of three drop impact pressure time histories measured at the plate centre.

Pressures were measured at three points across the plate (as shown in Figure 5.10) for a limited number of tests to obtain their spatial distribution. During the majority of the tests this distribution was used with the pressures measured at the centre of the plate to calculate the impact forces. The range of different test conditions are shown in Table 5.4.

The impact force maxima were found to decrease with increased aeration. This is demonstrated in Figure 6.63 which shows the results of 130 tests which involved a 1.85 kg drop mass.

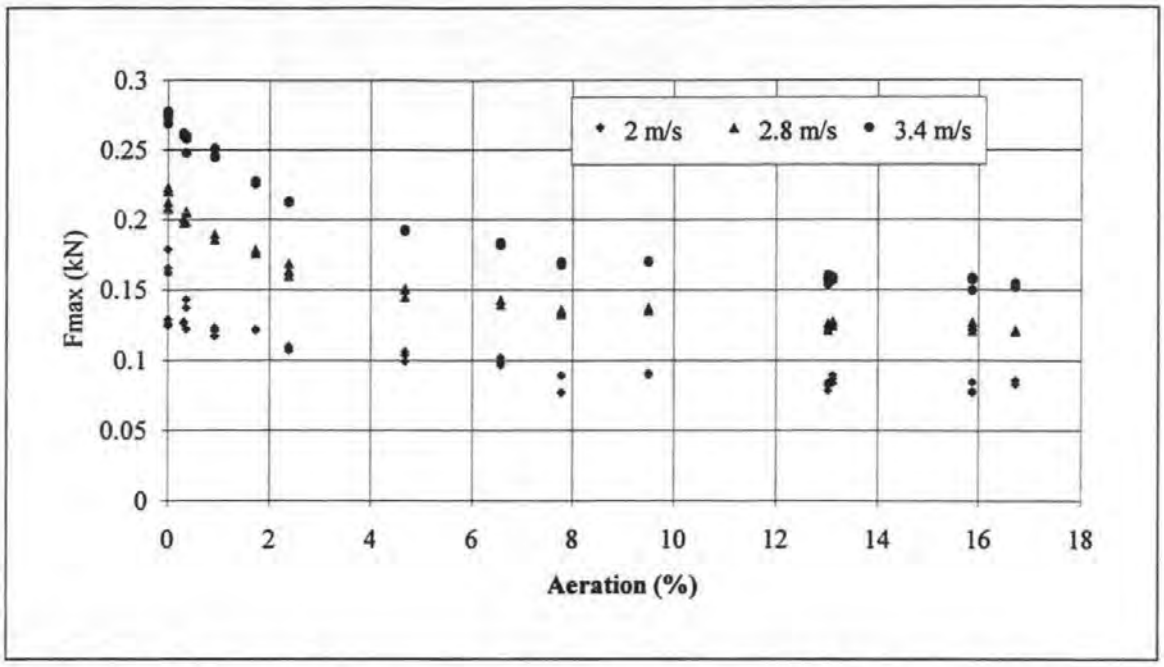

Figure 6.63. Influence of aeration on maximum impact force, 1.85 kg drop mass.

Similar trends were found with the 1.35 kg drop mass test results. There was also a relationship between maximum impact force and plate momentum, which is shown in Figure 6.64.

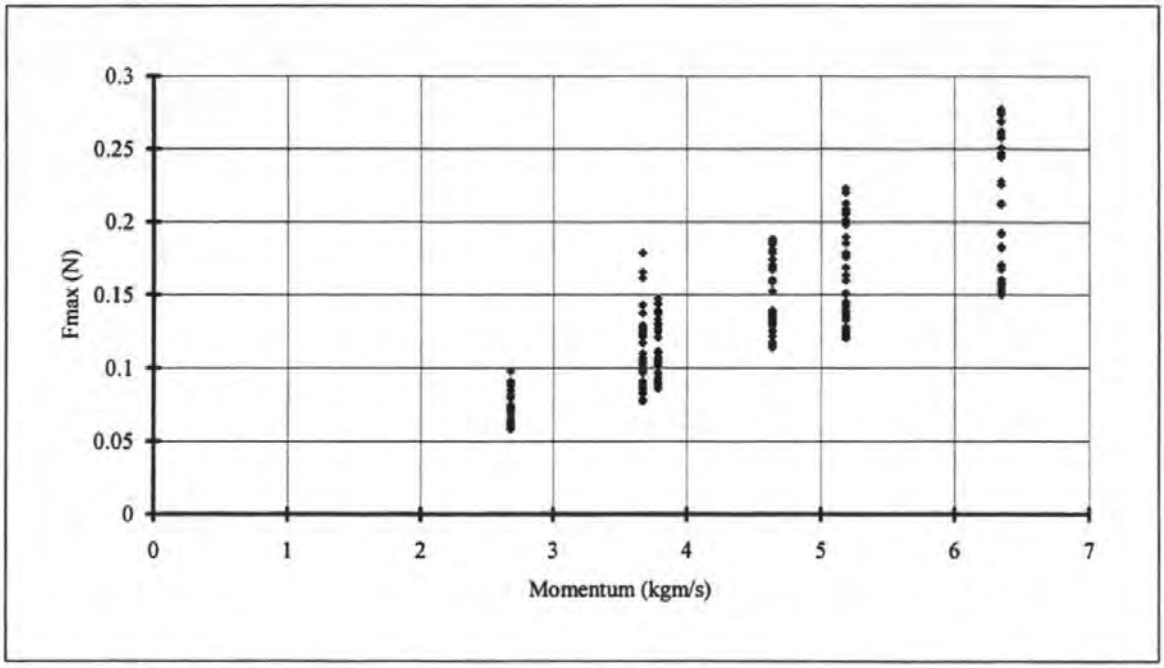

Figure 6.64. Scatter plot of maximum impact force and impact momentum, 1.35 and 1.85 kg impacts.

The scatter in F_{max} for any particular momentum mainly arises because of the variation in the quantities of entrained air.

When all the results are viewed in the F_{max} and rise time domain, as in Figure 6.65, an upper limit can be seen. This is formed by data from the tests with the highest momentum, the 1.85 kg, 3.4 m/s impacts.

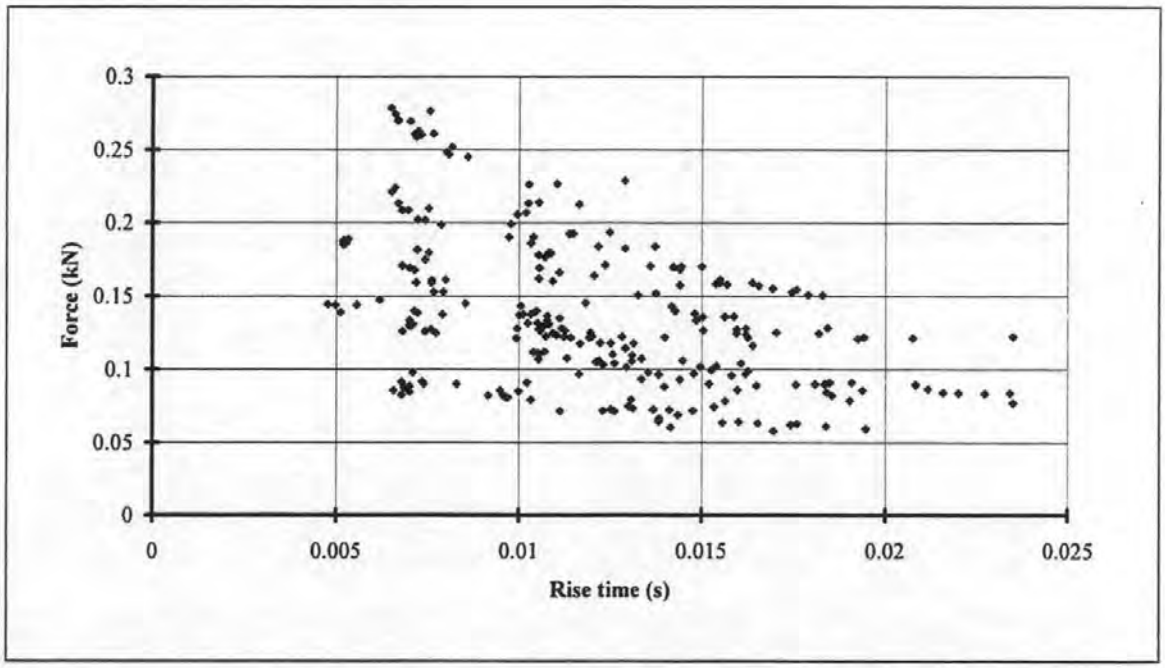

Figure 6.65. Scatter plot of maximum impact force and rise time for all the drop tests.

In Figure 6.66 the same data has been sorted by impact momentum. It can be seen that clear bands are formed so that there is a particular *Fmax* - rise time relationship for each impact momentum.

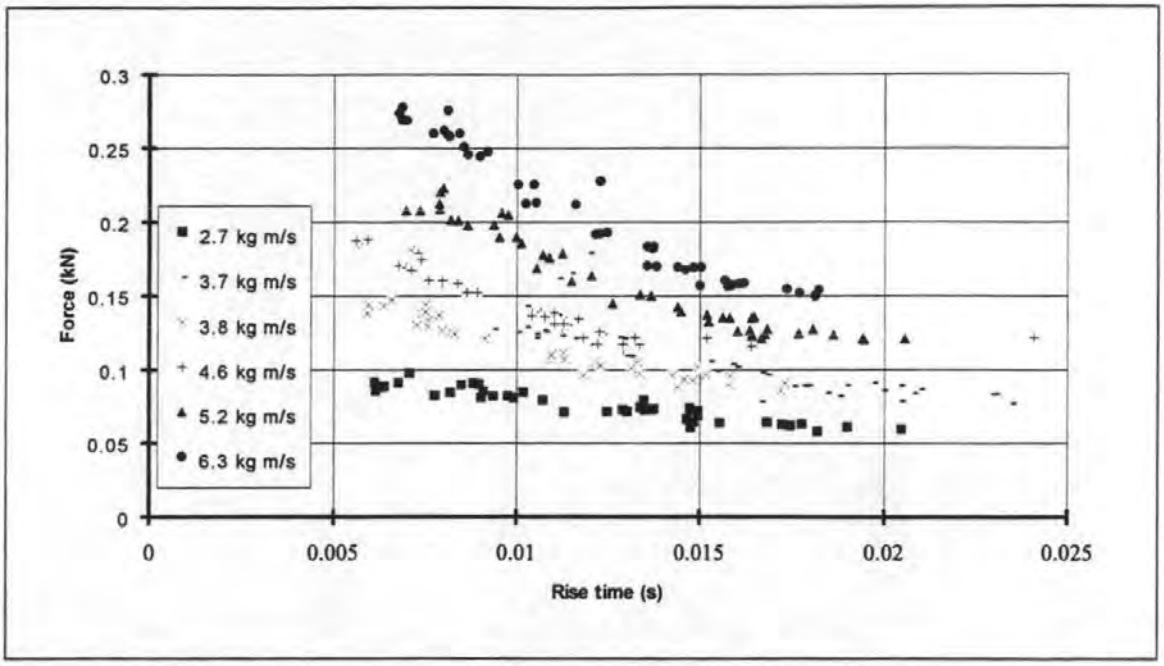

Figure 6.66. Drop test data sorted by impact momentum.

In Figures 6.67 and 6.68 the same data has been sorted by the quantity of entrained air. The data from the two different masses has been shown separately to make the banding clearer.

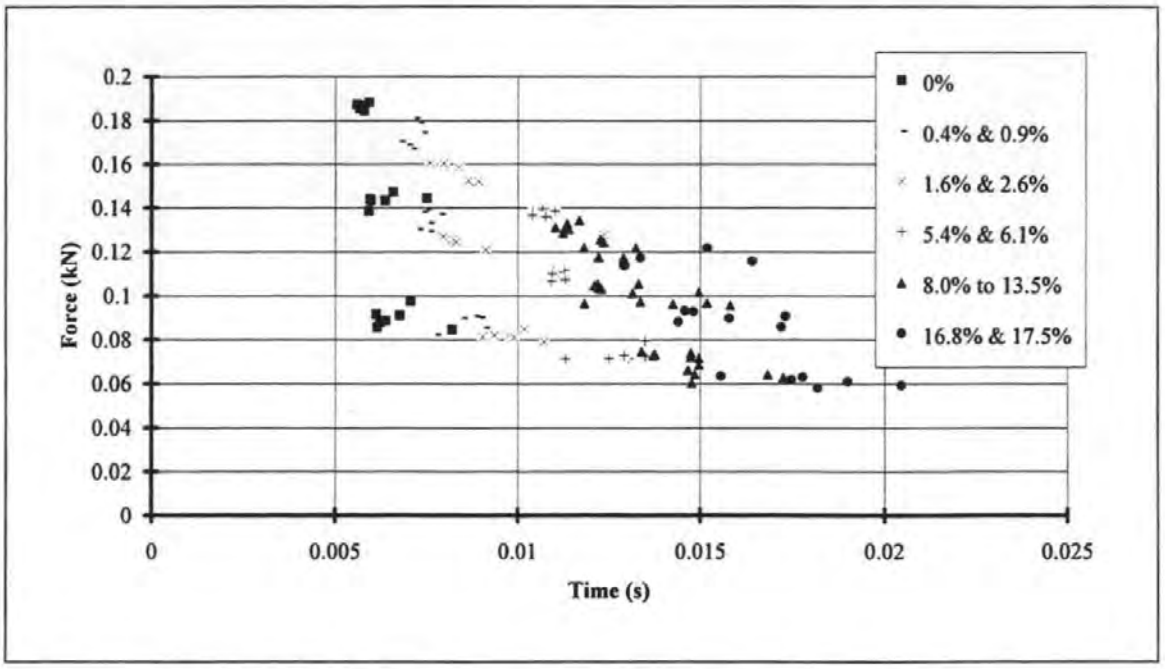

Figure 6.67. Data from the 1.35 kg tests, sorted by percentage of entrained air.

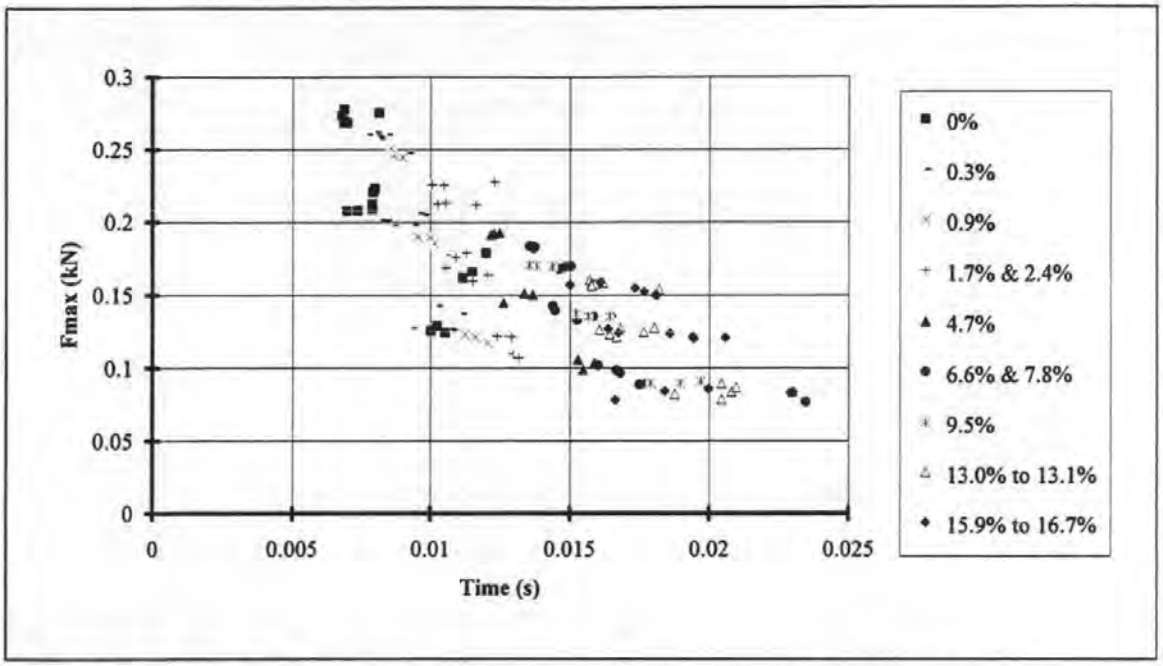

Figure 6.68. Data from the 1.85 kg tests, sorted by percentage of entrained air.

The low aeration results are grouped at the left of the data. Increasing aeration causes a clear increase in rise time and a decrease in force maxima. An empirical expression was derived to describe these relationships.

The area of the force time history up to the time at which F_{max} occurs must be equal to the momentum lost by the falling plate during the same period. The form of this part of the force time history is not linear, as can be in Figure 6.62, but it can be approximated with a triangle, so that;

$$0.5\, F_{max}\, T_{fr} = M_{fr} \tag{6.1}$$

Where M_{fr} is the momentum lost by the plate during the rise in force and T_{fr} is the rise time. The effect of the level of aeration (β) on the ratio M_{fr} / M_{om} (where M_{om} is the momentum of the drop plate at impact) was found to be small compared to its effect on the maximum impact force, it was therefore decided to make the rough assumption that M_{fr} / M_{om} did not vary with β. Therefore;

$$M_{om} = C\, F_{max}\, T_{fr} \tag{6.2}$$

Where C is a constant.

Values of M_{om} / T_{fr} were calculated for each impact and compared to measured values of F_{max} to obtain C. The correlation was analysed using least squares regression and this provided a value of 2.98 for C with a coefficient of determination of 0.8.

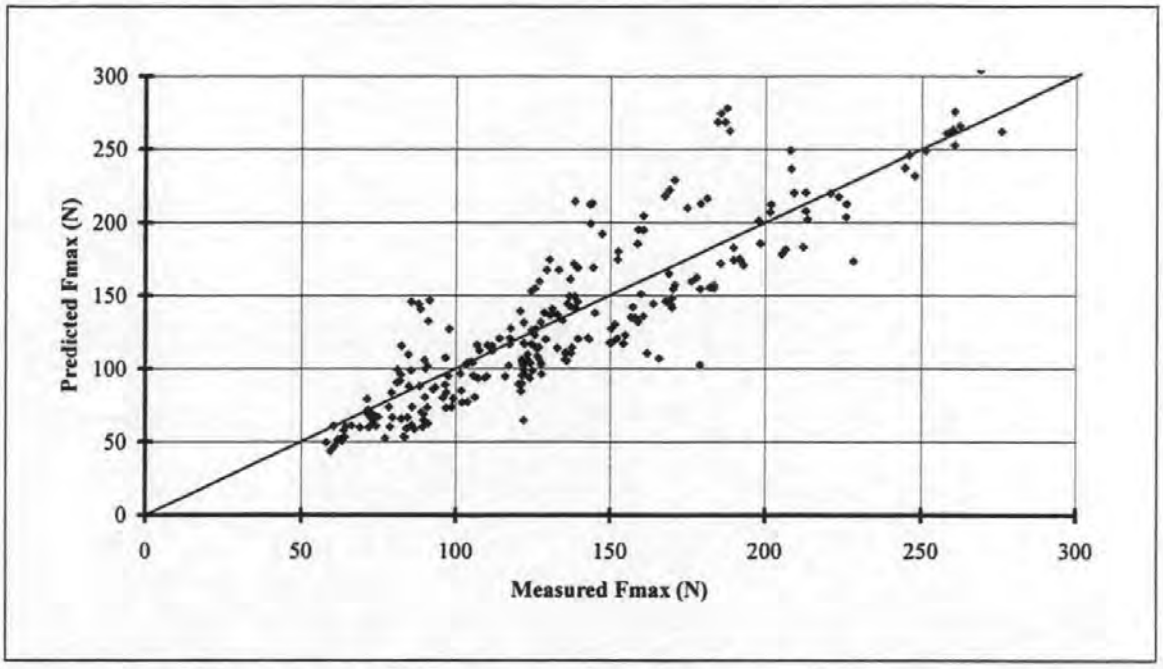

Figure 6.69. Comparison of force maxima measured during the drop tests and predicted with equation 6.2.

A similar linear regression was calculated on the relationship between the rise time and the aeration level. The relationship was found to be;

$$T_{fr} = 0.59\ \beta \times 10^{-3} + 8.6 \times 10^{-3} \qquad (6.3)$$

Which had a coefficient of determination of 0.7.

Using equation 6.3 in equation 6.2 provides;

$$F_{max} = M_{om} / ((0.59\ \beta \times 10^{-3} + 8.64 \times 10^{-3}) \times 2.98) \qquad (6.4)$$

This equation worked equally well for both the sea and fresh water data, as illustrated in Figure 6.70.

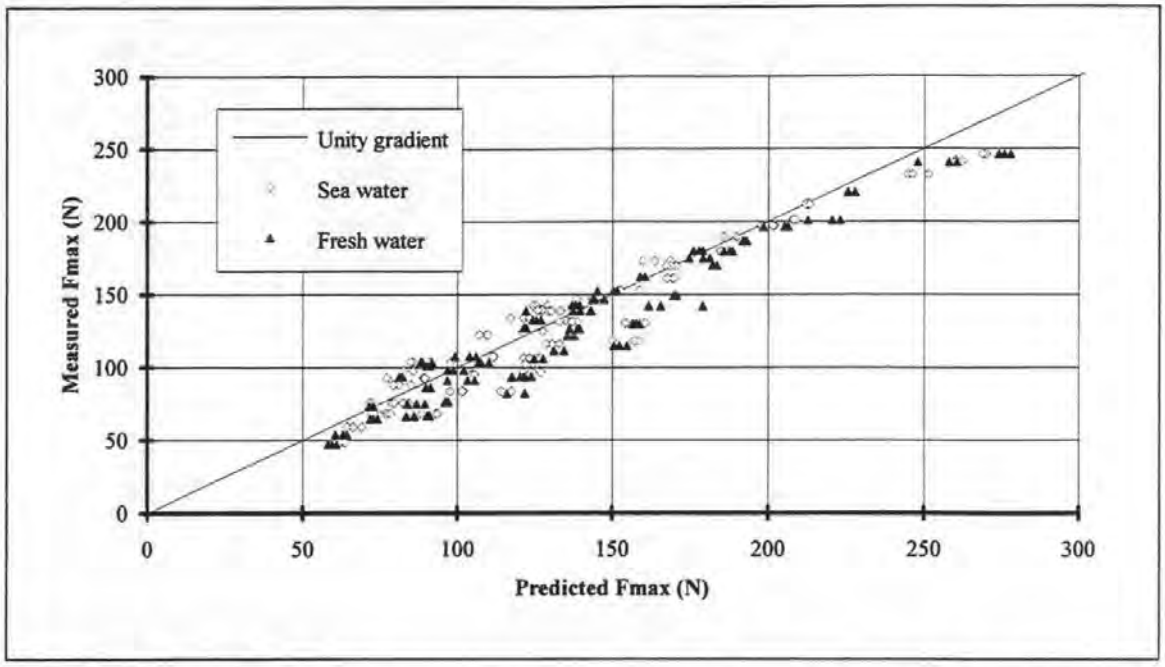

Figure 6.70. Comparison between impact force maxima measured from the drop tests and predicted with equation 6.4.

Consequently it was concluded that the distribution of bubble sizes did not significantly affect the force maxima. A least squares regression analysis was performed to assess the quality of the fit between the measured and predicted values. The coefficient of determination was found to be 0.93. Therefore equation 6.4 provides a reasonable prediction of the effect of entrained aeration on the maximum force for the drop test results. In order to provide a simple means of estimating what effect entrained aeration would have on wave impacts Equation 6.4 was used to calculate a series of force reduction factors (*FRF*) where;

$$FRF = F_\beta / F_0 \tag{6.5}$$

in which F_o is the force maxima at zero aeration and F_β is the force at β% aeration. In Figure 6.71 these factors have been calculated for the range of aeration up to 10 %.

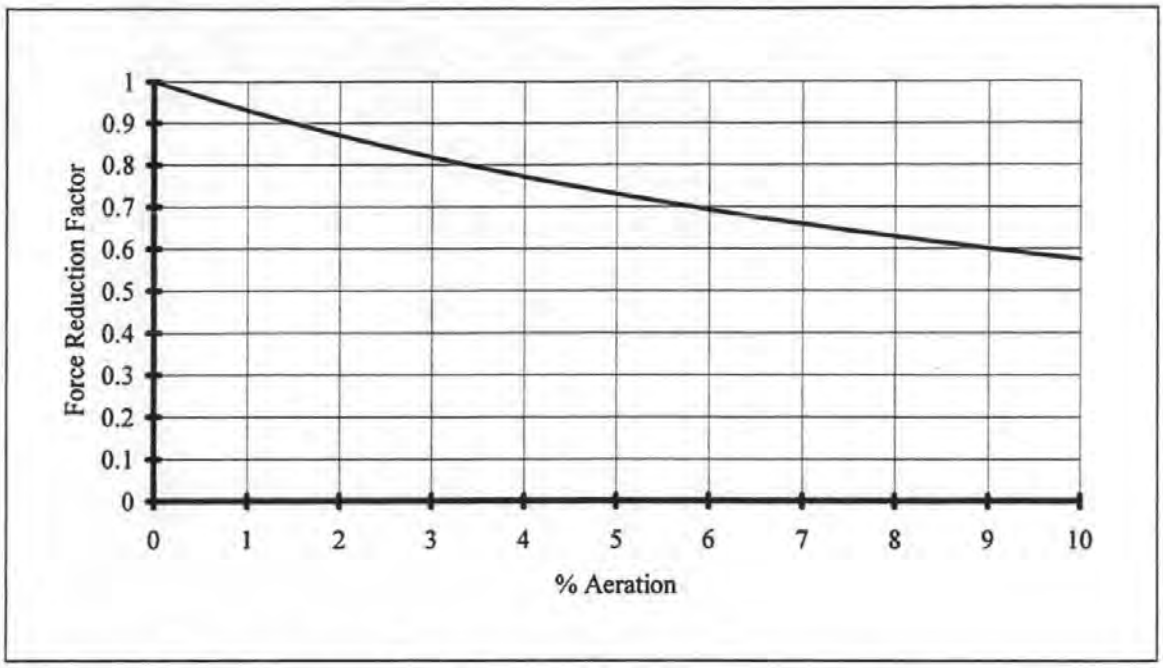

Figure 6.71. Force reduction factors as a function of percentage aeration.

In Chapter 9 an example is given of a scaling calculation in which this figure is used to estimate the effects of aeration on large scale wave impacts.

6.5 Summary

The large scale solitary waves showed that a comparison between the impact loads caused by different waves can only be meaningful if they have similar breaker shapes. However, the small scale aeration measurements revealed variation in entrapped air, and therefore breaker shape, during nominally identical events in a regular train. This variation causes scatter in impact load maxima with, in the case of thinner air pocket impacts, entrapped air acting to increase pressure maxima. This finding contrasts with the drop test results which showed that entrained air acts to reduce load maxima. The results of the artificial aeration tests showed the same relationship and implied that the change in load maxima was not necessarily associated with a change in average impulse area.

Chapter 7

Definition and measurement of the force impulse

7.0 Introduction

In Chapter 3 the magnitude and form of the force impulse were identified as useful properties of the wave impact load that had received relatively little attention. In this chapter a definition for the force impulse is proposed and applied to a variety of test results. The large scale solitary wave test results are used to investigate the relationship between force impulse magnitude and breaker form, and small scale regular wave tests are used to investigate scatter in impulse form and magnitude. Some comparison is made between these properties of the force impulse and related properties of the pressure impulse.

7.1 Definition of forces

Before the impulse could be considered, force time histories had to be calculated from the pressure records. This was done by integrating the pressures over the surface of the wave wall, as illustrated in Figure 7.1.

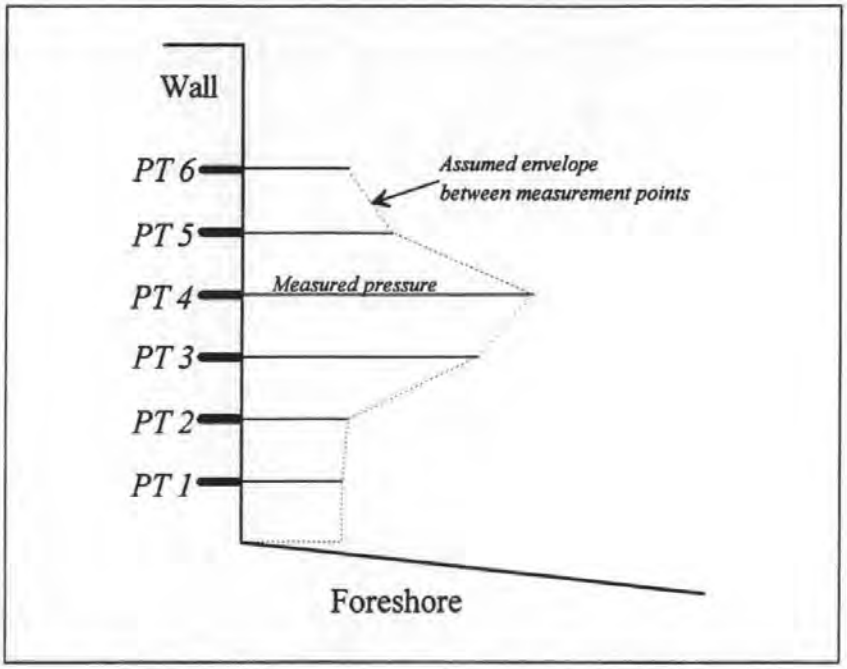

Figure 7.1. Interpolation between measured pressures and extrapolation beyond the range of instruments.

Three assumptions were made; that pressures varied linearly between the measurement points, that pressures were constant below the lowest transducer and that they were zero above the highest. The last of these is, in effect, an assumption that the top of the wall is located at the position of the upper transducer.

7.2 Definition of the force impulse

Several alternative definitions for the force impulse were considered. The first was based on the definition of the pressure rise impulse used by, amongst others, Bagnold (1939), Wegel and Maxwell (1970), Hattori (1994) and Blackmore and Hewson (1984). This approach defines the beginning of the impulse as the moment when the force rises above zero and its ending at the moment of load maxima, as illustrated in Figure 7.2.

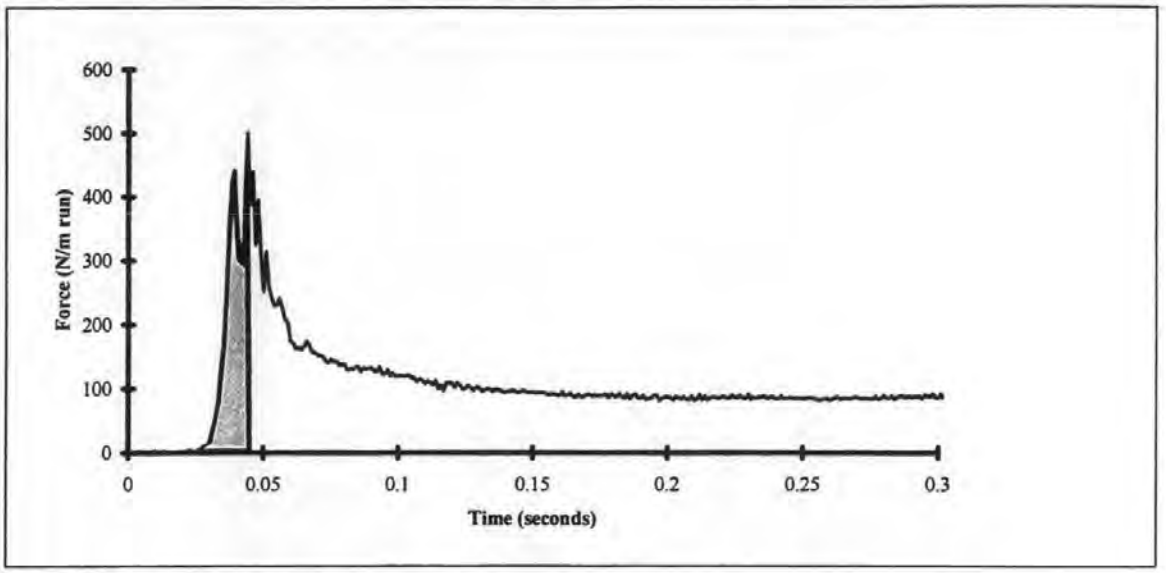

Figure 7.2. Definition of the force rise impulse.

This definition has the disadvantage that for impacts with very short rise times, as in the case of the flip-through impact described in section 6.1.4, the impulse becomes very small. In addition the high forces occurring after the force maxima are neglected.

Oumeraci and Kortenhaus (1994) defined the force impulse as a linear triangle within the actual force time history, as illustrated in Figure 7.3.

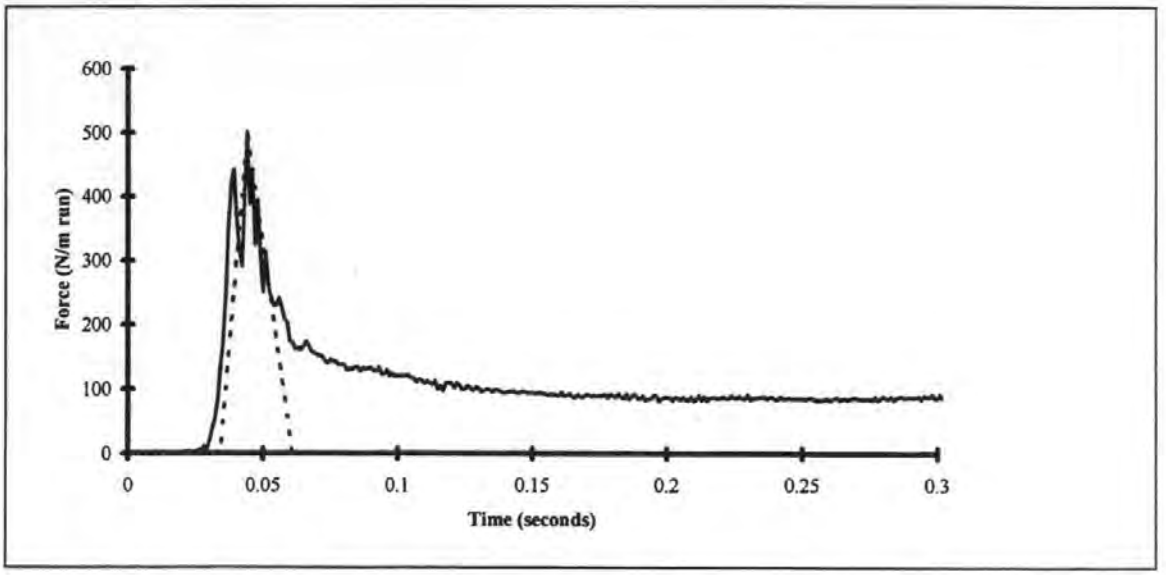

Figure 7.3. Force impulse used by Oumeraci and Kortenhaus (1994).

Using this definition Oumeraci and Kortenhaus overcame the problems associated with the previous method, but they did not provide definitions for the rise time or the impulse

duration. This approach was tried with the force records calculated from the results of the small scale tests 08089602 to 08089606 using a variety of algorithms to define the rise time and duration. None were found which could cope well with the natural variations and irregularities in the shape of the force time history.

A different approach was then tried in which the end of the impulse (t_{end}) was defined as the moment when the high impulse forces drop to the level of the quasi-static loads. This level was estimated from the later part of the force time history, as illustrated in Figure 7.4. Clearly the processes which generate the quasi-static loads do not begin instantaneously at the moment when the processes which generate the impulsive loads end. Instead there must be a transition from the impulse generation mechanisms, which end at t_{end}, to the non-impulsive load generation mechanisms, which begin at an earlier time. It is not possible to be certain of the boundary between these two regions, so an estimate was made in the form of a simple gradient running from the start of the impulse to the value of the force time history at t_{end}. This definition provided a simple means of measuring the area, or magnitude, of the force impulse. The appropriateness of this definition is discussed in greater detail in Section 10.3.

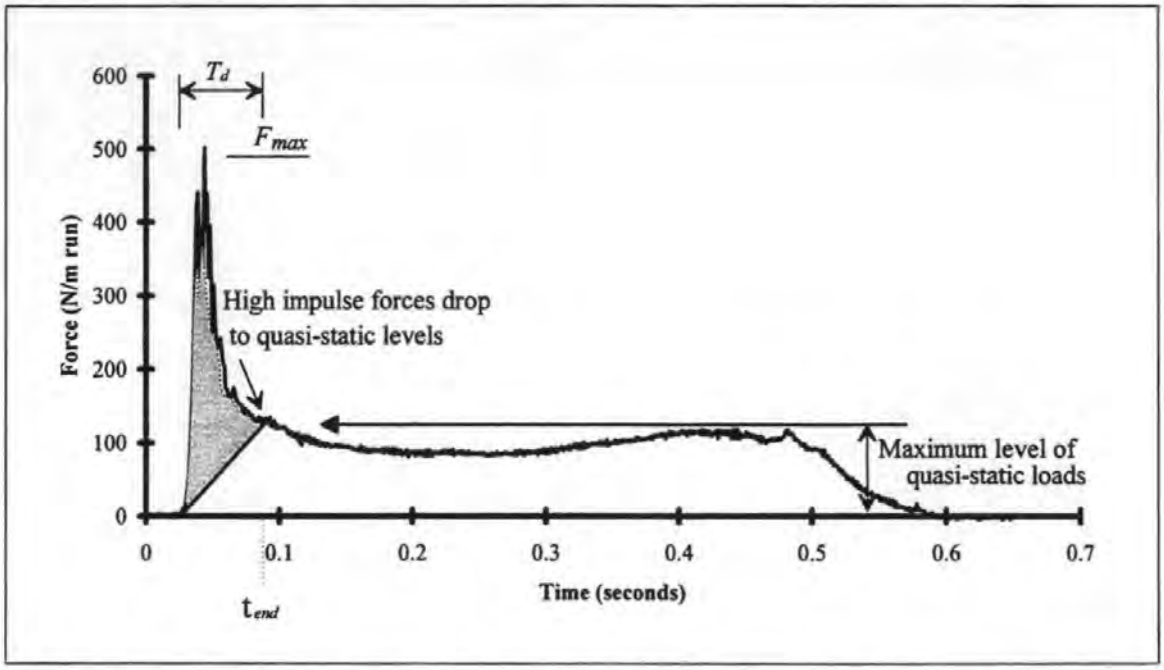

Figure 7.4. Assumed boundary between the impulsive (shaded) and quasi-static regions of a force time history.

The rise and fall times were found to be sensitive to minor irregularities in the force time histories so a standard signal analysis definition was adopted. The average rising gradient was assumed to be equal to the gradient between the points on the signal which were 10 % and 90 % of the maximum value. The same technique was used to calculate the average falling gradient.

7.3 Variation of impulse magnitude with breaker form

The large scale solitary waves described in Section 6.1 were used to investigate the variation of impulse magnitude with breaker shape. These waves were used because they included a range of breaker shapes which were well controlled. Their force time histories were processed using the method described above, to obtain the area of the impulse. Because the waves were of various sizes the measured impulse magnitudes were normalised before being compared. The natural parameter with which to normalise a wave impact load is the incident wave momentum. A relatively simple expression for the momentum of a solitary wave was found but none was identified that could provide the momentum of a regular wave. Consequently, the impulse was instead normalised against the total momentum change experienced at the wall, as measured by the pressure transducers, *i.e.* the shaded region in Figure 7.4 was normalised to the whole area of the force time history. The resulting non-dimensionalised impulse area was termed the impulse proportion of the wave (*IP*). Table 7.1 and Figure 7.5 show how the *IP* varied with wave height, and therefore breaker shape.

Test	Breaker type	Height	*IP*	$P_{max} / \rho.g.H$
O4O2940l	Beach breaker	1	0.28	3.9
O4O29402	Toe breaker	0.95	0.31	5.2
O4O29403	Large air pocket	0.9	0.29	7.9
O4O29404	Small air pocket	0.85	0.33	38.1
O4O29405	Steep front	0.8	0.32	33.8
O4O29406	Less steep front	0.75	0.29	19.2
O4O29407	Less steep front	0.7	0.25	12.8
O4O29408	Less steep front	0.65	0.21	5.5

Table 7.1. Normalised force impulse and impact pressure maxima of the large scale solitary waves.

The variation in *IP* between these waves was found to be much smaller than the variation in the normalised impact pressure maxima which is also shown in Table 7.1.

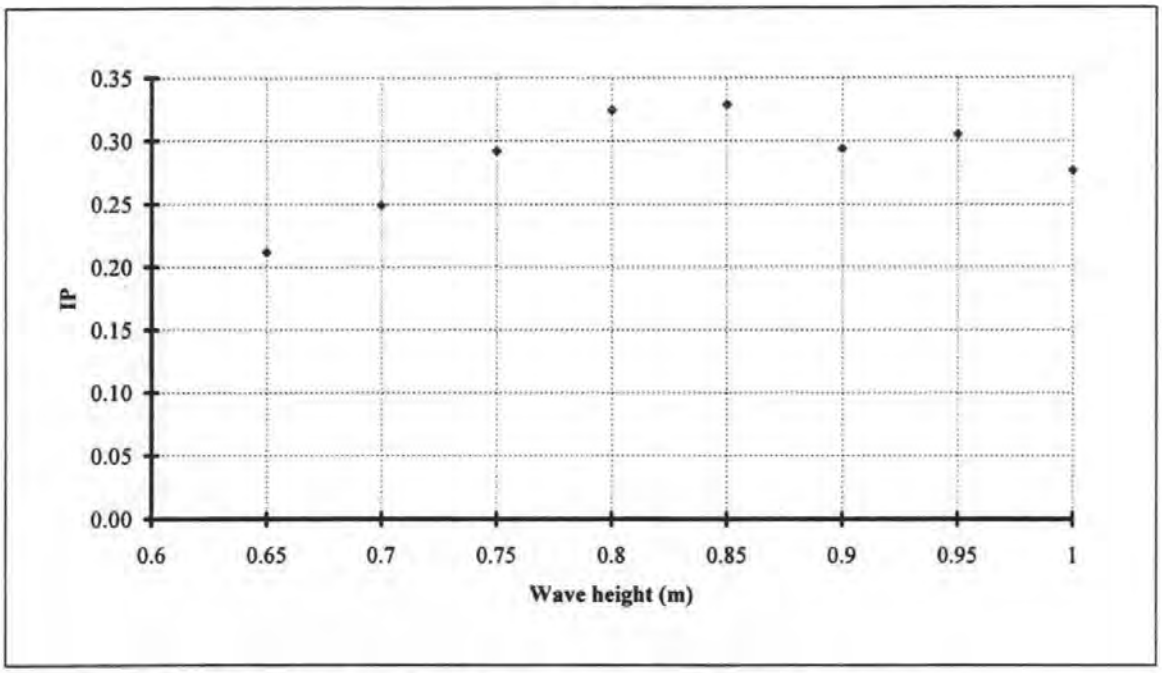

Figure 7.5. Variation of *IP* with wave height, large scale solitary waves.

The relationship which emerged was that under developed waves (steep, non-breaking) and overdeveloped waves (broken before impact) were associated with lower impulse magnitudes. The highest values of *IP* were associated with the air pocket impacts.

7.4 Variation in impulse magnitude for regular waves

When regular wave tests were examined the magnitudes of the force impulses were found to be more constant than the maximum impact pressures. Figures 7.6 and 7.7 show typical normalised values of the maximum impact pressure and impulse magnitudes that were obtained from test 08089603.

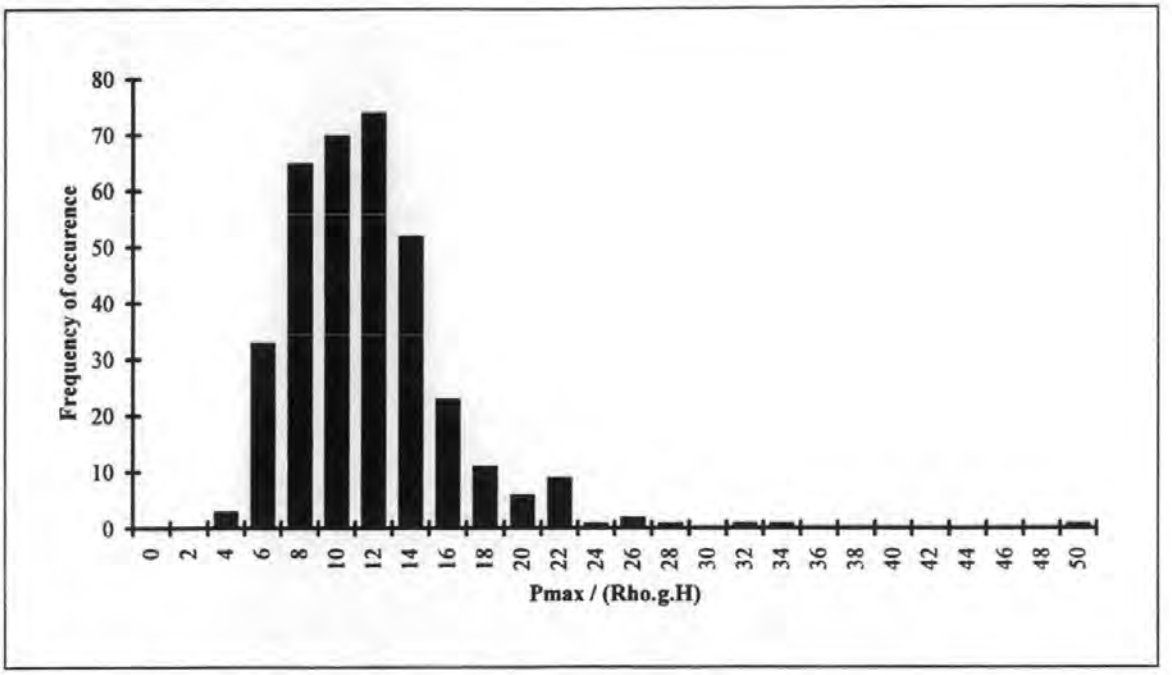

Figure 7.6. Frequency distribution of normalised impact pressure maxima, Test 08089603, transducer 3.

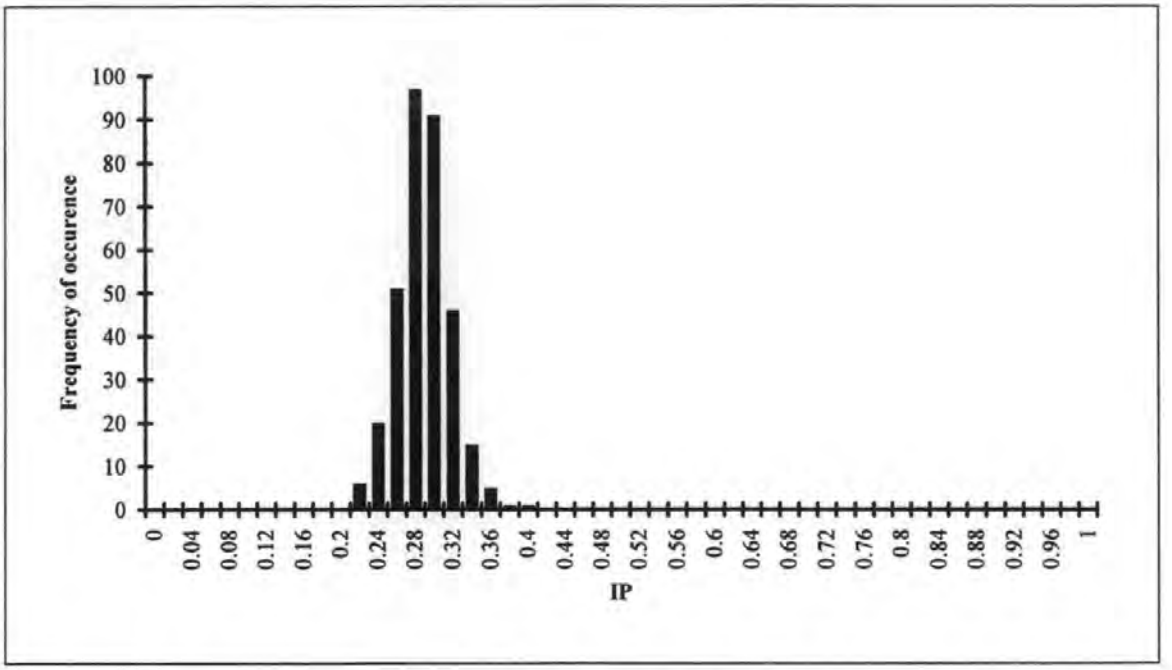

Figure 7.7. Frequency distribution of *IP*, Test 08089603.

In Figure 7.6 it can be seen that P_{max} varies from 4 to 50 ρgH, which is greater than an order of magnitude. In contrast the impulse magnitude has a range which is less than half its maximum value. Distributions of *IP* calculated from other tests can be seen in Appendix B.

7.5 Variation in impulse form for regular waves

Several researchers have published relationships between the maximum impact pressure (P_{max}) and the pressure rise time (T_{pr}) which result from regular wave impacts (see section 3.3). Such relationships were observed in the results of the small and large scale regular wave test data. A particularly clear example was found with test 08089603 and is shown in Figure 7.8, other examples are shown in Appendix B.

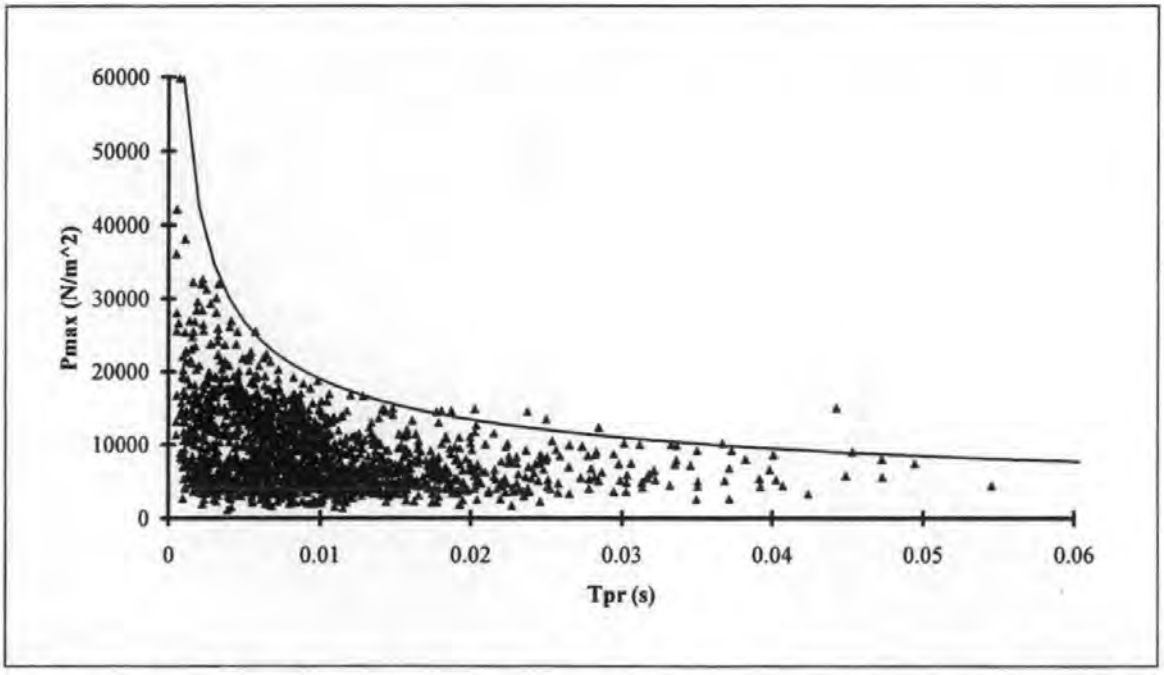

Figure 7.8. Maximum impact pressures and rise times from all transducers, Test 08089603, with an upper limit function of $P_{max} = 1900\ T_{pr}^{-0.5}$.

The upper boundary indicates some limit to the magnitude of the pressure rise impulse but any physical significance beyond this is not immediately clear. It is not evident how the magnitude of the constant (1900) or its units ($Ns^{0.5}/m^2$) can be related to the physics of the impact.

Similar relationships were found to exist between two of the properties which determine the form of the force impulse, the force maxima (F_{max}) and the impulse duration (T_d), an example from test 08089603 is shown in Figure 7.9.

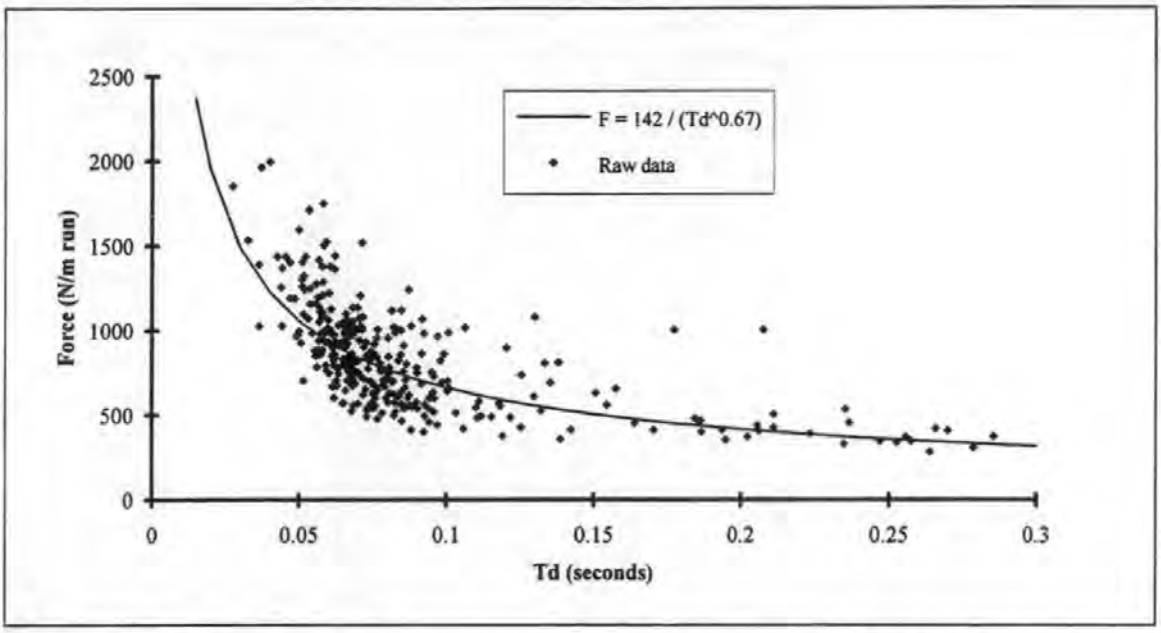

Figure 7.9. Relationship between maximum impulse force and impulse duration, Test 08089603.

This data is clustered along a trend rather than being spread below an upper limit function. A line of best fit was found by least squares regression and is plotted in Figure 7.9. As was the case with the P_{max} T_{pr} relationships seen in Figure 3.2 the physical meaning of this trend is not immediately clear. The value of the constant (142) and its units ($Ns^{0.67}/m_{run}$) can not be easily related to the physics of the impact.

7.6 Summary

A definition has been proposed for a boundary between the impulsive and quasi-static regions of wave impact force time histories. This has been used to measure the magnitude of force impulses (I_{mp}) caused by solitary and regular waves. The solitary wave data were used to show a variation of I_{mp} with breaker shape. The regular wave data showed that I_{mp} is a less scattered property of the impact load than the property most often measured during wave impact tests, the maximum impact pressure P_{max}. The form of the force impulses was found to be highly variable, but a relationship was found to exist between the maximum force and the impulse duration. It appears that this relationship is related to the P_{max} T_{pr} relationships that have been observed during other studies. It is not yet clear what the significance of the relationship is or whether it can be usefully employed. In the following two chapters this relationship and the impulse proportion will be considered further and applied to the problems of scale and the prediction of structural motion.

Chapter 8

The prediction of structural dynamic behaviour

8.0 Introduction

Chapter 2 described some of the methods that have been used to predict the dynamic behaviour of caisson breakwaters. They all relied on numerical models, either applied directly to measured or simplified force time histories, or indirectly through the use of dynamic amplification factors. This latter approach has the advantage that it reduces the solution to a one line calculation. In this chapter the appropriateness of using dynamic amplification factors with wave impact forces will be considered. Predictions made with them are compared to others made using the numerical model from which they were derived. Significant discrepancy is found. It is also found that the range of values of effective static load (F_{stat}) associated with nominally identical regular impact events is extreme due to the large variation in impulse form found in the previous chapter. Both these problems are solved by parameterising the impulse magnitude and form with an equivalent force maximum and impulse duration. This enables the prediction of a single maximum value of F_{stat} and helps explain the relationship between F_{max} and T_d seen in the previous chapter.

8.1 Numerical model of caisson motion

The equation of motion for a simple unforced single degree of freedom mass-spring-dashpot system, as illustrated in Figure 8.1 is the second order differential;

$$Mx'' + Cx' + Kx = 0$$

Where M is the involved mass, C is the coefficient of damping, K is the spring stiffness and x is the displacement.

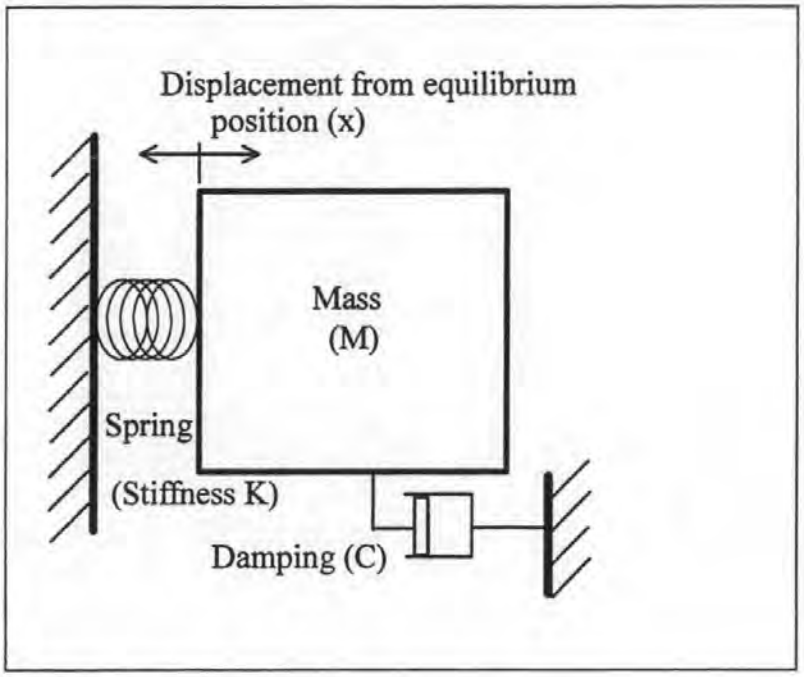

Figure 8.1. Mass-spring-dashpot system.

Introducing a driving force function $F(t)$ and rearranging leads to;

$$x'' = (F(t) - Kx' - Cx) / M \qquad (8.1)$$

This equation was divided into two equations of first order so that it could be solved using a fourth-order Runge-Kutta method.

In order that the model should describe the motion of a semi-submerged caisson mounted on a rubble mound, it was necessary to select appropriate values of K, C and M.

8.2 Mass, spring stiffness and damping terms

Because the large scale tests were conducted using a model caisson that had been the subject of extensive dynamic tests (Oumeraci & Kortenhaus, 1994) it was decided to base the numerical model on this structure. This made the selection of the mass, spring and damping terms relatively easy since detailed guidance was available in Marinscki &

Oumeraci, (1992), Oumeraci & Kortenhaus, (1994) and Oumeraci and Kortenhaus, (1994b).

8.2.1 Mass terms

Oumeraci & Kortenhaus defined the involved mass as having three components:

$$M = M_{Cai} + M_{Hyd} + M_{Geo}$$

Where M_{Cai}, M_{Hyd} and M_{Geo} are the caisson mass, the added mass from the water and the geodynamic mass. The mass of the caisson is given as 57.5 Tonnes, and the hydrodynamic mass as;

$$M_{hydro} = 0.543\rho_w d_w^2$$

for horizontal oscillations. Where d_w is the water depth at the caisson toe and ρ_w is the water density. Oumeraci & Kortenhaus (1994b) give the geodynamic mass as;

$$.M_{Geo} = \frac{0.76\rho_s R^3}{2-\gamma}$$

Where ρ_s and γ are the density and Poisson's ratio of the foundation soil and R is the equivalent 'radius' of the caisson base, given by;

$$R = \sqrt{\frac{BL}{\pi}}$$

Where B and L are the caisson breadth and length respectively. Using; ρ_w = 1000 kg/m^3, ρ_s = 1800 kg/m^3, γ = 0.35 and B = 3.1 m the mass was calculated to be, (in kN/m$_{run}$);

$$M = 17.5 + 0.543\, d_w^2$$

8.2.2 Stiffness terms

Oumeraci & Kortenhaus (1994b) define the stiffness coefficient as;

$$K = C_x A$$

Where C_x is the modulus of subgrade reaction (for horizontal motion) and A is the area of the foundation base. C_x is defined as;

$$Cx = 0.7Co\left[1 + \frac{2(B+L)}{A_m}\right]\sqrt{\frac{P}{Po}}$$

where C_0 is the modulus of subgrade reaction which was experimentally determined for a static normal stress (P_o) of 20 kN/m$_2$, A_m is the area of the foundation base per meter run and P is the actual static normal stress. Using;

$C_0 = 21000$ kN/m^3 (from Marinscki & Oumeraci, 1992) and $P = \frac{17.5g}{3.1}$ the stiffness was calculated to be;

k = 227.5 M/N per metre run.

8.2.3 Damping term

Oumeraci & Kortenhaus (1994) measured structural oscillations of the GWK model during pendulum tests. They calculated the logarithmic decrement of the oscillations (D) and found an average value for shallow water of 0.08. They suggest:

$$C = D(\sqrt{k_x \ M})$$

8.3 Model validation

The behaviour of this numerical model was tested in three ways. Firstly the model was made to 'ring' so that the natural frequency (T_n) could be observed. This was found to match the theoretical value for an undamped system of;

$$Tn = \sqrt{\frac{K}{M}}$$

A stepped driving force function was then applied to the model to provide a series of deflections under static loads. These were compared to values predicted using:

$$x = K/F \tag{8.2}$$

Finally a series of dynamic amplification factors ν were calculated, using the method described below in Section 8.2, for a range of saw tooth impulses of the form shown in Figure 8.2. These were compared to values calculated using the following standard equation which was obtained from the Shock and Vibration Handbook;

$$\nu = \left[1 - \frac{Tn}{\pi Td}\sin\frac{2\pi Td}{Tn} + \left(\frac{Tn}{\pi Td}\right)^2 \sin^2\frac{\pi Td}{Tn}\right]^{\frac{1}{2}} \tag{8.3}$$

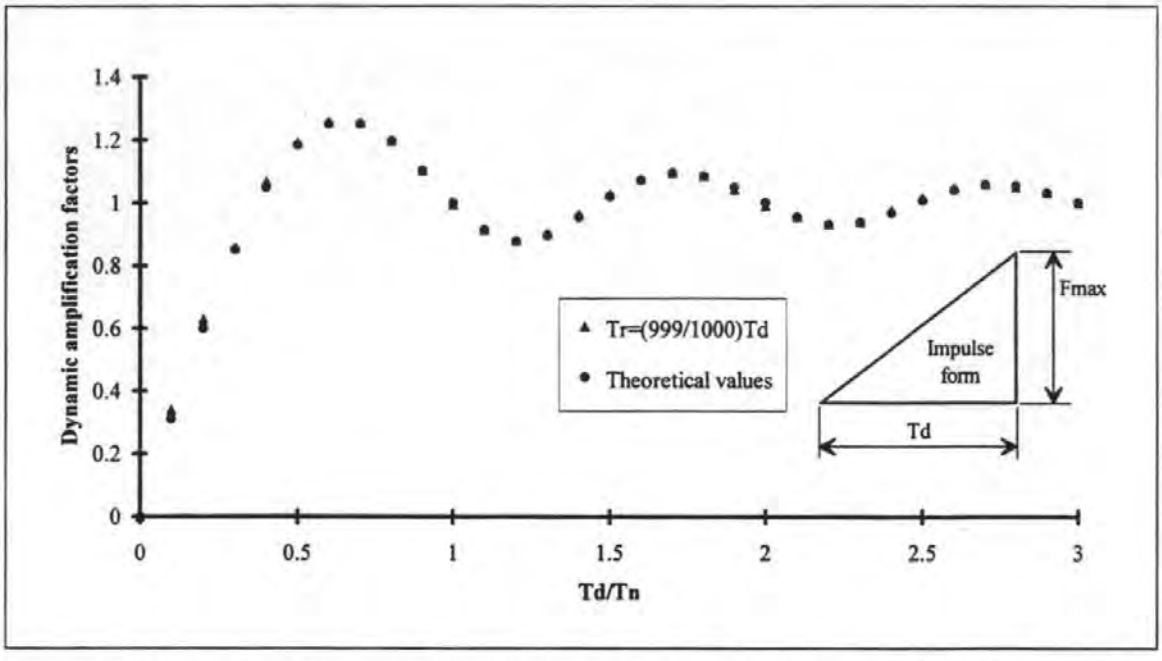

Figure 8.2. Comparison between dynamic amplification factors predicted by the numerical model (indicated with triangle) and calculated using equation 8.3 (indicated with small circles) for an impulse with a rise time equal to 99.9 % of the impulse duration.

The numerical model produced values which compared well to equation 8.3, as can be seen in Figure 8.2. Having performed well under these three tests the model was considered to be an accurate means of solving equation 8.1.

8.4 Calculation of dynamic amplification factors

The numerical model was used to calculate a larger range of dynamic amplification factors. Triangular impulses of varying duration (T_d) and relative rise time (T_r/T_d) were applied to the model to predict displacements. The maximum displacement caused by each impulse was used to calculate an effective static load using equations 2.3 and 2.4. Damping was set to zero to obtain the worst case. The results are presented in Figure 8.3 in the format used by Marinscki *et al*, (1992), and Oumeraci and Kortenhaus, (1994).

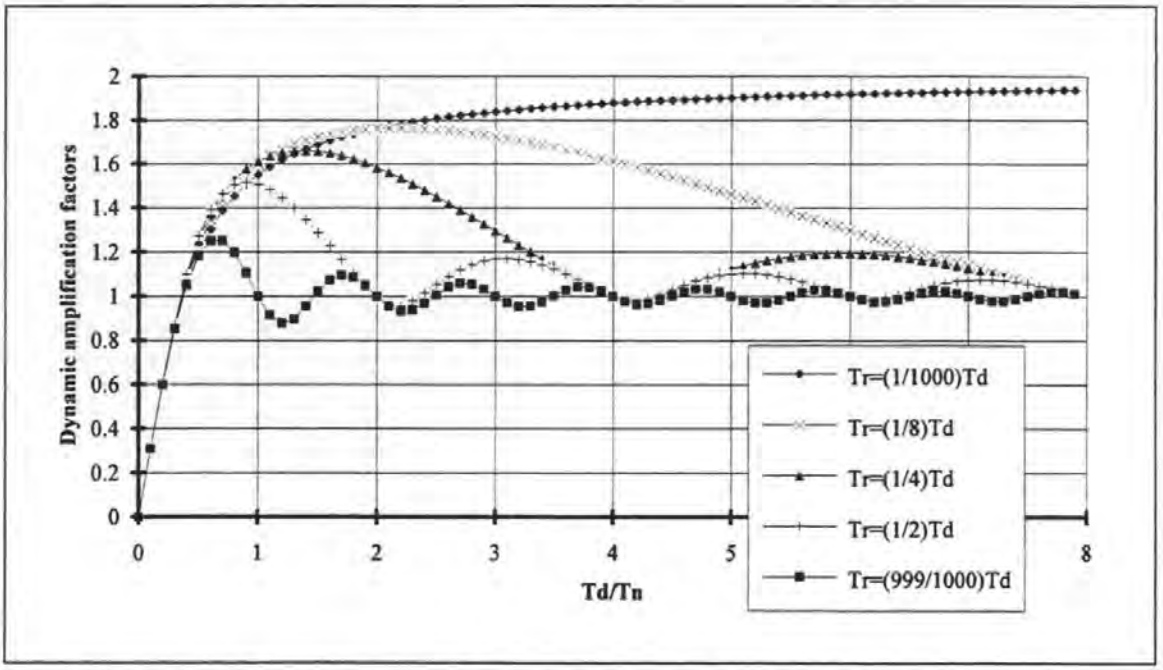

Figure 8.3. Dynamic amplification factors for triangular impulses of varying relative duration (T_d/T_n) and relative rise time (T_r/T_d).

It can be seen that in the region below $T_d/T_n = 0.5$, the form of the impulse is not important in determining v. Above this threshold the rise time becomes increasingly important, with the short, near instantaneous rise providing the largest values of v.

8.5 Prediction of effective static loads using dynamic amplification factors

The appropriateness of using dynamic amplification factors with wave impact force time histories as a replacement for a numerical model was tested. Regular wave force time histories were analysed to obtain the maximum force, rise time and impulse duration of each event. A characteristic relative rise time (T_r/T_d) was selected for each test and used to choose one of the functions illustrated in Figure 8.3. After assuming a natural period of 0.028 seconds (a prediction based on a scaled down version of the GWK caisson) the relative impulse duration of each event (T_d/T_n) was used to select a dynamic amplification factor. Equation 2.3 was then used to calculate an effective static load (F_{stat}) for each event. The accuracy of these predicted values was checked by driving the numerical model with the original force time history and using the maximum deflection of each event to calculate a value of F_{stat} with equation 2.4. The result obtained for test 290998 can be seen in Figure 8.4.

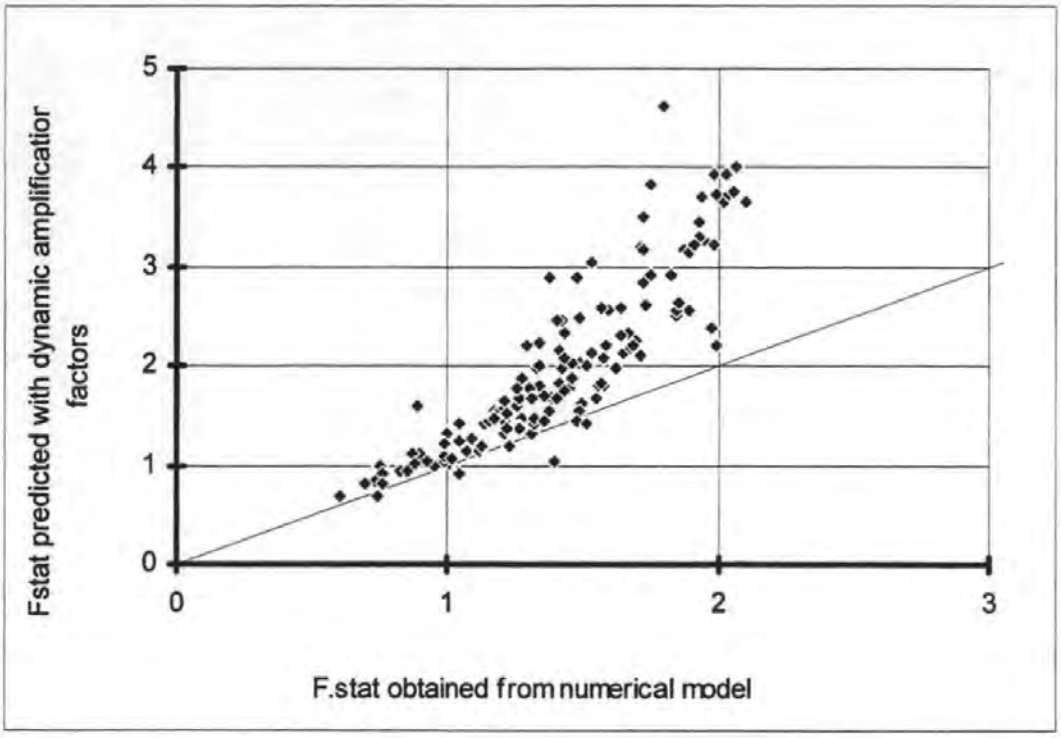

Figure 8.4. Comparison between effective static loads (in kN/m run) obtained with the numerical model and by applying dynamic amplification factors, Test 29099801.

The dynamic amplification factors were found to overpredict the response of the numerical model. Upon investigation it was found that this occurred because of the deviation of the shapes of the impulses from the simple triangle assumed in the derivation of the dynamic amplification factors.

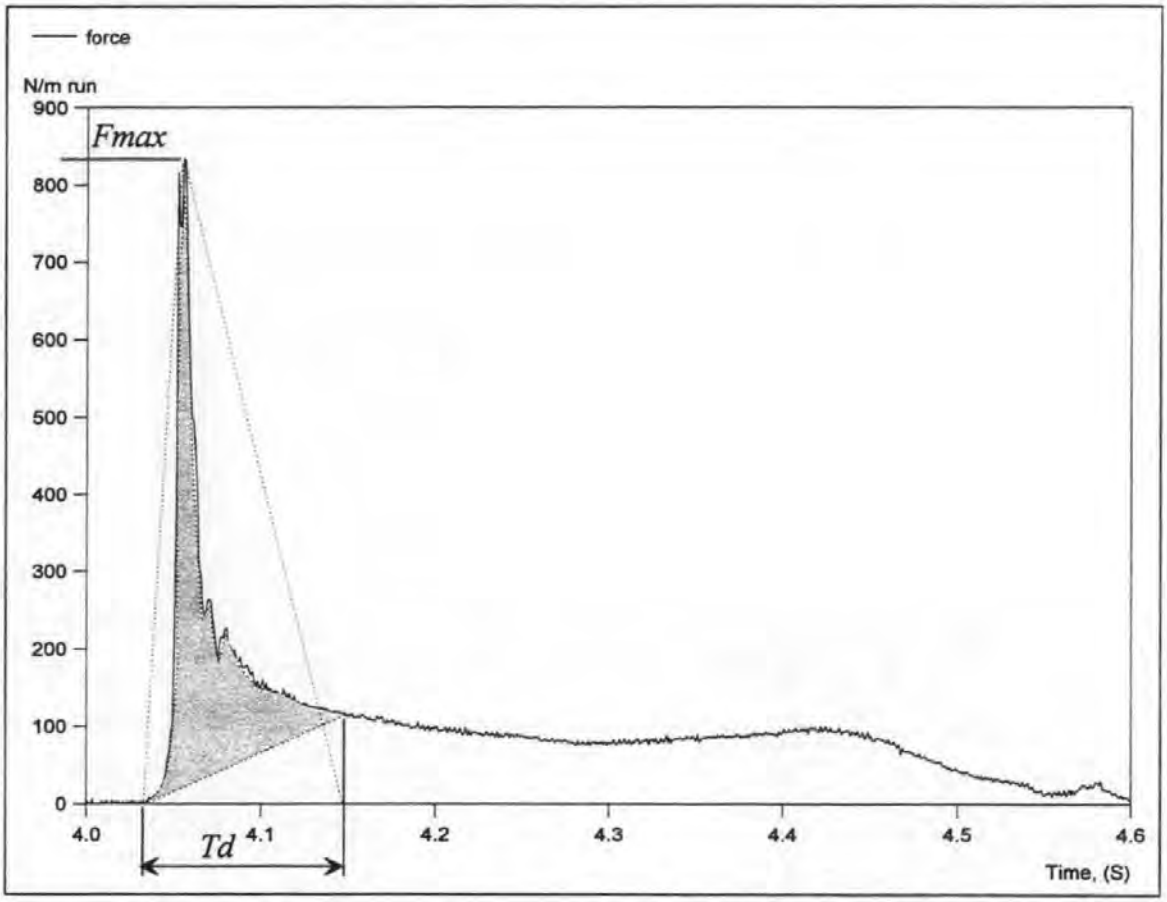

Figure 8.5. Typical wave impact force time history, the shaded region indicates the real impulse magnitude, whilst the region within the dotted line indicates the effective area.

Figure 8.5 shows a typical force time history. The actual impulse area (shaded) is less than that of a triangle of width T_d and height F_{max}. By using values of F_{max} and T_d with dynamic amplification factors derived for triangular impulses, the impulse area is, in effect, increased and the response overpredicted.

Two alternative solutions to this problem were considered; to calculate new dynamic amplification factors that were appropriate for the forms of the impulse under analysis, or to modify the form of the impulses to make them more suitable for factors already calculated. The former option was rejected because the near unique form of each wave impact force time history would require the calculation of so many dynamic amplification

factors that it would be simpler to predict dynamic response with the numerical model and the original force time history. Consequently, it was decided to modify the forms of the measured impulses.

One of the assumptions made in the derivation of Goda's design method was that the force impulse had the form shown in Figure 8.6. This assumption allowed Goda to interface a hydrodynamic model with a structure dynamic model (see section 2.6.4).

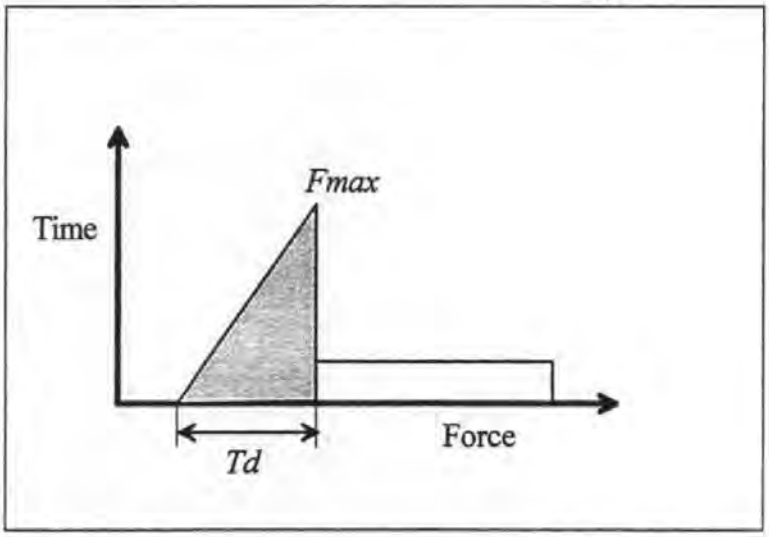

Figure 8.6. Impulse form assumed by Goda (1994), the shaded area indicates the impulse.

This meant that the impulse area was equal to:

$$I_{mp} = 0.5\, T_d\, F_{max} \tag{8.4}$$

Following this approach it was decided to transform the measured impulses from their various forms into simple triangles. Each impulse was processed to calculate an equivalent impulse force maximum ($F_{max.eq}$) and duration ($T_{d.eq}$) using:

$$I_{mp} = 0.5\, T_{d.eq}\, F_{max.eq} \tag{8.5}$$

Rather than limiting the form of the impulse to one standard shape, as Goda had done, it was decided to retain the overall proportion of the original impulse using;

$$\frac{T_{d.eq}}{F\max.eq} = \frac{T_d}{F\max} \tag{8.6}$$

All the regular wave data were processed in this way. The results obtained for test 29099801 can be seen in Figure 8.7.

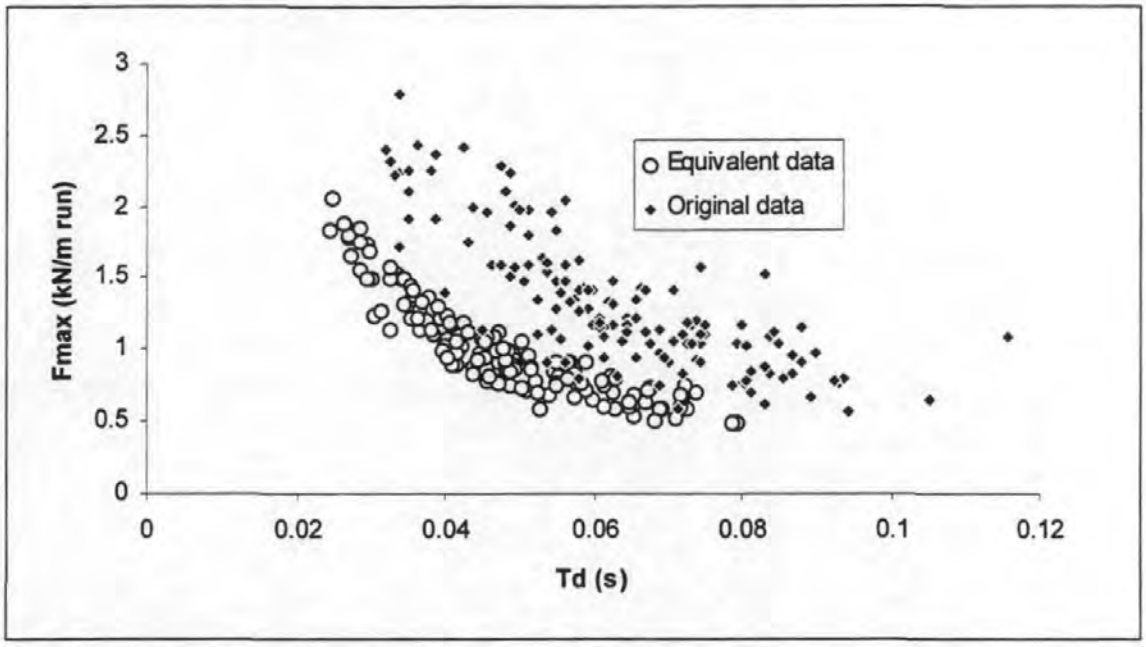

Figure 8.7. Effect of processing the results of test 29099801 using equations 8.5 and 8.6

The effect of this transformation was to group the data closely along a trend. The equivalent impulses allowed more accurate prediction of structure response, as can be seen in Figure 8.8.

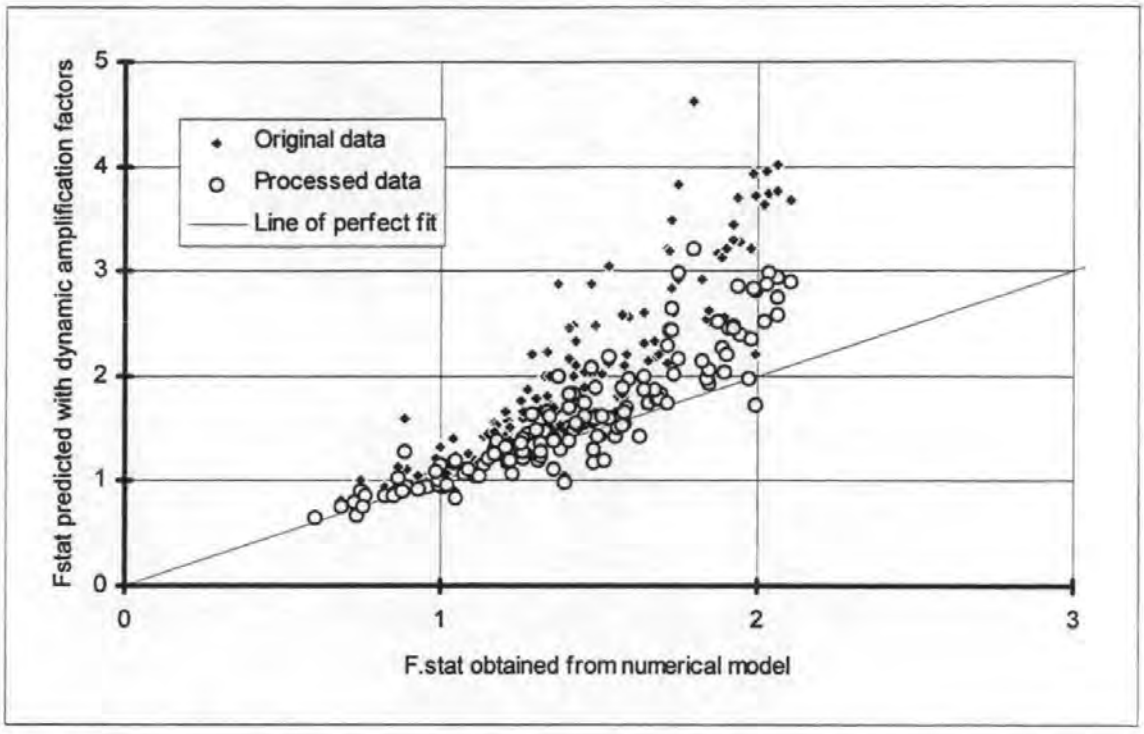

Figure 8.8. Comparison between effective static loads (in kN/m_{run}) obtained with the numerical model and by applying dynamic amplification factors, results of original and processed data from Test 29099801.

It can be seen in Figure 8.8 that the improvement is significant. However it can also be seen that despite the fact that all the impact events represented in this figure were nominally identical, they caused a wide range of effective static loads. This scatter arises from the wide variability in impulse form observed in the previous chapter.

8.6 Scatter in effective static loads

In Section 7.5 it was shown that a strong relationship exists between F_{max} and T_d. It can be seen in Figure 8.7 that the relationship between $F_{max.eq}$ and $T_{d.eq}$ is even stronger. The 'equivalent' data are shown again in Figure 8.9 which also shows a simple function;

$$F_{max.eq} = 0.044 / T_{d.eq} \qquad (8.7)$$

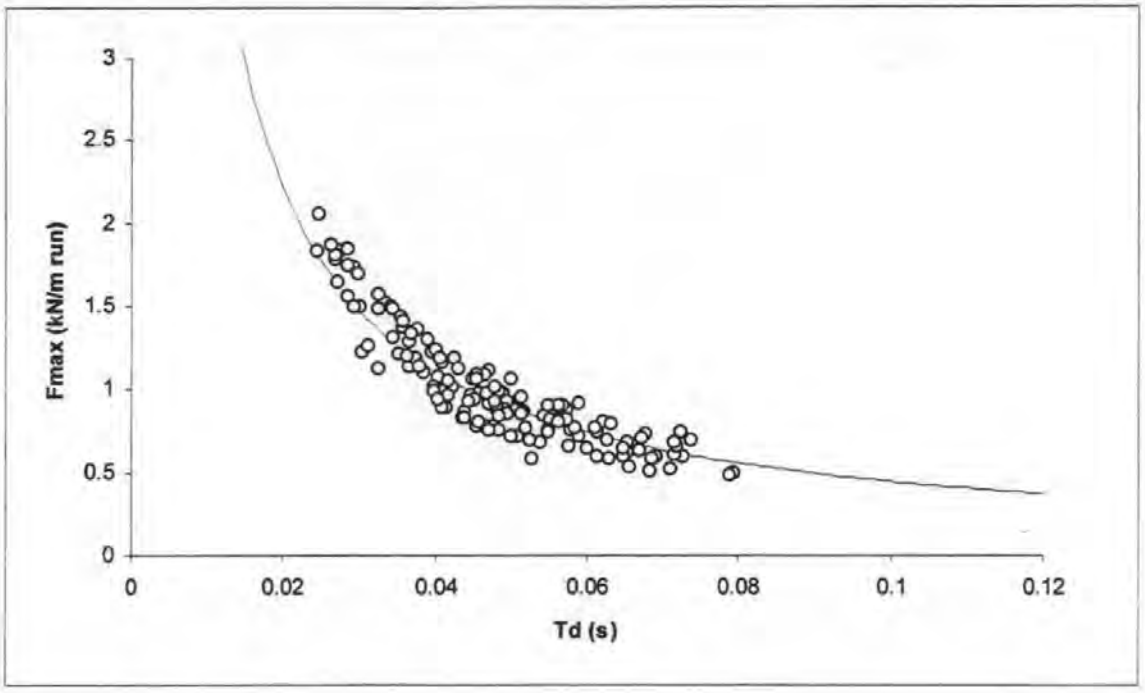

Figure 8.9. Equivalent loads from Test 29099801, with the trend line $F_{max.eq} = 0.044 / T_{d.eq}$.

This trend, which will be referred to as the dynamic load function, provides a good fit to the data and throws some light on the physical significance of the trends seen in the F_{max} T_d domain in the previous chapter.

The trend has a form similar to the one seen in Figure 7.9, in this case the constant has units of kNs/m_{run} or impulse per metre run. Since the equivalent impulse is a triangle, the product of $F_{max.eq}$ and $T_{d.eq}$, (and therefore the constant in equation 8.7) is double the average impulse area ($2I_{mp.average}$). Therefore;

- The scatter above and below the line in Figure 8.9 indicates scatter in the impulse magnitude, I_{mp}.
- The variation along the line indicates scatter in the impulse form.

Consequently;

- The scatter in impulse magnitude is relatively small.
- The scatter in impulse form is relatively large.

It follows that;

- Relatively few events are needed in order to establish the location of the

dynamic load function for regular wave impacts

- A relatively large number of events are needed to establish the spread of the data along the dynamic load function.

These observations help to explain the significance of the trends seen in the F_{max} T_d domain in the previous chapter. The dynamic load function is also useful in overcoming the large scatter in F_{stat} seen in Figure 8.8.

8.7 Prediction of effective static loads using the dynamic load function

In Figure 8.10 the form of equation 8.7 is shown with a set of dynamic amplification factors taken from Figure 8.3 which relate to test 29099801, *i.e.* $T_r = 0.25\ T_d$.

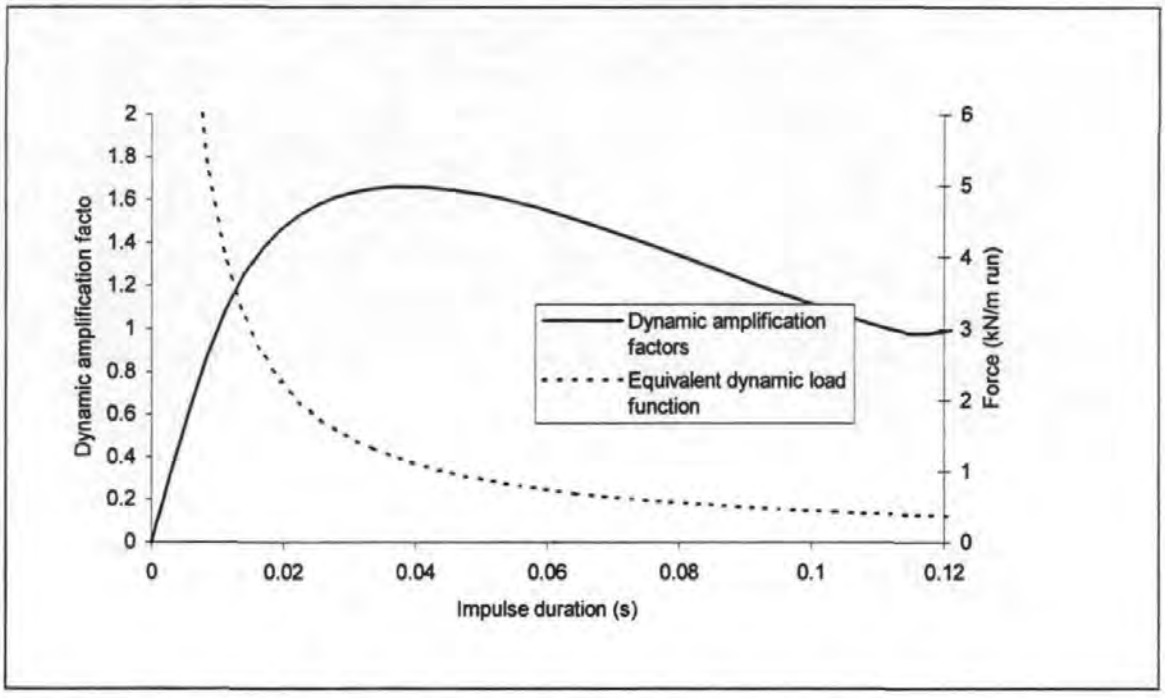

Figure 8.10. Dynamic load function from Figure 8.9 and dynamic amplification factors (from Figure 8.3), as functions of impulse duration.

The product of these two functions, which is shown in Figure 8.11 is the effective static load as a function of the impulse duration.

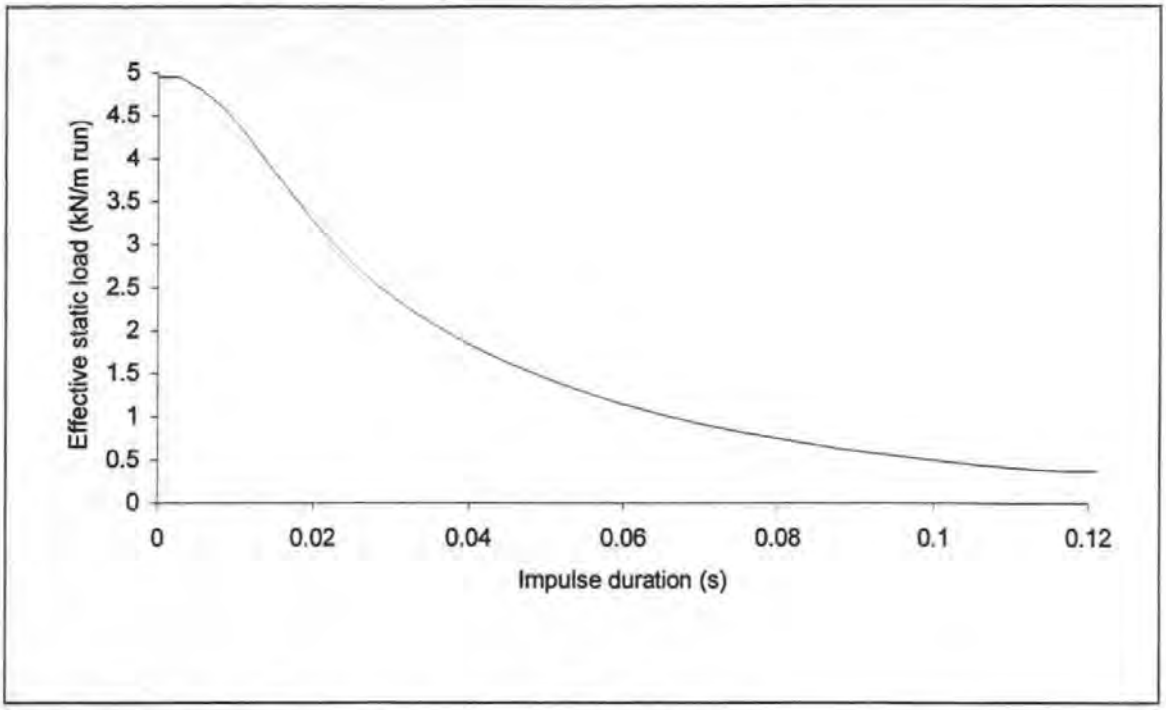

Figure 8.11. Effective static load function for Test 29099801.

It can be seen that this product reaches a definite maximum, in this case approximately 5 kN/m_{run}. This maxima might be considered by the designer as the maximum possible effective static load that the structure in question would have to cope with under the given wave conditions.

Considering the realities of impact events extremely low values of T_d associated with the highest values of F_{stat} are unrealistic. A more useful maximum value of F_{stat} could be found by investigating the distribution of the measured data along the dynamic load function as in Figure 8.9. Since such data is obtained from model tests the designer must also consider how scale might effect this spread. This subject will be considered further in Chapter 9.

8.8 Summary

A single degree of freedom mass-spring-dashpot numerical model was developed to describe the motion of the large scale GWK caisson model. This was used to calculate a range of dynamic amplification factors. Both the numerical model and the dynamic amplification factors were then used to predict structure motion. The dynamic amplification factors are found to overpredict relative to the numerical model. This was found to be due to the tendency of wave impact force time histories to be concave, rather

than a simple triangle which was the impulse form used when the dynamic amplification factors were derived. A solution was found from the design method of Goda which largely corrects the error. However another significant problem was revealed, the range of effective static loads that are associated with nominally identical wave impact events is extreme. This implies a significant inherent uncertainty in any prediction of dynamic response that is based on only a single, or few impact events. The transformation of the impulse to an effective impulse form has the effect of modifying the relationship between F_{max} and T_d seen in the previous chapter and revealing its physical significance. This dynamic load function is then used with a range of dynamic amplification factors to overcome the problem of scatter in impulse form and provide a maximum F_{stat} which might be used for design purposes.

Chapter 9

Scaling of wave impulse loads

9.0 Introduction

A great need for a laboratory based scale comparison between wave impact tests was identified in Chapter 2. It was therefore decided to compare the results of the large and small scale tests. The flumes were not geometrically similar so it was not possible to match tests at the two scales by Froude scaling the wave heights and periods. Instead, attempts were made to relate tests through approximate geometric similarity of breaker form. An equivalent length scale was then found from the measured momentum exchanges at the walls. The scale comparison was made between the 'effective' impulses in order that it be meaningful in the context of the prediction of structural dynamic effects. In order to illustrate how this approach could be used for practical design, one of the scale comparisons was developed to predict an effective static design load. The force reduction factors developed in Chapter 6 were used to account for the effects of aeration. The predicted value is found to be larger than an equivalent value obtained using the design method of Goda.

9.1 Matched large and small scale tests

The GWK and UoP flumes were not geometrically similar. The large scale flume was 16.2 times longer, but only 5.6 times as wide and 4.6 times as deep. In addition the UoP foreshore was smooth with a simple slope of 1:4.5 whereas the GWK model had a 2 metre wide rubble mound berm with a 1:1.5 sloping front. Because of these differences, waves that were generated to achieve Froude similitude did not develop geometrically similar breaker forms. Since the breaker form is intrinsically linked to the wave impact loads no similarity could then be expected in the measured pressure and force time histories. It was felt that the great need for scale tests warranted the adoption of an unorthodox approach to

overcome this problem. Consequently the video records were examined to match large and small scale tests on the basis of approximate similarity of breaker shape.

As was seen in chapter 6, all the small scale tests involved breakers which entrapped air pockets. Due to the foreshore conditions these pockets tended to be sealed at the toe of the wall. Conversely the GWK foreshore geometry tended to produce air pocket breakers that sealed air higher up the wall. The breakers that occurred during test 08089603 were found to have the closest form to the GWK waves. Its air pockets were still rather low, but not as low as those of test 08089604, and the breaker form did not fluctuate between air pocket and flip through as they did during tests 08089602, 08089605 and 08089606. Three GWK tests were found to match 08089603, these were 01029404, 01029407 and 02029403. Drawings of the breaker shapes that occurred during these tests are shown in Figures 9.1 to 9.3.

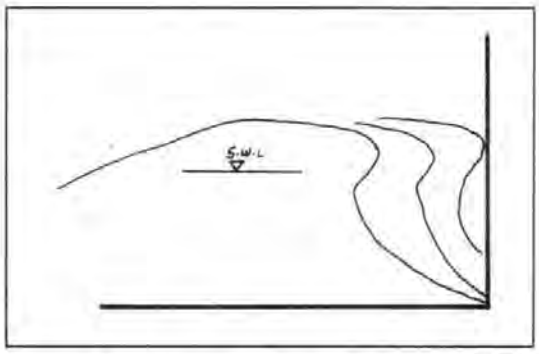

Figure 9.1. Breaker shape during test 01029404.

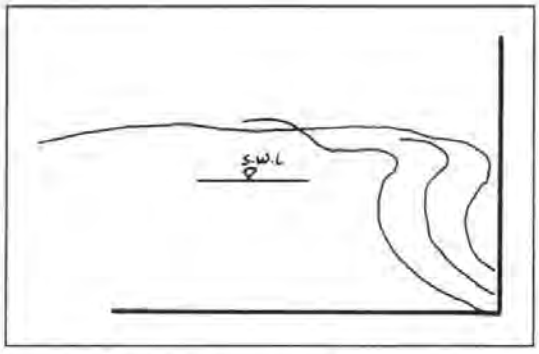

Figure 9.2. Breaker shape during test 01029407.

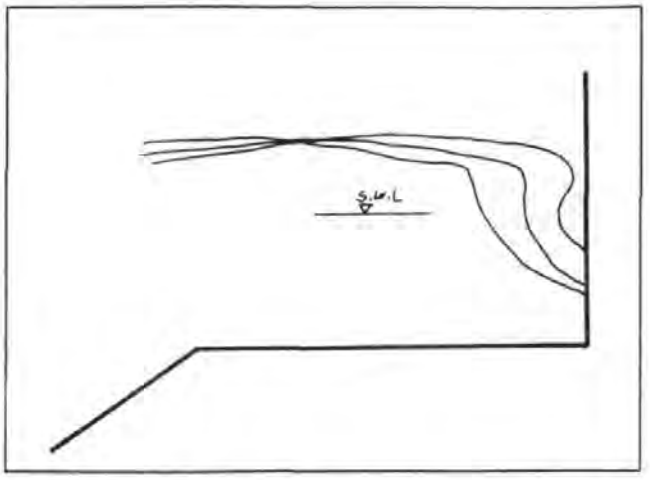

Figure 9.3. Breaker shape during test 02029403.

The wave heights and periods of these tests were then compared to those of the small scale tests to try and identify appropriate length scales. Due to the lack of similarity in the models, the scale ratio of wave period never matched the root of the period scale, i.e.

$$N_T \neq \sqrt{N_H}$$

Where the subscripts T and H refer to wave height and period respectively.

A length scale (N_L) was therefore established by comparing the momentum exchange measured during the two tests. This was found by integrating the area under the respective force time histories for one wave period, i.e.

$$N_L^{5/2} = \frac{\int F_{LS}\, dt}{\int F_{SS}\, dt} \qquad (9.1)$$

The resulting length scales are shown in Table 9.1.

Small scale test	Large scale test	N_L
O8O896O3	O1O294O4	7.19
O8O896O3	O1O294O7	8.43
O8O896O3	O2O294O3	10.25

Table 9.1. Length scale ratios.

9.2 Scale comparison of $F_{max.eq}$ and $T_{d.eq}$

A comparison of the equivalent force maxima and impulse durations of the large scale tests with the values obtained by scaling up the results of test 08089603 can be seen in Figures 9.4 to 9.6. The small scale data has been scaled using the Froude law. These figures also show the dynamic load function of the small scale test which has also been scaled using;

$$F_{\max.eq} = \frac{2\overline{Imp}}{T_{d.eq}} \qquad \text{(see Section 8.4)}$$

and,

$$I_{mp.LS} = \overline{Imp.ss} \times N_L^{5/2} \qquad (9.2)$$

where $\overline{Imp.ss}$ is the average of the impulse areas of the small scale test. +/- 10 % lines have also been shown to assist interpretation of the scatter in the data.

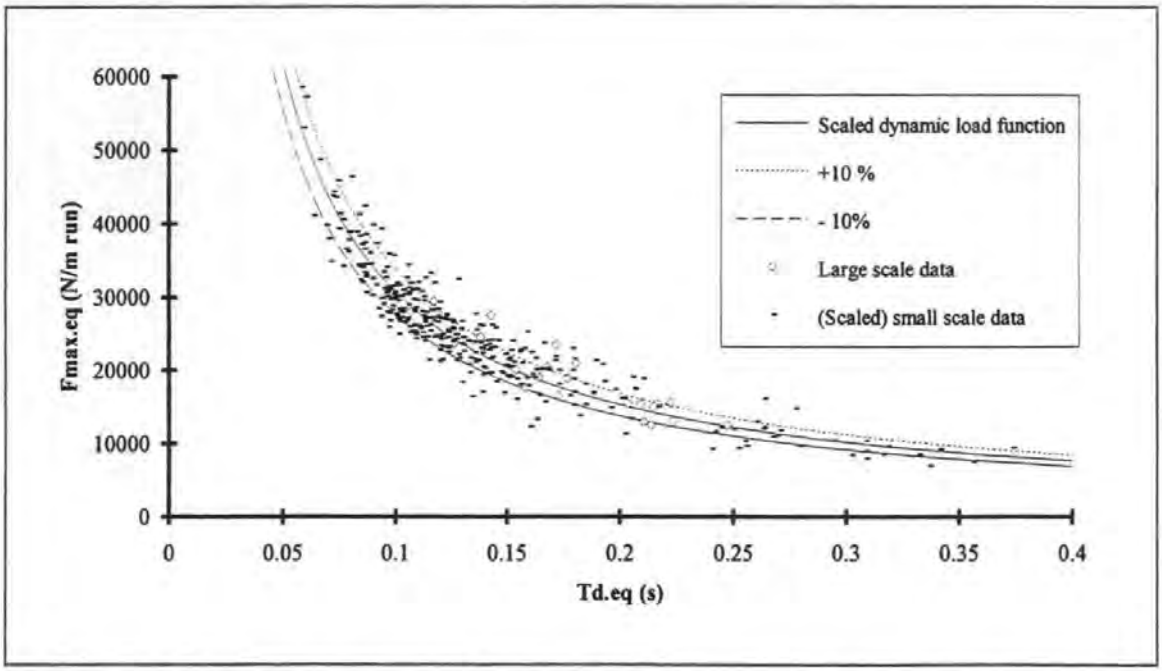

Figure 9.4. Large scale data from test 01029404 compared to data from 08089603 that has been scaled by Froude ($N_L = 7.19$).

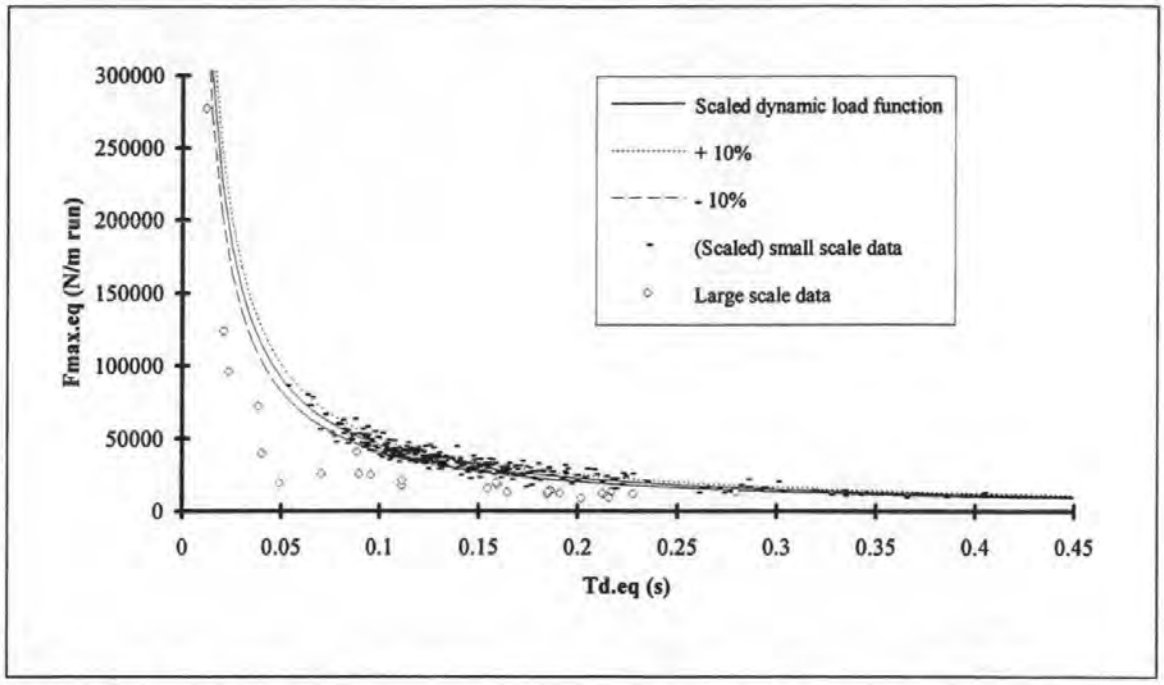

Figure 9.5. Large scale data from test 01029407 compared to data from 08089603 that has been scaled by Froude (N_L = 8.43).

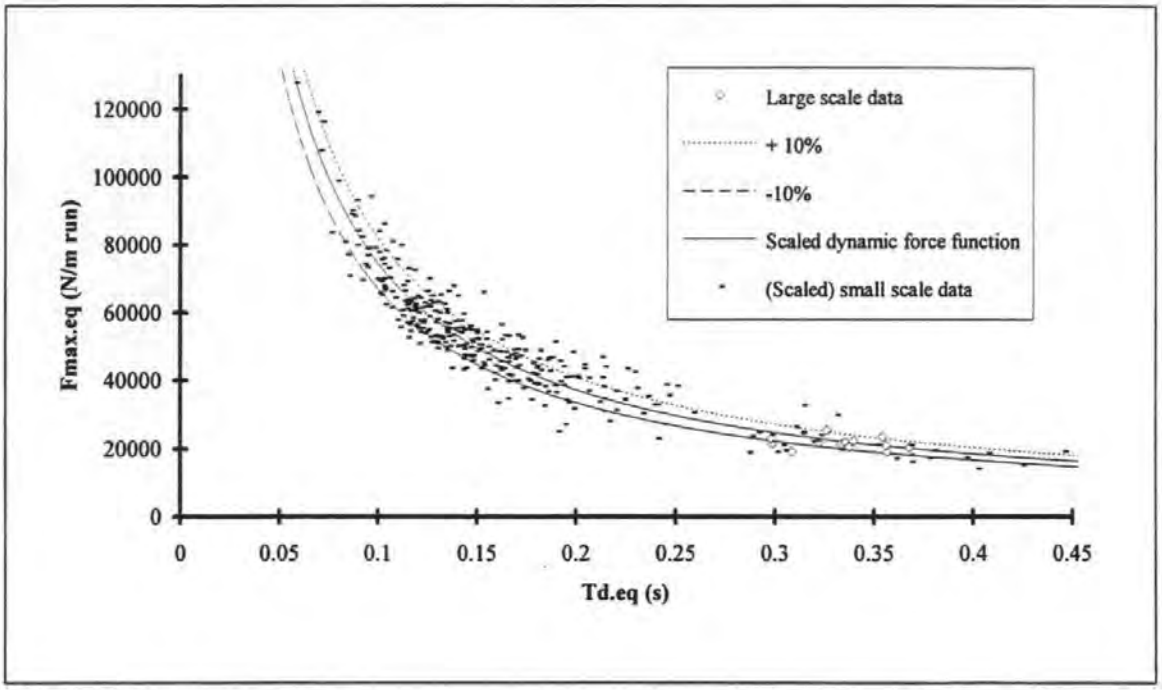

Figure 9.6. Large scale data from test 02029403 compared to data from 08089603 that has been scaled by Froude (N_L = 10.25).

Figures 9.4 to 9.6 suggest that the impulse magnitude scales by the Froude law, at least between small and large scale fresh water waves. The comparison of individual values of $F_{max.eq}$ and $T_{d.eq}$ was less strong.

Having translated results from small to large scale they were then used to calculate a design load for the large scale model using the method developed in Chapter 8. Given the unusual nature of the scale comparison and the rather inconclusive results for $F_{max.eq}$ and $T_{d.eq}$ this analysis was conducted for only one case, the comparison between tests 08089603 and 01029404.

9.3 A first estimation of design large scale effective static loads

It was seen in section 8.4 that a maximum value for F_{stat} could be obtained, as $T_{d.eq}$ tends towards zero, from the product of a dynamic load function and a range of dynamic amplification factors. This maximum F_{stat} will be conservative in most cases because of the very low values of $T_{d.eq}$, and associated very high values of $F_{max.eq}$. It is therefore reasonable to limit the range of the dynamic load function so that a proper lower limit can be established for the impulse duration. This limit can be based on the data from which it was derived. For example, the maximum and minimum values of $F_{max.eq}$ obtained from test 08089603 were 1216 N/m_{run} and 136 N/m_{run}. To avoid the use of extreme values, other limits could be found by statistical means, for example 95 % of the data were above 203 N/m_{run} and 95 % were below 770 N/m_{run}. These values can be used to limit the range of the dynamic load function at small scale. When this limited function is then translated to the large scale it is necessary to account for the associated increase in entrained aeration. The results of the drop tests implied that greater aeration tends to decrease the magnitude of the force maxima (see section 6.4). The scale comparison shown in the previous section suggested that the impulse magnitude scales by Froude. It follows that the impulse duration must increase at the large scale.

For this example a typical large scale level of entrained air of 5 % was assumed (see for example the prototype measurements of aeration given by Crawford, *et al*, 1997). Equations 6.4 and 6.5 were then used to calculate a first approximation of a force attenuation factor of 0.71. The large scale limits of the dynamic load function were then calculated using Froude and this force reduction factor;

$$F_{LS} = F_{SS} \times N_L^2 \times 0.71 \qquad (9.3)$$

This provided large scale limits of 7.5 kN/m_{run} and 28.3 kN/m_{run}. In Figure 9.7 these limits have been applied to the dynamic load function which was shown in Figure 9.4.

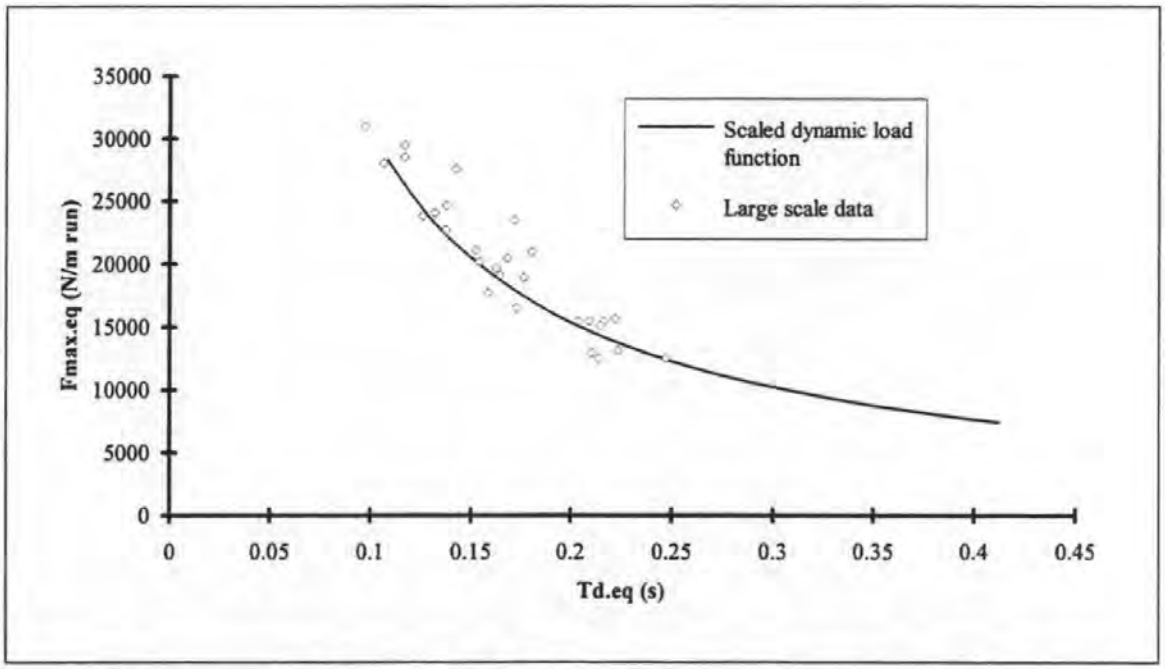

Figure 9.7. Dynamic load function from test 08089603 which has been scaled by Froude ($N_L = 7.19$) and limited in range, compared with large scale data from test 01029404.

Using the technique described in section 8.5 a range of dynamic amplification factors was then multiplied to the limited dynamic load function.

This provided a range of effective static loads which are shown as the solid line in Figure 9.8. Also shown are individual values of F_{stat} which were obtained by using the force time history of the large scale test as a forcing function for the numerical model described in Chapter 8. A prediction of F_{stat} obtained using the design method of Goda is shown as a horizontal dotted line.

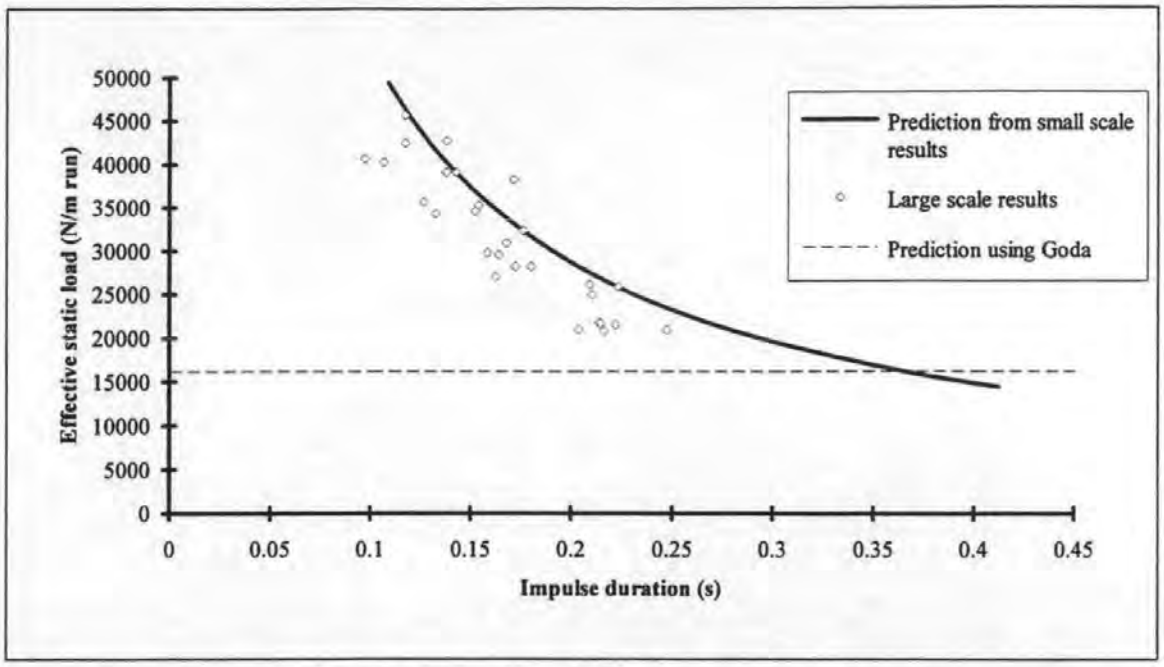

Figure 9.8. Effective static load function predicted using data from 08089603, compared to a value predicted with the design method of Goda and effective static loads obtained with the numerical model and the force time history of 01029404.

It can be seen that the predicted line matches the trend of the large scale results very well and their range moderately well. In practice the designer would be interested in the maximum value of F_{stat}, and this value is predicted to within 10 %. The effective static force predicted using the design method of Goda is considerably lower than the values obtained by the other two methods. The significance of this discrepancy will be discussed in Chapter 10.

9.5 Summary

In this chapter the results of a small scale wave impact test are scaled by Froude and attenuated to account for the effects of aeration. The large scatter in impulse form is then dealt with to enable a prediction of a large scale design load using dynamic amplification factors. This is shown to compare well with a value obtained by using a measured large scale force record as a driving function for a numerical model of dynamic behaviour.

Chapter 10

Discussion and further work

10.0 Introduction

The literature review presented in Chapter 2 established that the problem of scaling wave impact loads is intrinsically linked to problems associated with aeration, breaker shape and structural response. This can be appreciated by considering that at the moment when a wave impacting on a caisson breakwater causes its maximum load, the impact pressures, aeration, breaker shape and structural motion all influence each other.

The ability to describe wave impacts in a purely theoretical way would require a detailed description of wave development and internal kinematics under a comprehensive range of boundary conditions, in addition to temporal and spatial distributions of bubble quantity and size and a thorough description of the processes of compressible liquid - solid impact. In addition, the response of the structure and the way this influences the load would have to be understood. Studying one of these problems in isolation is philosophically questionable and raises the likelihood that results will not be suitable for interpretation in the contexts of the other aspects of the problem. This presents a significant problem when wave impacts are studied through physical modelling using the classical reductionist approach because the number of unknowns is so large that the matrix of test conditions is too great.

Despite the many unknowns, engineers have been able to successfully develop design methods for vertical breakwaters, the most successful of these was provided by Goda (1974). This has been achieved through the application of engineering judgement and the use of empirical data to overcome gaps in knowledge and by applying factors of safety to allow for inherent uncertainty. An implication can be drawn that though researching the problem through physical mode testing in a classical reductionist way is very difficult it may be productive to use physical models to develop design methods.

Consequently, this study is philosophically positioned between wave impact tests performed for classical research and those conducted for design purposes. Previous work has been reviewed to develop a philosophical framework that links impact loads, aeration, scale, breaker shape and structural response in a way that is meaningful to caisson breakwater design. This was used to determine which experiments were to be done and how they were interpreted.

Although the breadth of this study benefits the development of a design methodology, it also necessarily limits the extent to which any individual part could be developed. Practical limits also apply to the scope of the work. Attention has been limited to seaward sliding of the upright section. Reducing the problem in this way was useful because it simplified the description of structural response and made the form of the vertical distribution of pressure largely irrelevant. It is justified in the context of vertical breakwater research because it is the primary failure mode for most caisson breakwaters.

The approach that has been developed in this study is intended to predict the design effective static load. This is a particularly important property because it represents both the maximum wave load and the characteristics of the structural response, i.e. both hydrodynamics and structural dynamics. The methodology is based on the measurement and interpretation of the force impulse. It is shown that nominally identical waves in a train produce a band of data in the F_{max} T_d domain (see Figure 7.9). Similar bands were also shown in the results of the drop test data (Figure 6.66), each one representing a different level of momentum. From the perspective of the design engineer it is the band that is furthest from the origin (furthest from $F_{max} = T_d = 0$) that should be considered first, and the left hand limit of this band, i.e. the maximum value of F_{max} and lowest value of T_d that the structure should be designed against since these events will induce the greatest structural response. The designer needs to establish this point and use it to predict an effective static load.

Such data is obtained through model testing. The designer therefore needs to know how the data of interest varies with scale. The drop test results showed that additional entrained air should move the data towards greater values of T_d and smaller values of F_{max}. Prototype marine waves contain more entrained air, so in scaling data to describe prototype conditions F_{max} should be attenuated and T_d increased.

The banding seen in Figures 6.66 and 7.9 represents events with similar momentum. Clearly, the band that an event falls on to is linked to the size of the wave since bigger waves have more momentum. It is also linked with the breaker shape. Figure 7.5 showed that the proportion of the wave momentum that contributes to the impulse varies with the breaker type. Therefore, the band furthest from the origin will not necessarily be made up of the biggest waves but those with a combination of being both large and having a dangerous breaker shape.

At the end of Chapter 9 large scale effective static loads were predicted from the results of a small scale model test. The predicted values provided a good match to the data obtained by using a large scale force time history as a driving function for a numerical model. This one example is not enough to validate the analysis, so it is given as an example of a new procedure rather than a proof of it.

This work has been based on laboratory rather than field work. This is due to the lack of wave impact field data in general, and the lack of relevant data quoted in the literature that is available. Before the methodology in this thesis can be considered to be properly validated a comparison should be made between results in this study and field measurements of wave momentum, breaker shape, impulse magnitude, impulse form, aeration and structural response.

10.1 The measurement of wave impact pressures

The property of the wave loading most commonly quoted in literature is the maximum impact pressure P_{max}. Some of the problems which accompany the measurement of P_{max} were revealed in the literature review. It was shown that recorded pressures depend upon the experiment instrumentation and methodology as well as the physics of the impact. P_{max} is, in concept, the maximum pressure occurring at any elevation and at any time during the impact. In reality this pressure maxima is almost impossible to measure because it is highly transient and localised. For any given measurement of P_{max} a higher value could probably have been obtained if a greater number of transducers were used with smaller surface areas and sampled at higher rates. This naturally makes P_{max} difficult to measure with any confidence and an insubstantial focus of attention for wave impact research.

It is important to consider the extent to which these problems might have influenced the results presented in this study. Before doing this it should be noted that although some values of P_{max} are shown in this work (see for example Figures 6.52 and 7.6) they are not used in the new design methodology. The pressure time histories were used to calculate force time histories that were then used to make predictions of structural response.

During the experiments the sample frequencies were always less than the natural frequencies of the pressure transducers by approximately an order of magnitude. In addition, the measured pressures very rarely approached the upper limit of the working ranges of the transducers. Consequently no errors are expected due to poor instrument performance.

The results given in sections 6.1.3 and 6.1.4 show that for some tests the sample period was equal to the rise time and consequently inadequate for the accurate measurement of P_{max}. In addition, it is clear that the measured pressures depend upon the size of the sensitive area of the transducer. Pressures are measured more accurately with smaller transducers, whilst forces are measured more accurately with larger ones. This is illustrated in Figure 10.1 which shows how variations in pressure over the face of a transducer is averaged out to provide a single measurement. The greater the spatial coverage then the more accurate is the measurement of force.

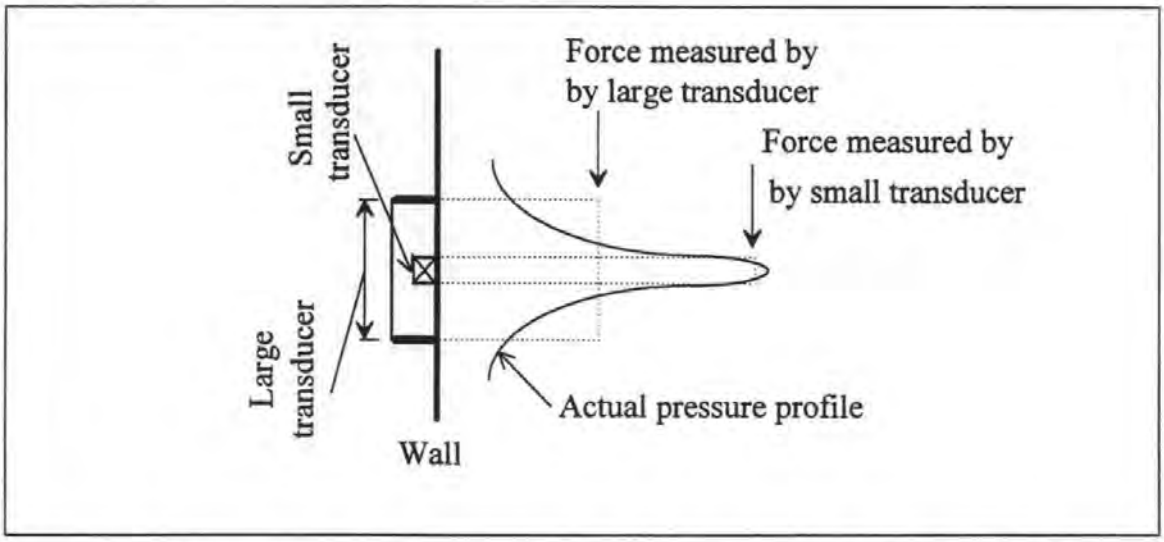

Figure 10.1. Measurement of a pressure profile using two pressure transducers of differing size.

Ultimately, if forces are to be measured using pressure transducers then the overall accuracy will depend upon the extent of the area covered by the transducers. During the small scale tests the coverage was good, with pressures being measured over 98 mm of the wall elevation during impacts of waves of up to 127 mm in height. At large scale the pressure transducers were small relative to the wave heights, the measurements were taken with 5 transducers 18 mm in diameter recording the forces caused by waves of up to 1.1 m.

It is very difficult, if not impossible, to determine the extent of the errors in the measured forces that have arisen due to the sample frequency and transducer size and location. This is because there are no perfectly correct pressure time histories or pressure profiles against which measurements can be compared. This problem is not specific to this study but general to wave impact tests. Instead, it is necessary to determine whether or not the experimental arrangement is adequate for the task. In this case it was necessary to obtain pressure time histories in order to calculate force time histories from which predictions of structural response are made. To test this it will be assumed that an extreme error occurs and the actual force maxima is twice the measured value, i.e. 50 % error in F_{max}.

This would result in an underestimation which can be visualised as an approximately triangular error impulse of width (T_d) equal to the sample period (0.5 ms) and height equal to F_{max}. It is possible to estimate the error that this would introduce into the predicted structural response by referring to Figure 8.3. The natural period (T_d) of the large scale physical model was estimated at 0.056 s, therefore the ratio of the duration of the error impulse to the natural period (T_d/T_n) was approximately 1/100. From Figure 8.3 the associated value of ν can be estimated to be 0.03. This value is independent of the form of the error impulse. Consequently, with a 50 % error in the measurement of F_{max}, a 3 % error is introduced into the predicted structural response. Considering the extent of the associated uncertainties this error is small.

The natural period of the large scale model was quite short probably because of the shallow depth of the GWK. Prototype measurement of natural period have shown values of T_n from 0.2 to 1 second. If the allowable error in predicted structure response is set to 5 %, and it is again assumed that F_{max} is only 50 % of the true value, then, using the above procedure, a sample frequency of 320 Hz is found to be adequate. If this is scaled down by a typical

1:50 then an equivalent small scale sample frequency of 2.3 kH is found. It is therefore concluded that the small scale sample frequencies are appropriate for the tests.

10.2 The importance of the force impulse

The review of previous research revealed that different aspects of the problem could be linked through the force impulse. Knowledge of the force impulse is particularly important in predicting structural response. Nevertheless, it has received relatively little attention during previous studies. In this study a definition has been proposed for the force impulse. It has been measured for multiple events and a range of breaker shapes and its relationship with aeration, scale and structural response has been considered.

An assumption has been made throughout this work that the impulse is basically triangular in form. This assumption is supported by observations made during this and many other studies. It is the case, however, that some impulses exhibit special features such as the double peaks and oscillations shown in section 6.1.9. Although Oumeraci and Kortenhaus (1994) showed that they could influence dynamic behaviour their effects have not been considered here. It was decided to study the basic impulse before investigating special cases.

It is not possible to measure impulse pressures in isolation from quasi-static pressures nor is there any theoretical means of distinguishing the two regions. The impulse definition chosen in Chapter 7 was based on the following reasoning: wave impacts are associated with steep fronted or breaking waves. A regular quasi-sinusoidal wave will steepen as it passes over a shallow foreshore because the shoaling drag apparently splits the monochromatic wave into a range of frequencies. Although in general wave velocity decreases with increasing frequency, in this case drag effects the lower frequencies more strongly and this causes the higher frequencies to translate forward and steepen the front of the wave. The force a wave imparts to the structure it strikes represents an exchange of momentum. The momentum exchange associated with any individual frequency may not in itself cause a large force, but when many frequencies arrive at the wall simultaneously, as with a steep or overhanging wave, the sum of their forces may be considerable. The approach to defining the impulse which is illustrated in Figure 7.4 represents an estimation

of the division between the forces associated with the original frequency, and the momenta of the higher frequencies.

It is worth considering that the term 'Impulse' is applied to wave impact loads in a rather loose way. The high initial values in breaking wave pressure and force time histories are usually described as being 'shock' or 'impulsive' loads because they are particularly high, not because the pressures necessarily arise due to compressible behaviour of the water. When the dynamic behaviour of the structure is considered the term 'impulsive' takes on a different meaning. In this case an impulsive load is one that is brief enough, relative to the natural period of the structure, to generate dynamic behaviour. This means that the load from a small non breaking wave may be impulsive relative to a structure with high inertia, or conversely that the forces from a large impacting wave of long duration may not be impulsive relative to a structural element with a short natural period.

When the force impulses of multiple events were measured, relationships emerged between the maximum force (F_{max}) and the impulse duration (T_d), as shown in Figure 7.9. It seems reasonable that they are related to the relationships in the maximum impact pressure (P_{max}), pressure rise time (T_{pr}) domain shown in Figure 3.2 and the bands in the F_{max} T_{fr} domain shown in Figure 6.66. The physical significance of these relationships is not immediately clear, but some meaning can be drawn from the 'equivalent' force maxima and impulse durations. The values of $F_{max.eq}$ and $T_{d.eq}$ obtained during any test lie closely along its dynamic force function;

$$F_{max.eq} = 2I_{mp}/T_{d.eq}$$

Where I_{mp} is the impulse magnitude. The trend observed in the F_{max} T_d domain is less perfect because the real impulses are not exactly triangular. Similarly, the trends which arise in the P_{max} T_{pr} domain are even less clear because, in addition to not being exactly triangular, the pressure rise impulses are only part of the whole force impulse.

The procedure of converting the real impulses into equivalent impulses was performed to improve predictions of structural response made through the application of dynamic amplification factors. The process modified the forces and durations significantly for most of the tests, but improved the predictability of the effective static loads. The process had a

strong precedent in a similar technique used by Goda (1994). The assumption that the proportion of the equivalent triangle should be the same as that of the original impulse (equation 8.6) is somewhat arbitrary, and may be open to improvement. This will have some influence on the range of the dynamic load function (see Figure 9.7) and may be used to improve the match between the higher values of F_{stat} shown in Figure 9.8. The deviation of the higher values from the line of perfect fit in this figure is noticeable. These data relate to the impacts which generated the highest force maxima and so were furthest from the form of a simple triangle. It is this which appears to have caused the deviation. The pressures measured during this test were the highest obtained during all the small scale tests (they included values of over $23\rho gH$). In this aspect they were extreme, even amongst those tests which were arranged to provide high impact loads, and not representative of the majority of impact events.

The relationship between force impulse and breaker shape was investigated using solitary wave impacts. It was found that the largest, and therefore potentially most dangerous impulse occurred with the air pocket impact. The magnitude of the impulse was normalised to the total momentum exchange at the wall to provide the impulse proportion (IP). This is an interesting property because it may provide a quantitative description of breaker form to replace the qualitative descriptions that have been used till now.

Since the impulse largely determines the dynamic behaviour of a given structure, its variation in form and magnitude should be investigated under a range of different foreshore slopes, wall angles, berm sizes, angle of wave attack and other factors known to influence wave impact loading. The force impulse has the practical advantage that it is much easier to accurately measure than the maximum impact pressure since it is not as sensitive to transducer location, sample frequency, or flume noise.

10.3 Calculation of dynamic response

The design of a stable caisson breakwater is a dynamic problem. This has been recognised since at least 1920 when Hiroi published his design method. The majority of caisson breakwaters are designed using Goda's method which deals with the structure as a dynamic system. However, this is not apparent to the user so is largely unrecognised.

In the methodology developed in this work the wave loads are measured then used to calculate structural response. This is done in two ways, through a single degree of freedom dynamic model and by applying dynamic amplification factors derived from that model. The latter approach was tried because previous studies had recommended it in order to simplify the calculation of dynamic response to a one line calculation. This recommendation is found to be unsupported in practice. This is because the amount of analysis and processing needed to apply a dynamic amplification factor means that it would normally be quicker to use a simple numerical model. However, it was also found that the scatter in F_{stat} caused by nominally identical regular waves impact events was very large. This means that any analysis based on a single or only a few impact events can not properly represent the range of possible structure responses. Dynamic amplification factors are very useful for describing a range of responses, as was shown in Figures 8.10 and 8.11.

It was found that the majority of the measured impulses were concave in form and this caused a problem when they were used with dynamic amplification factors that had been derived for triangular impulses. This problem was addressed by parameterising both the impulse magnitude and form with an equivalent force maxima ($F_{max.eq}$) and impulse duration ($T_{d.eq}$). Another approach that could have been adopted would have been to calculate other dynamic amplification factors for a range of concave impulse forms. This option was not taken in this study because of limited time available, but it may be a useful topic for future research, particularly if combined with the problem of impulse definition.

As was discussed in Chapter 7, the definition of the force impulse was based on the identification of a point on the force time history where the impulse loads end, and the forces become entirely quasi-static. This is a relatively simple task for regular waves because of the characteristic hump which appears during the second half of the force time history caused by the generation of the reflected wave (see Figure 7.4). It is often the case that random waves do not have this form and so it is difficult to use this definition. It may be productive to analyse the force time histories of random wave impact tests with a Wavelet Transform. The process could be linked to the problem of determining an appropriate impulse form with which to predict dynamic amplification factors. A wavelet transform works on a random waveform in a similar way to a Fourier Transform. Whereas the Fourier Transform provides the level of energy associated with a range of frequencies

of a sine wave, the Wavelet Transform performs a similar function on a wavelet of chosen form. This means that any impulse form could be chosen and used as both the wavelet and the basic shape upon for which the dynamic amplification factors are calculated.

It is interesting to note in Figure 9.8 that both the large scale results and the prediction from the small scale results are significantly above the effective static load predicted by the method of Goda. This may be partly due to the impulse form assumed by Goda (Figure 8.6) which causes relatively small dynamic amplification (see the $T_r = (999/1000)\ T_d$ line in Figure 8.3). However, Goda also assumes that each impulse is very transient which means that the rise time is relatively unimportant (see the left hand side of Figure 8.3). Though the numerical model which Goda used to predict dynamic behaviour was more advanced than the one used in chapter 8 it was still quite similar. The difference in the prediction may then arise from the prototype measurements of caisson sliding which Goda used to calibrate his model. If this is the case then it calls into question the suitability of MSD models for the prediction of structure response and highlights the need for further work on the modelling of the structural response of vertical breakwaters.

10.4 Small scale aeration measurements

The literature review established a great need for measurements of aeration at small scale in breaking and impacting waves. New equipment and analysis techniques were developed to achieve this. This equipment was based on measurements of electrical conductivity because designs for appropriate circuitry were already available. This method of measuring aeration is far from ideal for small scale breaking waves. A large measurement volume is needed to minimise the effects of individual bubbles. However, the need for spatially focused readings to provide detailed information and to minimise the effects of the water surface requires a small measurement volume. A balance could not be found at this small scale, so an ensemble averaging technique was developed. In effect this increased the size of the measurement volume by adding together all the measurements from many events.

The physical design of the probes was very important. The most significant factors were found to be the orientation and gap between electrodes, the array arrangement and the streamlined shape of the probes. Because the electrodes were inward facing their gap was

maximised and the disturbance of the water flowing between them was minimised. The size of the gap controlled the size of the measurement volume. The electrodes were arranged in a rectangular array which was plane parallel to the flowing water. This allowed simultaneous measurements close to the wall and further from it. This made it possible to tell whether measured aeration was entrapped or entrained which has important implications for the way the results are interpreted. The shape of the probes was important because, being intrusive to the flow, there was a danger that they would cause additional air to be mixed into the flow. During the development of the instruments this was the most difficult problem to overcome, mainly because very small amounts of air introduced on the probe surface passed directly over the electrodes and so had very strong effects on the output. However the streamlined shape shown in Figure 4.16 was ultimately developed and found to work well.

Although the new small scale apparatus performed well no expelled effects were discerned in the results. This is probably because of the scale of the experiment. This phenomena and the pressures associated with it may be best measured at larger scales using high speed imaging techniques and a vertical array of pressure and submersion transducers on the wall.

The array arrangement was found to be vital because it showed that the majority of the aeration measured during the impacts was trapped against the wall at closure rather than entrained as an ambient cloud. In fact it can be concluded from these results that the best way to describe the small scale waves involved in this study is as being unaerated but having a compressible layer separating them from the wall. It can also be concluded that small scale fresh water waves are not suitable for investigating the effects of entrained air on wave impacts since effects due to entrapped air appear to be dominant.

Entrapped air can not be defined as a void fraction within the water, so a concept of an aeration flux was introduced. A relationship was found between this flux and the load maxima. This relationship was strong for the thin air pockets, although quite weak for the larger ones. Consequently, the scatter seen in the bands such as those in Figure 8.9 can be explained, at least in part, by differences in the volume of entrapped air.

It was found that an increase in the size of a large air pocket can decrease P_{max}. This relationship is reasonable and is predicted by several theoretical models such as the one

provided by Bagnold (1939). The finding that an increase in the size of a thin air pocket is associated with an increase in P_{max} is, upon first consideration, counterintuitive. Support for this observation can be found in a recent theoretical study of the role of entrapped air by Wood *et al*, (1999). This shows that a slender air pocket can increase the momentum transfer at the wall during its expansion as it reverses the flow behind it. The horizontal velocity component of the water in this location is reversed (turned through 180 degrees) rather than turning up the wall (through 90 degrees). There is an associated increase in pressure/force impulse at the wall which may be associated with an increase in pressure maxima.

With the benefit of hindsight the analysis techniques developed for the results of the aeration equipment could have been different. The spatial averaging involved in the calculation of the aeration flux meant that the temporal averaging provided by the ensemble averaging was less necessary. Ultimately, the instruments were tuned to measure entrained air but in practice entrapped air was found. On a positive note the instruments have been developed and usefully applied. They can therefore be recommended for further use at small scale, particularly under conditions where more entrained air might be expected, such as with more developed broken waves in sea water.

10.5 Flume noise

The scatter in load maxima has emerged from this study as a very important aspect of wave impact loads. Nominally identical regular waves can produce very different pressure and force maxima and associated differences in impulse duration. This variation in impulse form leads to a wide scatter in F_{stat}. The drop test results showed that the variation can result from differences in entrained aeration. Although this may be the case for marine waves the lack of entrained air in the small scale fresh water tests indicates that this can not explain the scatter in these results. A relationship between load maxima and entrapped air was found and this partly explains the scatter. It seems that a significant factor is the random low energy disturbance or 'noise' on the surface of the water in the flume. Absolutely identical events would produce identical load time histories. Slight, unavoidable noise changes local geometry during impact causing significant variation in load maxima. This has to be accepted as a natural feature of both laboratory and marine

wave impacts and dealt with in the design process. The way this fluctuation can be dealt with has already been discussed in Chapter 8.

Clearly the noise level affects the quantity and location of entrapped air, and in this way affects the load. Since the noise makes localised random modification of the geometry of the impacting wave it seems likely that other processes are important. Further detailed work needs to be done before these minor changes and their major effects can be properly understood.

10.6 Scaling

The principal reason for the lack of knowledge of scale effects is the fact that no controlled laboratory scale tests have been done. A few related experiments are described in the literature such as studies with sloping revetments or vertical walls with submerged breakwaters, but the involved processes are so complex that it is difficult to extrapolate results from them. In fact there is relatively little experimental evidence to support the widely held belief that scale effects wave impact loads. It was one of the original intentions of the study to conduct such a scale comparison and large scale tests were performed. However limitations of resources prevented the construction of a geometrically similar small scale model. Consequently, differences in the small scale foreshore meant that a normal scale comparison was not justified.

The scale comparison which was made was unorthodox in that an attempt was made to identify geometrical similarity in the breaker forms rather than in the breakwater model. The adoption of this approach is justified because of the serious lack of scale data. The results supported Bagnold's observation that the impulse magnitude followed the Froude scale relationship. However no conclusions could be drawn, either for or against the existence of scale effects in $F_{max.eq}$ or $T_{d.eq}$. The idea that the impulse magnitude might be free of scale effects due to aeration is reasonable because it is a momentum property. Momentum is a product of mass and velocity, neither of which are necessarily influenced by the level of air entrained in the water. This is supported by the results of the artificial aeration test, which indicated that additional entrained air changed the form of the impulse but not its magnitude.

It was found that there is very little entrained air in small scale fresh water impacting waves. Clearly this is not the case for the majority of marine storm waves. The reason for this difference is not just scale. The bubble measurement tests showed that for the same entrainment rate sea water contains more air than fresh water, regardless of scale. This has important implications for large scale flume tests. It may be that large scale fresh water flume impacts do not correctly model prototype waves, even those of equal size.

The way in which the additional entrained air affects prototype waves can only be estimated at this stage. The drop test results were used to show that a rise in entrained aeration reduces the load maxima. An empirical relationship between aeration and attenuation of load maxima was then derived. In Chapter 9 this was used to predict the reduction of load maxima with an increase in scale. This approach, which assumes the small scale fresh water waves to be unaerated has some support in the literature. Peregrine and Thais (1996) proposed a similar approach. They derived reduction factors by numerically modelling violent filling flows within a cavity and calculating the extent to which compressibility attenuated the force maxima. Alternative reduction factors of between 0.4 and 0.45 were proposed by Allsop *et al*, (1996). These were based on model and prototype measurements of wave impacts on cob units. The values are lower than those obtained from the drop test results, probably for the following reasons;

- The waves broke onto a sloping surface covered with cob units, air entrapment and entrainment during impact and run-up was therefore probably considerable.
- The factor was derived for impact pressure maxima rather than force maxima.
- Draining water on a sloping revetment can have a significant influence on impact pressure maxima (Fuhrboter, 1986) this water would have been more aerated for the marine waves providing an additional cushioning effect.

Entrapped air was shown to be important for the small scale wave impacts. The effects of scale on entrapped air ought to be relatively simple to investigate since several models exist which describe the compression of entrapped air, see section 2.3.1. As with all the other aspects of the scaling problem, controlled laboratory scale tests are needed to investigate this thoroughly.

Chapter 11

Conclusions

11.0 General conclusions

The guidance available to assist engineers with the interpretation and scaling of the results of wave impact tests is very limited. This is usually thought to be due to uncertainty associated with the possible existence of scale effects. In reality there are much broader problems which need to be dealt with including accounting for the affects of aeration, overcoming natural variation between nominally identical impact events and the prediction of structural response. Although many studies have used physical model tests to research the physics of wave impact loads they have tended to be disconnected from the creation of design methodologies. This is because the phenomena studied tend to be complex, localised and transient. In addition the classical reductionist approach to this type of research tends to focus attention on details rather than the whole problem. The great deal of interest that has been shown in the maximum impact pressure (P_{max}) may be an example of this. It is almost impossible to measure correctly, can be highly variable between nominally identical events and is not very relevant to caisson stability. In contrast the force impulse has received relatively little attention but is relevant to structural dynamics and can be used to include aeration, scale, breaker shape and structure response in the design process. It also has the natural advantage that it can be more easily measured with accuracy than P_{max}.

Because questions associated with the scaling of wave impact loads are intrinsically linked to aeration, structural response and breaker shape, studying any of these in isolation raises the likelihood that the results will not be suitable for interpretation within the other aspects of the problem. Although at present the associated phenomena can not be fully described in physics, engineers have bridged the unknowns in the subject to provide design methods for caisson breakwaters. The most advanced and trusted of these methods is the one that was developed by Goda.

The measurements made during this study show that the force impulse is basically triangular in shape and is, for regular waves, relatively constant in magnitude but not in form. Consequently, an inverse relationship exists between F_{max} and T_d. This is the cause of the relationships observed by other researchers between P_{max} and T_{pr}.

Further research is specifically needed in the following areas;

- Field measurements of waves, their aeration and the impacts they produce.
- A laboratory based scale comparison of impacting waves.
- Developments in numerical models of the dynamics of caisson breakwaters.

11.1 Wave loads and aeration

It is not realistic to attempt to describe wave impacts without considering aeration. It has at least three fundamental roles in wave loading; expelled air generates a force on the wall before the wave arrives, entrapped pockets can 'focus' wave momentum or act as a cushion and entrained bubbles introduce compressibility to the water.

Resistance based probes can be used to measure air in small scale fresh water waves if some form of spatial and/or temporal averaging is used. This is not an ideal technique because of a conflict that arises over the size of the measurement region. The localised phenomena and small size of the waves demand a small measurement volume. However, the need to minimise the effect of individual bubbles requires a large volume. This can not be overcome by temporal averaging in the normal way because the rapidly changing phenomena necessitates a high sample frequency. This conflict can be overcome by a process of ensemble averaging in which several records are combined to produce a single one.

The physical design of the probes developed in this study was very important. Since they were intrusive to the flow they had to be streamlined to prevent self aeration. The location of the electrodes was also important, by arranging them in a plane that was parallel to the direction of flow in the flume it was possible to discern different types of aeration.

The wave impact results obtained for the small scale waves were affected by the amount of air they trapped against the wall. An entrapped air pocket can act to increase or decrease

impact pressure maxima depending upon its thickness. Slim pockets can cause impact loads to increase. This may be because they cause the water directly behind the pocket to 'bounce back'. Larger pockets may act as a cushion, reducing load maxima.

In general there was so little entrained air in the waves tested that they could be described as unaerated and incompressible.

Double peaks in the load time histories of the large scale impacts were found to be associated with pockets of air at low pressure.

It is concluded from the results of the drop tests and artificial aeration tests that an increase in entrained air is associated with a decrease in impact load maxima and an increase in impulse duration.

11.2 Wave loads and scale

The existence of scale effects in impact loads has been implied by the results of Bagnold (1939), Blackmore and Hewson (1984) and other related studies, but has not been proved. Scale effects have been demonstrated in related phenomena, but the results are not necessarily directly comparable.

Surface tension and friction forces are not correctly scaled in model tests of wave impacts. In addition, entrapped air is relatively less elastic at small scale.

For the same mass air entrainment rate sea water retains more air than fresh water due to reduced bubble size and the resulting increased bubble rise time. As a consequence, large scale fresh water wave impacts should not be assumed to have the same entrained aeration characteristics as marine waves of the same size.

The greater levels of entrained air within marine waves is likely to be associated with a reduction in load maxima, and an increase in impulse duration.

The results of the scale comparison indicate that impulse magnitude may be free of scale effects between large and small scale laboratory waves.

11.3 Wave loads and breaker shape

Impact pressure and force maxima are variable between nominally identical impact events. They are not therefore good parameters for quantifying breaker shape. The impulse magnitude and its normalised form the impulse proportion (*IP*) is more stable and so provides a better means of replacing the largely qualitative descriptions of breaker form that are currently used.

11.4 Wave loads and structure response

Goda's design method treats breakwaters as dynamic systems although this is not immediately evident to the designer so is often unrecognised. Any design methodology based on physical model tests should account for dynamic effects. Predicting an effective static load (F_{stat}) is useful way of doing this because it converts the dynamic problem into an equivalent static problem.

A lot of scatter has been shown to exist in values of F_{stat} associated with nominally identical impact events. This scatter has to be recognised as a feature of wave impacts in general, and dealt with in the design process. It shows that it is unsafe to use one or only a few results for force impulse in the prediction of dynamic behaviour.

Dynamic amplification factors can be used to predict F_{stat} but the difference between the impulse form and the ideal shape assumed in the derivation of the factors must be dealt with. This can be achieved using 'equivalent' impulses.

Dynamic amplification factors, which map the behaviour of the structure as a dynamic system, can be used to predict and account for the dynamic effects that can arise from a range of load conditions. Effective static loads calculated in this way have been shown to tend towards a definite maximum, unlike dynamic loads which tended to get bigger as measurement capabilities increase.

The advantage of dynamic amplification factors is not their simplicity of application, it is their potential for dealing with the effects of scatter in the impulse form.

References

Allsop, N.W.H., McKenna, J.E., Vicinanza, D., and Whittaker, T.T.J., (1996). "New design formulae for wave loadings on vertical breakwaters and seawalls". *Proc. 25th Int. Conf. on Coastal Engineering, ASCE.*

Allsop, N.W.H. and Muller, G. (1995). "Discussion on - Comparative study on breaking wave forces on vertical walls". *ASCE J. Waterways, Port, Coastal and Ocean Engineering, Vol. 121, No. 5.*

B.S. 6349, (1984). British Standard Code of Practice for Marine Structures, Part 1. *British Standards Institution, London.*

Bagnold, R.A., (1939). "Interim report of wave pressure research". *J. Inst. Civ. Eng. Vol. 12, London, pp. 202-226.*

Bird, P., Crawford, A., Hewson, P. and Bullock, G. (1999). "Measurement of wave impact pressures and sea water aeration". *Paper in print for publication in Coastal Engineering.*

Blackmore, P.A. (1982). "The evaluation of wave forces on sea walls". *Ph.D. thesis, University of Plymouth.*

Blackmore, P.A. and Hewson, P.J., (1984). "Experiments on full scale wave impact pressures". *Coastal Engineering, 8, pp. 331-346.*

Bullock, G.N. and Murton, G.J. (1989). "Performance of a wedge type absorbing wave maker". *J. Waterway, Port, Coastal and Ocean Engineering, Vol. 115, No. 1, pp. 1-18.*

CERC, 1984. Shore Protection Manual, 4th ed. *U.S. Army Waterways Experimental Station, U.S. Government Printing Office, Washington D.C.*

Chan, E.S. and Melville, W.K. (1988). "Deep water plunging wave pressures on a vertical plane wall". *Proc. Royal Soc. London. A 417, pp 95 - 131.*

Chan, E.S. (1994). "Mechanics of deep water plunging wave impacts on vertical structures". *Coastal Engineering 22, pp 115 - 133.*

Cooker, M.J. (1990). "The interaction of steep water waves and coastal structures". *Ph.D. thesis, Bristol University department of Mathematics.*

Cooker, M.J. and Peregrine, D.H. (1990). "Violent water motion at breaking wave impact". *Proc. 22nd Int. Conf. Coastal Eng.*

Crawford, A., Walkden, M., Bullock, G., Bird, P., Hewson, P. and Griffiths, J. (1994). "Wave impacts on sea walls and breakwaters". *Proc. Int. ASCE Conf. on Coastal Dynamics, pp 656 - 670.*

Crawford, A., Bullock, G., Hewson, P., and Bird, P. (1997). "Wave impact pressures and aeration at a breakwater". *Proc. Waves '97, 14 p.*

Crawford, A.R., (1999). "Measurement and analysis of wave loading on a full scale coastal structure" *Ph.D. thesis, University of Plymouth School of Civil and Structural Engineering.*

Davidson, M.A., Bird, P.A.D., Bullock, G.N. and Huntley, D.A., (1994). "Wave reflection: field measurement analysis and theoretical developments". *Proc. Conf. Coastal Dynamics, ASCE pp. 624-655.*

Denny, D.F. (1951). "Further experiments on wave pressures". *J. of the Ins. Civ. Eng. Vol. 35, pp 330-344.*

Dold, J.W. and Peregrine, D.H., (1984). "Steep unsteady water waves: an efficient computational scheme". *International Conference on Coastal Engineering.*

Ergin, A. and Abdulla, S. (1993). "Comparative study on breaking wave forces on vertical walls". *J. of Waterway, Port, Coastal and Ocean Engineering, ASCE, 119 (5), Tech. Note 2575, pp. 560-567*

Fuhrboter, A. (1969). "Laboratory investigation of impact forces". *Proc. Symp. Res. on Wave Action, Delft Hydr. Lab., Vol. II Delft.*

Fuhrboter, A. (1970). "Air entrainment and dissipation in breakers". *Int. Conf. on Coastal Eng. Ch. 24, pp. 391-399.*

Fuhrboter A. (1986). "Model and prototype tests for wave impact and run-up on a uniform 1:4 slope". *Coastal Engineering Vol. 10, pp. 49-84.*

Galliard, D.D. (1904). "Wave action in relation to engineering structures". *U.S. Army Corps of Engineers, reprinted 1935.*

Goda, Y. (1974). "New wave pressure formulae for composite breakwaters". *Proc. 14th Int. Conf. Coastal Engineering, Ch. 100, pp 1702-1720.*

Goda, Y. (1992). "The design of upright breakwaters". *Proc. of the Short Course on Design and Reliability of Coastal Structures, 23rd Int. Conf. Coastal Engineering, pp 547-568.*

Goda, Y., (1994), "Dynamic response of upright breakwaters to impulsive breaking wave forces". *Coastal Engineering 22, pp 135-158.*

Graham D.I., Hewson P.J. & Bullock G.N. (1992). "The influence of aeration on the impact pressures of model - scale waves breaking on a vertical structure". *University of Plymouth internal report.*

Graham D.I., Hewson P.J. & Bullock G.N. (1993). "The influence of entrained air upon wave impact pressures". *Paper presented at MAST EUROMAR meeting, Brussels, March.*

Griffiths, J. (1994). "The effects of aeration on wave impacts". *Ph.D. Thesis, University of Plymouth, School of Civil and Structural Engineering.*

de Groot, M.B., Anderson, K.H., Burchart, H.F., Ibsen, L.B., Kortenhaus, A., Lundgren, H., Magda, W., Oumeraci, H., and Richwen, w. (1996). "Foundation design of vertical breakwaters". *Norwegian Geotechnical Institute, Publication 198, Vol. 1, pp. 109-114.*

Hattori, M. (1994). "Wave impact pressures on vertical walls and the resulting wall deflections". *Proc. Int. Workshop on Wave Barriers in Deepwaters, Port and Harbour Research Institute, Yokosuka, Japan, pp. 333-346.*

Hattori M. & Arami A. (1992). "Impact breaking wave pressures on vertical walls". *Proc. 23rd Int. Conf on Coastal Engineering, Venice, Italy.*

Hattori, M., Arami, A., and Yui, T. (1994). "Wave impact pressure on vertical walls under breaking waves of various types". *Coastal Engineering, 22, pp 79-114.*

Hayashi, T., and Hattori, M., (1958). "Pressure of the breaker against a vertical wall". *Coastal Eng. in Japan, 1, pp 25-37.*

Hiroi (1920). "The force and power of waves". *The Engineer, pp. 184-185.*

Hughes, S, (1993). "Physical models and laboratory techniques in coastal engineering". *World Scientific. ISBN 981-02-1541-x.*

Hwung, H.H., Chyan, J.M., Chung, Y.C., (1992). "Energy dissipation and air bubble mixing inside surf zone". *Proc. 23rd Int. Conf. Coastal Eng.*

Kamel, M.A. (1970). "Shock pressures on coastal structures". *Proc. ASCE, Waterways, Harbours and Coastal Engineering Division, Vol. 96, 689-699.*

Karman, T.v., (1928). "The impact of seaplane floats during landing". *NACA Tech. Note 321, Washington D.C.*

Kirkgoz, S. (1982). "Shock pressure of breaking waves on vertical walls". *J. Waterway, Port Coastal and Ocean Engineering, ASCE, Vol. 108, pp 81-95.*

Kirkgoz, S. (1983). "Secondary pressures of waves breaking on seawalls". *J. Waterway, Port Coastal and Ocean Engineering, ASCE, Vol. 109, pp 487-494.*

Kirkgoz, S.M. and Mengi, Y., (1986). "Dynamic response of caisson plate to wave impact". *J. Waterways, Port, Coastal and Ocean Engineering, Vol. 112, pp. 285-296.*

Kirkgoz, S.M., (1990). "An experimental investigation of a vertical wall response to breaking wave impact". *Ocean Engineering, Vol. 14, pp. 379-391.*

Lamb and Killen, (1950). "An electrical method for measuring air concentration in flowing air-water mixtures". *Contract N6onr-246, Office of Naval Research.*

Lamarre, E. and Melville, W.K., (1992). "Instrumentation for the measurement of void-fraction in breaking waves: laboratory and field results". *IEEE J. of Oceanic Engineering, Vol. 17, No. 2 pp. 204-215.*

Longuet-Higgins, M.S. and Cokelet, E.D., (1976). "The deformation of steep surface waves on water I. A new method of computation". *Proc. R. Soc. London, A. 350, pp 1-26.*

Longuet-Higgins, M.S., and Turner, J.S., (1974). "An 'entraining plume' model of a spilling breaker". *J. Fluid Mech. Vol. 63, Pt. 1, pp 1-20.*

Losada, M., Martin, F. and Medina, R. (1995). "Wave kinematics and dynamics in front of reflective structures".

Lundgren, H. (1968). "Shock forces: an analysis of deformations and forces in the wave and in the foundation". *Proc. Symp. on Wave Action, Delft Hydro Lab, p 14.*

Marinski, J.G. and Oumeraci, H. (1992). "Dynamic response of vertical structures to breaking wave forces, -review of the CIS design experience-". *Proc. Int. Conf. Coastal Engineering, 1992, pp 1357-1370.*

Maxwell, C. (1873). "A treatise in electricity and magnetism". *Clarendon Press, Oxford, U.K.*

McKenna, J. (1997). "Wave forces on caissons and breakwater crown walls". *Ph.D. Thesis, The Queens University of Belfast, School of the Built Environment, Department of Civil Engineering.*

Meer, J.W.v.d., (1994). "Numerical modelling of wave structure interaction". *Proc. Instn. Civ. Engrs. Wat. Marit. and Energy, 106, pp. 359-362.*

Miller, R.L., (1972). "The role of surface tension in breaking waves". *Proc. 13th Int. Conf. Coastal Eng. pp. 433-448.*

Miller, R.L., Leverette, S., O'Sullivan, J., Tochko, J. and Theriault, K. (1974). "Field measurements of impact pressures in surf". *Proc. 14th Int. Conf. Coastal Eng, Vol 3, pp 1761-1777.*

Minikin, R.R. (1950). "Wind, waves and maritime structures". *Charles Griffin, London, pp. 38-39.*

Mitsuyasu, H. (1962). "Experimental study on wave force against a wall". *Coastal Eng. in Japan, Vol. 5, pp 23-47.*

Mitsuyasu, H. (1966). "Shock pressures of breaking wave". *Proc. 10th Int. Conf. Coastal Eng. pp 268-283.*

Molitor (1935) "Wave pressures on seawalls and breakwaters". *Trans. ASCE, 100, pp 984-1002.*

Muller, G. (1993). "A study of breaking wave loads on shoreline wave power station". *Ph.D. Thesis, The Queens University of Belfast, School of the Built Environment, Department of Civil Engineering.*

Muller, G.U. and Whittaker, T.J.T., (1993). "Dynamic response to breaking wave impact". *Proc. 2nd EU Conf. on Structural Dynamics.*

Muller, G. and Whittaker, T.J.T, (1995). "Field measurements of breaking wave loads on a shoreline wave power station". *Proc. Inst. Civ. Eng. Water, Maritime and Energy, Vol. 112, Issue 3, pp 187-197.*

Muller, G., and Walkden, M. (1998) "Survivability assessment of shoreline OWC wave power stations". *Proc. OMAE 1998, requested for review for the OMAE Journal.*

Oumeraci, H., (1994). "Review and analysis of vertical breakwater failures - lessons learned". *Coastal Engineering 22, pp 3-29.*

Oumeraci, H. and Partenscky, H.W., (1991). "Breaking wave impact loading of vertical structures, -effect of entrapped air on structure response-". *Proc. MAST G6 project 2 Workshop, Hannover, Germany.*

Oumeraci, H. and Kortenhaus, A., (1994). "Analysis of the dynamic response of caisson breakwaters". *Coastal Engineering 22, pp 159-183.*

Oumeraci, H., Klammer, P., and Kortenhaus, A., (1994). "Impact loading and dynamic response of vertical breakwaters". *Proc. Int. Wkshop. on Wave Barriers in Deepwaters, Jan. Yokosuka, Japan.*

Oumeraci, H., Bruce, T., Klammer, P. and Easson, W.J., (1995). "PIV measurement of breaking wave kinematics and impact loading of caisson breakwaters". *Proc. 4th Int. Conf. Coastal and Port Engineering in Developing Countries, pp. 2394-2410.*

Partenscky, H.W., (1988). "Dynamic forces due to waves breaking at vertical coastal structures". *Proc. 21st Int. Conf. on Coastal Engineering.*

Peregrine, D.H. and Thais, L., (1996). "The effect of entrained air in violent water wave impacts". *J. Fluid Mech. 325, pp 377-397.*

Plakida, M.E. (1970). "Pressure of waves against vertical walls". *Proc. 12th Int. Conf. Coastal Engineering, pp. 1451-1460.*

Raichlin, F. and Papanicolou, P., (1988). "Some characteristics of breaking waves". *Proc. 21st Int. Conf. on Coastal Engineering, pp. 377-392.*

Ramkema C. (1978). "A model law for wave impacts on coastal structures". *Proc. 16th Int. Conf. Coastal Eng. pp. 2308-2327.*

Rapp, R.J. and Melville, W.K., (1990). "Laboratory measurements of deep-water breaking waves". *Phil. Trans. Royal Society of London. A 331, pp 735-800.*

Richert, G. (1968). "Experimental investigation of shock pressures against breakwaters". *Proc. 11th Int. Conf. Coastal Engineering, pp. 954-973.*

Ross, C.W., (1955). "Laboratory study of shock pressures of breaking waves". *Beach Erosion Board, Tech. Memo No. 59.*

Rouville, A., Besson, P. and Petry, P. (1938). "Etudes internationales sur les efforts dus aux lames". *108, Annales des Ponts et Chassees, pp. 5-113.*

Sainflou, G. (1928). "Essai sur les digues maritimes verticals". *Annales Ponts et Chassees, Vol. 98, No. 4.*

Sakakiyama, T. and Ogasawara, M. (1994). "Scale effects on impulsive wave forces and reduction by submerged breakwater". *Proc. Int. Conf. Coastal Dyn. ASCE, pp. 628-641.*

Schmidt, R., Oumeraci, H., and Partenscky, H.W., (1992). "Impact loads induced by plunging breakers on vertical structures". *Proc. 23rd Int. Conf. on Coastal Engineering, Chap 118, pp 1545-1558.*

Schultz, K.P., (1992). "Further results on hydraulic model investigations on air enclosure caused by grid structures". *Proc. MAST II G6 Workshop, Hanover, Aug. 13 p.*

Scott, J.C. (1975). "The role of salt in whitecap persistence". *Deep Sea Research, Vol. 22, pp. 653-657.*

Skladnev, M.F., and Popov, I.Y., (1969). "Studies of wave loads on concrete slope protections of earth dams". *Proc. Symp. Research on Wave Action 1969, Delft, Vol. II, Paper 7.*

Stive, R.J.H. (1984). "Wave impact on uniformly steep slopes at approximately prototype scale". *Proc. Symp. on Scale Effects in Modelling Hydraulic Structures, Esslingen, 7-11, pp 1-7.*

Tanimoto, K. and Takahashi, S., (1994). "Design and construction of caisson breakwaters - the Japanese experience". *Coastal Engineering 22, pp 57-77.*

Takahashi, S., Tanimoto, K. and Shimosako, K. (1994). "Dynamic response and sliding of breakwater caisson against impulsive breaking wave forces". *Proc. Wave Barriers in Deepwaters, Yokosuka, Japan.*

Thorpe, S.A., (1982). "On the clouds of bubbles formed by breaking wind-waves in deep water, and their role in air-sea gas transfer". *Phil. Trans. R. Soc. London, A 304, pp. 155-210.*

Topliss, M.E., Cooker, M.J., and Peregrine, D.H., (1992). "Pressure oscillations during wave impact on vertical walls". *Proc. 23rd Int. Conf. on Coastal Engineering.*

Topliss, M.E., (1994). "Water wave impact on structures". *Ph.D. Thesis, University of Bristol, School of Mathematics.*

Vicinanza, D., (1997). "Pressioni e forze di impatto di onde frangenti su dighe a paramento verticale e composote". *Ph.D. Thesis, Universita di Napoli.*

Walkden, M.J.A., Crawford, A.R., Hewson, P.J., Bullock, G.N., and Bird, P.A.D., (1995). "Wave impact loading on vertical structures". *Proc. Coastal Structures and Breakwaters '95, London.*

Walkden, M.J., Hewson, P.J. and Bullock, G.N., (1996). "Wave impulse prediction for caisson design". *Proc. 25th Int. Conf. Coastal Engineering.*

Walkden, M., Muller, G. and Bruce, T. (1998). "Low-cost particle image velocimetry: system and application". *Proc. Conf. Offshore and Polar Engineering, 7p.*

Walkden, M.J., Wood, D.J., Bruce, T. and Peregrine, D.H. "Seaward loads on Caisson Breakwaters". *Submitted to the Journal of Coastal Engineering in Oct. '98. Also presented at MAST PROVERBS workshop in Caen, 1998.*

Weggel, J.R., and Maxwell, W.H. (1970). "Experimental study of breaking wave pressures". *Offshore Tech. Conf. Texas.*

Whillock, A.F., (1987). "Measurements of forces resulting from normal and oblique wave approaches to small scale sea walls". *Coastal Engineering, 11, pp. 297-308.*

Witte, H.H., (1990). "Wave impact loading on a vertical wall with respect to structure response". *Int. Rep. German Fed. Waterways and Research Institute, Hamburg, 30 p.*

Wood, D.J., (1998). "Pressure-impulse impact problems and plunging wave jet impact". *Ph.D. thesis, Bristol University department of Mathematics.*

Wood, D.J., Peregrine, D.H., and Bruce, T.B. (1999). "Study of wave impact against a wall with pressure-impulse theory. Part 1: trapped air". *Paper submitted to the Journal of Fluid Mechanics.*

Appendix A

Examples of raw data

A.1 Pressure time histories

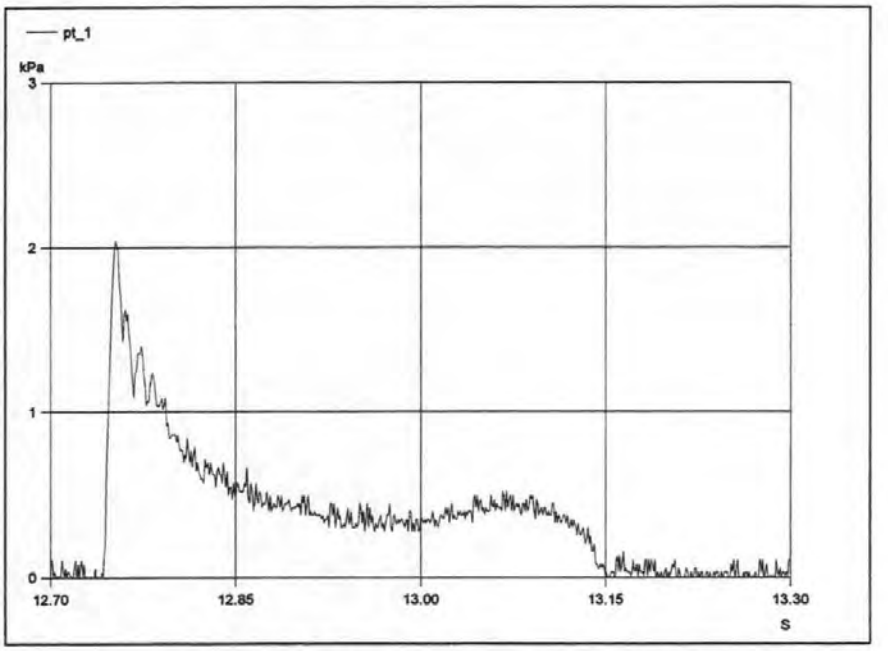

Figure A.1. Pressure time history, transducer 1, test 19059301.

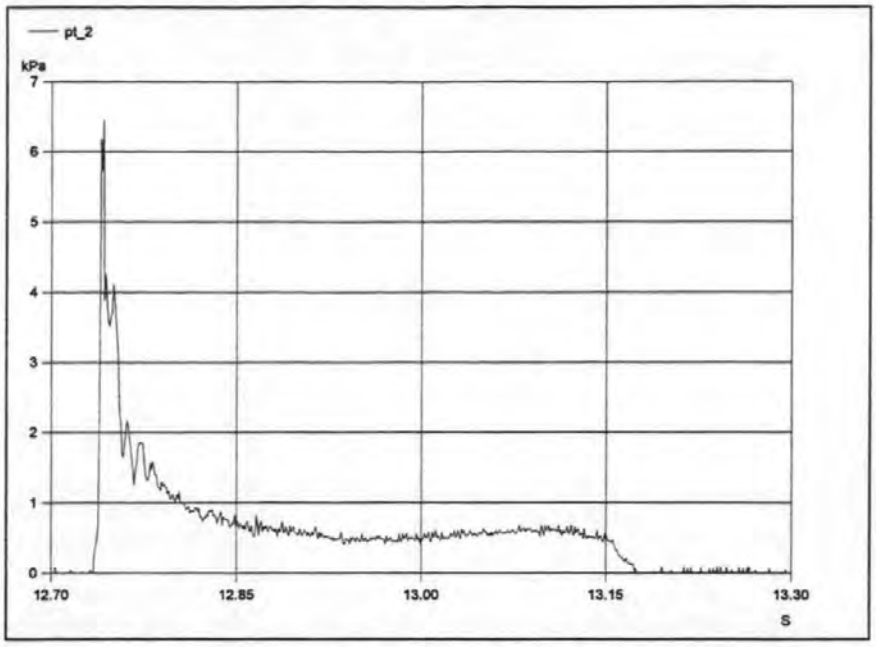

Figure A.2. Pressure time history, transducer 2, test 19059301.

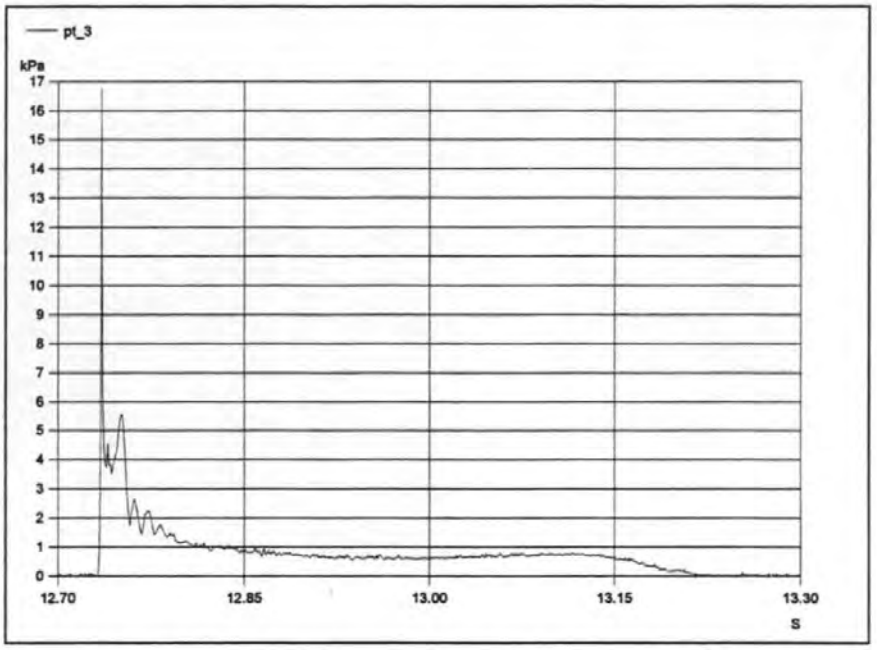

Figure A.3. Pressure time history, transducer 3, test 19059301.

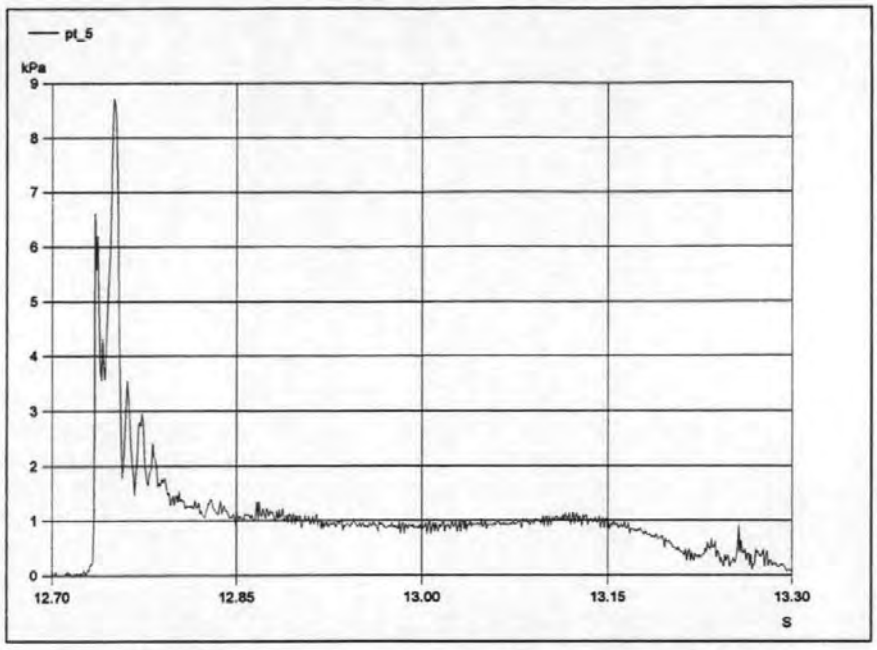

Figure A.4. Pressure time history, transducer 4, test 19059301.

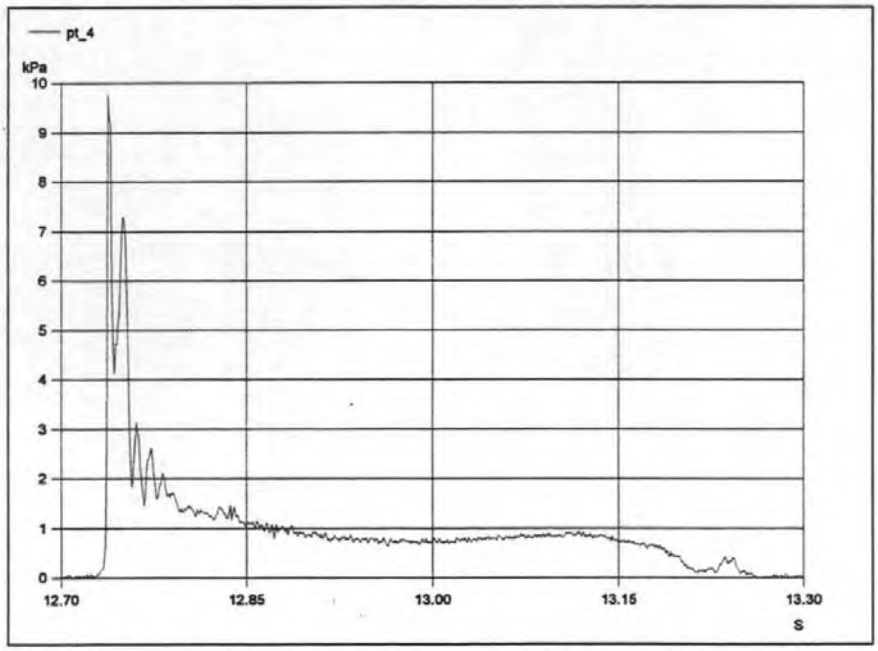

Figure A.5. Pressure time history, transducer 5, test 19059301.

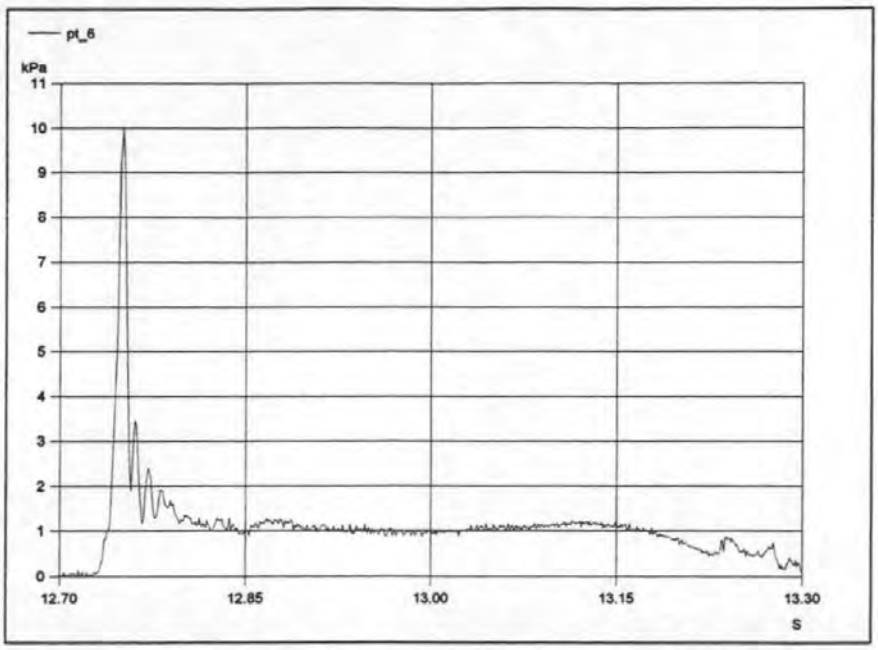

Figure A.6. Pressure time history, transducer 6, test 19059301.

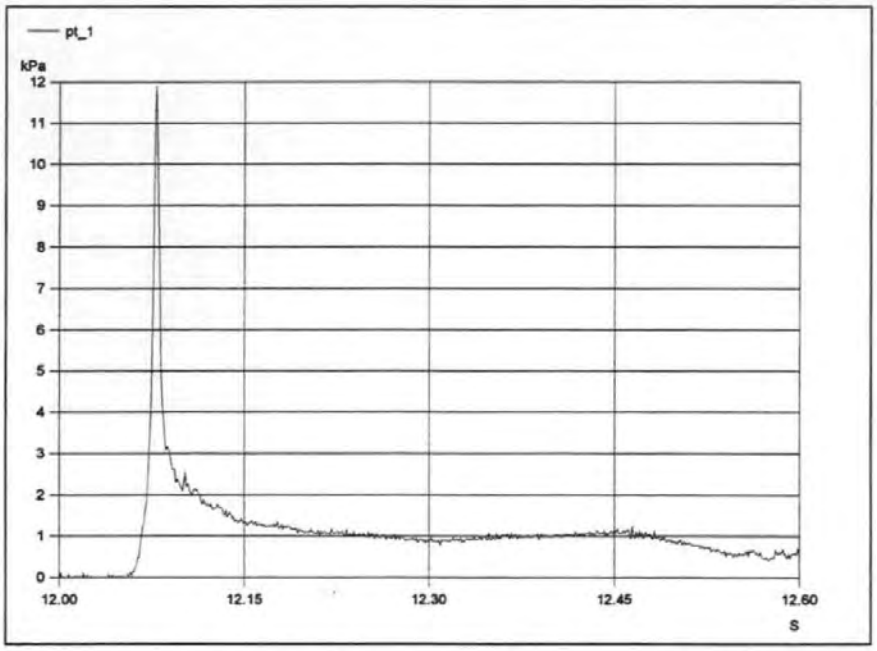

Figure A.7. Pressure time history, transducer 1, test 20059301.

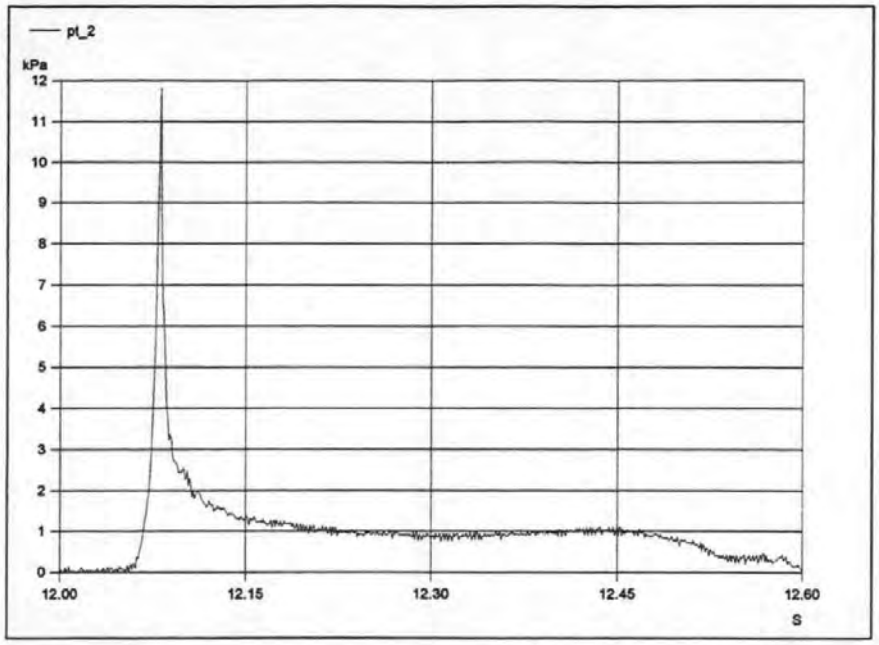

Figure A.8. Pressure time history, transducer 2, test 20059301.

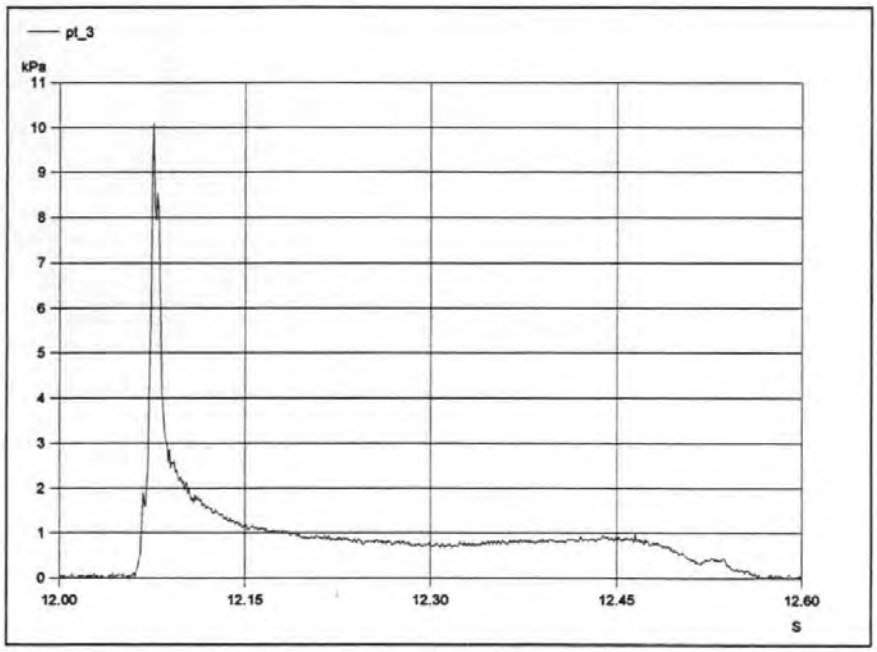

Figure A.9. Pressure time history, transducer 3, test 20059301.

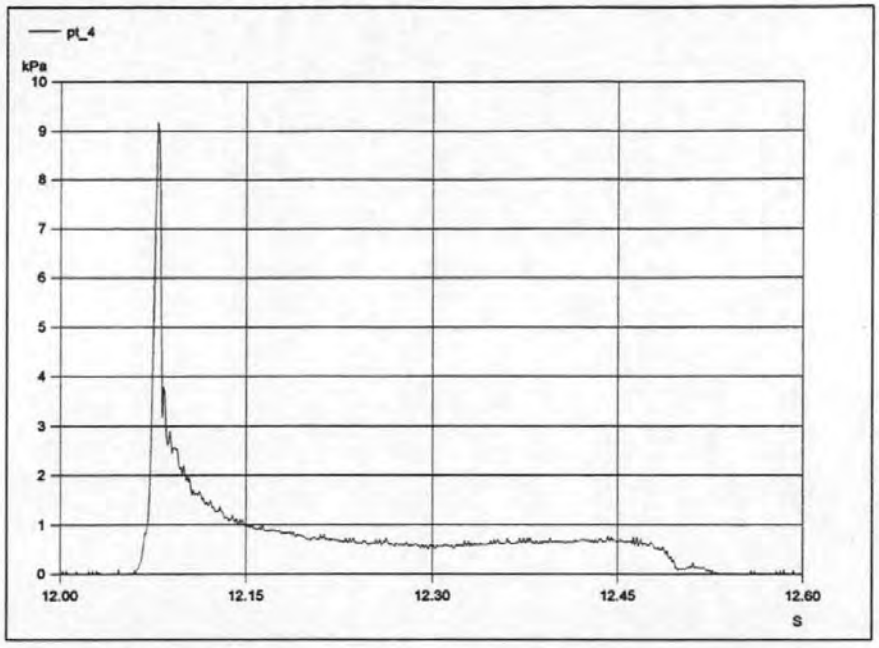

Figure A.10. Pressure time history, transducer 4, test 20059301.

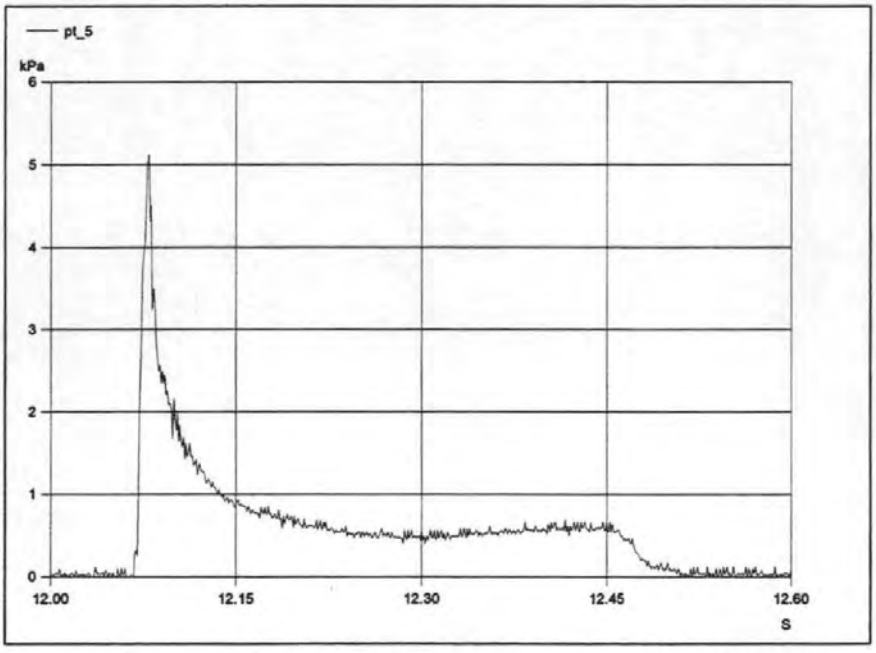

Figure A.11. Pressure time history, transducer 5, test 20059301.

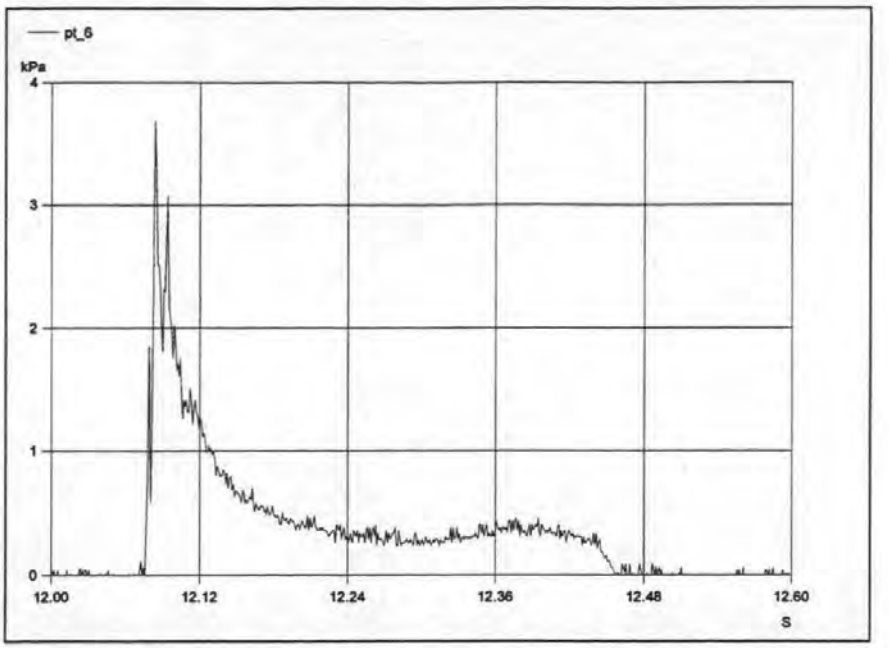

Figure A.12. Pressure time history, transducer 6, test 20059301.

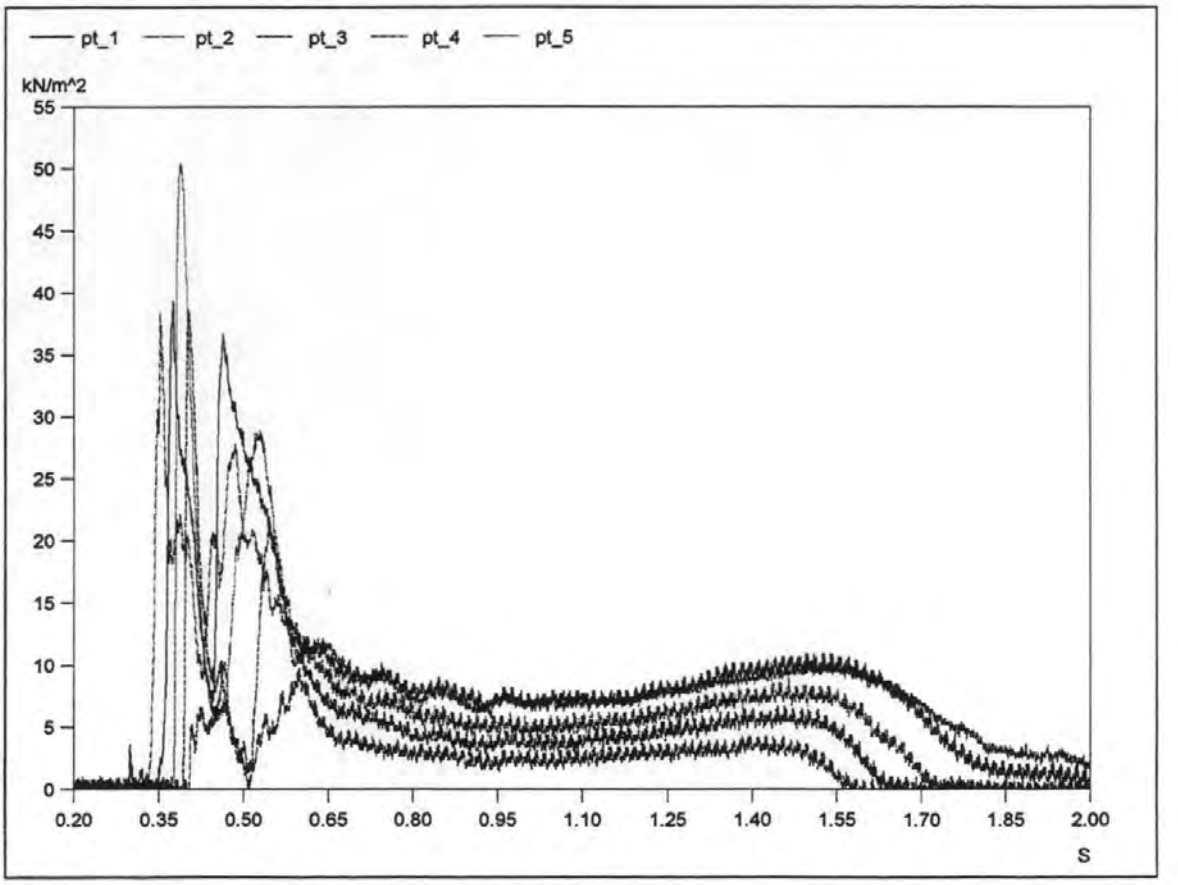

Figure A.13. Pressure time histories, test 04029401.

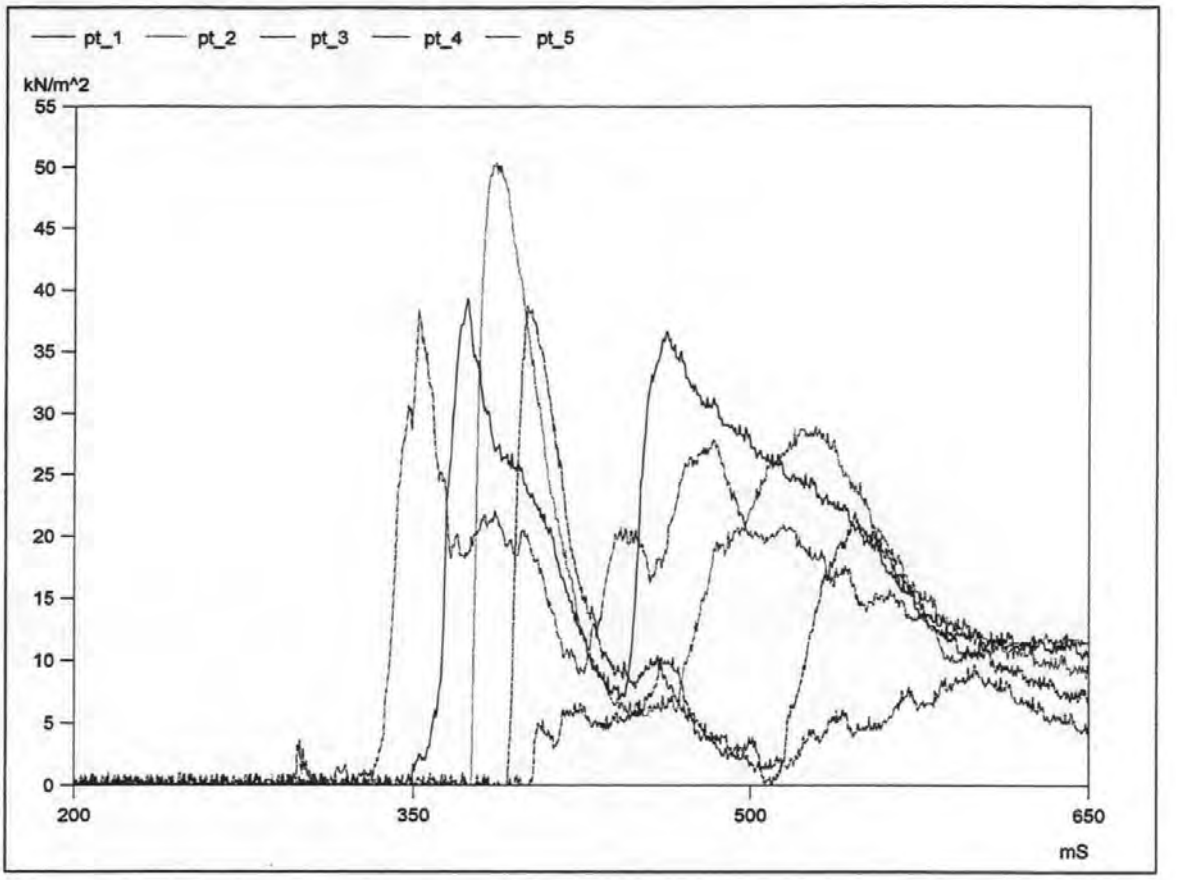

Figure A.14. Pressure time histories, test 04029401.

A.2 Large scale pressure and aeration time histories

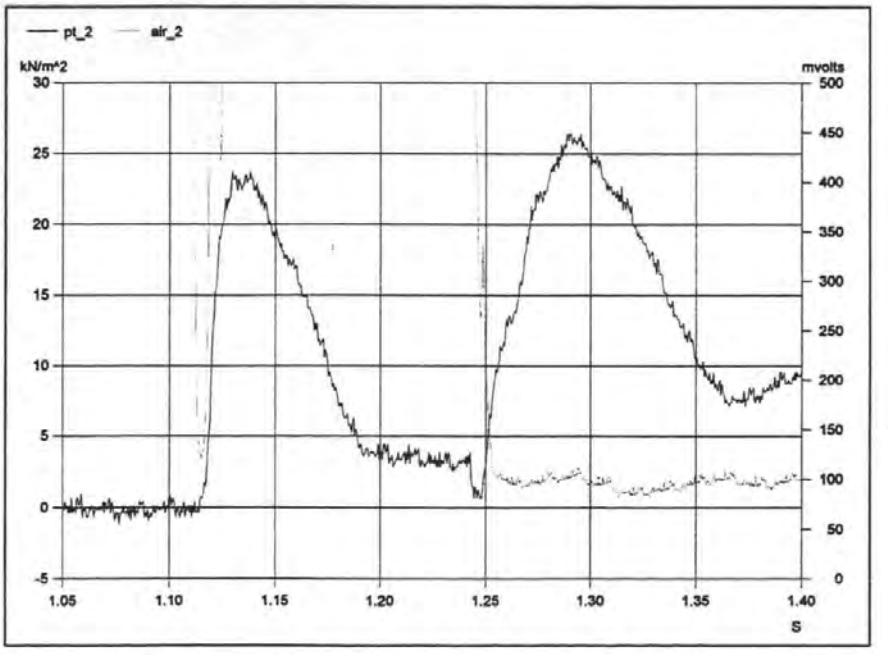

Figure A.15. Pressure and aeration time histories, level 2 test 04029403.

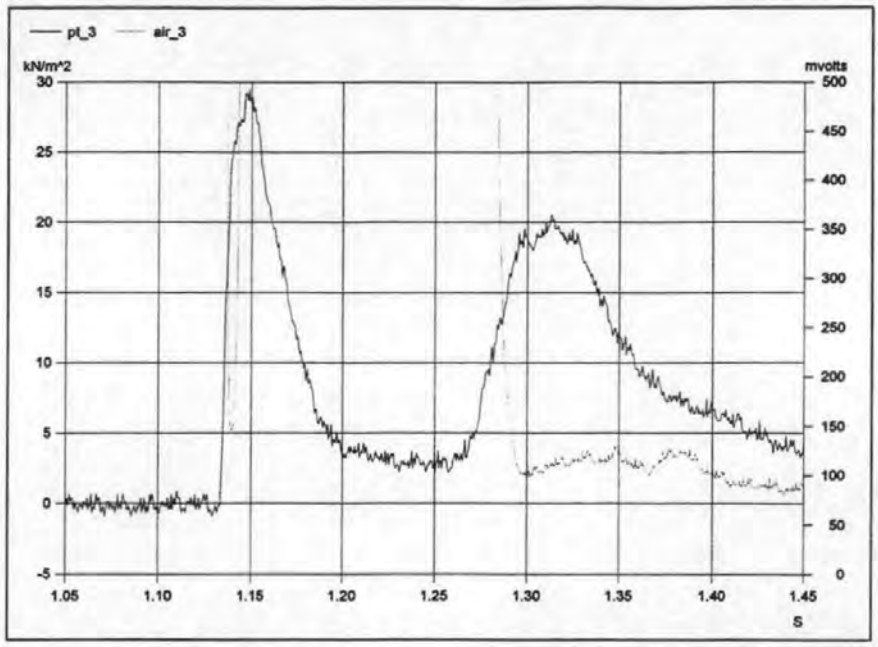

Figure A.16. Pressure and aeration time histories, level 2 test 04029403.

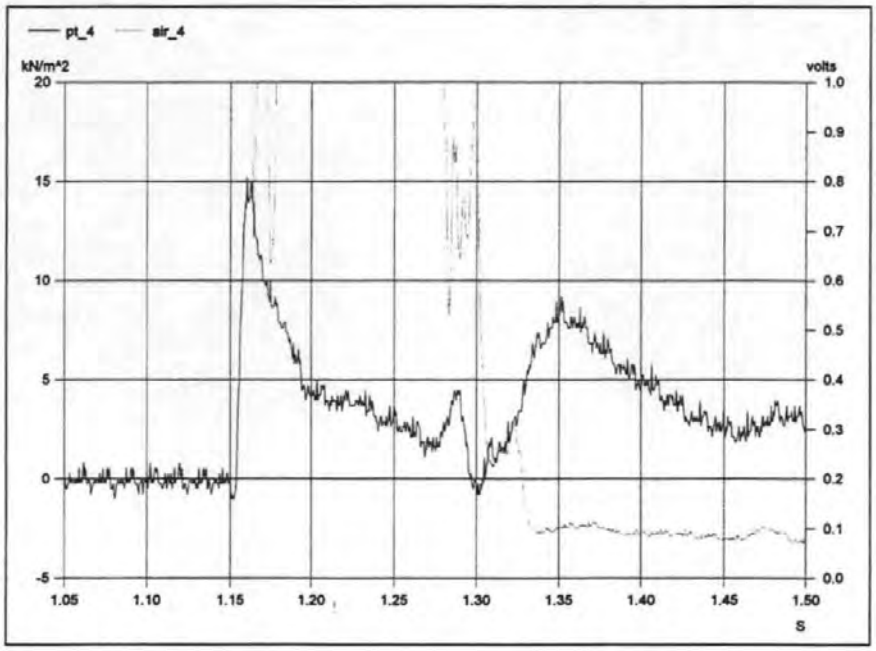

Figure A.17. Pressure and aeration time histories, level 4 test 04029403.

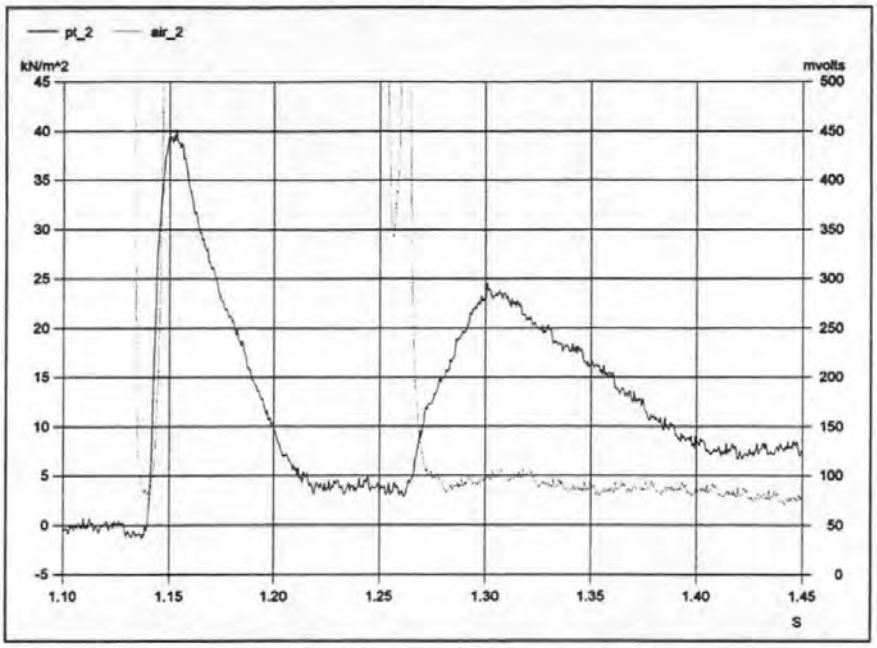

Figure A.18. Pressure and aeration time histories, level 2 test 04029402.

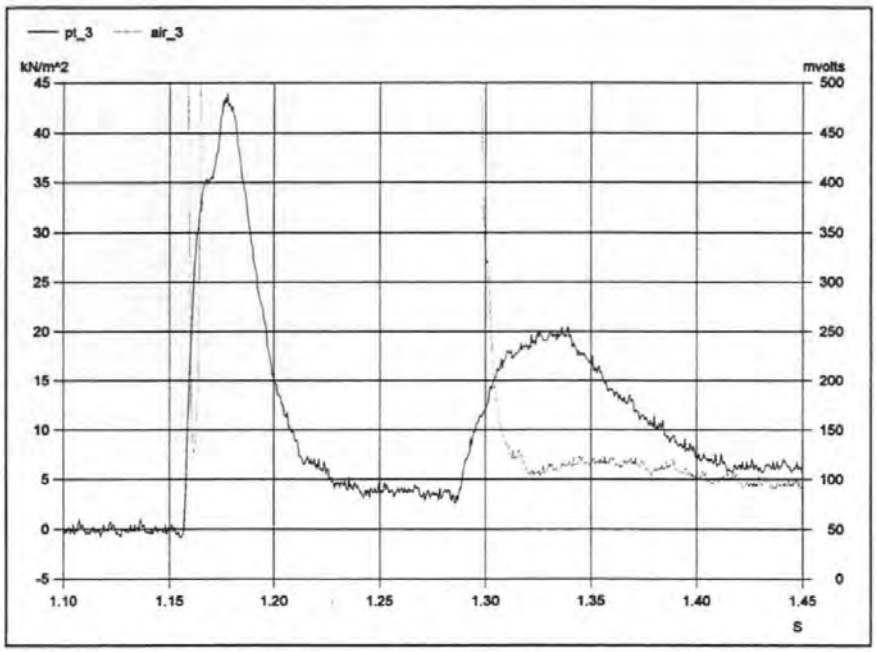

Figure A.19. Pressure and aeration time histories, level 3 test 04029402.

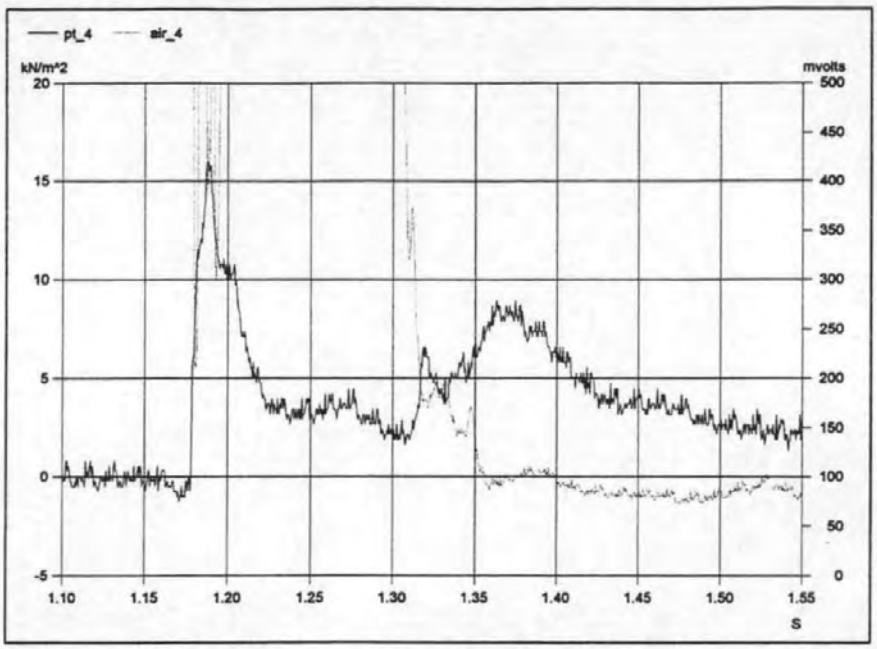

Figure A.20. Pressure and aeration time histories, level 4 test 04029402.

Appendix B

Examples of processed data

B.1 Trends in the P_{max} T_{pr} domain.

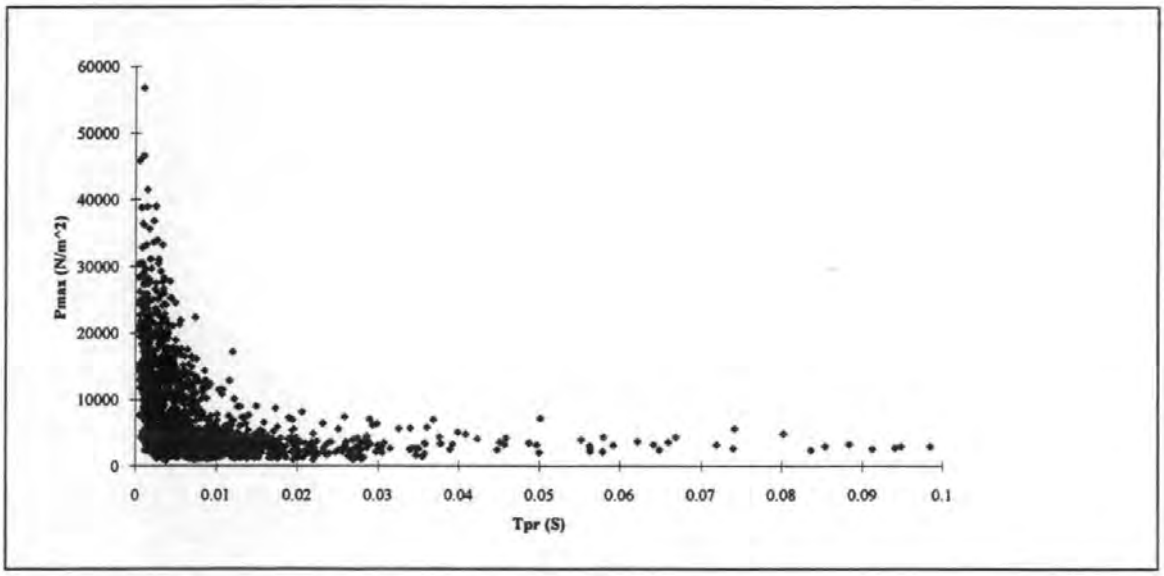

Figure B.1. Relationship between P_{max} and T_{pr} for test 08089602.

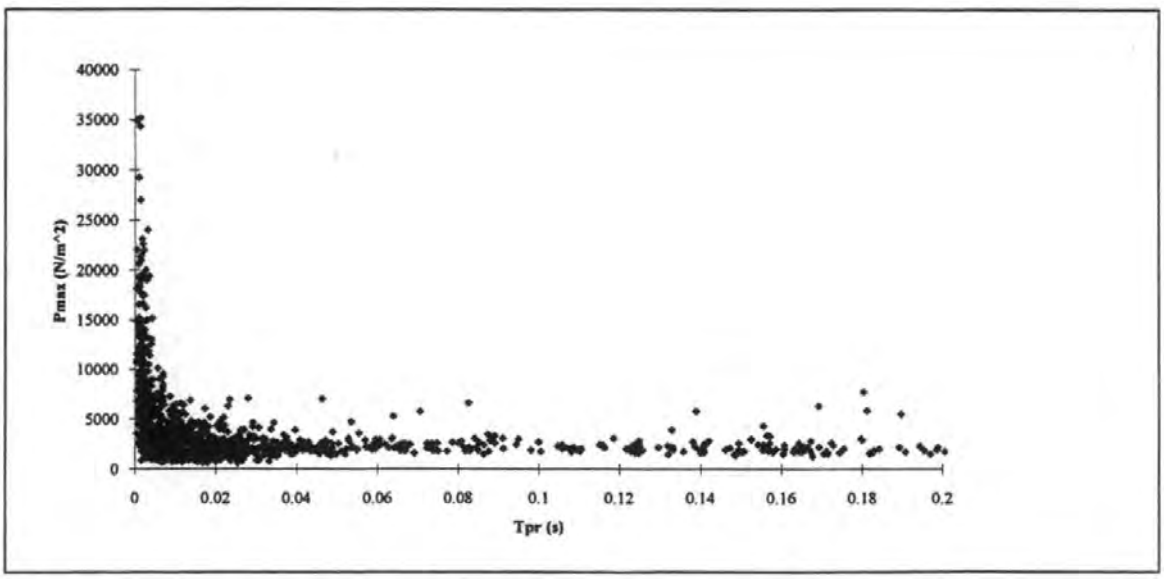

Figure B.2. Relationship between P_{max} and T_{pr} for test 08089604.

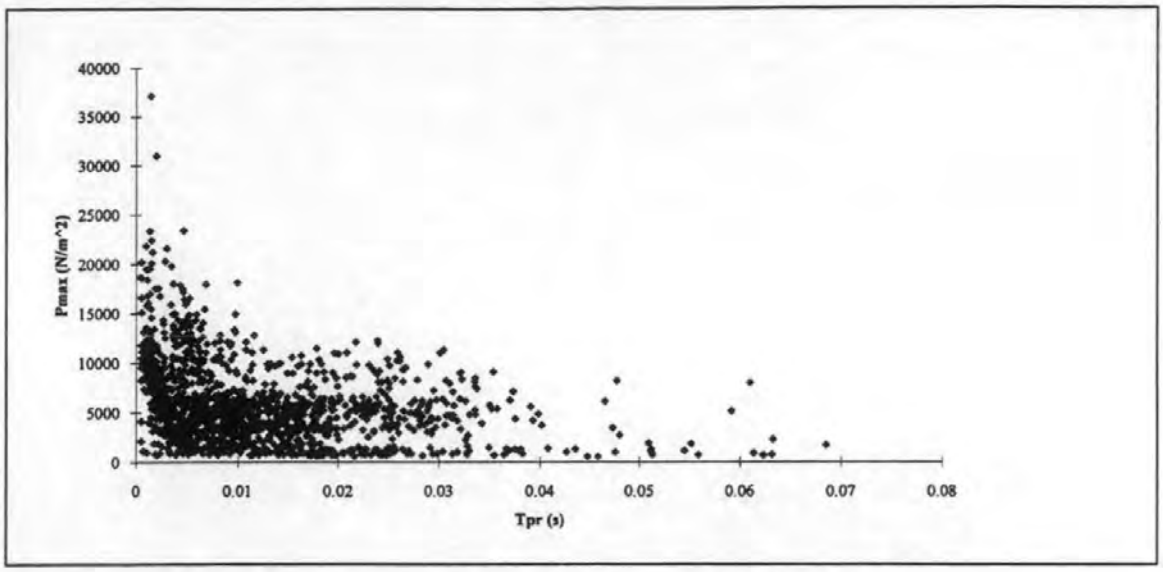

Figure B.3. Relationship between P_{max} and T_{pr} for test 08089605.

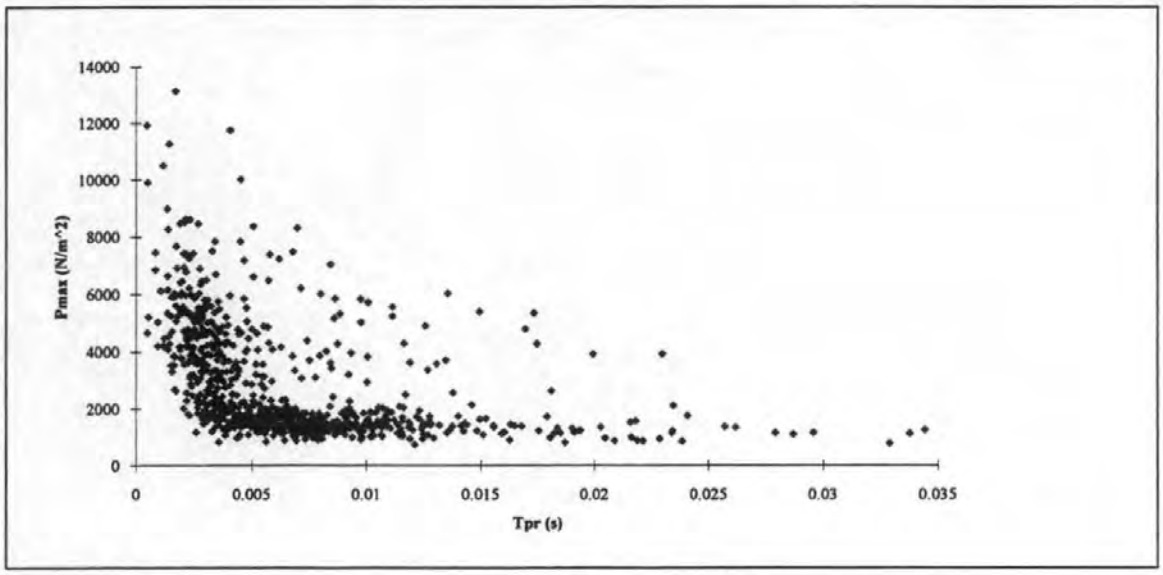

Figure B.4. Relationship between P_{max} and T_{pr} for test 08089606.

B.2 Histograms of impulse proportion

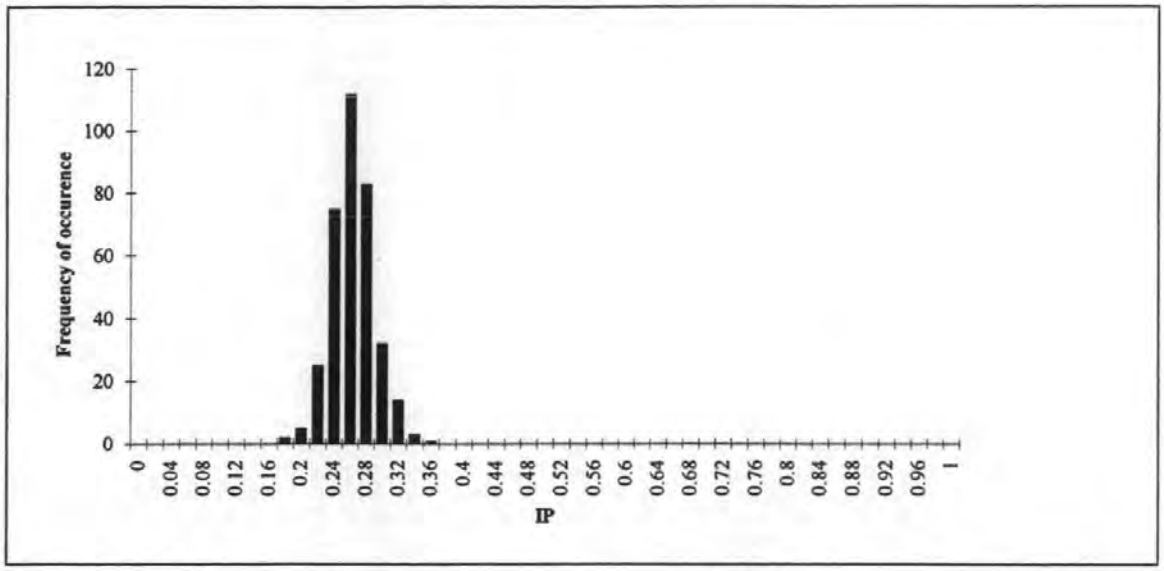

Figure B.5. Distribution of impulse proportion, test 08089602.

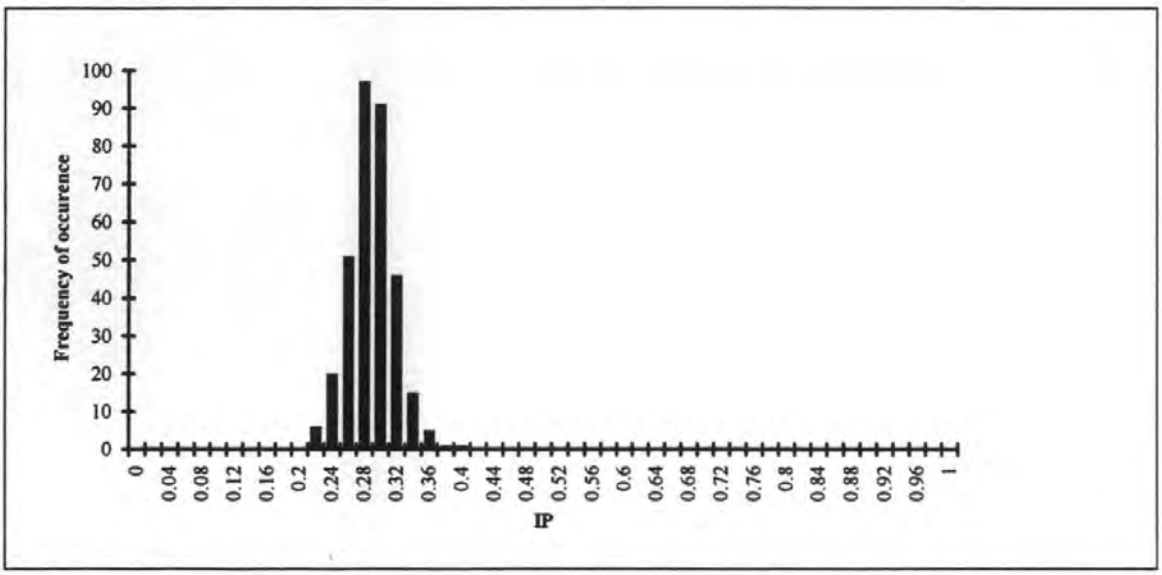

Figure B.6. Distribution of impulse proportion, test 08089603.

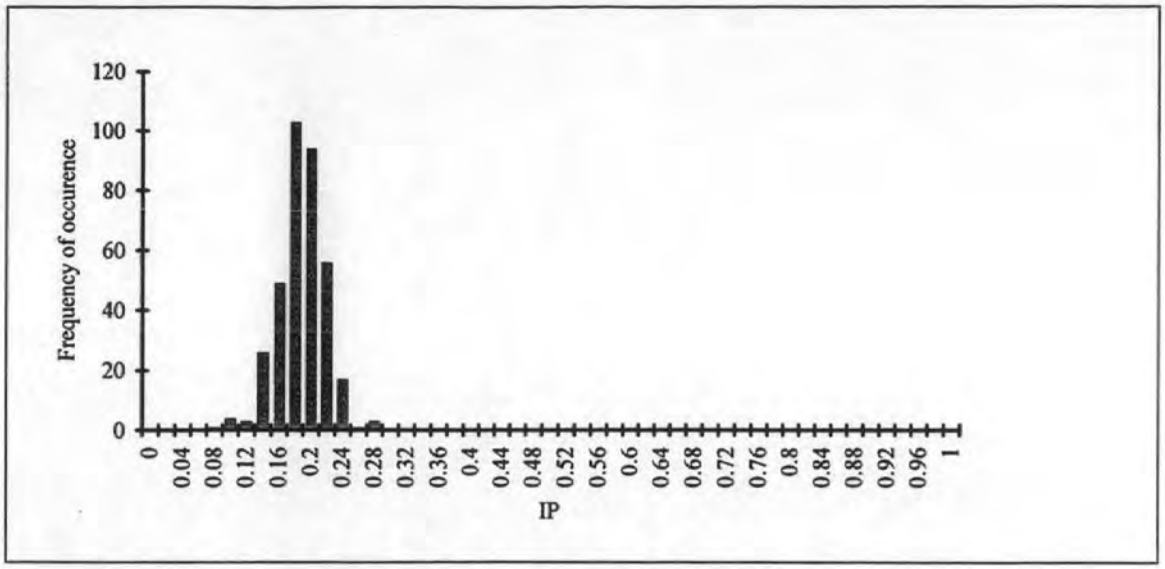

Figure B.7. Distribution of impulse proportion, test 08089604.

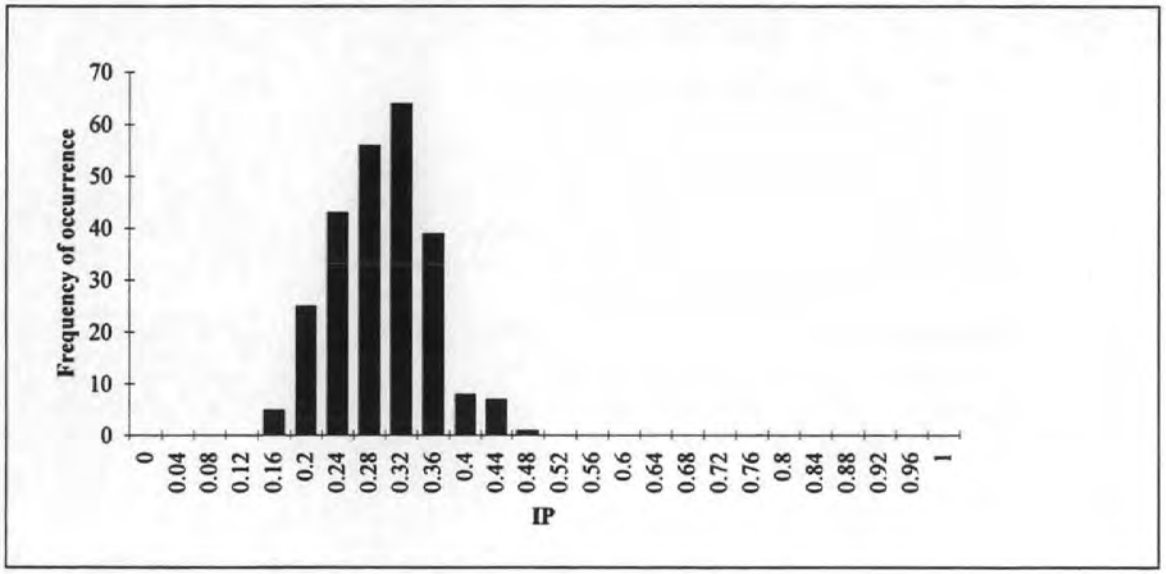

Figure B.8. Distribution of impulse proportion, test 08089605.

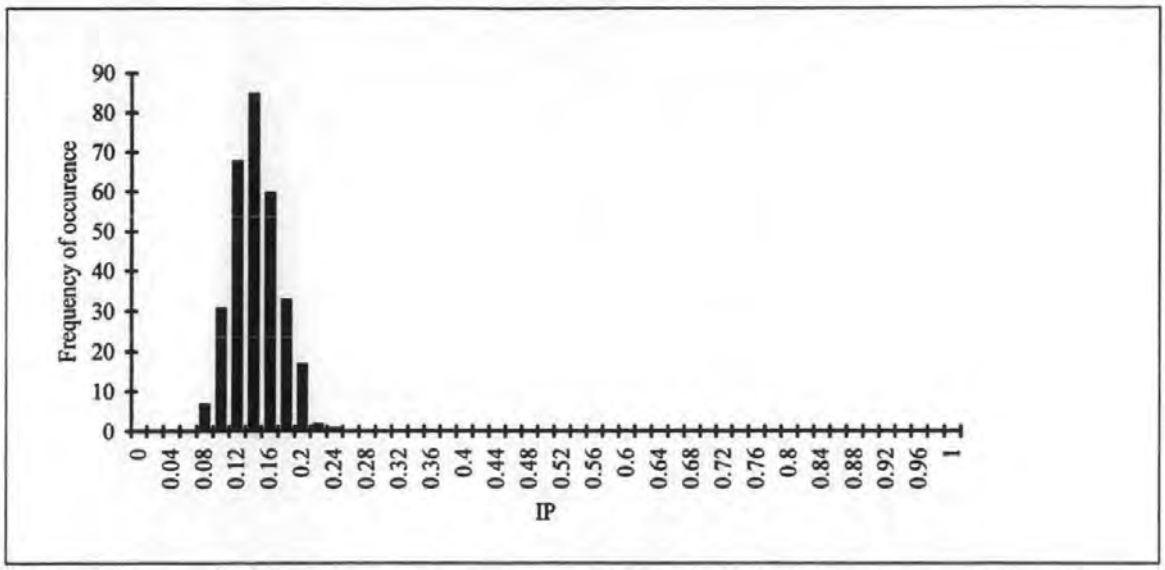

Figure B.9. Distribution of impulse proportion, test 08089606.

B.3 Histograms of normalised impact pressure maxima

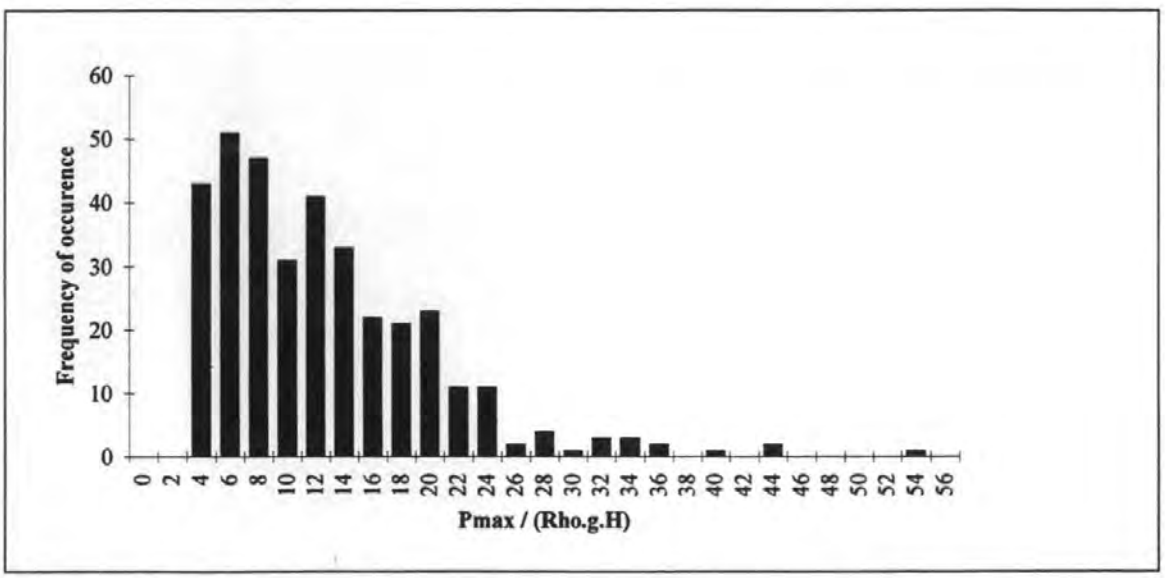

Figure B.10. Distribution of normalised impact pressure maxima, test 08089602.

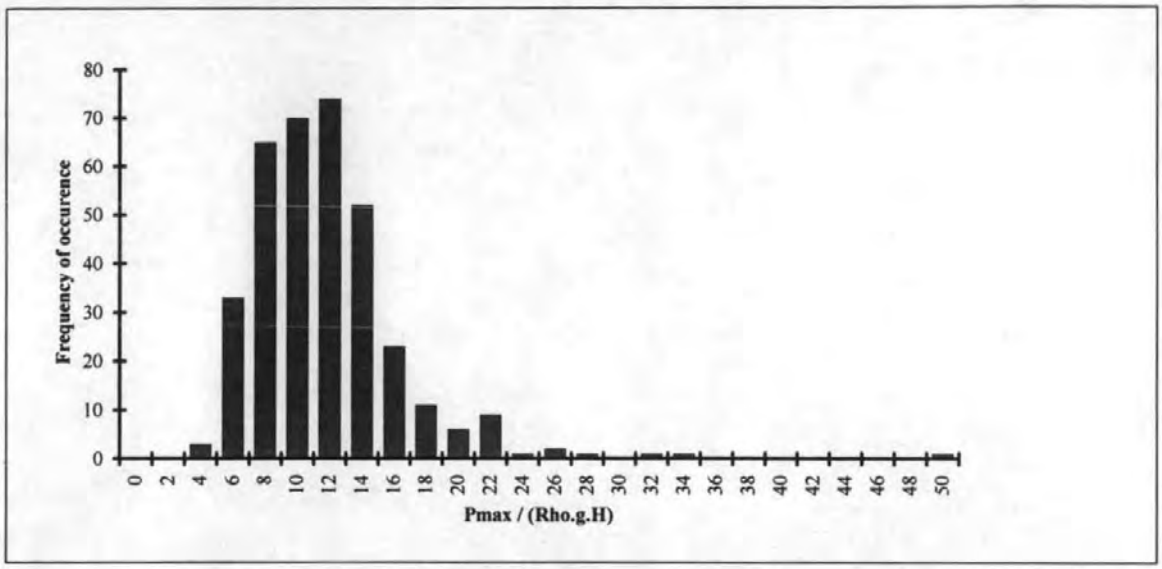

Figure B.11. Distribution of normalised impact pressure maxima, test 08089603.

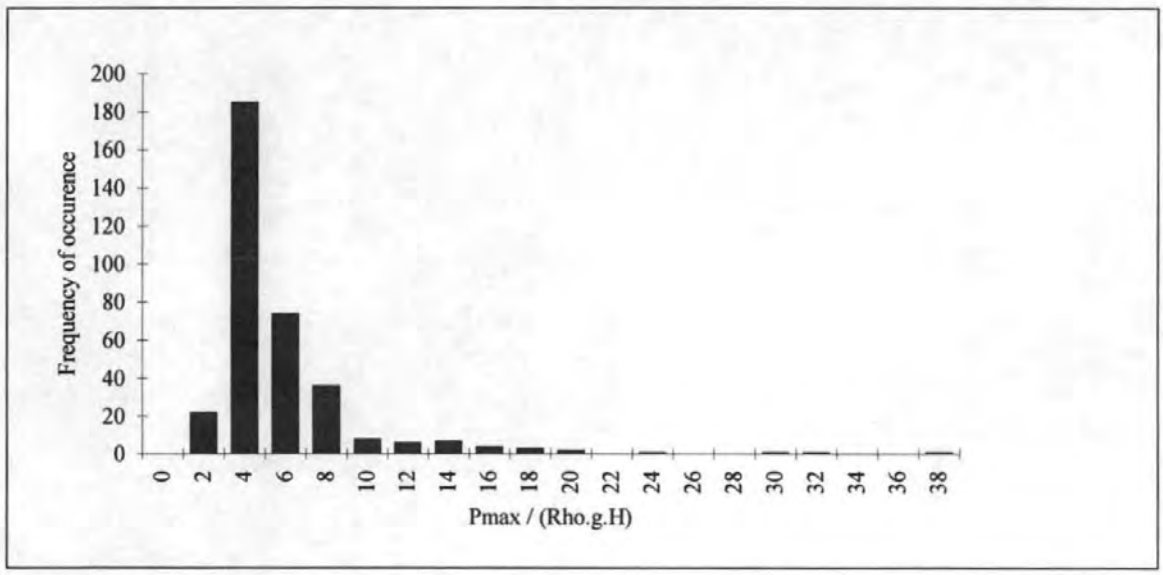

Figure B.12. Distribution of normalised impact pressure maxima, test 08089604.

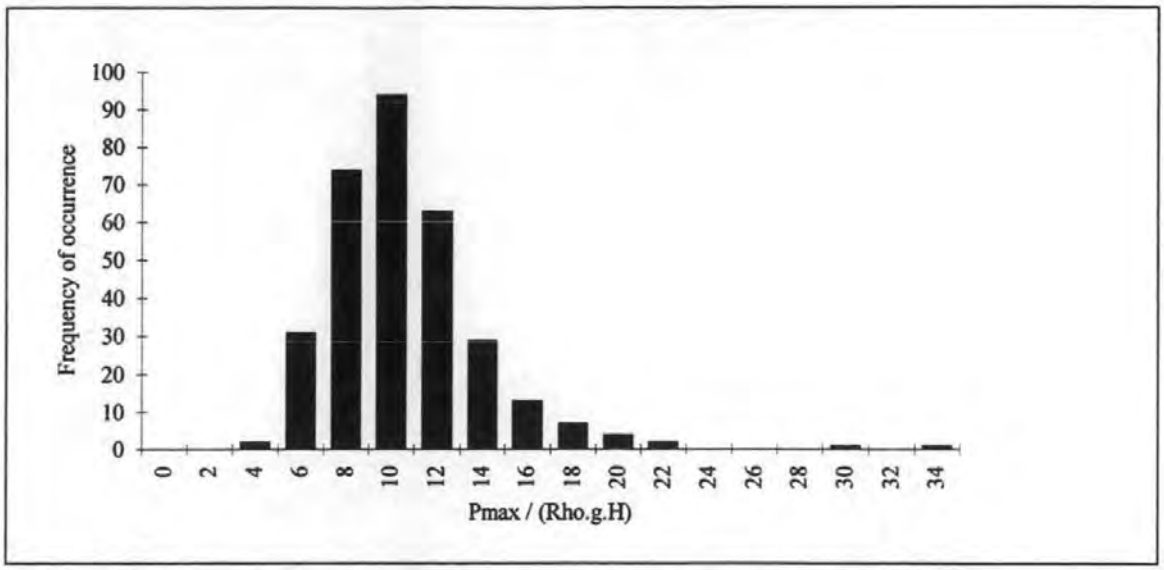

Figure B.13. Distribution of normalised impact pressure maxima, test 08089605.

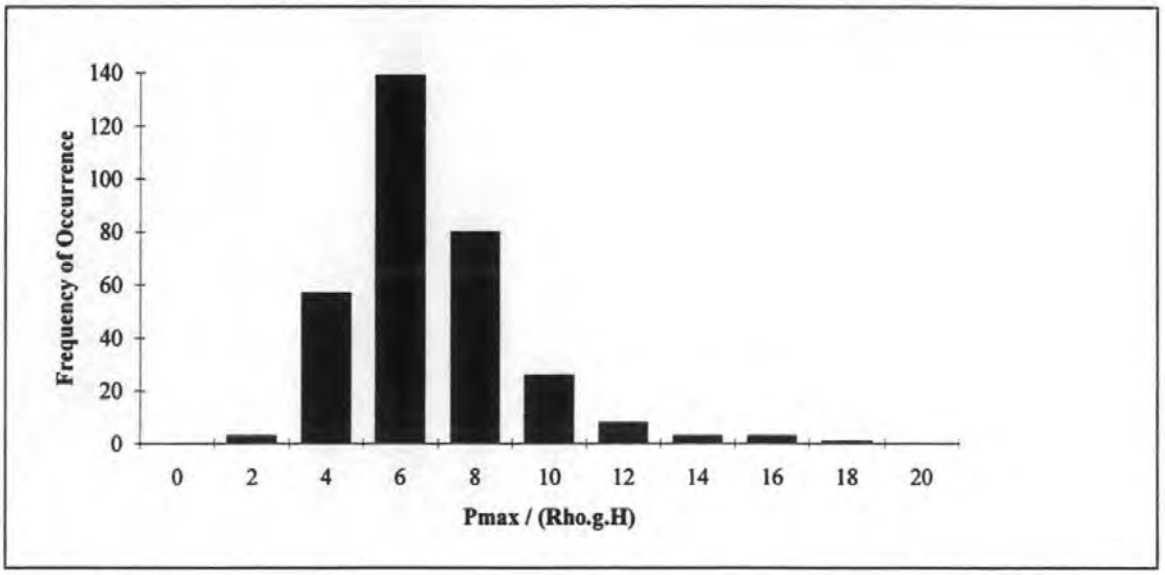

Figure B.14. Distribution of normalised impact pressure maxima, test 08089606.

B.4 F_{max} T_d relationships

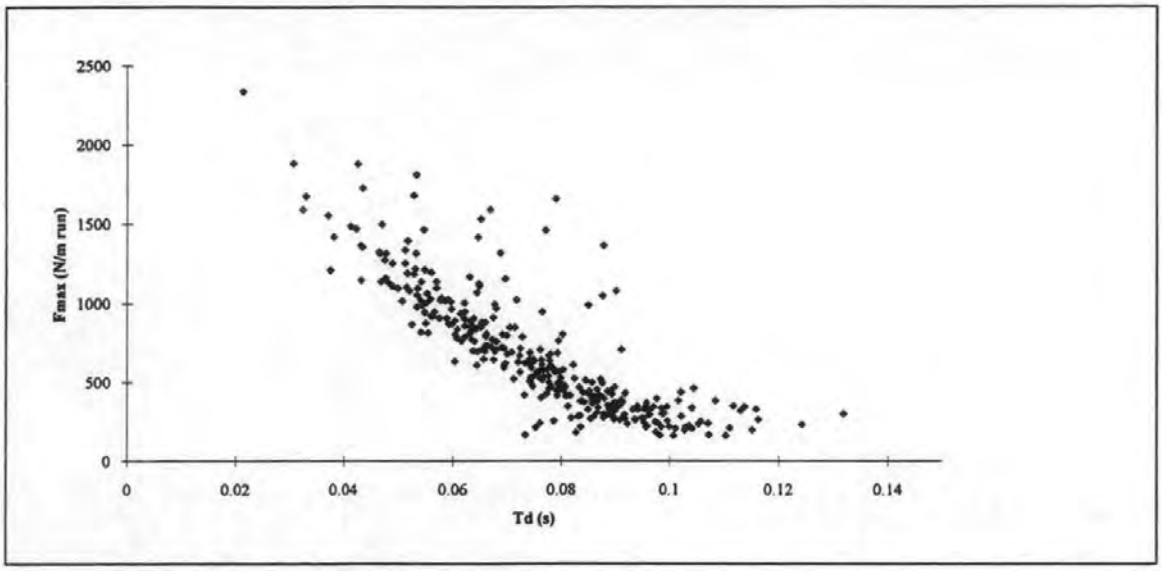

Figure B.15. F_{max} T_d relationship for test 08089602.

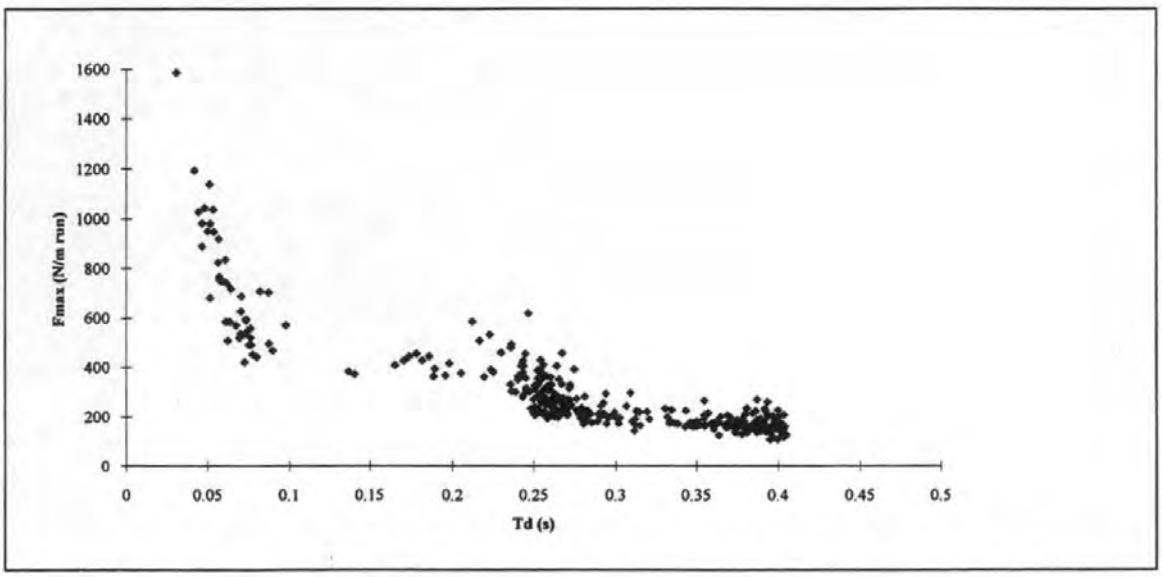

Figure B.16. F_{max} T_d relationship for test 08089604.

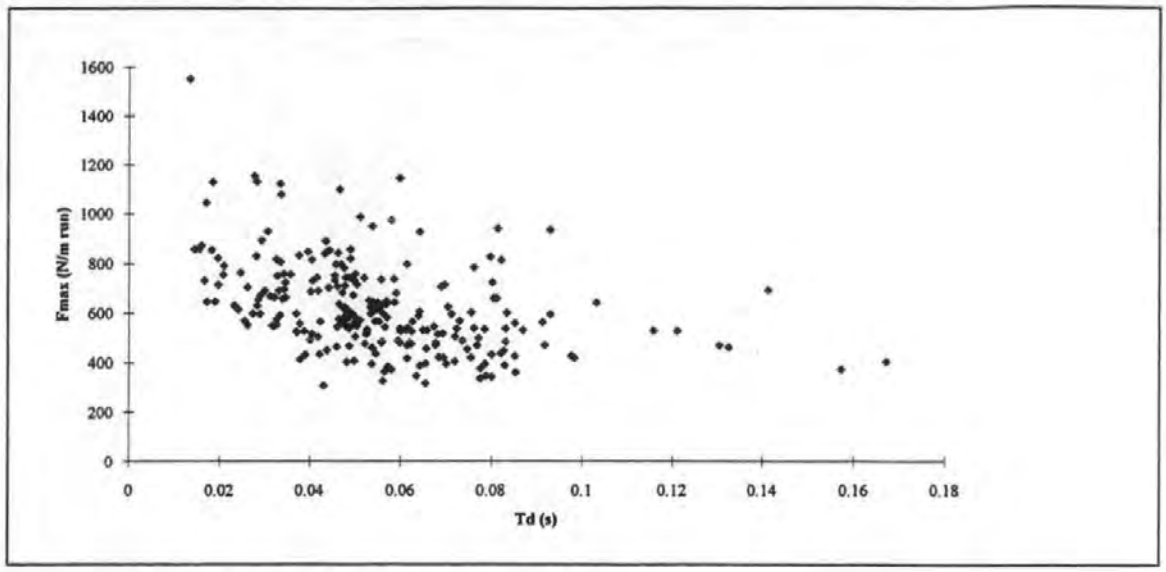

Figure B.17. F_{max} T_d relationship for test 08089605.

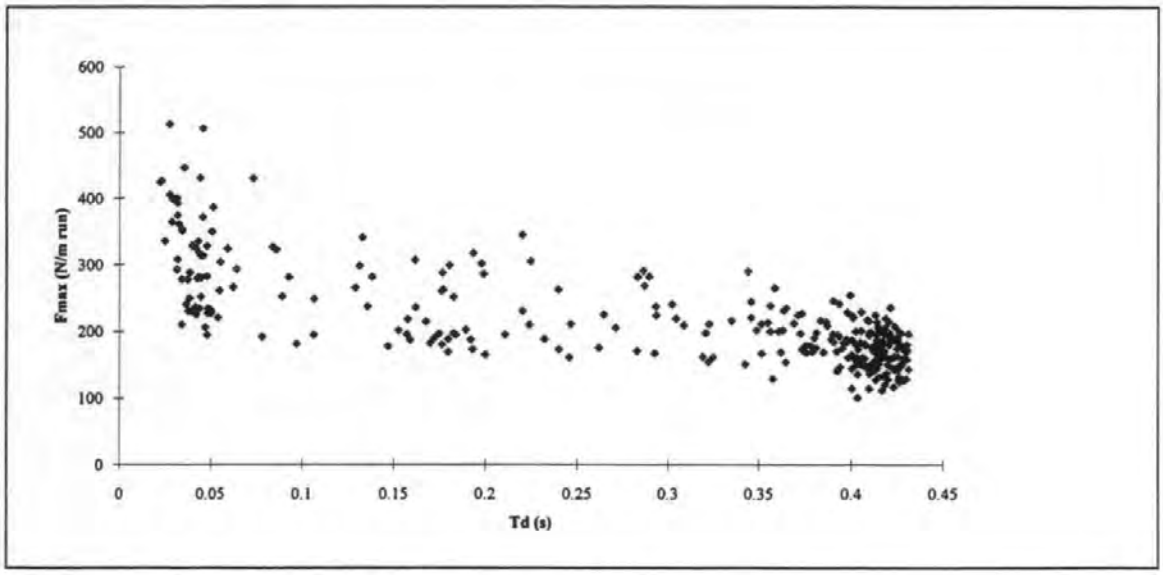

Figure B.18. F_{max} T_d relationship for test 08089606.